INSTITUTE OF SPACE AND ASTRONAUTICAL SCIENCE
YOSHINODAI, CHUO, SAGAMIHARA, KANAGAWA 252-5210

ISAS RESEARCH NOTE

ISAS RN 871

# Brown Dwarf Atmospheres Revealed with *AKARI* Near-Infrared Spectra

Satoko SORAHANA

June 2012

Department of Astronomy, Graduate School of Science,
The University of Tokyo

Department of Space Astronomy and Astrophysics,
Institute of Space and Astronautical Science (ISAS),
Japan Aerospace Exploration Agency (JAXA)

# Brown Dwarf Atmospheres Revealed with *AKARI* Near-Infrared Spectra

Satoko SORAHANA

Reproduced from the thesis submitted to
the University of Tokyo for
the Degree of Doctor of Science (Astronomy)
December, 2011

# Abstract

This thesis present new results on the nature of brown dwarf atmospheres revealed by the analysis based on the spectra taken by the infrared astronomical satellite *AKARI* and a brown dwarf atmosphere model. The main results of this thesis are summarized as follows.

1. We construct a spectral data set of brown dwarfs that continuously covers a new wavelength range, 2.5–5.0 $\mu$m,
2. we verify a generality of the molecular abundances deviating from a thermo-chemical equilibrium state for T dwarfs,
3. we show that L5 dwarfs with or without the $CH_4$ 3.3 $\mu$m band in their spectra differ in dust presence and mass (surface gravity) in addition to $T_{\rm eff}$,
4. we verify the theoretical prediction of radius inversion observationally for the first time,
5. we argue that the dust contribution to the atmospheric structure is larger than that in the current models, and
6. we suggest a possibility that relative C and O elemental abundances with respect to H are different in every objects.

Brown dwarfs are objects that are too light to maintain the hydrogen fusion in their cores. Their effective temperatures are very low as 2200–600 K. They are classified into newly introduced spectral types L and T. L dwarfs are warmer than T dwarfs. The study of brown dwarfs has been actively carried out since 1995, when the first genuine brown dwarf, Gl 229B, was discovered by Nakajima et al. Brown dwarfs are important as a bridge between stars and planets. With intermediate masses and temperatures, brown dwarfs are expected to have the blended properties of star and planet. However, their properties are actually quite unique, for example dusty photosphere, and it is not straightforward to understand their internal physical and chemical processes from our knowledges of stars and planets. Studies of brown dwarf atmosphere will lead us to understand the comprehensive nature of "atmospheres" of various objects from stars to planets.

Atmospheres of brown dwarfs are so cool and are dominated by molecules. When temperature decreases below the condensation temperature, dust forms in the photosphere. Dust affects the spectra of brown dwarfs by changing the photospheric structure and by extinction. The effects of dust are observed most apparently in the near-infrared spectra of L dwarfs. On the other hand, the spectra of T dwarfs show little sign of dust. This indicates that the dust in the photosphere disappears somewhere between L and T types. Since the mechanism of dust disappearance is not yet clear, current brown dwarf photosphere models implement dust segregation effect empirically through a model parameter. Such models can explain the observed SED more or less satisfactory. On the other hand, the models still have problems to

explain some molecular absorption bands especially in the spectra of late-L to T dwarfs. It is not clear whether the deviation of molecular abundance from theoretical prediction is general characteristics or not. This inconsistency is one of the essential problems in the study of brown dwarf atmospheres.

Spectroscopic observations in the infrared regime are the most powerful tools to obtain physical and chemical information of brown dwarf atmospheres through various molecular bands. So far, brown dwarf spectra shorter than 2.5 $\mu$m have been obtained by ground-based observations. The brown dwarf atmospheres have been investigated with the data, but it is difficult to discuss molecular abundances in detail and systematically because of weak and blended molecular overtone absorption bands. The wavelength range between 2.5 and 5.0 $\mu$m is the most suitable for this purpose as it contains features of major molecular spices, including the $CH_4$ $\nu_3$ fundamental band at 3.3 $\mu$m, $CO_2$ $\nu_3$ fundamental band at 4.2 $\mu$m, CO fundamental band at 4.6 $\mu$m and $H_2O$ $\nu_1$ and $\nu_3$ absorption bands around 2.7 $\mu$m. Since these fundamental bands of important molecules are non-blended each other, we can investigate these molecular bands in detail. However, observations in the wavelength range from the ground is always challenging. Severe absorption due to the Earth's atmosphere and limited wavelength coverage make the precise analysis difficult.

The Japanese infrared astronomical satellite *AKARI* was launched in February 2006. The InfraRed Camera (IRC) on-board *AKARI* is capable of yielding moderate-resolution (R$\sim$120) spectra in this important wavelength range devoid of any degradation by telluric features. We have conducted an observing program using the IRC to obtain continuous spectra of brown dwarfs in 2.5–5.0 $\mu$m wavelengths aiming to carry out systematic studies of physical and chemical processes in their atmospheres.

Twenty seven brown dwarfs, sixteen L dwarfs and eleven T dwarfs, were successfully observed by *AKARI*. The standard software toolkit *IRC_SPEC_TOOLKIT* was used for the data reduction. Wavelength and flux calibrations were all done in the toolkit. Spectral data are derived from two dimensional spectral image. We applied the following three additional processing to obtain better quality data. (1) derivation of appropriate sky background, (2) stacking of multiple observation data, and (3) correction of contaminated light from nearby objects. As a result, we obtain 18 continuous spectra of brown dwarfs from 2.5 to 5.0 $\mu$m for the first time. We validate the absolute flux calibration of the obtained *AKARI* spectra by comparing the integrated flux measured in the spectra with (i) the *AKARI* photometry data obtained simultaneously during the observation, and (ii) past photometry data in literatures. We find that absolute flux of the spectra is consistent with the both *AKARI* photometry and past photometry data within 30 % and 10 %, respectively.

As a first step, we investigate the behavior of various non-blended molecular fundamental bands in brown dwarf spectra, the $CH_4$ at 3.3 $\mu$m, CO at 4.6 $\mu$m and $CO_2$ at 4.2 $\mu$m, relative to their spectral types systematically with the 18 *AKARI* observed spectra. Carbon resides mostly in $CH_4$ rather than in CO in very cool (e.g. $T < 1000$K) and high density environment. The temperature of brown dwarf atmospheres is just around the boundary that $CH_4$ molecule starts appearing. The behavior of the $CH_4$ 3.3 $\mu$m fundamental band has not been investigated in detail because of fragmented and small number of data samples. It is also difficult to observe the CO 4.6 $\mu$m fundamental band. In the past study, two observed data of T6 and T8 dwarfs show that the CO absorption band strength is stronger than theoretical prediction, but its generality has not been ensured. We find that the $CH_4$ 3.3 $\mu$m fundamental band

appears in the spectra of dwarfs later than L5 and CO 4.6 $\mu$m band appears in the spectra of all spectral types until late-T dwarfs. Investigation of the $CO_2$ absorption band is the first attempt for the brown dwarf atmosphere. We detected $CO_2$ absorption band at 4.2 $\mu$m in the spectra of late-L and T type dwarfs. The result for the non-blended CO molecular band is very important because of the fact that CO generally exists in all brown dwarf atmospheres, which is against theoretical predictions. We also find that the $CO_2$ molecule is generally in the atmosphere of T dwarfs.

To understand the atmospheres of brown dwarfs better, we analyze the *AKARI* spectra using the Unified Cloudy Model (UCM) developed by Tsuji et al., which is one of the brown dwarf atmosphere models. We derive the physical parameters, effective temperature $T_{\rm eff}$, surface gravity log $g$ and critical temperature $T_{\rm cr}$, of *AKARI* samples by model fitting. We investigate how the parameters correlate with the spectral type. We confirm that the spectral types of late-L dwarfs are not a sequence of $T_{\rm eff}$, but a sequence of the decreasing of dust effect.

We investigate the property of the objects in which the $CH_4$ 3.3 $\mu$m band starts to appear. We find that the band is seen in two of four L5 dwarfs. We evaluate the physical condition of the photosphere of the objects by applying the UCM. We find that the model parameters of the sources with and without the $CH_4$ 3.3 $\mu$m band are systematically different, except for the effective temperature. Surface gravity and critical temperature, which is an additional parameter to determine the upper limit of the dust layer, of the objects with the $CH_4$ 3.3 $\mu$m band are higher than those of the objects without the band. Our model fitting analysis confirms that the appearance of the $CH_4$ absorption band at 3.3 $\mu$m in L5 type spectra depends on not only their effective temperatures but also dust presences and surface gravities. We suggest that the two groups are different in their masses.

Theoretical models of brown dwarf evolution predict that the radius of a young object follows a monotonically increasing function of mass and a decreasing function of age. On the other hand, for old object ($\geq 10^8$ yrs) the dependency of radius on mass inverts, i.e. the radii of less massive objects become larger because the less massive objects reach the terminal radii early. We derive the radii of the 18 *AKARI* objects using their parallaxes and the ratio of observed to model fluxes, and observationally verify this radius changes for the first time.

In this thesis we use the archived near-infrared spectra (IRTF/SpeX and UKIRT/CGS4, hereafter SpeX/CGS4) covering the shorter wavelength range (1.0–2.5 $\mu$m) along with *AKARI* to derive the physical parameters of the *AKARI* objects. With the additional short wavelength data we can constraint the model fitting better. However, a concern is that we could not determine a unique model that explains the entire wavelength range perfectly, and there are always some deviation. This has been pointed out in previous studies. In order to investigate this problem further, we fit the *AKARI* and SpeX/CGS4 spectra separately. We find that the *AKARI* spectra is more sensitive to the effective temperature, while the dust presence is better determined by the SpeX/CGS4 data. When the SpeX/CGS4 spectra show the presence of large amount of dust, the effective temperatures derived only from *AKARI* spectra show a higher value than those determined using the *AKARI*+SpeX/CGS4 data. The *AKARI* spectra also show higher effective temperatures when the SpeX/CGS4 spectra show a small amount of dust. These results imply that the warming up effect due to the dust in the photosphere is always underestimated in the model than that in the actual photosphere. Dust opacity is sensitive to the grain size distribution, their amount and

composition. We propose that a self-consistent, more realistic theory of condensation and sedimentation in the atmospheres is the most essential in the future brown dwarf atmosphere models.

The observed $CO_2$ absorption band in some objects is stronger or weaker than the prediction by the model. We discuss possible metallicity variation among brown dwarfs using the model atmosphere and the *AKARI* data. We construct a set of models with various elemental abundances as a first trial. We investigate the variation of the molecular composition and atmospheric structure. From the results, we suggest a possible reason of $CO_2$ 4.2 $\mu$m absorption feature in the late-L and T type spectra is the higher or lower C and O elemental abundances than the solar values used in the previous studies.

# Contents

# Chapter 1

# Introduction

## 1.1 What Are Brown Dwarfs?

Brown dwarfs play an important role as a bridge between stars and planets. They are intermediate mass objects in between them, and are expected to own blended properties of star and planet (including exoplanet). However their property is quite unique such as owing dusty photosphere, and it is not straightforward to understand their internal physical and chemical processes from our knowledges on stars and planets. Study of brown dwarf atmosphere will lead us to understand comprehensive nature of "atmospheres" of various objects from star to planet.

### 1.1.1 Definition of Brown Dwarfs

Brown dwarfs are generally defined as the objects that are too light to maintain hydrogen fusion in their cores. For the solar metallicity, the upper limit of their mass is 0.08 $M_\odot$ ($M_\odot$ means solar mass), i.e. is the hydrogen-burning main sequence edge mass. On the other hand, the lower limit of the mass is not defined clearly. The lower edge of mass range of brown dwarfs overlaps with that of planet, so the lightest brown dwarfs are not able to be distinguished from planets from their aspects. Instead they are defined by their formation process. Brown dwarfs are born in the interstellar medium similar to the processes by which stars arise. Objects that are born in protoplanetary disks by the processes different from those of stars should be referred to as planets. On the other hand, some researchers who are studying exoplanets define the lower mass limit of brown dwarfs as 0.0123 $M_\odot$, i.e. the deuterium-burning limit. In this thesis, we refer to the mass between 0.0123 $M_\odot$ and 0.08 $M_\odot$ as "brown dwarf mass", and to lower mass below 0.0123 $M_\odot$ as "planet mass", but both are called as brown dwarfs.

The effective temperatures ($T_{\rm eff}$) of brown dwarfs are as low as 2200–600 K. They are classified into two spectral types L and T (Kirkpatrick et al. 1999, 2000; Geballe et al. 2002). We show the L and T spectral classification defined by Geballe et al. (2002) in Table 1.1 as an example. L dwarfs adjacent to the hydrogen-burning main sequence, and warmer than T dwarfs. Recently, brown dwarfs much cooler than T dwarfs ($< 500$ K) are discovered (Leggett et al. 2009; Eisenhardt et al. 2010; Cushing et al. 2011; Kirkpatrick et al. 2011), and yet new spectral type, Y, is being considered. In August 2011, the

Table 1.1: Values of Indices for L and T subtyping

| Name | PC3 0.823–0.827/ 0.754–0.758 | Color-d 0.96–0.98/ 0.735–0.755 | $H_2O$ 1.2$\mu$m 1.26–1.29/ 1.13–1.16 | $H_2O$ 1.5$\mu$m 1.57–1.59/ 1.46–1.48 | $CH_4$ 1.6$\mu$m 1.56–1.60/ 1.635–1.675 | $CH_4$ 2.2$\mu$m 2.08–2.12/ 2.215–2.255 |
|---|---|---|---|---|---|---|
| L0..... | 2.4–2.6 | 4.5–5.5 | ... | 1.20–1.27 | ... | ... |
| L1..... | 2.6–2.85 | 5.5–6.5 | ... | 1.27–1.35 | ... | ... |
| L2..... | 2.85–3.25 | 6.5–7.5 | ... | 1.35–1.43 | ... | ... |
| L3..... | 3.25–4.25 | 7.5–10 | ... | 1.43–1.50 | ... | 0.91–0.94 |
| L4..... | 4.25–6.0 | 10–17 | ... | 1.50–1.55 | ... | 0.94–0.98 |
| L5..... | | 17–23 | ... | 1.55–1.60 | ... | 0.98–1.025 |
| L6..... | | 23–25 | ... | 1.60–1.65 | ... | 1.025–1.075 |
| L7..... | ... | ... | ... | 1.65–1.70 | ... | 1.075–1.125 |
| L8..... | ... | ... | ... | 1.70–1.80 | ... | 1.125–1.175 |
| L9..... | ... | ... | ... | 1.80–1.95 | ... | 1.175–1.25 |
| T0..... | ... | ... | 1.5–1.7 | 1.95–2.2 | 1.02–1.07 | 1.25–1.40 |
| T1..... | ... | ... | 1.7–1.9 | 2.2–2.5 | 1.07–1.15 | 1.40–1.60 |
| T2..... | ... | ... | 1.9–2.15 | 2.5–3.0 | 1.15–1.30 | 1.60–1.95 |
| T3..... | ... | ... | 2.15–2.5 | 3.0–3.5 | 1.30–1.50 | 1.95–2.75 |
| T4..... | ... | ... | 2.5–3.0 | 3.5–4.5 | 1.50–1.80 | 2.75–3.8 |
| T5..... | ... | ... | 3.0–4.5 | 4.5–5.5 | 1.80–2.50 | 3.8–5.5 |
| T6..... | ... | ... | 4.5–6.5 | 5.5–7.0 | 2.5–4.0 | 5.5–8.5 |
| T7..... | ... | ... | 6.5–10 | 7.0–9.0 | 4.0–6.0 | 8.5–12 |
| T8..... | ... | ... | 10–15(?) | 9.0-12(?) | 6.0–9.0(?) | 12–18(?) |

The spectral classification of L and T dwarfs. Each index is derived by calculating index $= \int_{\lambda_1}^{\lambda_2} f_\lambda d\lambda / \int_{\lambda_3}^{\lambda_4} f_\lambda d\lambda$, where $\lambda_i$ is the wavelength, which intervals in the numerator and denominator have the same length. (Geballe et al. 2002)

coolest brown dwarfs with temperatures as cool as the human body are detected from NASA's Wide-field Infrared Survey Explorer (WISE). The atmosphere temperature of WISE 1828+2650 are cooler than room temperature, or less than 298 K. Their spectral classification is not yet well defined.

### 1.1.2 The History of Brown Dwarf Studies

Astronomers had already conceived the presence of substellar objects, brown dwarfs, in 1960s (Hayashi & Nakano, 1963; Kumar, 1963). Theoretical works of brown dwarfs have been extensively studied by Burrows et al. (1997, 2001). However, it is so difficult to detect such a faint objects in the optical wavelength, and efforts of researchers are fruitless for long time. In 1988, an infrared detection of a faint companion around the white dwarf GD165 (Becklin & Zuckerman 1988) opened up a new field of brown dwarfs. The color of GD165B was very red and needed to be classified as much cooler object than M dwarfs (Zuckerman & Becklin 1992). Cooler brown dwarfs classified as T-dwarfs, were more difficult to find. The first genuine brown dwarf, Gl 229B, was discovered by Nakajima et al. (1995), and the study of brown dwarfs are dramatically evolved by this discovery thanks to the development of instruments. Recently, many brown dwarfs were detected with the Deep Near-Infrared Survey (DENIS, Delfosse et al. 1997; Martín et al. 1999), the Two Micron All Sky Survey (2MASS, Kirkpatrick et al. 1999, 2000) and

the Sloan Digital Sky Survey (SDSS, Fan et al. 2000). About 100 T dwarfs and much cooler Y dwarfs have been detected from WISE. So far, more than 800 brown dwarfs have been detected.

### 1.1.3 L Dwarfs

L dwarfs have relatively higher effective temperature than T dwarfs. The first possible was GD165B discovered by Becklin & Zuckerman (1988). GD165B is a companion of the white dwarf GD165A. Kirkpatrick et al. (1993) obtained an optical spectrum of GD165B and showed that it was quite different from those of M dwarfs and of planets. The spectrum of GD165B lacks TiO bands at 8432 and 8859 Å, which are usually seen in M-type stars. Figure 1.1 shows the lacking of these band features in the spectra of GD165B.

L dwarfs are characterized by red $J-Ks$ colors, which have been generally attributed to dust extinction (Leggett et al. 1998). The reddest colors of L dwarfs are $J-Ks \sim 2.1$ (Kirkpatrick et al. 1999, 2000). Their near infrared spectra between 0.8 and 2.5 $\mu$m are dominated by $H_2O$ and CO absorption bands (Leggett et al. 2001; Reid et al. 2001; Testi et al. 2001; Wilson et al. 2001) as shown in Figure 1.3, while in the optical and $J$ band spectra, several features attributed to K I, Na I, and FeH (McLean et al. 2000) present. In the later spectral types, these features are generally weaken, while both $H_2O$ and CO bands get strenger (Leggett et al. 2001; Reid et al. 2001). Due to these changes, $J-Ks$ color changes slightly toward blue from L6 to L8 (Kirkpatrick et al. 2000). Most radiation from these objects are emitted in the 1– 2.5 $\mu$m range.

### 1.1.4 T Dwarfs

The first ultra cool dwarf, Gliese 229B, was discovered by Nakajima et al. (1995) in the image obtained with the 200-inch Hale telescope at Palomar with coronagraph. Figure 1.2 shows the image taken by NASA's Hubble Space Telescope wide field planetary camera. Gliese 229B is a companion of the M1 V dwarf Gliese 229A. The follow up spectroscopic observation by Oppenheimer et al. (1995) confirmed that this object is bona fide brown dwarf with presence of $CH_4$ absorption in its near infrared spectrum as Jupiter. $J-Ks$ color is bluer than L-type due to $CH_4$ absorption band at $Ks$ band. $CH_4$ and CIA $H_2$ opacity dominates $K$ band flux in T dwarfs. The presence of $CH_4$ in T dwarfs distinguishes them from the L dwarfs (Kirkpatrick et al. 1999). Figure 1.3 shows the $CH_4$ absorption at 2.2 $\mu$m. We can see the $CH_4$ absorption in the spectra of T dwarf GL 229B. The CIA $H_2$ in $K$ band also plays an important role in shaping the peak of this band (Tokunaga & Kobayashi 1999).

### 1.1.5 Photospheres of Brown Dwarfs

Photospheres of brown dwarfs are so cool ($T_{\rm eff}$ = 600 – 2200 K) and dense ($\log P_g \sim 6.0$), thus dominated by molecules and dust. The condensation of dust under the thermochemical equilibrium photosphere has been discussed already in 1960s (e.g. Lord, 1965; Larimer, 1967; Larimer & Anders, 1967). The elements that construct dust grains are Fe, Mg, Si, O, and Al. When temperature decreases below a certain threshold (∼2000K), condensation starts in the photosphere. For L dwarfs the dust exists in the

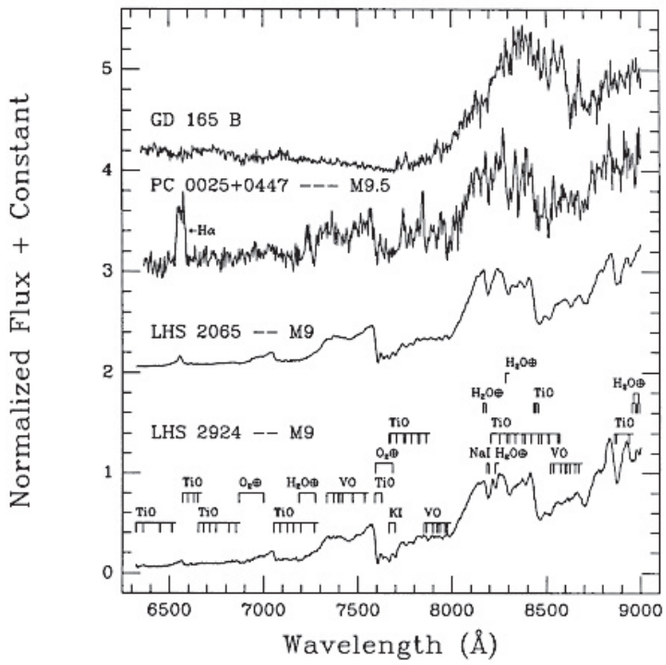


Figure 1.1: Optical spectra of GD 165B and three late-M dwarfs, LHS 2924 (M9 V), LHS 2065 (M9 V), and PC 0025+0447 (M9.5 V). Molecular, atomic, and telluric features are showed in the spectrum of LHS 2924. (Kirkpatrick et al. 1993)

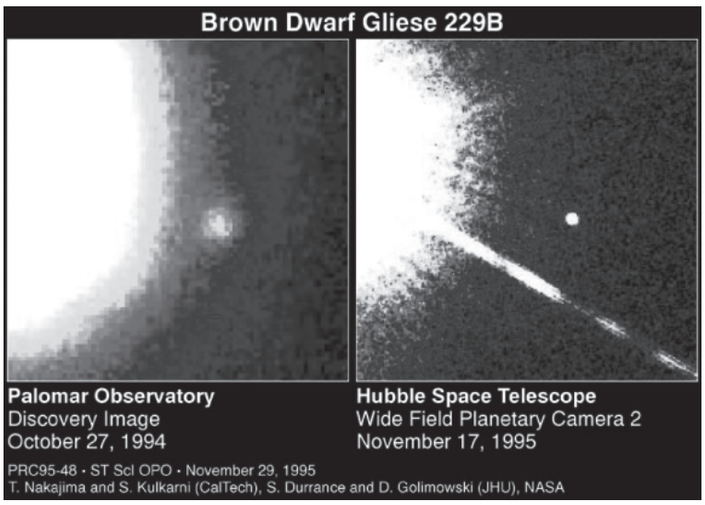


Figure 1.2: Image of Gliese 229B. Gliese 229B was detected as the genuine brown dwarfs by Nakajima et al. (1995) for the first time. (NASA, http://starchild.gsfc.nasa.gov/Images/StarChild/questions/)

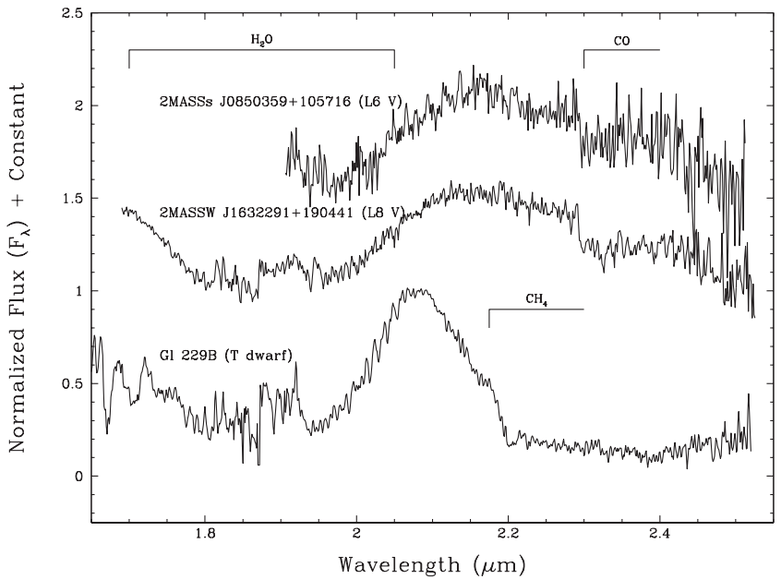


Figure 1.3: 1.7–2.5 $\mu$m spectra for two late-L dwarfs and Gliese 229B. The $CH_4$ absorption band at 2.2 $\mu$m, which is a key feature for T classification, are indicated (Kirkpatrick et al. 1993).

upper photosphere that contributes to its spectral features. On the other hand, for T dwarfs with lower $T_{\rm eff}$ the dust disappears in the photosphere and does not play any role on the spectral features.

Chemistry in the photosphere and resulted molecular abundances determine the spectra of brown dwarfs. Hydrogen is predominantly in the form of $H_2$. The dominant equilibrium form of carbon is CO and $CH_4$, oxygen is $H_2O$, and nitrogen is $N_2$ and $NH_3$. Silicates, TiO and VO are found at temperatures $T_{\rm eff}$ above 1600–2000 K. Neutral alkali metals are found at $T_{\rm eff}$ above $\sim$ 1000 K (Fegley & Lodders 1996). These have been derived by solving the thermo-chemical equilibrium in theory. Now, these data can be obtained from various sources.

## 1.2 Radiation from Brown Dwarfs

Cores of brown dwarfs are convective hydrogen and helium. No nuclear fusion takes place in the core. Instead, heavier brown dwarfs maintain deuterium burning in their cores when they are young ($\sim 10^6$ yrs). Hence, they simply cool off after the deuterium burning, and thermonuclear processes do not dominate their evolution (see Figure 1.4 from Burrows et al. 2001). They radiate mostly in the near infrared regime. In addition, the radiation from inner photosphere become weaker by the effect of dust extinction which is different between spectral types, L and T.

## 1.3 Spectral Features of Brown Dwarfs

Spectroscopic observations in the infrared regime are the most powerful tools to obtain physical and chemical information of brown dwarf photospheres, since brown dwarf emits majority of energy in these

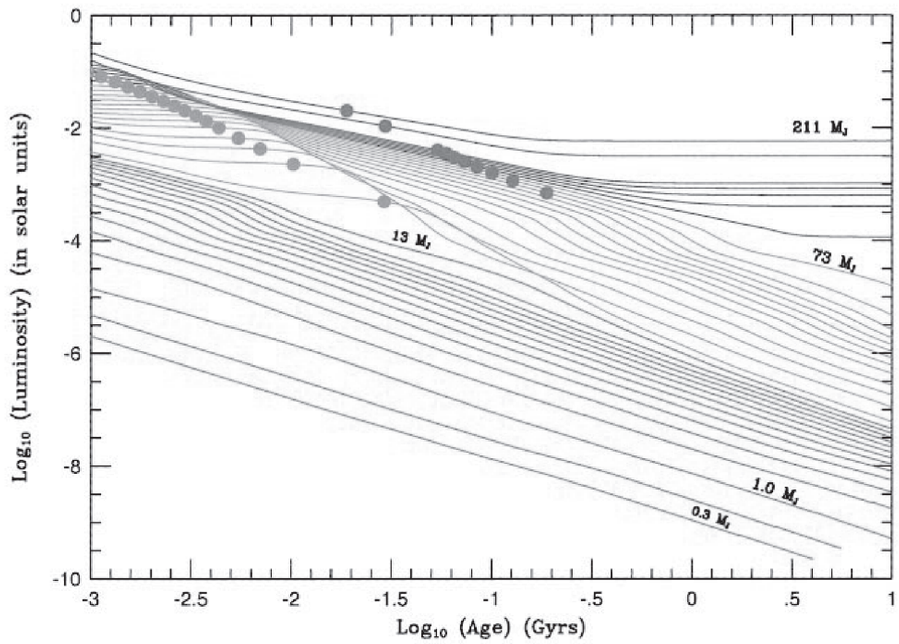


Figure 1.4: Evolution of the luminosity (in $L_{\odot}$) of isolated solar-metallicity substellar mass objects versus age (in years). Stars above $73M_J$ are shown in blue, brown dwarfs above $13M_J$ are shown in green, and brown dwarfs/giant planets equal to or below 13 $M_J$ are shown in red. The object with the mass heavy enough for hydrogen burning are shown in blue, that with deuterium are shown in green, and another mass are shown in red. The gold dots show the age when 50 % of the deuterium has burned and the magenta dots mark when 50 % of the lithium has burned. The masses of the substellar objects/stars portrayed are 0.3, 0.5, 1.0, 2.0, 3.0, 4.0, 5.0, 6.0, 7.0, 8.0, 9.0, 10.0 11.0, 12.0, 13.0, and $15.0M_J$ and 0.02, 0.025, 0.03, 0.035, 0.04, 0.045, 0.05, 0.055, 0.06, 0.065, 0.07, 0.075, 0.08, 0.085, 0.09, 0.095, 0.1, 0.15, and $0.2M_{\odot}$ ($\equiv 211M_J$). (Burrows et al. 2001)

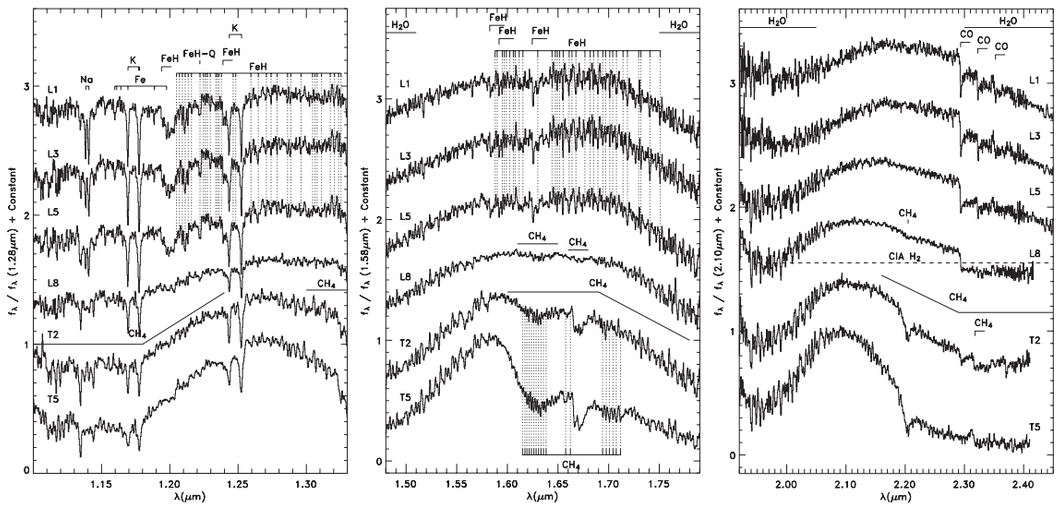


Figure 1.5: $J, H, K$ band spectra of 2MASS J1439+1929 (L1), 2MASS J1506+1321 (L3), 2MASS J1507–1627 (L5), DENIS J0255–4700 (L8), SDSS J1254–0122 (T2), and 2MASS J0559–1404 (T5). The most prominent molecular and atomic features are indicated. (Cushing et al. 2005)

wavelengths and various molecular and dust features present in the range. Dust in the photosphere contributes to the spectra directly by filling in the molecular absorption bands and by dust extinction as well as indirectly by changing the structure of the photosphere. The effect of dust appears mainly in the near infrared spectra of L dwarfs (Tsuji et al. 1996b; Nakajima et al. 2001). Meanwhile, the spectra of T dwarfs are less affected by the dust. This indicate that the dust disappears somewhere in the L-T boundary.

### 1.3.1 Wavelength Range between 0.7 and 2.5 $\mu$m

Many photometric/spectral observations have been made in the near-infrared wavelength range between 0.7 and 2.5 $\mu$m for studying the brown dwarf photosphere, since this wavelength range contains the spectral peaks for L dwarfs and is relatively easy to observe. This wavelength range contains features of various molecular spices (e.g. TiO, VO, FeH, $H_2O$ and $CH_4$). These molecular bands in the $J$, $H$ and $K$ bands have been used for classification of brown dwarfs in a wide range of spectral types (Geballe et al. 2002, hereafter G02). L dwarfs are characterized by the disappearance of gas-phase TiO (0.82, 0.84$\mu$m) and VO (0.79$\mu$m). T dwarfs are characterized by $CH_4$ absorption band at 1.6$\mu$m and 2.2$\mu$m (Martin 1997; Martín et al. 1999; Kirkpatrick et al. 1999, 2000; Strauss et al. 1999; Leggett et al. 2000, 2002b; Geballe et al. 2002; Burgasser et al. 2002; Hawley et al. 2002). In addition, $J$ and $H$ band wavelengths are sensitive to dust extinction, and enable us to understand dust contribution to the brown dwarf spectra.

### 1.3.2 Wavelength Range between 2.5 and 5.0 $\mu$m

The wavelength range between 2.5 and 5.0 $\mu$m contains molecular features of $CH_4$, $CO_2$, CO and $H_2O$. The fundamental bands of CO (4.6 $\mu$m) and $CH_4$ (3.3 $\mu$m) are strong and rather isolated from other

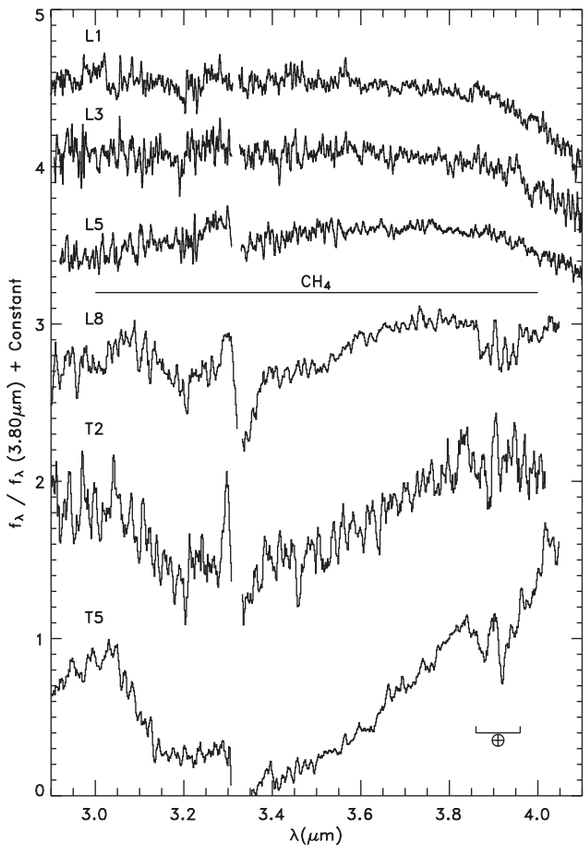


Figure 1.6: $L$ band spectra of same objects shown in Figure 1.5. The absorption features seen in the spectra of DENIS J0255–4700 and 2MASS J0559–1404 centered at $\sim$3.9 $\mu$m are due to incomplete removal of the $N_2O$ telluric feature. (Cushing et al. 2005)

molecular bands. This wavelength range is especially important for investigating structures of brown dwarf photosphere by measuring the fundamental bands of two major carbon-containing molecule, CO and $CH_4$. CO is the most abundant molecule after $H_2$ in the atmosphere of cool stars (M-type). As the temperature decreases, carbon is transferred from CO to $CH_4$, then carbon resides mostly in $CH_4$ rather than in CO in the very cool (e.g. $T < 1000$K and high density) environment (Tsuji 1964). In addition, there is $CO_2$ fundamental absorption band at 4.2 $\mu$m. However, these molecular absorption bands are hardly observed from the ground due to $H_2O$ and $CO_2$ in the telluric atmosphere except for $M$ and $L'$ band. CO and $CH_4$ absorption bands are presented in the $M$ and $L'$ band respectively, but it is difficult to obtain high quality spectral data. Since observation of these bands is an ideal tool for studying brown dwarf atmosphere, we have to observe this wavelength range from space based telescopes.

### 1.3.3 Wavelength Range beyond 5.0 $\mu$m

In the wavelength range longer than 5.0$\mu$m, there are absorption bands of $H_2O$ centered at 6.27$\mu$m, $CH_4$ $\nu_4$ at 7.65$\mu$m, and $NH_3$ at 10.5 $\mu$m. The presence of the $\nu_2$ fundamental band of $NH_3$ at 10.5 $\mu$m is one of

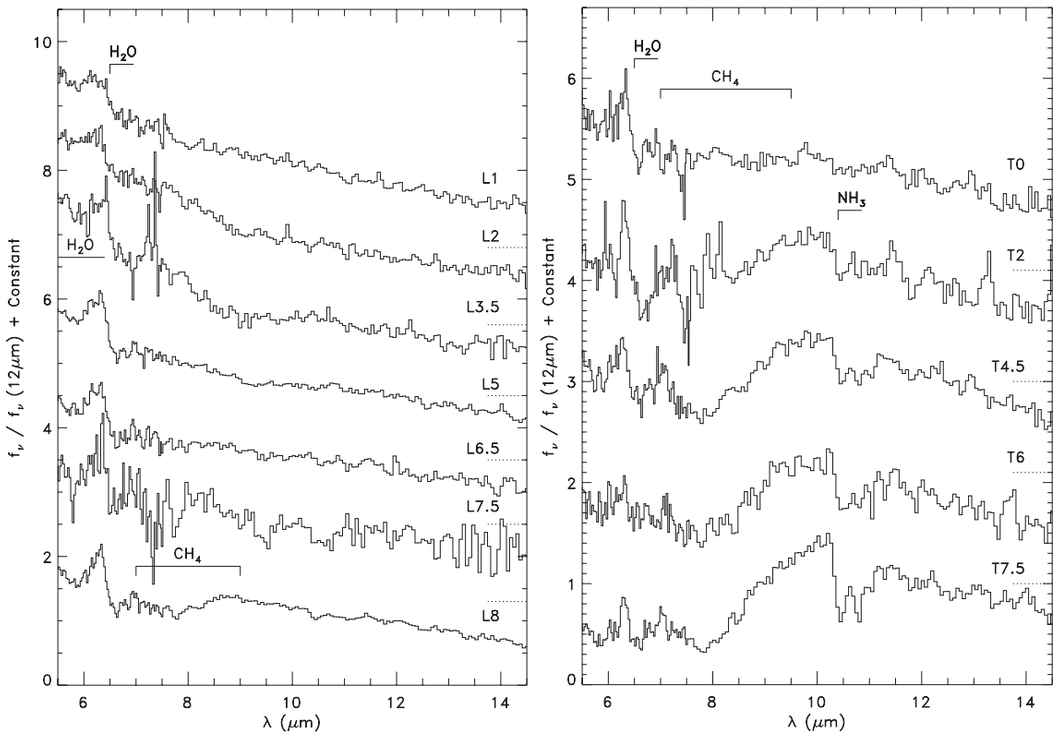


Figure 1.7: The 5.5–14.5 $\mu$m spectra of SDSS J0423–0414 (T0), SDSS J1254–0122 (T2), 2MASS J0559–1404 (T4.5), SDSS J1624+0029 (T6), and Gl 570D (T7.5). The spectra have been normalized at 12 $\mu$m and offset by constants (dotted lines). (Cushing et al. 2006)

the most important features for understanding the atmosphere structure of brown dwarf. For example, the abundance of $NH_3$ is found to depart from chemical equilibrium (Saumon et al. 2006, see section 1.4), and the investigation of $NH_3$ may lead us to understand the non-equilibrium chemical abundances in brown dwarf atmospheres. Saumon et al. (2006) attempt to solve this problem considering the kinetics of nitrogen chemistry in the presence of vertical mixing using the $NH_3$ absorption detected by IRS onboard Spitzer Space Telescope, which is launched in 2003.

## 1.4 The Purpose of This Thesis Study

**Possible Non-Equilibrium Effects on the Molecular Abundances**

Since almost all carbon atoms are transferred from CO to $CH_4$ in the photosphere of T-type dwarfs with $T_{\rm eff}$ less than about 1300K under thermochemical equilibrium, we had expected that CO absorption band did not appear in the spectra of these coldest dwarfs. However strong CO absorption band at 4.6 $\mu$m was unexpectedly observed in Gl 229B (Oppenheimer et al. 1998; Noll et al. 1997; Geballe et al. 2009). Figure 1.8 shows the strong CO absorption in the T8 dwarf Gl 570D. Another example of deviation from the thermal equilibrium chemistry was found in the nitrogen containing molecule. $NH_3$ absorption band at 10.5 $\mu$m was also inconsistent with that expected by an atmosphere model (Saumon et al. 2006). Further,

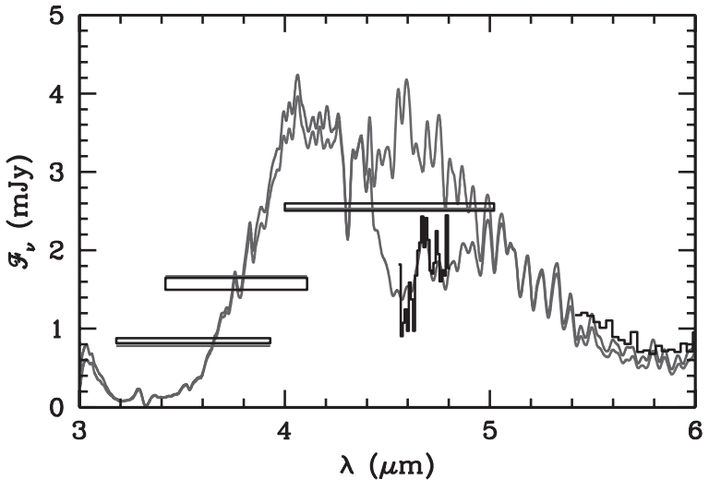


Figure 1.8: The M-band spectrum of Gl 570D. The data are the black histogram. The red curve is the local thermodynamic equilibrium (LTE) model and the blue curve is the non-equilibrium (vertical mixing) model. While the LTE model does not explain the observed spectra, the vertical mixing model explain the observation. (Geballe et al. 2009)

$CO_2$ absorption band at 4.2 $\mu$m detected by *AKARI*, the Japanese infrared astronomical satellite, was also stronger than expected (Yamamura et al. 2010). These discrepancy between observed and model spectra are a critical problem for the study of brown dwarf atmospheres. To interpret the unusual abundance of these molecules, Griffith & Yelle (1999) suggested the vertical mixing that CO are dredged up from inner area to surface region. Yamamura et al. (2010) attempted to explain the discrepancy of CO band strength in late-L to late-T dwarfs by vertical mixing effect. They argue that the CO band in late-T dwarfs could be reproduced by this effect, but earlier brown dwarfs between late-L and mid-T dwarfs can not be. The excess of $CO_2$ abundance can not be also explained by the vertical mixing. Thus alternative ideas are required to solve these problems.

**Presence of $CH_4$ in L-Dwarfs**

The presence of $CH_4$ absorption in near-infrared spectrum ($J, H, K$ bands) is one of the key features to define the T-type brown dwarf (Oppenheimer et al. 1995) On the other hand, Noll et al. (2000) reported detections of $CH_4$ 3.3 $\mu$m fundamental band in L8 (2MASSI J0825+2115) and L5 (2MASSW J1507–1627) dwarfs (Figure 1.9). This result indicated that $CH_4$ molecule could be present in the photosphere of mid-L dwarfs. They argued that the effective temperature gave little influence on the appearance of methane 3.3 $\mu$m band in the model spectra with $T_{\rm eff}$ ranging 1400–2000K, but did not know which physical parameters concern the spectral feature. Nakajima et al. (2001) confirmed "non" detection of the $CH_4$ band in the $H$ and $K$ band of the same object (2MASSW J1507–1627) reported by Noll et al. (2000). They analyzed the observed data with "dusty model" by Tsuji (2000) and concluded that the dust veils the molecular bands in $H$ and $K$ band. To understand the behavior of $CH_4$ molecule in the photospheres of L-type brown dwarfs, we have to study the 3.3 $\mu$m band, which are less affected by the dust than $H$

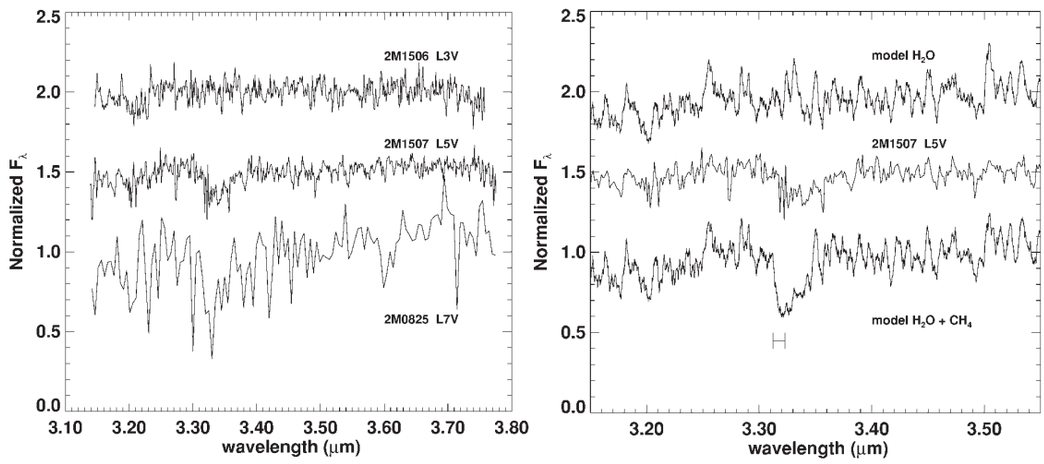


Figure 1.9: Spectra of three brown dwarfs, 2MASS J1506+1321(L3), 2MASS J1507–1627(L5), and 2MASS J0825+2115(L7). (a) The spectra have been rebind, normalized, and offset. The broad absorption feature at 3.3 $\mu$m is the $\nu_3$ Q-branch of $CH_4$. It presents in both the L5 and L7 objects but the spectrum of 2MASS J0825+2115 is difficult for precise analysis. (b) Spectra of 2MASS J1507–1627 and two model spectra of effective temperature 1800 K. One of these model spectra is with only water vapor and other is with water and methane.

and *K* band. However, spectroscopic observation of the $CH_4$ band in the *L* band from the ground for faint brown dwarfs are always challenging. Severe atmospheric absorption and limited wavelength coverage make the precise analysis difficult. High quality data taken from the space have been desired.

**Fitting the Spectra of Brown Dwarfs**

Cushing et al. (2008) reported that their model spectra result only poorly fits the observed spectra in the 0.95–14.5 $\mu$m for the mid- to late-L dwarfs and the early-T dwarfs (Figure 1.10). They used data observed by IRTF (0.9–2.5 $\mu$m and 3.0–4.0 $\mu$m) and Spitzer (5.0–14.5 $\mu$m). They also concluded that the relatively poor fits at the L/T boundary, where dust give the largest contribution on the SED of brown dwarfs, is most likely due to the limitations of their simple cloud model (Marley et al. 2002). Especially, 3.0–4.0 $\mu$m range spectra of the L/T boundary objects, DENIS 0255–4700 (L8) and SDSS 1254–0122 (T2), resulted in the poorest fits. To understand the cause of the poor fits at the L/T boundary, we have to observe 3.0–4.0 $\mu$m spectra of more objects.

## 1.5 Significance of Wavelength Range between 2.5 to 5.0 $\mu$m

In the wavelength range of 2.5 to 5.0 $\mu$m, there are several prominent molecular absorption bands; $CH_4$ $\nu_3$ fundamental band at 3.3 $\mu$m, $CO_2$ $\nu_3$ fundamental band at 4.2 $\mu$m, CO fundamental band at 4.6 $\mu$m and $H_2O$ $\nu_1$ and $\nu_3$ absorption bands around 2.7 $\mu$m (see Figure 1.11). The CO and $CH_4$ absorption bands also present in the shorter wavelength range ($\leq$ 2.5 $\mu$m) as shown in Figure 1.11 and these bands have been used in the previous studies. However, it is impossible to analyze these molecular bands in-

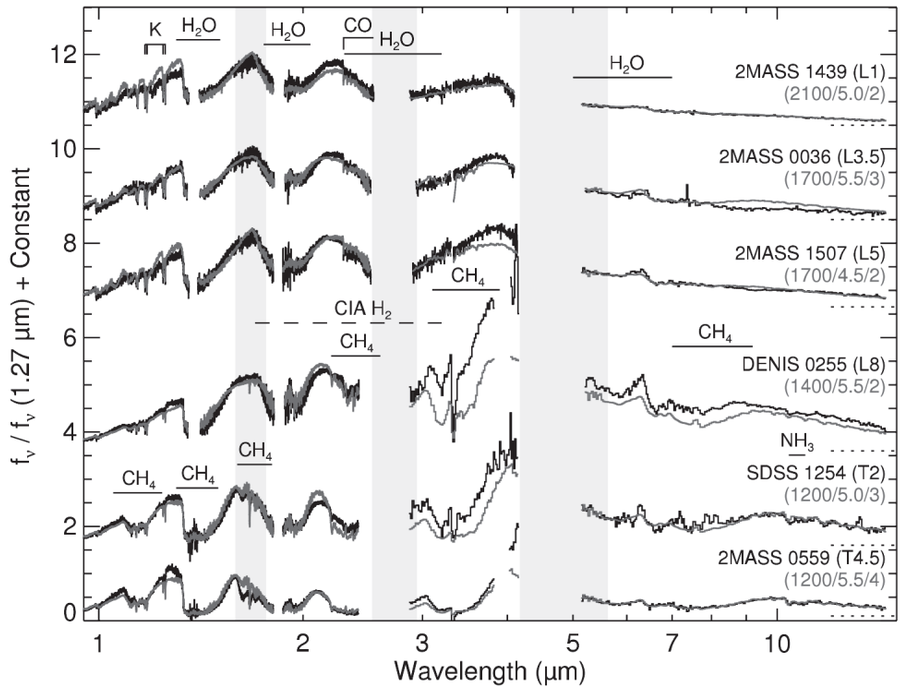


Figure 1.10: The 0.95–14.5 $\mu$m spectra of 2MASS 1439+1929(L1), 2MASS 0036+1821(L3.5), 2MASS 1507–1627(L5), DENIS 0255–4700(L8), SDSS 1254–0122 ( T2), and 2MASS 0559–1404 (T4.5) (black lines). The data have been normalized to unity at 1.27 $\mu$m and offset (dotted lines) for clarity. The best-fitting models are shown in gray and are normalized and offset with the same constants as the data. The models were multiplied by the constant value before normalization to preserve the relative flux levels between the data and models. Regions not included in the fits are shown in light gray (Cushing et al. 2008).

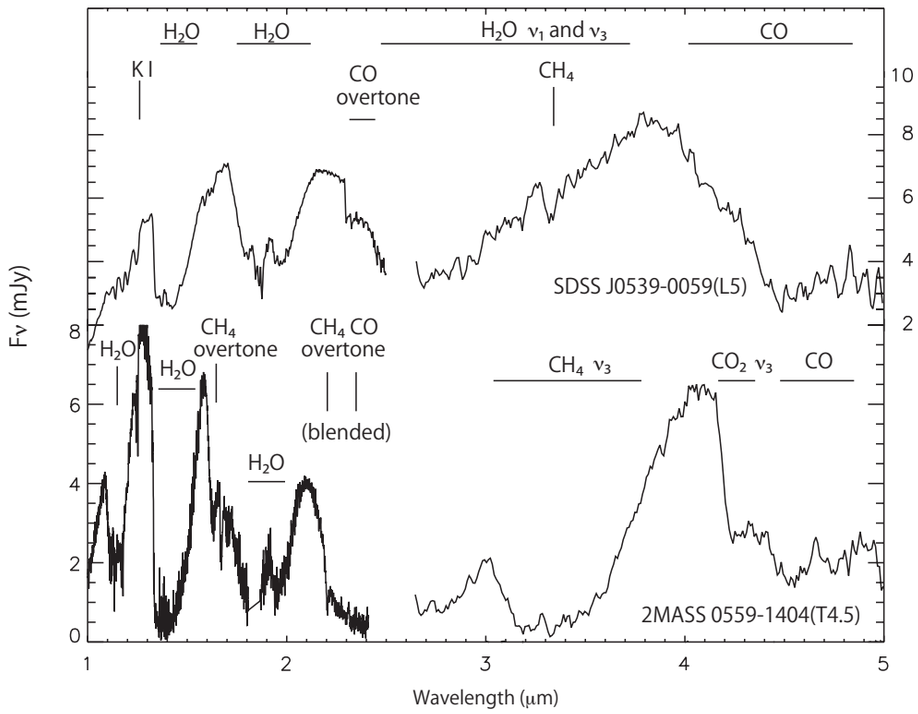


Figure 1.11: Major absorption bands present in 1.0 to 5.0 $\mu$m. Fundamental bands of CO, $CO_2$ and $CH_4$ in 2.5 to 5.0 $\mu$m and overtone bands in 1.0 to 2.5 $\mu$m.

dependently because they are blended especially in the spectra of late-L to T-type dwarfs. In addition, almost all absorption bands present in the wavelength shorter than 2.5 $\mu$m, for example CO at 2.3 $\mu$m and $CH_4$ at 1.6 and 2.2 $\mu$m, are overtones, and are about 10 $\sim$ 100 times weaker than the fundamental bands, which exist between 2.5 and 5.0 $\mu$m. These fundamental bands are mostly non-blended and suitable for the detailed analysis. Thus, the wavelength of 2.5–5.0 $\mu$m is important to understand brown dwarf atmospheres. However, observations in this wavelength range from the ground is always challenging. Severe absorption due to the Earth's atmosphere and limited wavelength coverage make the precise analysis difficult. Continuous spectra of brown dwarfs in 2.5–5.0 $\mu$m wavelengths were obtained by *AKARI* for the first time, which opened the door to the new insight into the brown dwarf atmosphere.

## 1.6 Outline of This Thesis

Throughout this thesis, we will study brown dwarf atmosphere based on the *AKARI* near-infrared spectra. So far, a great deal of observation and theoretical works have been done, and these studies have given us many information about physics and chemistry in the photosphere of brown dwarfs and its evolution. However many questions about brown dwarfs remain unanswered yet. For example, the deviation of molecular abundance from the thermal equilibrium, mechanism of dust formation and disappearance, the mixing in the photosphere, and the difficulties in modeling spectra in broad wavelength range. These questions are our motivation for studying brown dwarfs with *AKARI*. We attempt to understand the pho-

tosphere of brown dwarfs better by analyzing molecular absorption bands in the spectral data taken by *AKARI*. The outline of this thesis is as follows.

We explain observations and data reduction of *AKARI* spectral data in chapter 2. In chapter 3, we analyze the *AKARI* spectral data. We investigate the behavior of various molecular absorption bands in brown dwarf spectra relative to their spectral types systematically with 18 *AKARI* observed spectra. We also evaluate colors from *AKARI* data, and confirm that the *AKARI* objects are normal brown dwarfs. In chapter 4, we describe the analysis with one of the brown dwarf atmosphere models, Unified Cloudy Models (UCM). We explain the method of deriving model parameters for each *AKARI* object, and discuss two results; onset of the $CH_4$ absorption (in section 4.6.1) and radii of *AKARI* observed brown dwarfs (in section 4.6.2). In chapter 5, we confirm the problem of fitting the broad wavelength range together by investigating the best models fitted to each *AKARI* and SpeX/CGS4 spectral data, and discuss the results toward solving this problem. Finally we introduce the possible improvement of the model in chapter 6. We demonstrate effects of elemental abundance to the model spectra, and discuss the possible variation of metallicity of brown dwarfs. We discuss a possible reason of $CO_2$ 4.2 $\mu$m stronger or weaker absorption feature in late-L and T type spectra.

# Chapter 2

# Observations and Data Reduction

To understand the photospheres of brown dwarfs better, we need to use spectral data including various molecular band and effects of dust. Especially important are the data of the little observed wavelength range, particularly continuous spectra between 2.5 and 5.0 $\mu$m. *AKARI* has observed 35 brown dwarfs, including with two binaries, in this valuable wavelength of 2.5–5.0 $\mu$m. In this chapter, we explain observations and data reductions of *AKARI* spectral data.

## 2.1 *AKARI*

The Japanese infrared astronomical satellite *AKARI* (Murakami et al. 2007) was launched in February 22 (JST) 2006. *AKARI* was in a sun-synchronous polar orbit with the altitude of about 700 km. *AKARI*'s primary mission is to carry out an all-sky survey at six wavelength bands, with higher sensitivity and spatial resolution than the previous survey by IRAS (Infrared Astronomical Satellite, a joint mission by the United States, the United Kingdom and Netherlands, launched in 1983). Thousands of pointed observation of specific targets were also carried out. The diameter of telescope on board *AKARI* is 68.5 cm (Figure 2.1). *AKARI* observed in the wavelength range from 1.7 to 180 $\mu$m with two scientific instruments; the Far-Infrared Surveyor (FIS; Kawada et al. 2007) and the Infrared Camera (IRC; Onaka et al. 2007). These instruments carried out observations in the liquid-He cool holding period (Phase1, 2) until 2007 August. After that the observation continued with cryocooler only with for near-infrared camera (NIR; one of the channels of IRC) only (Phase 3).

## 2.2 The InfraRed Camera (IRC)

The Infrared Camera (IRC; Onaka et al. 2007) onboard *AKARI* covers the wavelength range of 1.8–26.5 $\mu$m with three independent cameras operated simultaneously, namely the NIR (near-infrared), MIR-S (mid-infrared short), and MIR-L (mid-infrared long) channels. The IRC is capable of yielding moderate-resolution ($R\sim$120) spectra in the near-infrared camera NIR devoid of any degradation by telluric atmospheres. The grism mode of the NIR channel (NG) was used for the observations of our program (see section 2.3). The source was placed in the $1\times1$ arcmin$^2$ aperture mask, referred to as 'Np', prepared

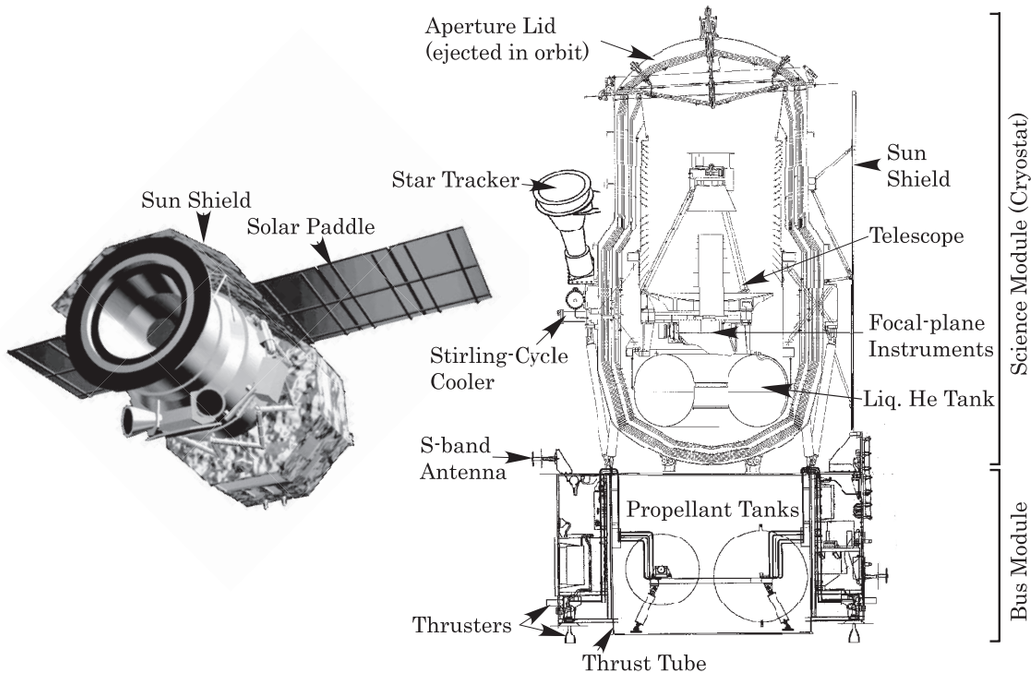


**Fig. 1.** Illustration of AKARI in orbit (left panel) and a sectional view (right panel).

**Table 1.** Design features of the AKARI satellite.

| | |
|---|---|
| Size | diameter 2.0 m max., hight 3.7 m (launching configuration)<br>width 5.5 m, hight 3.3 m (observation configuration in orbit) |
| Mass | 952 kg in the launch configuration |
| Orbit | Sun-synchronous polar orbit, altitude 700 km |
| Downlink rate | 4 Mbps for scientific data |
| Data generation rate | approximately 2 GBytes $d^{-1}$ |
| Data recorder capacity | 2 GBytes |

Figure 2.1: The overview of *AKARI* satellite. (Murakami et al. 2007)

for spectroscopy of point sources. The Np aperture prevents contamination of the spectra from nearby sources. Our observations were all carried out in the AOT (Astronomical Observation Template) IRC04 for Phase 2 and IRCZ4 for Phase 3 with the observation parameter of 'b;Np' (Lorente et al. 2008). In this mode, the entire 2.5–5.0 $\mu$m wavelength range is covered with a dispersion of 0.0097 $\mu$m/pixel or an effective spectral resolution of $R = \lambda/\Delta\lambda$ =120 at 3.6 $\mu$m for point sources (Ohyama et al. 2007). A pointed observation by *AKARI* allowed about 10 minutes of exposure.

## 2.3 Observations and Data Reduction

### 2.3.1 The Mission Program NIRLT

The *AKARI* observation program is divided into three categories, Large-Area Surveys (LS) conducted by the project, Mission Programs (MP) by the project members, and Open-Time programs (OT). We have conducted a mission program using the IRC to obtain continuous spectra of brown dwarfs in the 2.5–5.0 $\mu$m wavelengths. The program is titled "Near-InfraRed spectroscopy of L and T dwarfs" (NIRLT; P.I. I. Yamamura). The program aimed to construct a set of legacy data for studies of physical and chemical structure of brown dwarfs in wide range of spectral type from L to T. The initial results based on the *AKARI* spectra of six brown dwarfs taken in phase 2 are reported in Yamamura et al. (2010) and Tsuji et al. (2011).

Our target list included 40 objects selected by their expected fluxes (to be bright enough for the *AKARI*/IRC instrument to provide high-quality spectra within the reasonable amount of exposures) and their spectral types (to sample various types from M to T). Seventeen L dwarfs, fourteen T dwarfs, and nine M dwarfs were included in the target list.

### 2.3.2 Observations

Thirty-five (15 L dwarfs, 11 T dwarfs and 9 M dwarfs) of 40 objects were actually observed, and thirty-three objects (14 L dwarfs, 10 T dwarfs and 9 M dwarfs) are detected. There was a bonus data of the L dwarf GJ 1001B during the observation of its primary star, the M dwarf GJ1001A. We list 27 observed objects except for 9 M dwarfs in Table2.1. Table 2.2 summarizes all NIRLT observation records. The table lists the object name, their spectral types, observed date (year/month/date), observation ID, and remarks. We observed 10 brown dwarfs in Phase 2; liquid-He cool holding period before 2007 August, and 17 sources in Phase 3; the post liquid-He phase cooled by the onboard cryocooler.

Table 2.2: Summary of the Observation in the NIRLT program

| Object Name | Sp. Type | Date | ObsID: | remarks |
|---|---|---|---|---|
| 2MASS J14392+1929 | L1 | 2008.7.22 | 1770009-001 | not detect[1] |
| 2MASS J14392+1929 | L1 | 2008.7.22 | 1770009-002 | not detect |

*table continued on next page*

[1]not detect: observed with wrong coordinates

*Table 2.2 (continued)*

| Object Name | Sp. Type | Date | ObsID: | remarks |
|---|---|---|---|---|
| 2MASS J14392+1929 | L1 | 2010.1.19 | 1771009-001 | |
| 2MASS J14392+1929 | L1 | 2010.1.19 | 1771009-002 | |
| GD 165B | L3 | 2007.7.24 | 1720074-001 | Data lost[2] |
| GD 165B | L3 | 2008.7.22 | 1770010-001 | |
| GD 165B | L3 | 2008.7.22 | 1770010-002 | |
| GD 165B | L3 | 2010.1.20 | 1771010-001 | Too faint[3] |
| GD 165B | L3 | 2010.1.20 | 1771010-002 | Too faint |
| GD 165B | L3 | 2010.1.20 | 1771010-003 | Too faint |
| GD 165B | L3 | 2010.1.20 | 1771010-004 | Too faint |
| Kelu-1 | L3 | 2008.7.16 | 1770018-001 | not detect |
| Kelu-1 | L3 | 2008.7.16 | 1770018-002 | not detect |
| 2MASS J0036+1821 | L4 | 2008.7.6 | 1770024-001 | |
| 2MASS J0036+1821 | L4 | 2008.7.6 | 1770024-002 | |
| 2MASS J0036+1821 | L4 | 2010.1.5 | 1771024-001 | |
| 2MASS J0036+1821 | L4 | 2010.1.5 | 1771024-002 | |
| 2MASS J2224-0158 | L4.5 | 2009.5.29 | 1770019-001 | |
| 2MASS J2224-0158 | L4.5 | 2009.5.29 | 1770019-002 | |
| SDSS J0539–0059 | L5 | 2006.9.17 | 1720009-001 | |
| SDSS J0539–0059 | L5 | 2009.9.16 | 1770007-001 | |
| SDSS J1446+0024 | L5 | 2007.8.2 | 1720072-001 | |
| 2MASS J1507-1627 | L5 | 2008.8.12 | 1770020-001 | |
| 2MASS J1507-1627 | L5 | 2009.2.7 | 1770120-001 | |
| GJ 1001B | L5 | 2009.6.2 | 1770036-001 | |
| GJ 1001B | L5 | 2009.6.2 | 1770036-002 | |
| 2MASS J0825+2115 | L6 | 2008.10.26 | 1770016-001 | |
| 2MASS J0825+2115 | L6 | 2009.4.23 | 1770016-002 | |
| 2MASS J0825+2115 | L6 | 2009.10.26 | 1771016-001 | |
| 2MASS J0825+2115 | L6 | 2009.10.26 | 1771016-002 | |
| 2MASS J1711+2232 | L6.5 | 2007.3.5 | 1720001-001 | |
| 2MASS J1711+2232 | L6.5 | 2008.9.5 | 1770001-001 | Data lost |
| 2MASS J1711+2232 | L6.5 | 2008.9.5 | 1770001-002 | Data lost |
| 2MASS J1632+1904 | L7.5 | 2009.2.21 | 1770025-001 | Too faint |
| 2MASS J1632+1904 | L7.5 | 2009.2.21 | 1770025-002 | Too faint |
| 2MASS J1523+3014 | L8 | 2007.1.26 | 1770002-001 | |
| 2MASS J1523+3014 | L8 | 2008.7.30 | 1770002-002 | |

*table continued on next page*

[2]Data lost: data downlink failed due to troubles in the ground system
[3]Too faint: The objects was too faint

*Table 2.2 (continued)*

| Object Name | Sp. Type | Date | ObsID: | remarks |
|---|---|---|---|---|
| SDSS J0830+4828 | L9 | 2006.10.20 | 1720007-001 | |
| SDSS J0830+4828 | L9 | 2006.10.21 | 1720007-002 | |
| SDSS J0830+4828 | L9 | 2009.4.17 | 1770006-001 | |
| 2MASS J0310+1648 | L9 | 2008.8.12 | 1770011-001 | |
| 2MASS J0310+1648 | L9 | 2008.8.13 | 1770011-002 | |
| 2MASS J0328+2302 | L9.5 | 2009.8.19 | 1770027-001 | Too faint |
| 2MASS J0328+2302 | L9.5 | 2010.2.14 | 1771027-001 | Too faint |
| 2MASS J0328+2302 | L9.5 | 2010.2.14 | 1771027-002 | Too faint |
| SDSS J0423-0414 | T0 | 2008.8.25 | 1770015-001 | |
| SDSS J0423-0414 | T0 | 2008.8.25 | 1770015-002 | |
| SDSS J1254-0122 | T2 | 2008.7.3 | 1770012-001 | not detect |
| SDSS J1254-0122 | T2 | 2008.7.4 | 1770012-002 | not detect |
| SDSS J1254-0122 | T2 | 2010.1.2 | 1771012-001 | |
| SDSS J1254-0122 | T2 | 2010.1.3 | 1771012-002 | |
| SIMP J0136+0933 | T2.5 | 2008.7.17 | 1770031-001 | |
| SIMP J0136+0933 | T2.5 | 2008.7.17 | 1770031-002 | |
| SIMP J0136+0933 | T2.5 | 2010.1.16 | 1771031-001 | |
| SIMP J0136+0933 | T2.5 | 2010.1.16 | 1771031-002 | |
| SDSS J1750+1759 | T3.5 | 2007.3.17 | 1720050-001 | Too faint |
| SDSS J1750+1759 | T3.5 | 2007.3.17 | 1720050-002 | Too faint |
| 2MASS J0559–14044 | T4.5 | 2006.9.22 | 1720006-001 | |
| 2MASS J0559–14044 | T4.5 | 2006.9.22 | 1720008-001 | |
| 2MASS J0559–14044 | T4.5 | 2008.9.22 | 1770005-001 | |
| 2MASS J0559–14044 | T4.5 | 2008.9.22 | 1770005-002 | |
| Gl 229B | T6 | 2008.9.25 | 1770013-001 | not resolve[4] |
| Gl 229B | T6 | 2008.9.25 | 1770013-002 | not resolve |
| 2MASS J1553+1532 | T7 | 2008.8.15 | 1770022-001 | |
| 2MASS J1553+1532 | T7 | 2008.8.15 | 1770022-002 | |
| 2MASS J1553+1532 | T7 | 2008.8.15 | 1770022-003 | |
| 2MASS J1553+1532 | T7 | 2009.2.9 | 1770022-004 | |
| 2MASS J1553+1532 | T7 | 2009.2.9 | 1771022-001 | Too faint |
| 2MASS J1553+1532 | T7 | 2009.2.9 | 1771022-002 | Too faint |
| 2MASS J1217–0311 | T7.5 | 2007.6.26 | 1720068-001 | Too faint |
| Gl 570D | T8 | 2009.8.10 | 1770023-001 | |
| Gl 570D | T8 | 2009.8.10 | 1770023-002 | |
| Gl 570D | T8 | 2009.8.10 | 1770023-003 | |

*table continued on next page*

[4]This object was not resolved from primary star.

*Table 2.2 (continued)*

| Object Name | Sp. Type | Date | ObsID: | remarks |
|---|---|---|---|---|
| Gl 570D | T8 | 2009.8.11 | 1770023-004 | |
| 2MASS J0415–0935 | T8 | 2007.2.18 | 1720005-001 | Ghosting[5] |
| 2MASS J0415–0935 | T8 | 2007.2.18 | 1720005-002 | Ghosting |
| 2MASS J0415–0935 | T8 | 2007.2.18 | 5125080-001 | Re-observed[6] |
| 2MASS J0415–0935 | T8 | 2007.2.18 | 5125081-001 | Re-observed |
| 2MASS J0415–0935 | T8 | 2008.8.21 | 1770004-001 | Too faint |
| 2MASS J0415–0935 | T8 | 2008.8.21 | 1770004-002 | Too faint |
| 2MASS J0415–0935 | T8 | 2008.8.21 | 1770004-003 | Too faint |
| 2MASS J0415–0935 | T8 | 2008.8.21 | 1770004-004 | Too faint |
| $\varepsilon$ Ind Ba+Bb | T1+T6 | 2006.11.2 | 1720003-001 | |
| $\varepsilon$ Ind Ba+Bb | T1+T6 | 2006.11.2 | 1720004-001 | |
| $\varepsilon$ Ind Ba+Bb | T1+T6 | 2008.11.1 | 1770003-001 | |
| $\varepsilon$ Ind Ba+Bb | T1+T6 | 2008.11.1 | 1770003-002 | |

### 2.3.3 Data Reduction

The standard software toolkit *IRC_SPEC_TOOLKIT* (Ohyama et al. 2007) was used for the data reduction. We used the toolkit version 20110301, released in 2011 March. Wavelength and flux calibrations were all done automatically in the toolkit. Spectral data are extracted from two dimensional spectral images. An example spectral image is shown in the lower panel of Figure 2.2. Two axes of this image correspond to the spatial and wavelength directions respectively. Along the spatial direction the signal is extended by the point spread function (PSF), and on the wavelength direction the signal extension is determined by the spectral resolution and the PSF. The typical wavelength calibration error is 0.5 pixel of the detector or $\sim$0.005$\mu$m (Ohyama et al. 2007), but could be larger for some data (see Table 2.3). We applied a small correction (0.01–0.03$\mu$m) to the data by comparing the position of the $CH_4$ Q-branch feature with other objects. The overall flux calibration error is 10 % in the middle of the wavelength range, and 20 % at the short / long wavelength edges.

We carry out the following three additional processing to obtain the better quality data. (1) derivation of appropriate sky background, (2) stacking of multiple observations, and (3) correction of contaminated light from nearby objects.

#### (1) Derivation of Probable Sky

We modified the *IRC_SPEC_TOOLKIT* program to improve the sky subtraction. The original program subtracts the sky derived from same pixel width with the signal (Figure 2.2). Since the Phase3 data are

[5]The data was not obtained by contamination of ghosting.
[6]observed in the director's time (DT).

Table 2.1: Observed L and T Objects in the NIRLT Program

| Object Name | R.A. (J2000) | Decl.(J2000) | Sp. Type | Distance[pc] |
|---|---|---|---|---|
| 2MASS J14392837+1929150 | 14:39:28.400 | +19:29:15 | L1[1] | 14.36[a] |
| GD 165B | 14:24:39.09 | +09:17:10.4 | L3[2] | 31.69[a] |
| Kelu–1 | 13:05:40.200 | –25:41:06 | L3[2] | 18.74[a] |
| 2MASS J00361617+1821104 | 0:36:15.900 | +18:21:10 | L4[2] | 8.76[a] |
| 2MASS J22244381–0158521 | 22:24:43.800 | –1:58:52 | L4.5[1] | 11.35[b] |
| 2MASS J05395200–0059019 | 05:39:52.00 | –00:59:01.9 | L5[2] | 13.13[b] |
| SDSS J144600.60+002452.0 | 14:46:00.61 | +00:24:51.9 | L5[2] | 22.00[b] |
| 2MASS J15074769–1627386 | 15:07:47.600 | –16:27:38 | L5[1] | 7.33[a] |
| GJ 1001B | 0:04:36.400 | -40:44:03 | L5[1] | 9.55[a] |
| 2MASS J08251968+2115521 | 8:25:19.600 | +21:15:52 | L6[2] | 10.46[b] |
| 2MASS J17114573+2232044 | 17:11:45.73 | +22:32:04.4 | L6.5[1] | 30.34[b] |
| 2MASS J16322911+1904407 | 16:32:29.100 | +19:04:41 | L7.5[2] | 15.73[b] |
| 2MASS J15232263+3014562 | 15:23:22.63 | +30:14:56.2 | L8[2] | 17.45[b] |
| SDSS J083008.12+482847.4 | 08:30:08.25 | +48:28:48.2 | L9[2] | 13.09[b] |
| 2MASS J03105986+1648155 | 3:10:59.900 | +16:48:16 | L9[2] | 25.00[c] |
| 2MASS J03284265+2302051 | 3:28:42.600 | +23:02:05 | L9.5[2] | 30.32[b] |
| SDSS J042348.57–041403.5 | 4:23:48.600 | –4:14:04 | T0[2] | 15.24[b] |
| SDSS J125453.90–012247.4 | 12:54:53.900 | –1:22:47 | T2[2] | 13.21[b] |
| SIMP J013656.5+093347.3 | 1:36:56.600 | +09:33:47 | T2.5[3] | 6.4[d] |
| SDSS J175032.96+175903.9 | 17:50:32.93 | +17:59:04.2 | T3.5[2] | 27.72[b] |
| 2MASS J05591914–1404488 | 05:59:19.14 | –14:04:48.8 | T4.5[2] | 10.47[b] |
| Gl 229B | 6:10:34.700 | –21:51:49 | T6[2] | 5.8[a] |
| 2MASS J15530228+1532369 | 15:53:02.200 | +15:32:36 | T7[3] | 12.0[e] |
| 2MASS J12171110–0311131 | 12:17:11.10 | –03:11:13.1 | T7.5[2] | 9.1[b] |
| Gl 570D | 14:57:15 | –21:21:51 | T8[2] | 5.9[f] |
| 2MASS J04151954–0935066 | 04:15:19.54 | –09:35:06.6 | T8[3] | 5.74[b] |
| $\epsilon$ Ind Ba+Bb | 22:04:10.52 | –56:46:57.7 | T1+T6[3] | 3.62[g] |

[1]Spectral type are referred from Kirkpatrick et al. (2000).
[2]Spectral type are referred from Geballe et al. (2002).
[3]Spectral type are referred from Burgasser et al. (2006).
–note: Distances are estimated based on trigonometric parallaxes.
The parallaxes are referred from (a) Dahn et al. (2002), (b) Vrba et al. (2004), (c) Stampf et al. (2010), (d) Artigau et al. (2008), (e) Jameson et al. (2008), (f) Burgasser et al. (2000), (g) King et al. (2010)
The mean parallax error is about 4 mas.

–note: Object names are hereafter 2MASS J1439+1929, 2MASS J0036+1821, 2MASS J2224–0158, 2MASS J0539–0059, SDSS J1446+0024, 2MASS J1507–1627, 2MASS J0825+2115, 2MASS J1711+2232, 2MASS J1632+1904, 2MASS J1523+3014, SDSS J0830+4828, 2MASS J0310+1648, 2MASS J0328+2302, SDSS J04234–0414, SDSS J1254–0122, SIMP J0136+0933, SDSS J1750+1759, 2MASS J0559–1404, 2MASS J1553+1532,2MASS J1217–0311, 2MASS J0415–0935.

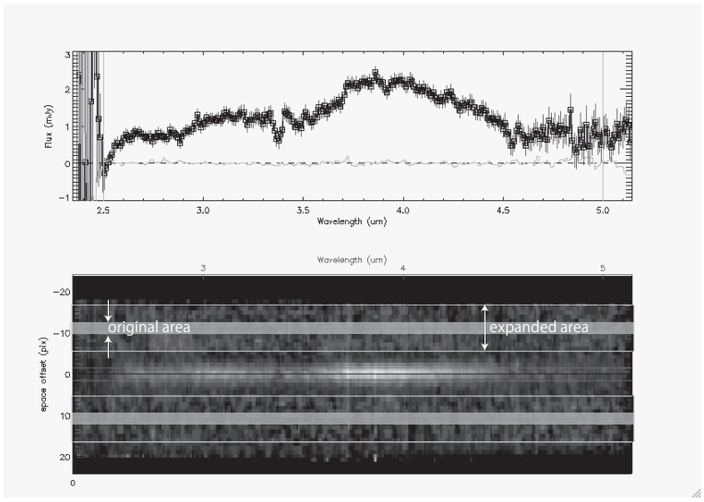


Figure 2.2: The range for deriving sky level of 2MASS J1523+3014(L8). The nominal range for deriving sky level draws in yellow. We expand that to the area drawn in blue.

so noisy, sky level derived only from a few pixels (3–5 pixels) are not sufficient. We modify the program to derive the probable sky level from larger area ($\sim$10 pixels).

**(2) Stacking of multiple observations**

Since brown dwarf are generally very faint (a few mJy $< F_\nu <$ 25 mJy), one pointed observation is not always enough to obtain good quality data. It is especially true for the Phase 3 observations, where noise level is about a factor of 2.5 higher than that of Phase 2 (Figure 2.3). Seven or eight spectral data are taken per single pointing. The toolkit stacks all available exposure frames within a pointing. However the data of single pointing are insufficient for detailed analysis. We observed at least twice per object, unless the observations failed by any reasons. To achieve as good quality data as possible, we stack the multiple pointing data for Phase3 observations using the stack toolkit *IRC_SPEC_TOOLKIT_wSTACMULTI* version 20100918[7]. The stack toolkit uses the original frames before stacking by *IRC_SPEC_TOOLKIT*. The total number of frames used for stacking are 14 or 16 frames. The stacked data are better than single pointing data in most cases. We show the effects of stacking in Figure 2.4, and list the stacked objects in Table 2.3. When the quality of one of two pointing data is quite bad because of the worse observation condition, the stacking effect is no longer significance.

**(3) Subtraction of Signal from Nearby Object**

This process is partially applied to GJ 1001B. GJ 1001 is the low-mass binary system, and GJ 1001B is the companion of the M dwarf, GJ 1001A. The difference in the magnitude is about 3 mag at $L'$ band, e.g. the flux of GJ 1001A is about 16 times larger than that of GJ 1001B. Since GJ 1001B is separated from GJ 1001A by only 13 arcsec (11pix), the shoulder of spectra of GJ 1001B is contaminated by intense

[7]URL: http://komatta.astron.s.u-tokyo.ac.jp/$\sim$onaka/AKARI/IRC_SPEC_TOOLKIT_wSTACMULTI.20100918.tar.gz

Table 2.3: Summary of data reduction. Wavelength correction value (x shift) and with (Y) or without (N) stacking of multiple pointings are shown. The total number of frames using for stacking are 14 or 16 frames (2 pointings).

| Object Name | Sp. Type | x shift[$\mu$m] | stack | remarks |
|---|---|---|---|---|
| 2MASS J1439+1929 | L1 | 0.00 | Y | |
| GD 165B | L3 | 0.00 | Y | too faint |
| Kelu-1 | L3 | 10.78 | – | not detect |
| 2MASS J0036+1821 | L4 | 0.015 | Y | |
| 2MASS J2224–0158 | L4.5 | -0.010 | Y | |
| SDSS J0539–0059 | L5 | 0.00 | N | |
| SDSS J1446+0024 | L5 | 0.00 | N | |
| 2MASS J1507–1627 | L5 | -0.020 | N | |
| GJ 1001B | L5 | 0.00 | N | |
| 2MASS J0825+2115 | L6 | 0.00 | Y | |
| 2MASS J1711+2232 | L6.5 | 0.00 | N | too faint |
| 2MASS J1632+1904 | L7.5 | 0.00 | Y | |
| 2MASS J1523+3014 | L8 | -0.030 | N | |
| SDSS J0830+4828 | L9 | 0.00 | N | |
| 2MASS J0310+1648 | L9 | 0.00 | Y | |
| 2MASS J0328+2302 | L9.5 | – | – | too faint |
| SDSS J0423–0414 | T0 | 0.00 | N | binary |
| SDSS J1254–0122 | T2 | 0.00 | N | |
| SIMP J01365+0933 | T2.5 | 0.010 | Y | |
| SDSS J1750+1759 | T3.5 | – | – | too faint |
| 2MASS J0559–14044 | T4.5 | 0.00 | N | |
| Gl 229B | T6 | 12.28 | – | not detect |
| 2MASS J1553+1532 | T7 | -0.010 | Y | |
| 2MASS J1217–0311 | T7.5 | – | – | too faint |
| Gl 570D | T8 | 0.00 | Y | |
| 2MASS J0415–0935 | T8 | -0.020 | N | |
| $\varepsilon$ Ind Ba+Bb | T1+T6 | 0.00 | N | binary |

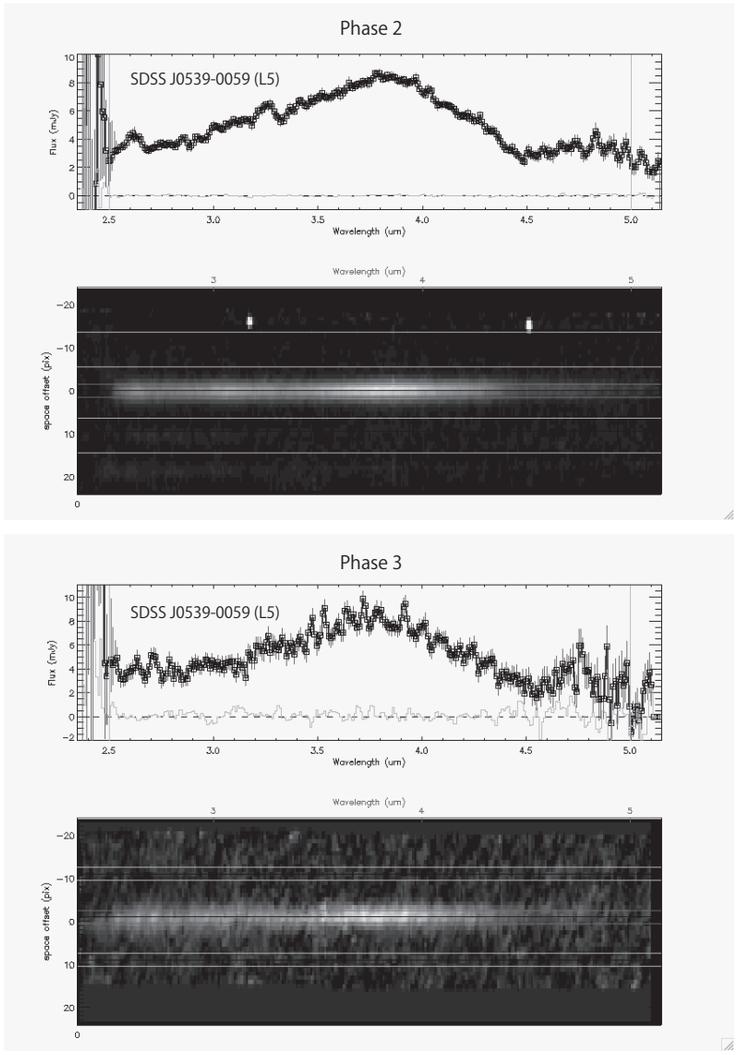


Figure 2.3: The comparison of noise level in Phase2 and Phase3 for SDSS 0539–0059 (L5).

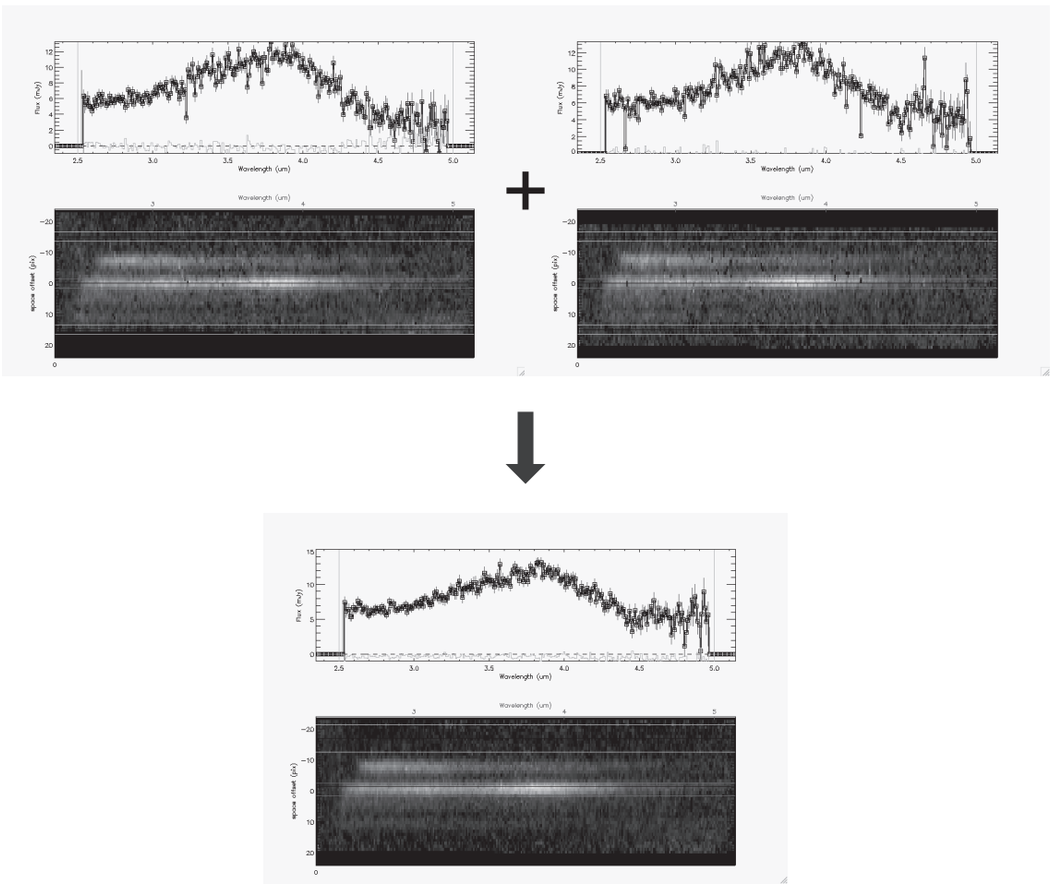


Figure 2.4: Stacking data and 2 pointing of 2MASS J0036+1821(L4) .

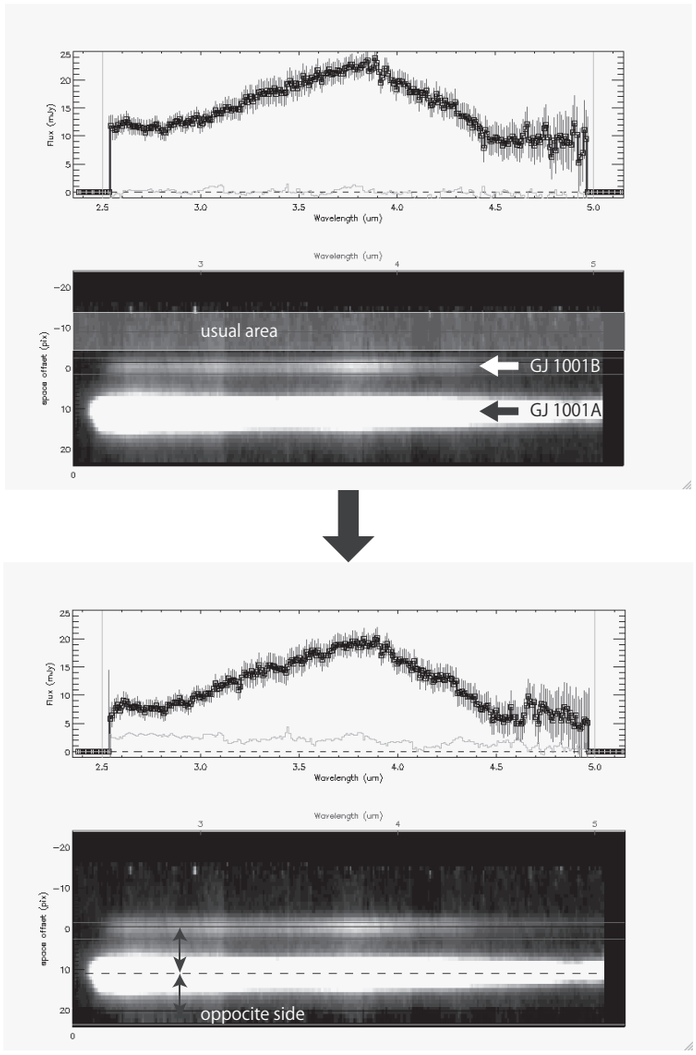


Figure 2.5: The spectrum of GJ1001B without the effect of GJ1001A. We can see the drop to a lower value over all wavelength, especially shorter wavelength from 2.5 to 3.0$\mu$m.

flux of GJ 1001A, within the PSF of IRC/NIR channel of FWHM $\sim$ 3.2 pix (Figure 2.5). To measure the signal of GJ 1001B accurately, we took account of the extended signal of GJ1001A. We assume that the spectral image of GJ 1001A is symmetric in the spatial direction with respect to the flux peak pixels, and measure the "background" level at the same distance from GJ 1001A to GJ 1001B in the opposite side.

### 2.3.4 Validation of Absolute Flux Calibration

We validate the absolute flux calibration for the obtained *AKARI* spectra by comparing the integrated signal spectra (hereafter *S*3) with the photometry data N3 taken in the same pointing. In this analysis we use the spectral data for the eighteen objects with S/N greater than 2.0. Two binary objects, $\varepsilon$ Ind Ba+Bb (T1+T6) and SDSS J0423–0414(T0), are excluded in our analysis. The NIR channel has 3

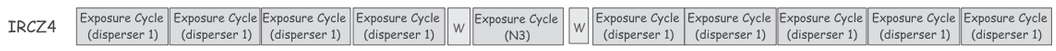


Figure 2.6: Observation sequences of the AOT IRC04. Large boxes labeled as "Exposure cycle (disperser 1)" indicate exposure frames for spectroscopy, and as "Exposure cycle (N3)" indicate that for imaging. Dead time for a Filter Wheel change depends on the relative position of the elements. (from *AKARI* IRC Data User Manual).

filters, N2, N3, N4. AOT:IRC04 used for NIRLT has an imaging observation using N3 filter inserted between the spectroscopic observations as shown in Figure 2.6. The imaging observation is used to determine the wavelength reference for slit-less spectroscopy. Basic data processing (dark subtraction and flat-fielding) is applied to the imaging frame with IRC Imaging Toolkit (Phase 2 data: Version 110225 and Phase 3 data: Version 08924P3). Photometry was made with SExtractor (Version 2.8.6). We applied aperture correction following the description in IRC Data Reduction Support Page (URL; http://www.ir.isas.jaxa.jp/AKARI/Observation/DataReduction/IRC/). The systematic error of the measured flux is about 10 % for photometry (H. Matsuhara private communication). We note that this uncertainty, 10 %, is the standard deviation obtained by stacking multi photometric data in a single pointing. Thus the error of N3 photometric data a single image from AOT:IRC04 should be larger than 10 %. Since the error decreases as the square root of the number of images, 7 or 8 per pointing, the actual error for the single observed data should be as large as 30 %. We calculate the integrated flux $S3$ from the spectra as

$$S3 = \frac{\int_{\lambda_{is}}^{\lambda_{ie}} F_\lambda R(\lambda) d\lambda}{\int_{\lambda_{is}}^{\lambda_{ie}} \frac{\lambda_c}{\lambda} R(\lambda) d\lambda}, \tag{2.1}$$

where $F_\lambda$ is the flux density of spectra, $\lambda_c$ is the band center, 3.2$\mu$m, and $R(\lambda)$ is the Relative Spectral Response (RSR) function of the IRC N3 band (Tanabé et al. 2008). The integration range is $\lambda_{is} = 2.6$ $\mu$m and $\lambda_{ie} = 3.9$ $\mu$m. These are different from the values used in Tanabé et al. (2008), $\lambda_{is}$ 1.60 $\mu$m and $\lambda_{ie}$ 5.77 $\mu$m. The values of 2.6 $\mu$m is an edge of the *AKARI* spectra and 3.9 $\mu$m is the shortest wavelength at which RSR becomes less than 0.01. Figure 2.8 shows the RSR of the IRC camera. The comparison of N3 photometry vs. $S3$ is shown in Figure 2.9, where $S3$ photometry is, actually, calculated by following equation equivalent to eq. (2.1),

$$S3 = \frac{\int F_\nu R(\nu) d\nu}{\int \frac{\nu}{\nu_c} R(\nu) d\nu}. \tag{2.2}$$

The integrated flux $S3$ is almost consistent with N3 photometry within the random and systematic error of about 30 % estimated for single image, except for SDSS J1446+0024 and 2MASS J1553+1532 (Figure 2.9 and Table 2.4). The difference of SDSS J1446+0024 and 2MASS J1553+1532 are 54 $\pm$ 2 % and 36 $\pm$ 16 %, respectively. We also show the random errors of 1 $\sigma$ in Table 2.4. 2MASS J0036+1821(L4), 2MASS J1507–1627(L5) and GJ 1001B(L5) are saturated on the image data, and SDSS J1446+0024(L4) and 2MASS J1523+3014(L8) images are affected by *column-pull-down*, therefor the

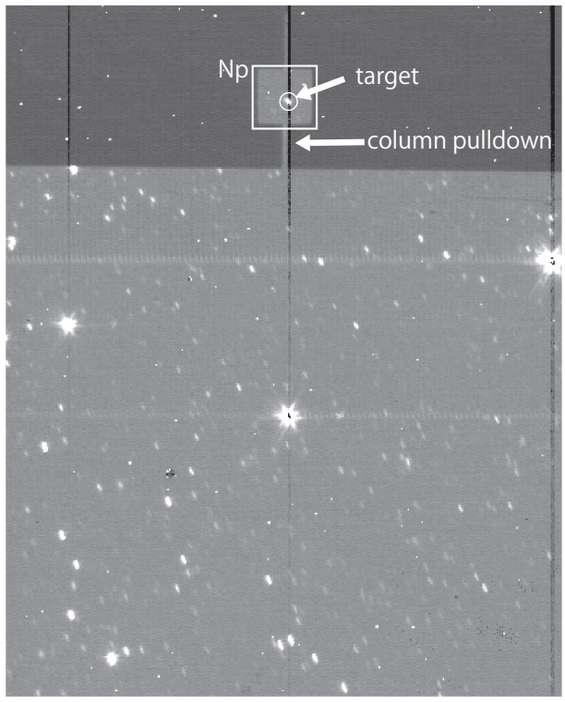


Figure 2.7: A raw data of N3 photometry of SDSS J1446+0024. The source was placed in the $1\times1$ arcmin$^2$ aperture mask, referred to as 'Np' shown in a square. The *column-pull-down* from a bright star at the center of the imaging area disturbs the target in the Np aperture.

photometry data are underestimated. *Column-pull-down* is caused by very bright neighborhood object. When there are bright objects near the target, pixels on the same column of the bright object become negative values (Figure 2.7). Although 2MASS J1553+1532 is not saturated and does not have column pull-down, the difference is relatively large, 36%. This is because that this object is one of the noisiest (S/N $\sim$ 2) object in the analyzed *AKARI* samples, and the integrated flux may not be estimated correctly.

We also check the *AKARI* absolute flux calibration by comparing the past $L'$ photometry data from Leggett et al. (2002a,b) and Golimowski et al. (2004). The $L'$ photometry are listed in Table 2.5. We derive the integrated $L'$ flux from *AKARI* spectral data using Mauna Kea Observatory (MKO) $L'$ filter used by Leggett et al. (2002a,b) and Golimowski et al. (2004) (see Figure 2.10). No previous $L'$ photometry data is available for SIMP J01365+0933 and 2MASS J1553+1532. The wavelength range of the filter is between 3.43$\mu$m and 4.11$\mu$m (50 % cut-off wavelength). Figure 2.11 shows the comparison of $L'$ flux from *AKARI* and past $L'$ photometry values. We see that the $L'$ flux from *AKARI* spectral data are consistent with the past $L'$ photometry within 10 %.

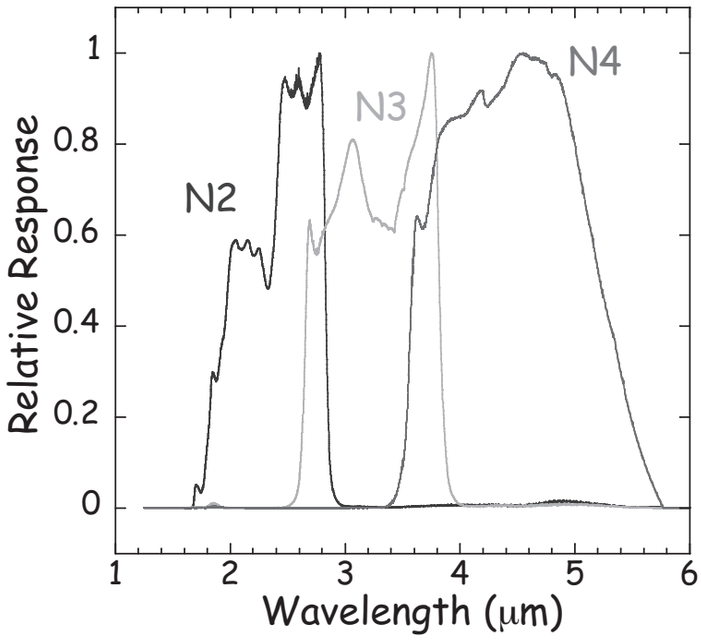


Figure 2.8: The Relative Spectral Response (RSR) function of the filters of the IRC camera (from IRC Data Reduction support page, URL; http://www.ir.isas.jaxa.jp/AKARI/Observation/DataReduction/IRC/).

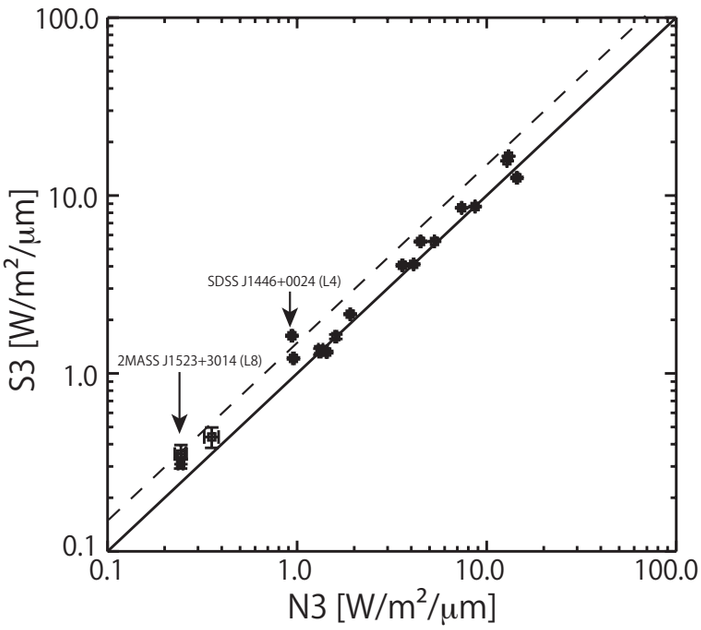


Figure 2.9: The integrated flux $S3$ is consistent with N3 within 30 % except for SDSS J1446+0024 and 2MASS J1553+1532. The border of +30 % is shown in a dashed line. SDSS J1446+0024 is affected by detector column pull-down. The large difference in 2MASS J1553+1532 may be caused by bad S/N ($\sim$ 2).

Table 2.4: Deviation of *S*3 to N3 of *AKARI* samples. The random error is also shown.

| Object Name | Sp. Type | *S*3/N3 (error) |
|---|---|---|
| 2MASS J1439+1929 | L1 | 0.002(0.009) |
| 2MASS J0036+1821 | L4 | 0.243(0.006) |
| 2MASS J2224-0158 | L4.5 | 0.146(0.009) |
| SDSS J0539–0059 | L5 | 0.040(0.006) |
| SDSS J1446+0024 | L5 | 0.538(0.017) |
| 2MASS J1507-1627 | L5 | 0.203(0.006) |
| GJ 1001B | L5 | 0.138(0.016) |
| 2MASS J0825+2115 | L6 | 0.121(0.017) |
| 2MASS J1632+1904 | L7.5 | 0.007(0.033) |
| 2MASS J1523+3014 | L8 | 0.239(0.018) |
| SDSS J0830+4828 | L9 | 0.122(0.012) |
| 2MASS J0310+1648 | L9 | 0.004(0.043) |
| SDSS J1254–0122 | T2 | 0.022(0.053) |
| SIMP J0136+0933 | T2.5 | 0.208(0.014) |
| 2MASS J0559–1404 | T4.5 | 0.083(0.018) |
| 2MASS J1553+1532 | T7 | 0.364(0.159) |
| Gl 570D | T8 | 0.213(0.165) |
| 2MASS J0415–0935 | T8 | 0.247(0.076) |

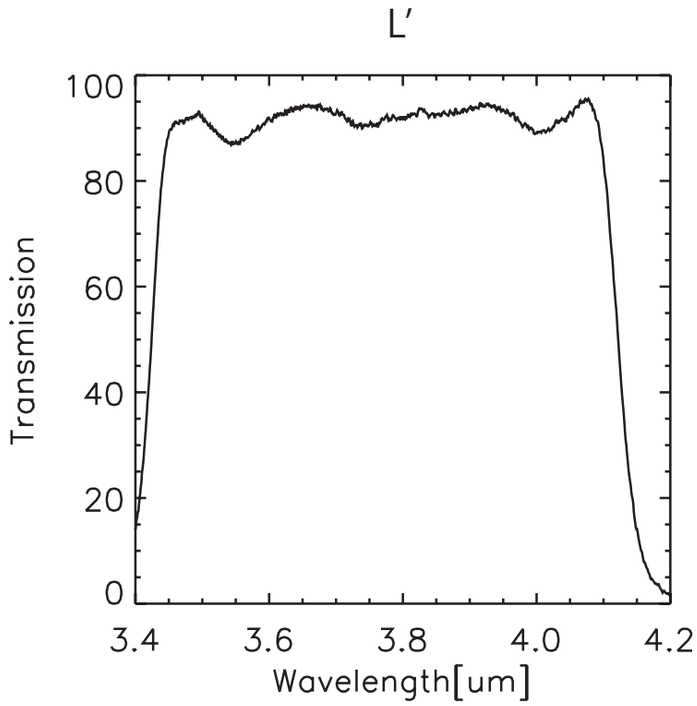


Figure 2.10: The transmission profiles of the "Mauna Kea" $L'$ band filter used by Leggett et al. (2002a,b), Knapp et al. (2004) and Golimowski et al. (2004) (NSFCam Filter Transmission Profiles: http://irtfweb.ifa.hawaii.edu/∼nsfcam/filters.html).

Table 2.5: $L'$ magnitude of brown dwarfs. The error of photometry data is about 0.05 [mag].

| Object Name | Sp. Type | $L'$ | references |
|---|---|---|---|
| 2MASS J1439+1929 | L1 | 10.80 | 1 |
| 2MASS J0036+1821 | L4 | 10.08 | 1 |
| 2MASS J2224-0158 | L4.5 | 10.90 | 2 |
| SDSS J0539–0059 | L5 | 11.32 | 1 |
| SDSS J1446+0024 | L5 | 12.54 | 2 |
| 2MASS J1507-1627 | L5 | 9.98 | 1 |
| GJ 1001B | L5 | 10.41 | 4 |
| 2MASS J0825+2115 | L6 | 11.53 | 1 |
| 2MASS J1632+1904 | L7.5 | 12.54 | 2 |
| 2MASS J1523+3014 | L8 | 12.86 | 1 |
| SDSS J0830+4828 | L9 | 11.98 | 1 |
| 2MASS J0310+1648 | L9 | 12.54 | 1 |
| SDSS J1254–0122 | T2 | 12.25 | 2 |
| SIMP J0136+0933 | T2.5 | no data | 3 |
| 2MASS J0559–1404 | T4.5 | 12.14 | 1 |
| 2MASS J1553+1532 | T7 | no data | 3 |
| Gl 570D | T8 | 12.98 | 2 |
| 2MASS J0415–0935 | T8 | 13.28 | 2 |

1; Leggett et al. (2002a)
2; Golimowski et al. (2004)
3; derived from SpeX spectra
4; Leggett et al. (2002b)

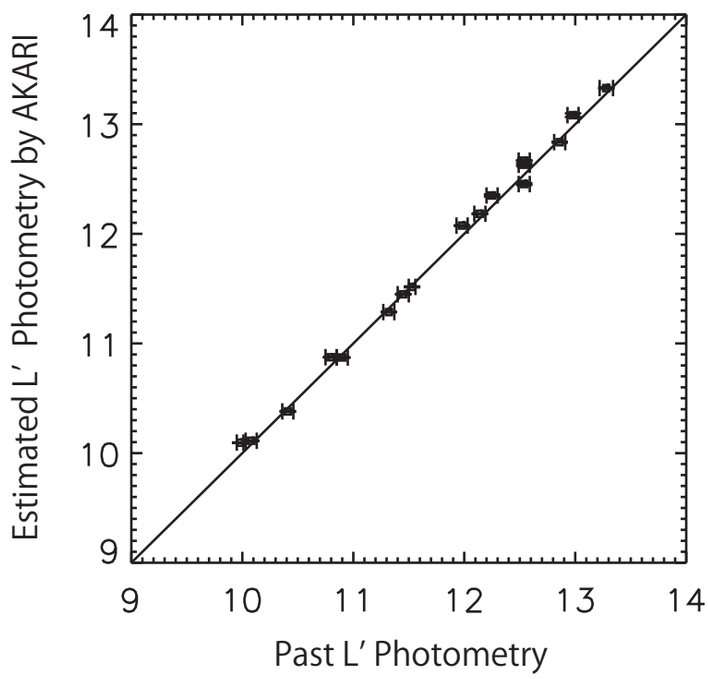


Figure 2.11: The comparison of the $L'$ flux from *AKARI* spectra and $L'$ photometry (Leggett et al. 2002a,b, Knapp et al. 2004 and Golimowski et al. 2004). We see that the $L'$ flux from *AKARI* data are consistent with the past $L'$ photometry within 10 %.

# Chapter 3

# Analysis of the *AKARI* spectra of Brown Dwarfs

In this chapter we present the results of an initial analysis of the *AKARI* spectral data. In section 3.1, we overview the *AKARI* spectral dataset from early-L to late-T dwarfs. This is the first spectral dataset continuously covering from 2.5 to 5.0 $\mu$m for L and T dwarfs. We investigate the characteristics of the spectral features along the spectral types using this dataset. We explain our results of investigation of molecular absorption bands in the *AKARI* spectra to characterize the objects in section 3.2, and then show the colors index measured in the *AKARI* spectra in section 3.3.

## 3.1 The 2.5 – 5.0 $\mu$m Spectral Dataset from L to T Dwarfs

Among the observed 25 brown dwarfs (15 L dwarfs and 10 T dwarfs) by *AKARI*, we obtained high quality spectra for 18 brown dwarfs (12 L dwarfs and 6 T dwarfs) whose signal to noise ratio (S/N) per data point averaged over the spectra is higher than 3.0. The highest value of S/N and mean of S/N for *AKARI* spectra is about 18 and 8, respectively. The corresponding flux level is about 1 mJy for Phase2 data and 2.5 mJy for Phase3 data. We include 2MASS J1553+1532 (T7) in our sample, despite of its relatively low quality (S/N $\sim$ 2) to complete the T-type samples. Two known binary brown dwarfs, $\epsilon$ Ind Ba+Bb (T1+T6) and SDSS J0423–3014 (T0), are excluded. The dataset is summarized in Table 2.10. Six objects taken in Phase 2 and 13 objects in Phase 3 are used for the analysis in this paper. Figure 3.1 shows the spectra of the brown dwarfs in the sequence of their spectral types from L (bottom) to T (top).

## 3.2 Molecular Absorption Bands in Brown Dwarfs

Following molecular absorption bands are clearly recognized in the *AKARI* data; $H_2O$ (broad absorption bands around 2.7 $\mu$m and in longer than 4 $\mu$m), CO (4.6$\mu$m), $CO_2$ (4.2$\mu$m), and $CH_4$ (3.3$\mu$m). $CO_2$ is detected for the first time. Figure 3.2 shows identification of these bands in the AKARI spectra of two objects. The *AKARI* spectra of L-type dwarfs are gently peaking at 3.8 $\mu$m, and are rather smooth and featureless with the current resolution throughout 2.5–5.0 $\mu$m except for the positions of $H_2O$ and

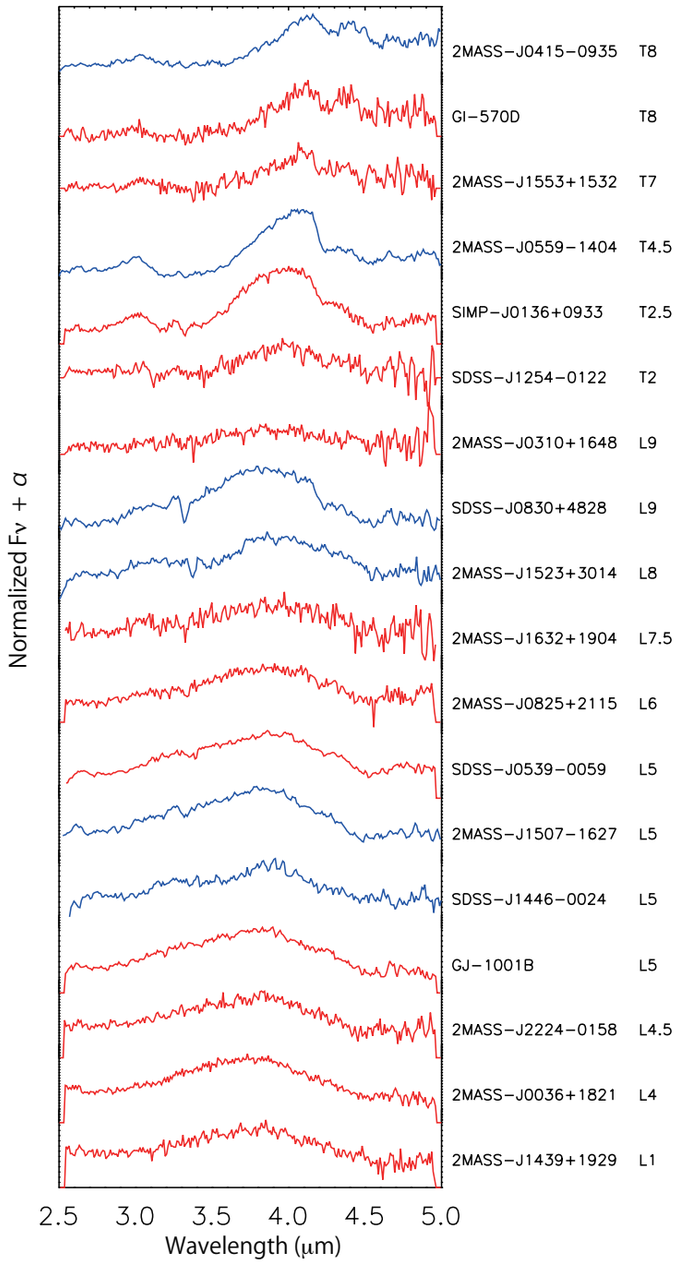


Figure 3.1: *AKARI* spectra of brown dwarfs. 12 L-dwarfs and 6 T-dwarfs are successfully observed. Data taken in Phase2 are drawn in blue line and these in Phase3 are drawn in red. The Phase2 data are generally in better quality than the Phase3 data. The spectra are normalized at 4.0 $\mu$m flux values.

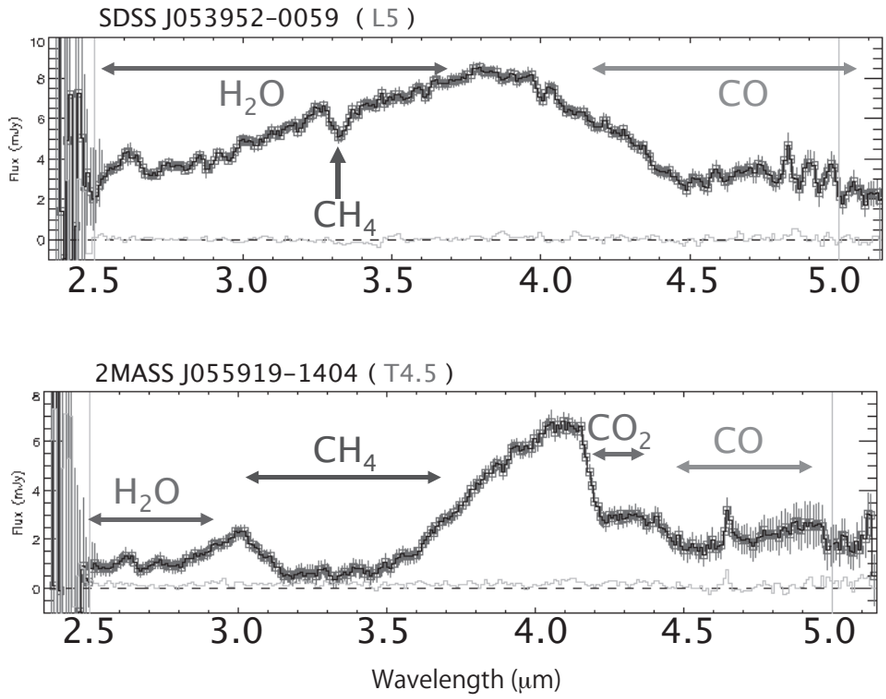


Figure 3.2: The typical L-type and T-type spectra taken by the *AKARI*/IRC. The spectrum of L-type dwarf is rather smooth and featureless in 2.5–5.0 $\mu$m except for the broad absorption bands of $H_2O$ and CO. On the other hand, the spectrum of T-type dwarf exhibits deep molecular absorption features of $CH_4$ and $CO_2$ in addition to the broad bands of $H_2O$ and CO.

CO. $CH_4$ at 3.3$\mu$m exists in the L-type brown dwarfs later than L5. On the other hand, the spectra of T-type dwarfs exhibit deep molecular absorption features further to the broad $H_2O$ bands and CO band. The bands get deeper toward to the late-type spectra. This variation of the feature can be explained qualitatively by the molecular abundance in the photosphere changing according to the decreasing $T_{\rm eff}$. Profiles of molecular abundances along the position in the photosphere are shown in Figures 3.3 and 3.4. The data are calculated using the unified cloudy model (UCM ; see chapter 4). In these figures the partial pressure of the molecules is indicated against the total gas pressure. Two plots are typical cases for L and T dwarf, ($T_{\rm eff}$ / log $g$)=(1900K/5.5) and (1200K/4.5), respectively. We can see that CO abundance in the photosphere of the T-type brown dwarf is significantly less than that in the L-type brown dwarf, while $CH_4$ becomes more major ingredient than that in the L-type brown dwarf. We will show more detailed behavior of each molecule in the following subsections.

### 3.2.1 CO Absorption Band at 4.6 $\mu$m

Only few spectra have been taken in the *M* band wavelength range (Noll et al. 1997; Oppenheimer et al. 1998; Geballe et al. 2009). They reported the detection of the CO absorption band in middle- to late-T spectra. This result was a very important problem for the physics and chemistry in the brown dwarf

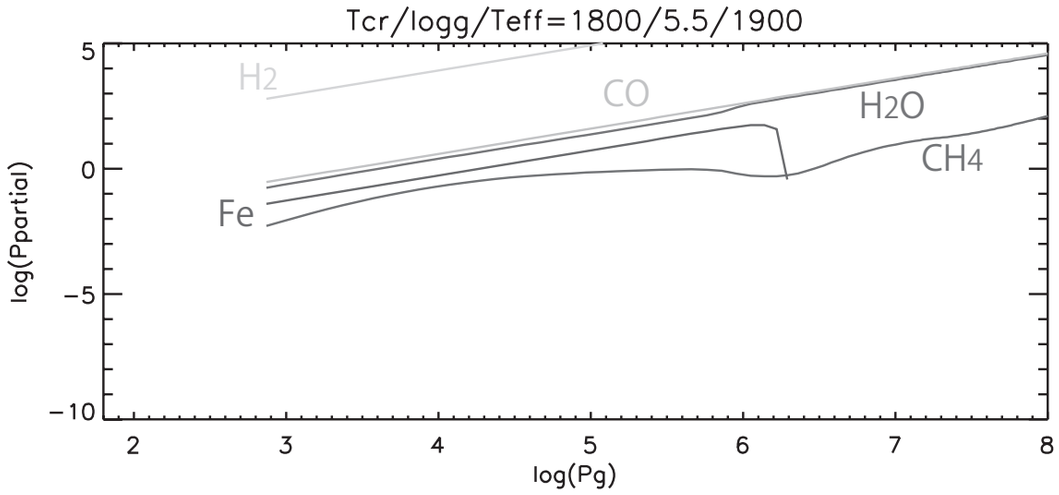


Figure 3.3: Partial pressure of major molecules in the photosphere of a brown dwarf is plotted against total gas pressure. The model parameters are ( $T_{\rm cr}$ / log $g$ / $T_{\rm eff}$ )=(1800/5.5/1900) corresponding to a L4 type.

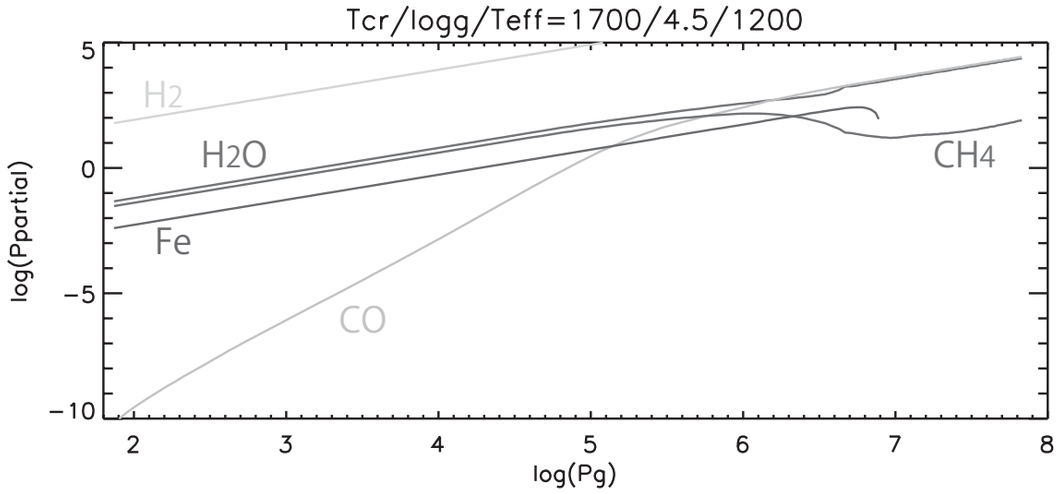


Figure 3.4: Partial pressure of major molecules in the photosphere of a brown dwarfs is plotted against total gas pressure. The model parameters are ( $T_{\rm cr}$ / log $g$ / $T_{\rm eff}$ )=(1700/4.5/1200) corresponding to a T5. CO abundance is rapidly decreasing toward the surface (log $P_g < 6$), and $CH_4$ takes over the position of the most abundant carbon containing molecule.

atmospheres. Because CO is expected to disappear from the spectra of middle- to late-T dwarfs, since under the local thermodynamic equilibrium (LTE) carbon resides mostly in $CH_4$ rather than in CO in a very cool and high-density (T$\sim$1000 K, log $P_g$ $\sim$6.0) environment (Tsuji 1964). However, due to disturbance of the Earth's atmosphere the quality of these data was not excellent and the wavelength coverage was limited, then the detection was not confident (see Figure 1.9).

We have obtained much better spectra around the wavelength region by *AKARI*. The *AKARI* data show that CO appears in the all observed brown dwarf spectra from L to T type. Especially, we confirm that the spectra of our T-type brown dwarfs clearly exhibit CO absorption band, consistently with the past studies (Noll et al. 1997, Oppenheimer et al. 1998, Geballe et al. 2009). It is now clear that the presence of CO is a general characteristic of late-T dwarfs. Some researchers have argued that CO in the photosphere of late-T dwarfs is maintained by vertical mixing (Griffith & Yelle 1999; Saumon et al. 2000; Yamamura et al. 2010). The vertical mixing transfers CO molecules from the inner region, where CO is still abundant under LTE, to the surface. However the mechanism does not completely explain all chemical abundances deviating from the thermochemical equilibrium. Especially, excess of CO in late-L to early-T dwarfs is not explained by the vertical mixing (Yamamura et al. 2010). We need further consideration on this problem.

### 3.2.2 $CO_2$ Absorption Band at 4.2 $\mu$m

We detected $CO_2$ absorption band at 4.2 $\mu$m in the spectra of brown dwarfs for the first time. The band is recognized in all T dwarfs and some late-L dwarfs. We see the band in the spectra of 2MASS J0825+2115 (L6) and SDSS J0830+4828 (L9) clearly, but not in the spectra of 2MASS J1523+3014(L8) and SDSS J0423–0414 (T0) (Figure 3.6). We investigate which spectral types of objects show the $CO_2$ band. Figure 3.5(a) shows the variation of partial pressure of $CO_2$ for different effective temperatures in the models under the LTE. We see that the partial pressure of $CO_2$ increases with decreasing temperature from 2600 to 1600K, then turns to decrease with decreasing temperature from 1600 to 700K. This indicates that the $CO_2$ is most abundant in the photosphere of $T_{\rm eff}$ $\sim$1600 K dwarfs. Thus it is expected that the $CO_2$ absorption band appears in the spectra from L6 to early T dwarfs. However, $CO_2$ 4.2 $\mu$m absorption band does not appear in some observed spectra of late-L to early-T despite of expecting abundant $CO_2$ in the models. We find that the behavior of $CO_2$ absorption at late-L to early-T dwarfs is very complicated. It may be caused by the effect of dust, or it may reflect the difference in the elemental abundances. We discuss the $CO_2$ absorption further in section3.4.1 and chapter 6.

### 3.2.3 $CH_4$ Absorption Band at 3.3 $\mu$m

It is known that $CH_4$ $\nu_3$ absorption band at 3.3 $\mu$m already appears in the spectra of mid-L dwarfs (Noll et al. 2000), but the $CH_4$ $\nu_2$ and $\nu_4$ absorption band at 2.2 $\mu$m, which are used for classification of T-type dwarfs, were not detected in the spectra of L dwarfs (Nakajima et al. 2004). The *AKARI* data including 3.3$\mu$m region should push forward our understanding of the $CH_4$ molecule behavior in the photosphere of L dwarfs. We find that the $CH_4$ 3.3 $\mu$m fundamental band appears in the spectra of brown dwarfs later

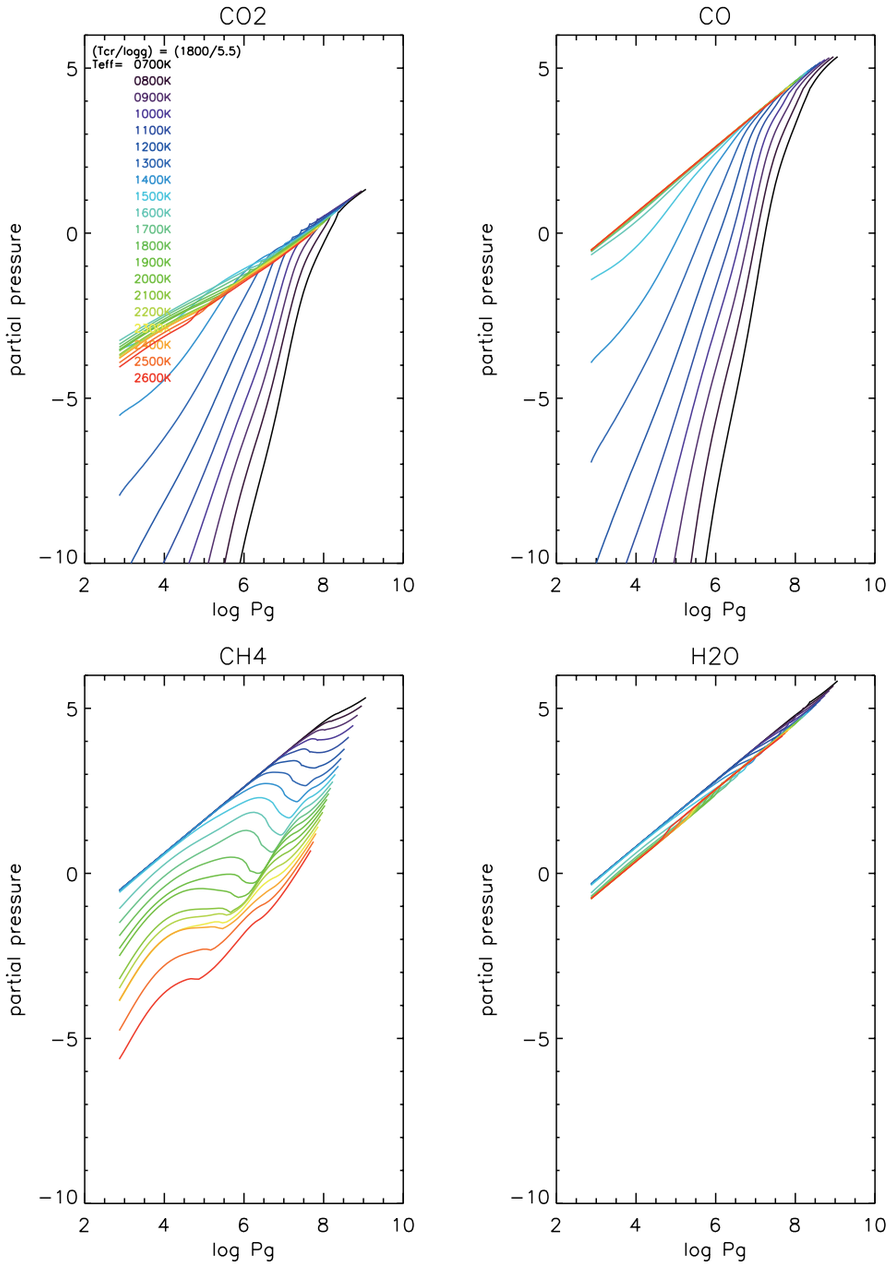


Figure 3.5: Partial pressure of major molecules are plotted against total gas pressure for different $T_{\rm eff}$. (a)$CO_2$ partial pressure increases with decreasing effective temperature to 1600K, and decreases for lower temperature. (b)CO partial pressure decreases monotonically with decreasing effective temperature. (c)$CH_4$ partial pressure increases with decreasing effective temperature. This is complementary with that of CO. (d)$H_2O$ partial pressure is generally high and slightly increases with decreasing temperature.

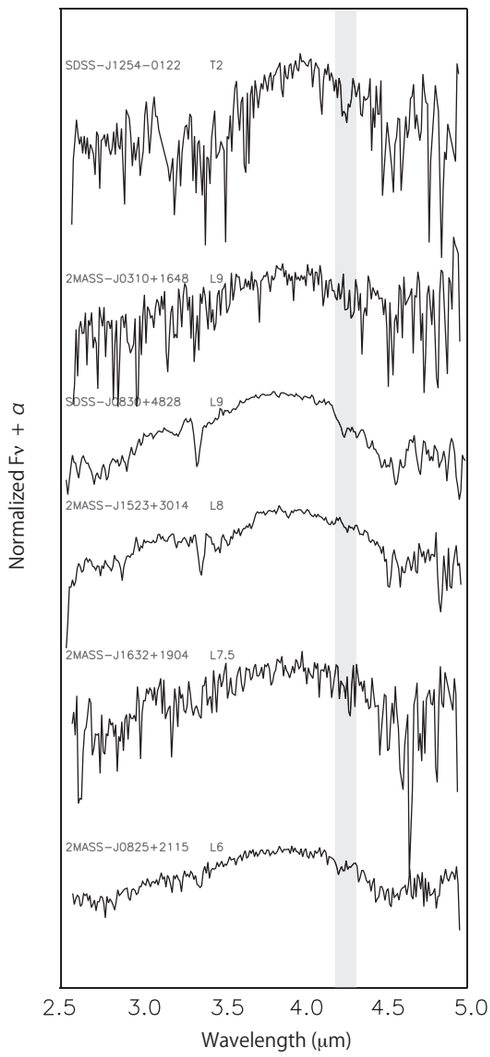


Figure 3.6: The $CO_2$ absorption band at 4.2 $\mu$m in the spectra of late-L to early-T dwarfs. The area painted in gray shows the position of the $CO_2$ fundamental absorption band.

than L5. In addition, it is interesting that we see the band in only two sources out of four L5 dwarfs in our *AKARI* sample. The band is seen in SDSS J0539–0059 and 2MASS J1507–1627, but not in the other two L5 sources, SDSS J1446+0024 and GJ 1001B (Figure 3.8).

Based on the *AKARI* spectra from L1 to L9 dwarfs, we investigate the appearance of the $CH_4$ band quantitatively to confirm this result in detail. We derive equivalent width at the position of the 3.3 $\mu$m $CH_4$ Q-branch feature in each spectrum, and calculated the ratio between the equivalent width and the standard deviation of the data points in the nearby off-feature wavelengths. We evaluate "$CH_4$ index" $B_{CH_4}$ as below.

$$B_{CH_4} = \frac{EW}{\left(\frac{\sigma}{F_{\rm center}} \times d\lambda \times \sqrt{N-1}\right)}, \tag{3.1}$$

where EW is the equivalent width, $\sigma$ is the standard deviation in the off-band wavelengths, $F_{\rm center}$ is the estimated flux at the wavelength of band center derived by linear interpolation from the off-feature region flux, $d\lambda$ is the wavelength grid interval and $N$ ($\sim$ 20) is the number of data points within the defined region. We show the results in Table 3.1 and Figure 3.7. We regard that the detection is significant when $B_{CH_4}$ is larger than 5. We use "5" as a border of $CH_4$ band detection, because the $B_{CH_4}$ of L7.5 dwarf that the $CH_4$ band is confirmed by visual reference is 5.25 and L1 and L4 dwarfs that the band is not confirmed are 4.19 and 4.24, respectively. We find that the $CH_4$ 3.3 $\mu$m Q-branch feature starts appearing at L5 Type, and the band appears in only two of four L5 dwarfs,SDSS J0539–0059 and 2MASS J1507–1627 (Figure 3.7 and Table 3.1). The detection of the $CH_4$ absorption band in the spectra of 2MASS J1507–1627 is consistent with the past result reported by Noll et al. (2000). The presence of $CH_4$ absorption band at 3.3 $\mu$m in L5 spectra is confirmed by *AKARI* spectral data, but there are L5 objects without the band. We discuss these results more in detail in section 3.4.2 and 4.6.1.

Table 3.1: The $CH_4$ index for L5 dwarfs. The position of $B_{CH_4}$ based on the threshold of $CH_4$ detection are also shown in third column with "Y" or "N".

| object | $B_{CH_4}$ | $CH_4$ |
|---|---|---|
| 2MASS J1439+1929 | 4.12 | N |
| 2MASS J0036+1821 | 4.24 | N |
| 2MASS J2224–0158 | 3.03 | N |
| SDSS J0539–00590 | 9.95 | Y |
| SDSS J1446+0024 | 4.11 | N |
| 2MASS J1507–1627 | 6.26 | Y |
| GJ 1001B | 3.86 | N |
| 2MASS J0825+2115 | 6.27 | Y |
| 2MASS J1632+1904 | 5.25 | Y |
| 2MASS J1523+3014 | 9.06 | Y |
| SDSS J0830+4828 | 19.78 | Y |
| 2MASS J0310+1648 | 6.45 | Y |

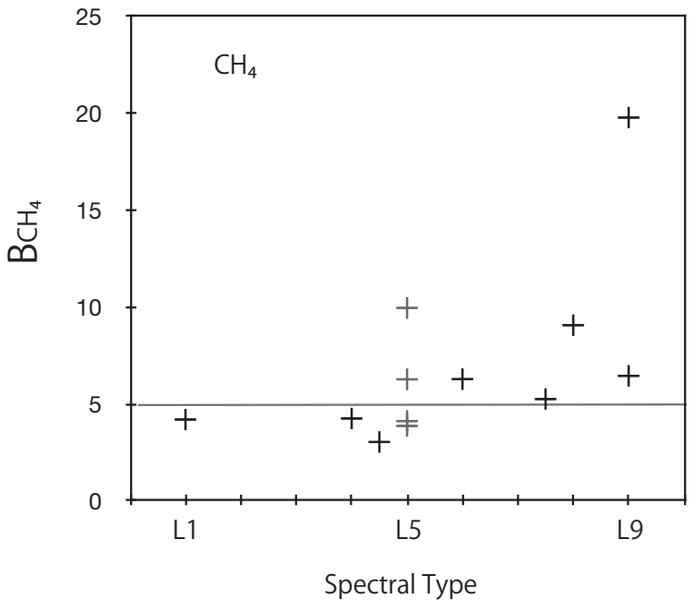


Figure 3.7: $CH_4$ index $B_{CH_4}$ measured on the *AKARI* spectra versus spectral type. $B_{CH_4}$ is ratio of equivalent width of $CH_4$ Q-branch to its uncertainty from the standard deviation of the data points in the nearby off-band wavelengths. It is found that the onset of the $CH_4$ feature is L5-type dwarfs. The line indicates the threshold of $CH_4$ detection.

## 3.3 Infrared Colors in the *AKARI* Wavelength

We investigated the various colors extracted from the *AKARI* spectral data. Studies of brown dwarf colors have been carried out mainly on $J$, $H$, $K$, $L'$ and $M'$ band photometry data (e.g. Stephens et al. 2001; Leggett et al. 2002a, 2007; Knapp et al. 2004; Golimowski et al. 2004). While photometry of $L'$ band has been made extensively in ground-based observations only few spectroscopic observations of the 3.3 $\mu$m region have been carried out. Quality of the obtained spectra is not sufficient for detailed studies. Therefor the $CH_4$ $\nu_3$ fundamental band data observed with *AKARI* are quite valuable. In section 2.3.4 we extract $L'$ flux from *AKARI* spectral data using Mauna Kea Observatory (MKO) $L'$ filter transmission and compare the results with previous $L'$ photometric data from Leggett et al. (2002a,b), Knapp et al. (2004) and Golimowski et al. (2004). As a result, the $L'$ flux from the *AKARI* spectral are consistent with the previously $L'$ photometric data within 10 %. In this section we also examine several infrared colors with the *AKARI* spectral data. The wavelength range of MKO $J, K, L', M'$ band filters and the range of 3.3 $\mu$m band, [3.3], are shown in Figure 3.9.

### 3.3.1 $K - L'$

First we discuss about $K - L'_A$ color, where $L'_A$ is the $L'$ flux estimated from the *AKARI* spectra (see section 2.3.4). We compare the previous measurements $K - L'$ color to confirm validity of the *AKARI* samples. We use MKO-NIR $K$ photometry derived by Leggett et al. (2000, 2001, 2002a,b) and Knapp et al. (2004).

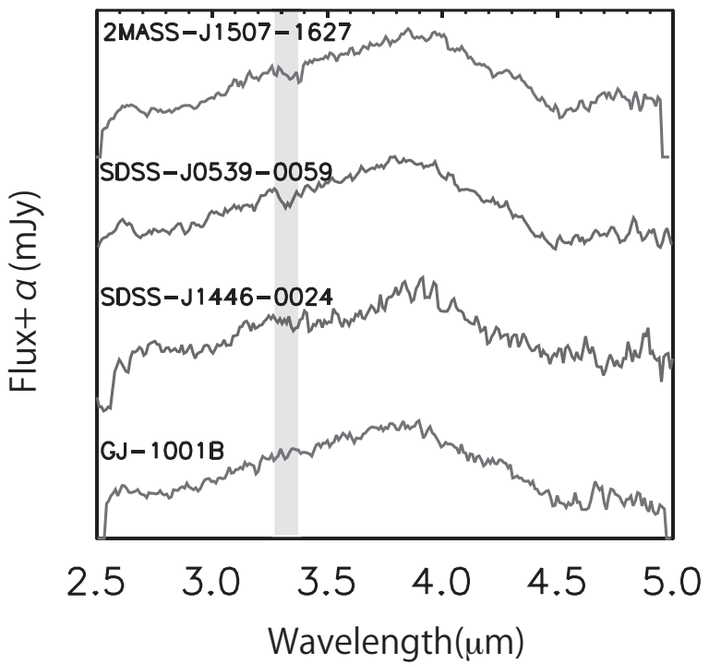


Figure 3.8: The 2.5–5.0 $\mu$m spectra of four L5 dwarfs, 2MASS J1507–1627, SDSS J0539–0059, SDSS J1446+0024 and GJ 1001B. 2MASS J1507–1627 and GJ 1001B are observed spectra taken in Phase 2 and the other two objects are observed in Phase 3. The $CH_4$ $\nu_3$ absorption band is seen in SDSS J0539–0059 and 2MASS J1507–1627, but not in the other two L5 sources, SDSS J1446+0024 and GJ 1001B

Table 3.2: $J$, $K$ and $L'$ magnitude of brown dwarfs.

| Object Name | Sp. Type | $J$ | $K$ | $K-L'_A$ | J$-L'_A$ | [3.3]$-L'_A$ | index [4.2] | index [1.27/4.12] | index [1.14/4.12] | references |
|---|---|---|---|---|---|---|---|---|---|---|
| 2MASS J1439+1929 | L1 | 12.66 | 11.47 | 0.60 | 1.79 | 0.47 | 0.02 | 1.63 | 2.05 | 1 |
| 2MASS J0036+1821 | L4 | 12.31 | 11.03 | 0.92 | 2.20 | 0.46 | 0.03 | 1.88 | 2.38 | 1 |
| 2MASS J2224–0158 | L4.5 | 13.89 | 11.98 | 1.11 | 3.02 | 0.45 | 0.09 | 2.80 | 3.41 | 2 |
| SDSS J0539–00590 | L5 | 13.85 | 12.40 | 1.13 | 2.56 | 0.57 | -0.00 | 2.34 | 2.86 | 1 |
| SDSS J1446+0024 | L5 | 15.56 | 13.80 | 1.19 | 2.89 | 0.44 | -0.13 | 2.63 | 3.12 | 1 |
| 2MASS J1507–1627 | L5 | 12.7 | 11.29 | 0.98 | 2.60 | 0.58 | -0.03 | 2.41 | 2.98 | 1 |
| GJ 1001B | L5 | 13.06 | 11.36 | 1.41 | 2.68 | 0.47 | 0.06 | 2.32 | 2.87 | 1 |
| 2MASS J0825+2115 | L6 | 14.89 | 12.93 | 1.52 | 3.37 | 0.80 | -0.28 | 3.43 | 4.06 | 1 |
| 2MASS J1632+1904 | L7.5 | 15.77 | 13.97 | 1.51 | 3.32 | 0.96 | -0.09 | 3.28 | 3.91 | 1 |
| 2MASS J1523+3014 | L8 | 15.95 | 14.35 | 1.49 | 3.11 | 0.90 | 0.12 | 3.02 | 3.73 | 1 |
| SDSS J0830+4828 | L9 | 15.22 | 13.68 | 1.68 | 3.14 | 1.11 | -0.36 | 2.98 | 3.73 | 1 |
| 2MASS J0310+1648 | L9 | 15.88 | 14.18 | 1.55 | 3.25 | 0.92 | 0.11 | 2.88 | 3.64 | 1 |
| SDSS J125–0122 | T2 | 14.66 | 13.84 | 1.49 | 2.31 | 1.48 | -0.14 | 2.41 | 3.47 | 1 |
| SIMP J0136+0933 | T2.5 | 13.26 | 12.562 | 1.68 | 2.23 | 1.58 | -0.27 | 2.32 | 3.35 | 4 |
| 2MASS J0559–1404 | T4.5 | 13.57 | 13.73 | 1.55 | 1.39 | 2.55 | -0.47 | 1.86 | 3.29 | 1 |
| 2MASS J1553+1532 | T7 | 15.49 | 15.507 | 1.99 | 1.70 | 2.38 | -0.45 | 1.99 | 4.82 | 4 |
| Gl 570D | T8 | 14.82 | 15.52 | 2.44 | 1.74 | 2.02 | -0.37 | 2.32 | 5.39 | 1 |
| 2MASS J0415–0935 | T8 | 15.32 | 15.83 | 2.5 | 1.99 | 3.56 | -0.11 | 2.50 | 6.03 | 2 |

1; Legget et al. (2002a)
2; Knapp et al. (2004)
4; deriving from SpeX spectra
The error of the photometry data are about 0.05 [mag].

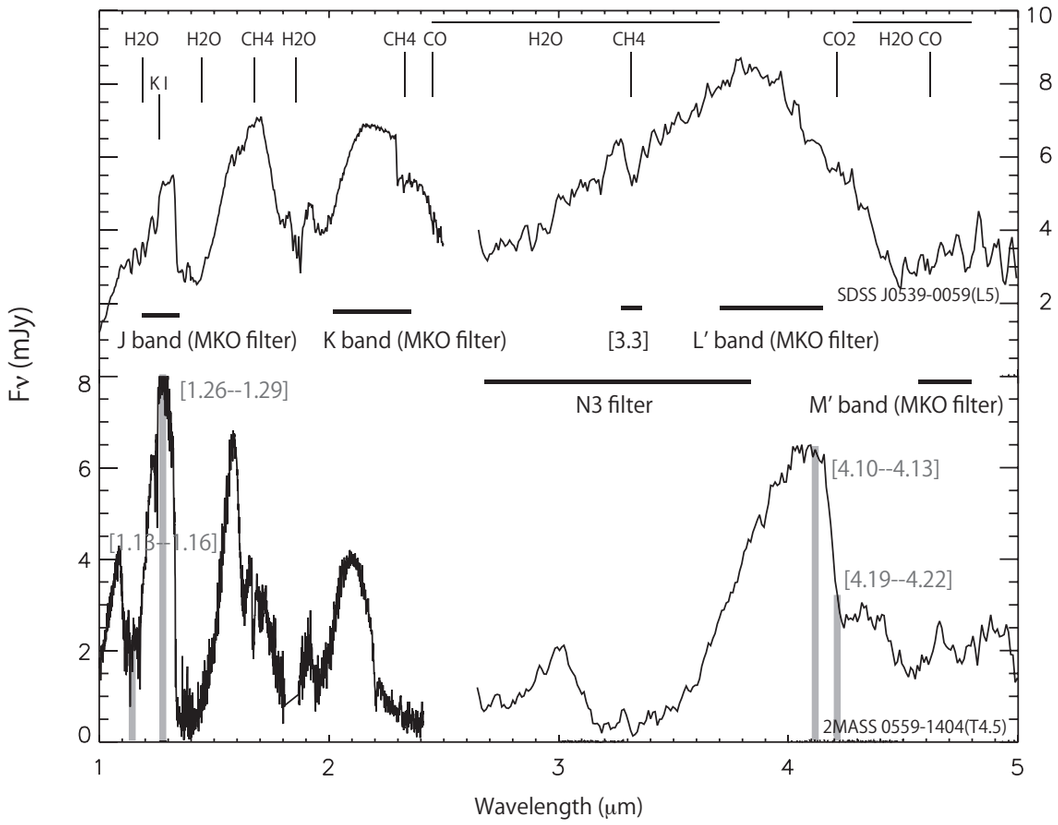


Figure 3.9: The wavelength range of the MKO $J, K, L', M'$ band filters and the averaging range of [3.3] . We show the observed spectra of typical L dwarf SDSS 0539-0059(L5) and of typical T dwarf 2MASS J0559–1404(T4.5). The wavelength range of [1.13–1.16] and [1.26–1.29] used for deriving "index 1.14" by Geballe et al. (2002) and of [4.10–4.13] used for deriving "index 4.2" in section 3.4.1, "index 1.27/4.12" and "index 1.14/4.12" in section 3.4.3 are also shown. The wavelength range of [4.19–4.22] used for "index 4.2 " in section 3.4.1 is also shown.

We compare the $K - L'_A$ with $K - L'$ color given by Golimowski et al. (2004) in Table 3.2. Two objects, SIMP J0136+0933 and 2MASS J1553+1532 do not have previous $K$ band photometry data. Therefor we estimate their $K$ band flux using 2MASS $J$ band flux and IRTF/SpeX spectral data (see section 4.4.3). We calibrate the absolute flux of their spectra by comparing the measured flux applying 2MASS $J$ band filter transmission and the 2MASS photometric data. After then, we derive $K$ band flux by integrating the SpeX spectra with the MKO-NIR $K$ band filter.

Figure 3.10 compares $K - L'$ color of our *AKARI* brown dwarfs (red square) and that from Golimowski et al. (2004) (black square). The $K - L'_A$ color from *AKARI* data are confirmed to be consistent with the previous results. The plot tells that $K - L'$ stays almost unchanged between late-L and mid-T type. It is interpreted by the effects of growing $CH_4$ absorption in 3.3–3.7 $\mu$m (Leggett et al 2002) that start to appear in the L5 spectra (section 1.4 and section 3.2.3).

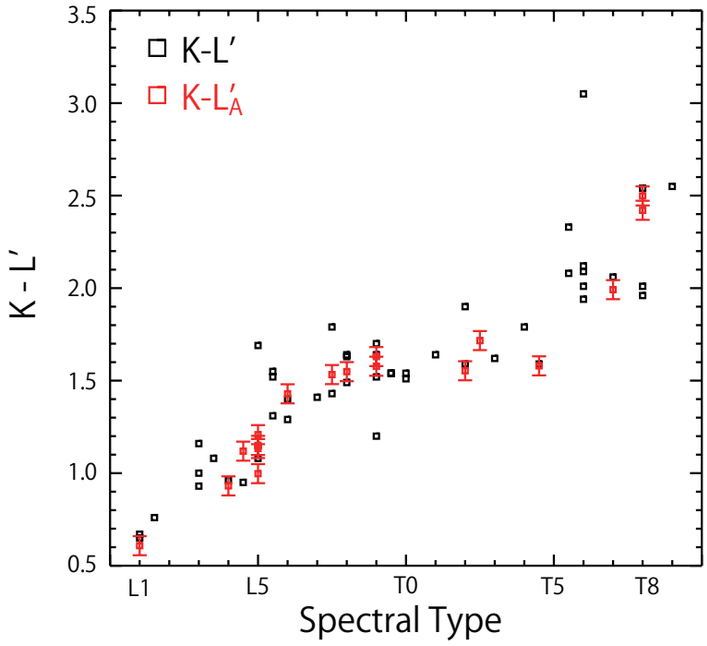


Figure 3.10: $K - L'$ color as a function of spectral type. Previous results by Golimowski et al. (2004) are drawn with black square and our results are with red square. Our colors from *AKARI* spectra are consistent with the past result.

### 3.3.2 [3.3] – $L'_A$

$B_{CH_4}$ used in section 3.2.3 is only applicable for L-type dwarfs, because the $CH_4$ absorption band in T-type spectra becomes broader and deeper, and P- and R- branches are not ignorable any more. In order to understand the $CH_4$ 3.3 $\mu$m absorption in spectra of brown dwarfs including T-type, we define a photometry band [3.3], which is measured by simply averaging the flux between 3.27 and 3.36 $\mu$m. [3.3]–$L'_A$ for *AKARI* objects are listed in Table 3.2, and plotted against spectral types in Figure 3.11. The large error of the color for late-T type sources are caused by lack of data points around 3.3 $\mu$m in the *AKARI* spectra due to the heavy absorption of $CH_4$. The [3.3]–$L'_A$ color gets redder monotonically along L to T sequence. This result indicates that the $CH_4$ $\nu_3$ absorption develops simply toward late spectral types. This trend is consistent with the $CH_4$ index $B_{CH_4}$ derived in section 3.2.3.

### 3.3.3 $J - L'_A$

The trend of $J - L'$ color has not been investigated in the past study. While $J$ band flux is the most sensitive to dust extinction and molecular absorption, $L'$ band reflects the $CH_4$ absorption. Thus $J - L'$ color would give us mixed information of dust condition and molecular abundance.

We show $J - L'_A$ color of our *AKARI* brown dwarfs in Figure 3.12. We see a trend of being redder from L1 to L6, then staying unchanged between L6 and L9. $J - L'_A$ becomes bluer near the L/T boundary, and gets redder again for the objects later than T5. This complicated trend is similar to $J - K$ color (Leggett et

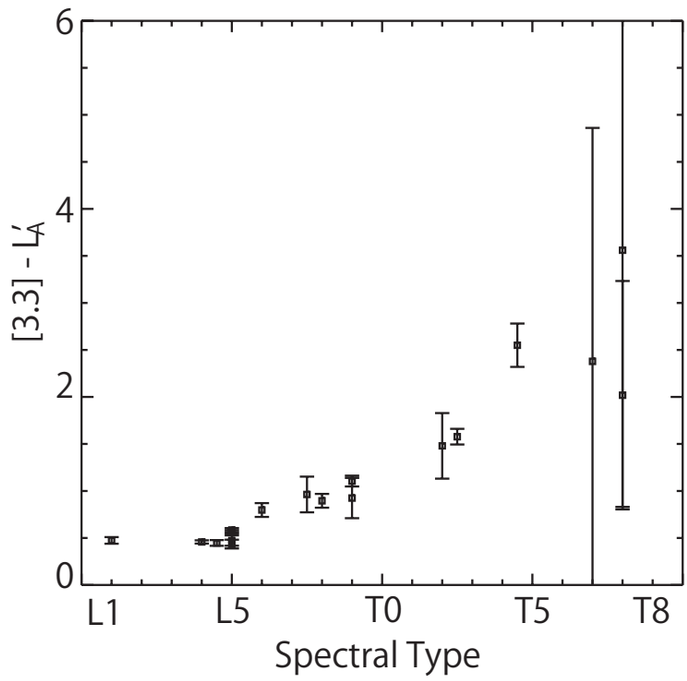


Figure 3.11: [3.3]–$L'_A$ color as a function of spectral class. Whereas the color of early type dwarfs do not change, the color of later than L5 dwarfs tend to bluing. This indicate that the $CH_4$ absorption band at 3.3 $\mu$m become stronger toward late spectral types.

al. 2002b) except for the late-T part. Red color of early- to mid-L dwarfs is thought be due to increasing dust extinction at *J* band. The red color of late-T dwarfs are seen with the *AKARI* data for the first time. We discuss the cause of this red color in late-T dwarfs in section 3.4.3.

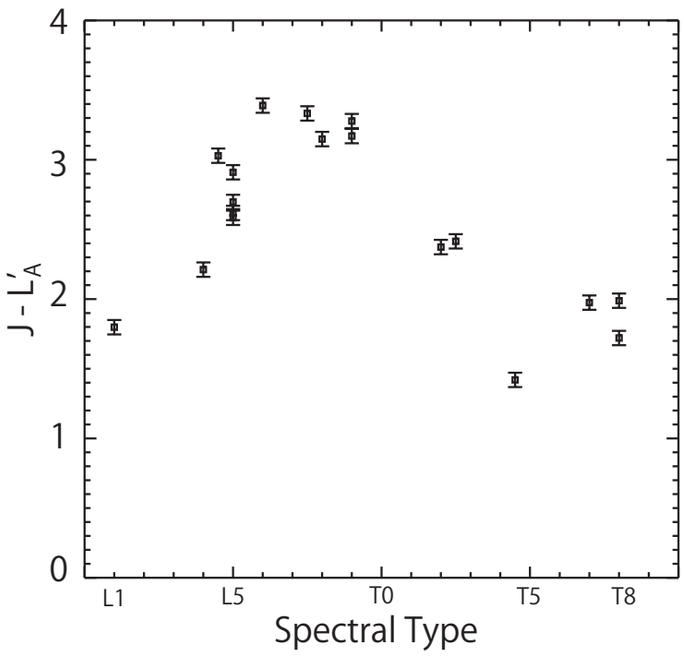


Figure 3.12: $J - L'_A$ color for objects observed by *AKARI*. The color becomes redder at early-L and late-L dwarfs. The color from late-L to mid-T becomes slightly bluer, and gets redder again for the objects later than T5.

## 3.4 Discussion

### 3.4.1 $CO_2$ Absorption Band at 4.2 $\mu$m in the Spectra of Late-L Dwarfs

As noted above the behavior of the $CO_2$ 4.2 $\mu$m absorption band is complicated. To confirm the presence of the 4.2 $\mu$m band we evaluate [4.10–4.13]–[4.19–4.22] (hereafter "index 4.2") color from the *AKARI* spectra (Figure 3.13). [4.10–4.13] and [4.19–4.22] are measured by simply averaging the flux between 4.10 and 4.13 $\mu$m, and 4.19 and 4.22 $\mu$m, respectively, and are converted to magnitude. [4.19–4.22] represent the $CO_2$ absorption band, and [4.10–4.13] does not have any strong band. The "index 4.2" decreases slowly from L to T dwarfs. We see a scatter in late-L dwarfs. "index 4.2" of 2MASS J0825+2115(L6) and SDSS J0830+4828(L9) are bluer than that of 2MASS J1632+1904(L7.5), 2MASS J1523+3014(L8), and SDSS J0830+4828(L9) relative to SDSS J1254–0122(T2) that shows a prominent blue color. One possible reason of the different behavior is the effect of the dust. If objects have large dust effect, the $J - L'_A$ should show redder than that of little dust effect. However, $J - L'_A$ of the objects with the 4.2 $\mu$m absorption are redder than the objects without the absorption. This trend is opposite to the result expected from the dust effects. This result indicates that the presence of 4.2 $\mu$m absorption band is not relative to the dust presence.

The other possible reason we suggest is that these difference of 4.2$\mu$m band in the spectra of late-L to early-T dwarfs is caused by the difference of $CO_2$ abundance in their photosphere. Tsuji et al. (2011) indicate that SDSS J0830+4828(L9) is possibly a high metallicity object. The effects of elemental abundances to the brown dwarf spectra are argued in chapter 6.

### 3.4.2 $CH_4$ $\nu_3$ Absorption Band at 3.3 $\mu$m in the Spectra of Four L5 Dwarfs

The $CH_4$ $\nu_3$ absorption band is seen in SDSS J0539–0059 and 2MASS J1507–1627, but not in the other two L5 sources, SDSS J1446+0024 and GJ 1001B (Figures 3.7, 3.8 and Table 3.1). This result may be distinguished by spectral classification. Their spectral types "L5" of 2MASS J1507–1627 and GJ 1001B are determined by Kirkpatrick et al. (2000), and for SDSS J0539–0059 and SDSS J1446+0024 by Geballe et al. (2002). They use optical or infrared ($J$, $H$ and $K$ band) color and molecular absorption band strength for classification, and show that the results are different depending on the criteria used. The study by Knapp et al. (2004) classified 2MASS J1507–1627 as L5.5. Martín et al. (1999) classified GJ 1001B as L4 from molecular absorption band strengths in the optical region. Classifications of SDSS J0539–0059 and SDSS J1446+0024 are different depending on the band used as shown in Table 3.3. We see that the spectral types of SDSS J0539–0059 and SDSS J1446+0024 derived by $CH_4$ at 2.2 $\mu$m index are L6 and L5 respectively, and consistent with our speculation. Our results indicate that the appearance of the $CH_4$ absorption at 3.3 $\mu$m reflect the spectral classification with $CH_4$ 2.2 $\mu$m index. Contrary, our analysis using *AKARI* spectral data proposes their spectral types are earlier side and later side of L5 for SDSS J1446+0024 and SDSS J0539–0059, respectively.

We consider that the discrepancy in $CH_4$ 3.3 $\mu$m in the four L5 dwarfs are caused by the effects of dust. In section 3.3.3, we have mentioned that the red color in $J - L'_A$ at mid-L dwarfs shown in Figure 3.12 is due to by dust extinction. The larger effect of dust is the redder $J - L'_A$ color. The color of SDSS

J1446+0024 and GJ 1001B are redder than that of SDSS J0539–0059 and 2MASS J1507–1627, and thus more affected by dust. We discuss this speculation in section 4.6.1 further.

Table 3.3: The spectral type determined from each molecular band, optical color, $H_2O$ in $H$ band, $CH_4$ in $K$ band (Geballe et al. 2002).

| object | (0.95-0.98)/ (0.735-0.755) | $H_2O$ 1.5$\mu$m | $CH_4$ 2.2$\mu$m | mean Sp.T. |
|---|---|---|---|---|
| SDSS J0539–0059 | L4.5 | L5 | L6 | L5 |
| SDSS J1446+0024 | L5.5 | L4.5 | L5 | L5 |

### 3.4.3 Red $J - L'_A$ Color of Late-T Dwarfs

In section 3.3.3 we find that $J - L'_A$ becomes redder in the late-T dwarfs. Two possible reasons for this phenomenon are considered; (1) evolving $H_2O$ absorption around 1.14 $\mu$m towards late-T dwarfs (2) the decreasing $T_{\rm eff}$ that brings the $J$ band wavelength to the Wien side of the spectral energy distribution (SED). We carry out the following analyses to confirm these hypotheses.

The wavelength range of MKO $J$ band filter is 1.16–1.32 $\mu$m that includes a part of the $H_2O$ absorption band. The ratio of [1.26–1.29] to [1.13–1.16] (hereafter "index 1.14") of 2MASS J0559-1404 (T4.5) and GD 570D (T8) are defined by Geballe et al. (2002) to measure the 1.14 $\mu$m $H_2O$ band strength following as,

$$\text{index} = \frac{\int_{\lambda_1}^{\lambda_2} f_\lambda d\lambda}{\int_{\lambda_3}^{\lambda_4} f_\lambda d\lambda} \tag{3.2}$$

where $\lambda_i$ $(i = 1,2,3,4)$ is the wavelength, which are chosen so that intervals in the numerator and denominator have the same length. Here, $\lambda_1$=1.26 $\mu$m, $\lambda_2$=1.29 $\mu$m, $\lambda_3$=1.13 $\mu$m, and $\lambda_4$=1.16 $\mu$m. While [1.26–1.29] does not include any strong absorption band, [1.13–1.16] have strong $H_2O$ 1.14 $\mu$m absorption band. Thus this "index 1.14" indicates the $H_2O$ absorption strength. The "index 1.14" values for 2MASS J0559–1404 and GD 570D are 3.1 and 13.3, respectively, indicating that the $H_2O$ absorption band becomes greatly deeper from T4.5 to T8.

We also consider the other possible reason. If $J$ band located in the Wien side of the spectrum the flux drops down rapidly with the decreasing temperature, while the $L'$ band flux does not change much because the wavelength is near the peak of the black body for temperature of 1200 $\sim$ 700 K. We derive the [1.26–1.29]–[4.10–4.13] (hereafter "index 1.27/4.12"). [1.26–1.29] are measured with same method as deriving [4.10–4.13] in section 3.4.1. Both wavelength range have no strong absorption band. [1.26–1.29] is measured by simply averaging the SpeX spectral data between 1.25–1.29 $\mu$m, and [4.10–4.13] are derived from the *AKARI* spectra by the same method in 4.10–4.13 $\mu$m. Figure 3.14 shows that "index 1.27/4.12" plotted against the spectral type. We see that "index 1.27/4.12" becomes also redder in the late-T dwarfs.

We derive the [1.13–1.16]–[4.10–4.13] (hereafter "index 1.14/4.12") to confirm which of the two reasons affects for the reddening of late-T dwarfs more. [1.13–1.16] are measured with same method as deriving [4.10–4.13] in section 3.4.1. [1.13–1.16] represent $H_2O$ absorption strength and [1.26–1.29] indicates continuum, then the two effects can be separated by comparing "index 1.14/4.12" and "index 1.27/4.12". Figure 3.16 shows the plots. We see a significantly large reddening "index 1.14/4.12" of late-T dwarfs, which is shown by a blue circle. It means that the effect of SED shift to the reddening in late-T dwarfs is less than that of the 1.14 $\mu$m $H_2O$ absorption. We conclude that the redder colors in $J - L'_A$ appeared in late-T dwarfs are caused by the combination of the increasing $H_2O$ 1.14$\mu$m absorption and the effect of shift of the SED, but the effect of increasing $H_2O$ absorption is larger than that of the SED shift.

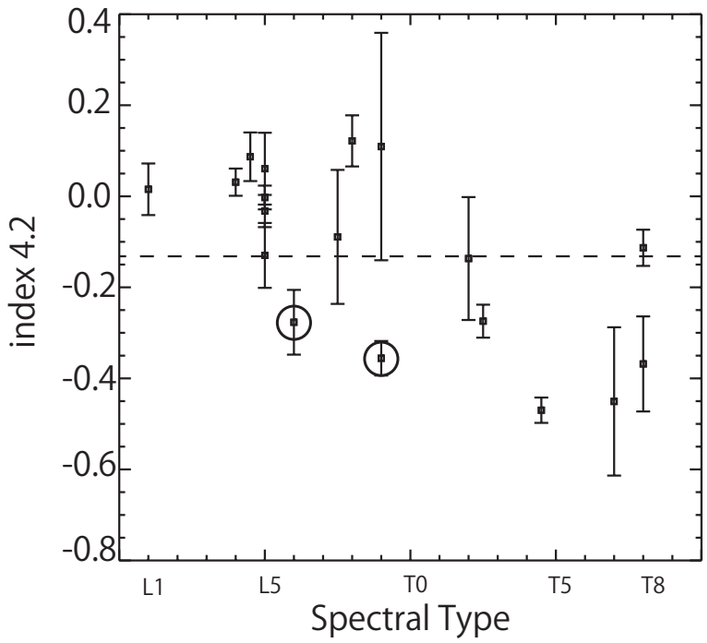


Figure 3.13: "index 4.2" color for objects observed by *AKARI*. 2MASS J0825+2115(L6) and SDSS J0830+4828(L9), which are the objects with 4.2 $\mu$m absorption band are -0.28 and -0.36, respectively. They are shown in open circle.

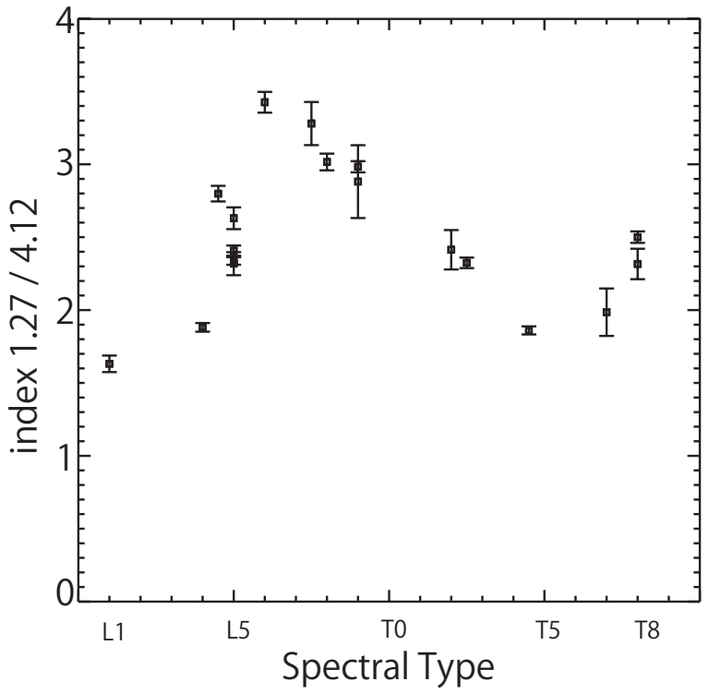


Figure 3.14: "index 1.27/4.12" for objects observed by *AKARI*. The "index 1.27/4.12" at the late-T dwarfs become also redder.

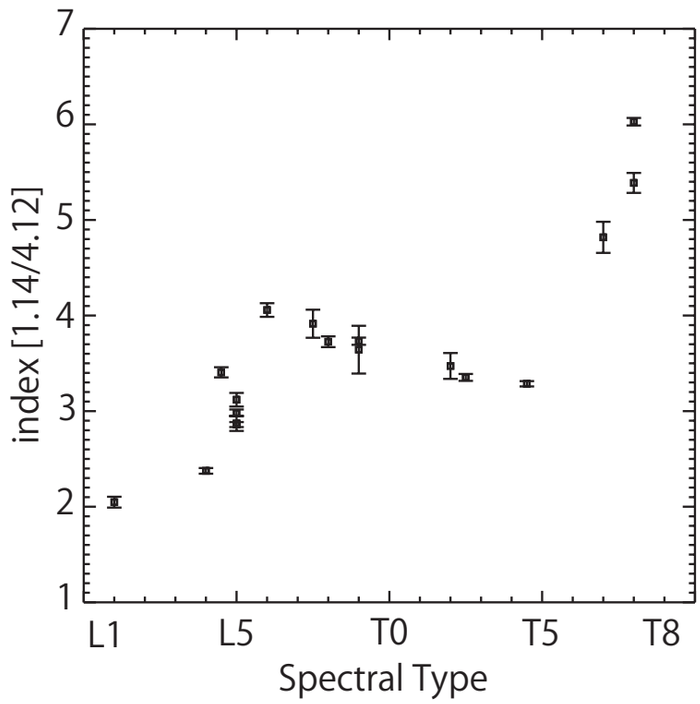


Figure 3.15: "index 1.14/4.12" for objects observed by *AKARI*. The "index 1.14/4.12" at the late-T dwarfs become also redder.

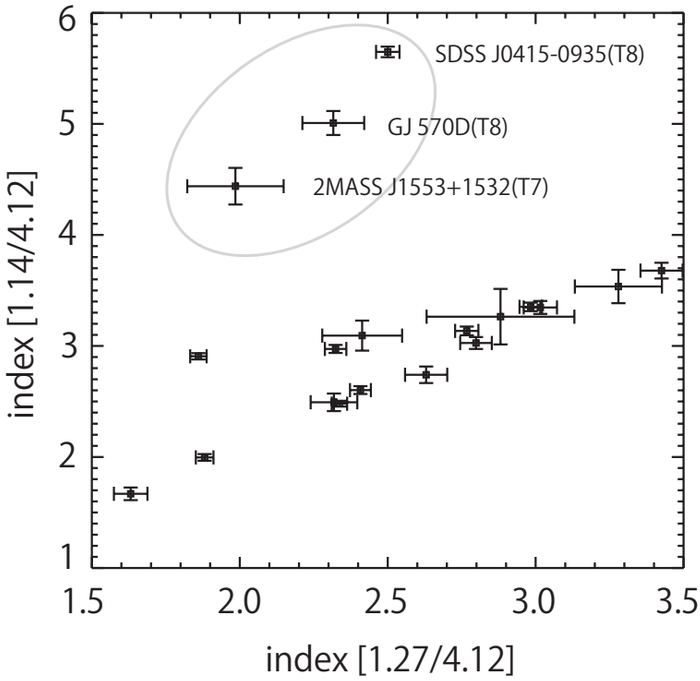


Figure 3.16: "index 1.27/4.12" versus "index 1.14/4.12". The The "index 1.14/4.12" at the late-T dwarfs is redder than "index 1.27/4.12". This result is shown by a blue circle.

# Chapter 4

# Analysis with the Unified Cloudy Model

To understand the atmospheres of brown dwarfs better, we analyze the *AKARI* spectra using the Unified Cloudy Model (UCM, Tsuji 2002, 2005). We introduce the general description of the modeling of brown dwarf atmospheres in section 4.1. We explain the UCM in section 4.2, and its physical free parameters in section 4.3. We describe the fitting evaluation method to derive the best parameter set (best model) for each *AKARI* object in section 4.4. Then we show the results and the uncertainty of this analysis in section 4.5. We discuss the results in section 4.6

## 4.1 Modeling of Brown Dwarf Atmospheres

So far various models of brown dwarf atmospheres have been developed by several groups: Tsuji et al. (1996a) and Tsuji (2002, 2005), Allard et al. (2001, 2003), Ackerman & Marley (2001), Cooper et al. (2003), Woitke & Helling (2003, 2004) and Helling et al. (2001, 2008) etc. These models all assume hydrostatic equilibrium, gas-phase chemical equilibrium under local-thermodynamic equilibrium (LTE), and mixing length theory for treating the convective energy transport. In a dense environment like brown dwarf photospheres, LTE can be justified (Hauschildt et al. 1997; Schweitzer et al. 2000). The largest difference of these brown dwarf atmosphere models from stellar model is incorporation of dust formation in the photosphere. Generally, stellar spectra can be interpreted in terms of effective temperature $T_{\rm eff}$, surface gravity log $g$, chemical composition, and micro-turbulent velocity. However it is difficult to explain the brown dwarf spectra by only these four basic parameters because of the presence of dust in the photosphere. Opacity of dust affects significantly to the atmospheric temperature – pressure profile and the emergent flux. The composition, opacity and formation physics of dust differ in different models.

Helling et al. (2001a) and Woitke & Helling (2003, 2004) considered the dust formation similar to that in the circumstellar of asymptotic giant branch (AGB) stars. Ackerman & Marley (2001) and Cooper et al. (2003) incorporated terrestrial cloud formation process. Tsuji et al. (1996a,b) and Allard et al. (2001a) applied practical implementation. Tsuji et al. (1996b, 2002, and 2005) considered that dust forms at the condensation temperature, $T_{cond}$, following LTE condition under the high density gas in the photospheres of cool dwarfs.

Observations revealed that the effect of dust, masking molecular bands and changing photospheric

structure, appears most prominently in the near infrared spectra of L-dwarfs (Tsuji et al. 1996b; Nakajima et al. 2001). On the other hand, the spectra of T-dwarfs are less affected by the dust. These results indicate that the dust disappears somewhere in the L-T boundary (Burgasser et al. 2002). The dust cloud may migrate from surface to deep inside the photosphere around these spectral types, thus the effects of dust opacity in T-type spectra become smaller. However, the mechanism of dust disappearance is not yet clear. Current brown dwarf atmosphere models include dust segregation effect as one of the model parameters, and such models can explain the observed SED more or less satisfactorily (e.g. Tsuji 2002, 2005; Saumon & Marley 2008).

## 4.2 The Unified Cloudy Model (UCM)

The Unified Cloudy Model (UCM) is one of the brown dwarf atmosphere models that has been developed by Tsuji and colleagues (Tsuji et al. 1996ab, Tsuji 2002, 2005). They incorporate the dust effect in UCM as following. Dust forms at a layer where temperature drops down to the condensation temperature, $T_{\rm cond}$. The UCM assumes that the dust disappears at somewhat lower temperatures given as an additional parameter called critical temperature $T_{\rm cr}$. Thus the dust would exist only in the layer of $T_{\rm cr} < T < T_{\rm cond}$. $T_{\rm cr}$ is not predictable by any physical theory at present and required from observations semiempirically. The UCM assumes local thermodynamical equilibrium (LTE) in the calculation of the molecular abundances and dust formation. Our calculation assumes that the chemical composition of all objects is solar elemental abundances based on Allende Prieto et al. (2002). In the UCM, effect of molecular-line absorption is calculated by the band model method during the construction of the model photosphere until the model has converged, and then detailed line lists are used to evaluate the final emergent spectra. For the detail of molecular line opacities, please refer to Tsuji (2002). We mainly use the models calculated by Tsuji[1]. We compensate some models along with Tsuji models in our analysis. When the model atmosphere structure is not provided by Tsuji's caliculation, we calculate them using UCM program. The model spectra and model structure calculated by ourselves are summarized in Figure 4.1.

## 4.3 Effects of Physical Parameters to the Brown Dwarf Spectra

UCM takes five parameters to describe the property of the model effective temperature $T_{\rm eff}$, surface gravity log $g$, chemical composition, micro-turbulent velocity and critical temperature $T_{\rm cr}$. The brown dwarfs observed with *AKARI* are all neighborhood of the solar system, thus we consider that the solar chemical composition can be applied. Since the micro turbulent velocity in brown dwarf atmospheres has not been measured yet, we apply the solar value (1 km/s). In our analysis, this assume of the micro turbulent velocity is reasonable as shown in Figure 4.2. This figure shows that it is no longer different of two spectral features with the different of the micro turbulent velocity. The other three parameters, $T_{\rm eff}$, log $g$ and $T_{\rm cr}$, are the free parameters to be determined by fitting the observed spectra. In this section we present the effects of these parameters to the brown dwarf spectra.

[1]URL: http://www.mtk.ioa.s.u-tokyo.ac.jp/ ttsuji/export/

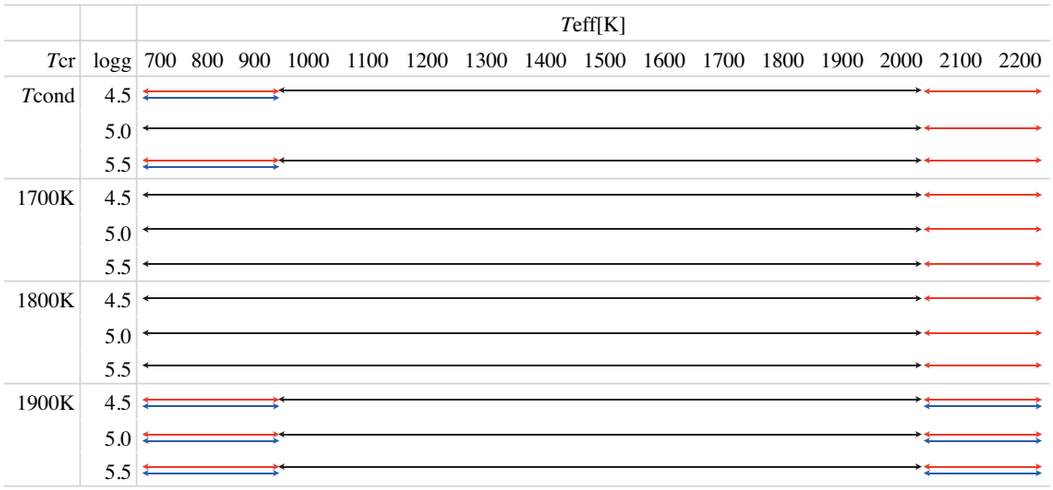


Figure 4.1: Summary of the models calculated by Tsuji and ourselves. A model consist with an atmosphere structure and a spectrum. The model spectra derived by ourself are shown in red lines, and another thing the model atmosphere structure calculated by ourself are shown in blue lines.

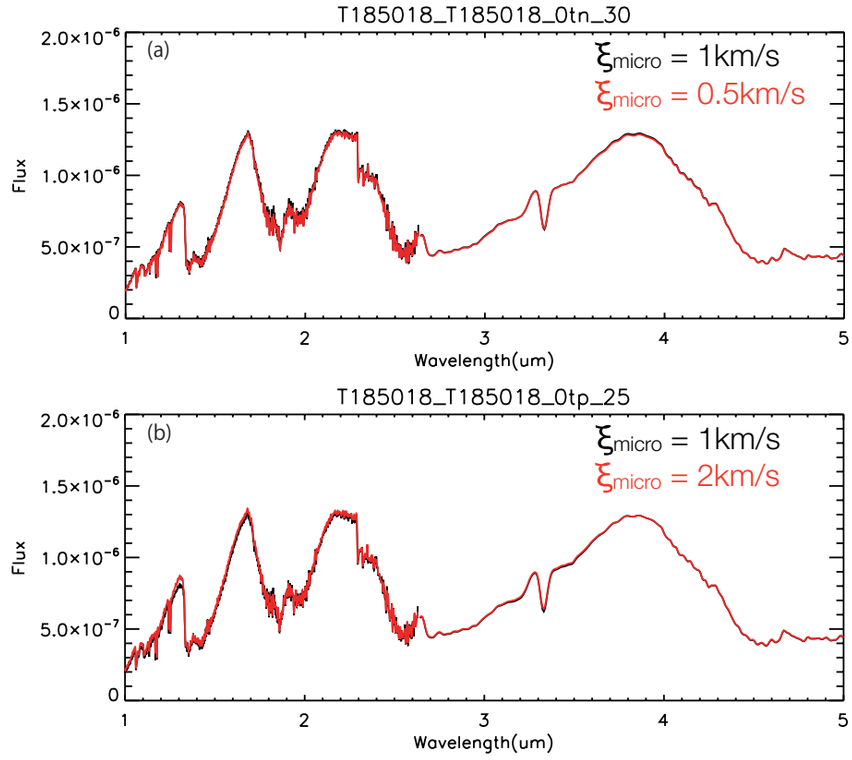


Figure 4.2: The effect of micro turbulent velocity for the spectral features. Two spectra with different values are drawn. (a) The black and red lines are the cases of a micro turbulent velocity is 1 km/s and 0.5 km/s, respectively. (b) The black and red lines are the cases of a micro turbulent velocity is 1 km/s and 2 km/s, respectively. It is not different for every case.

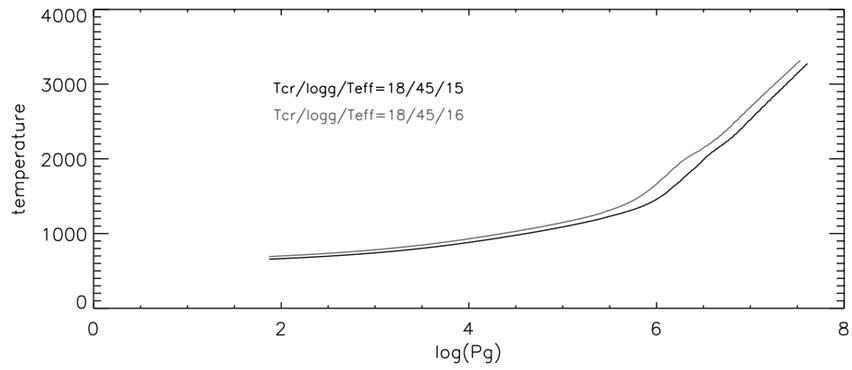


Figure 4.3: The temperature versus total gas pressure of brown dwarf photosphere for two $T_{\rm eff}$ cases. The black line is the case of ($T_{\rm eff}$ / log $g$ / $T_{\rm cr}$) = (1500/4.5/1800). The line drawn in gray is the case of ($T_{\rm eff}$ / log $g$ / $T_{\rm cr}$) = (1600/4.5/1800). The gas temperature of $T_{\rm eff}$ = 1600 K case is always higher than that of 1500 K.

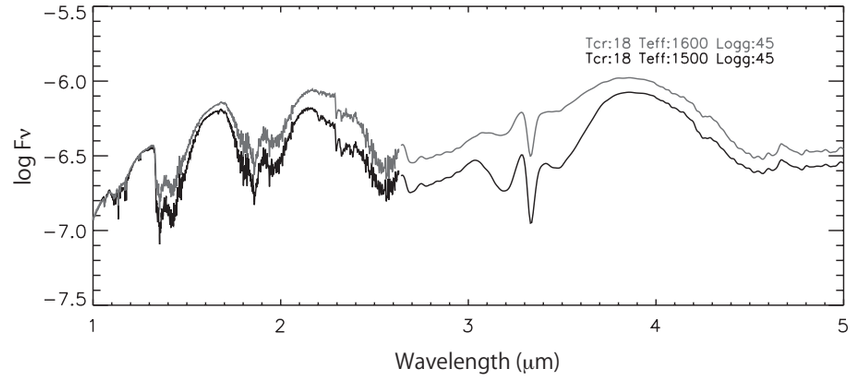


Figure 4.4: The spectrum between 1.0 and 5.0 $\mu$m for two cases of $T_{\rm eff}$. The black spectrum is the case of ($T_{\rm eff}$ / log $g$ / $T_{\rm cr}$) = (1500/4.5/1800) and the gray spectrum is the case of ($T_{\rm eff}$ / log $g$ / $T_{\rm cr}$) = (1600/4.5/1800).

### 4.3.1 Effective Temperature ($T_{\rm eff}$)

Effective temperature is defined as

$$F = \sigma T_{\rm eff}^4. \tag{4.1}$$

In UCM $T_{\rm eff}$ is treated practically as the temperature at Rosseland mean optical depth equal unity. It is not exact because of the large non-grayness of the opacity. In UCM, $T_{\rm eff}$ contributes to the temperature structure of overall photosphere. The aspect of spectral feature depend on the temperature structure. The corresponding spectra between 1.0 and 5.0 $\mu$m are shown in Figure 4.4. We can see the effects of $T_{\rm eff}$ on the spectral features.

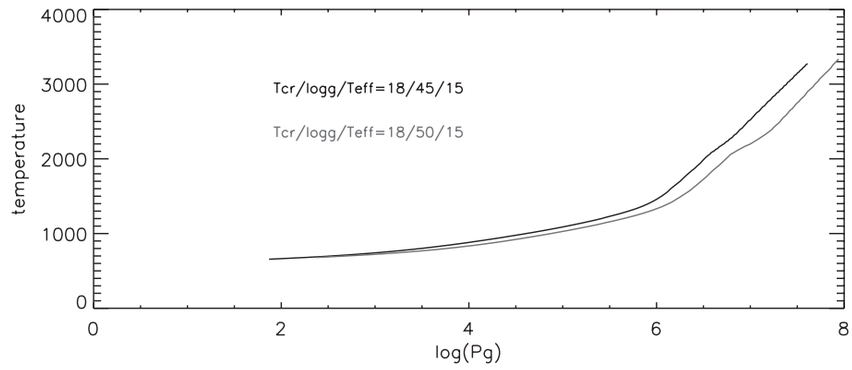


Figure 4.5: The temperature versus total gas pressure of brown dwarf photosphere for two log $g$ cases. The black line is the case of ($T_{\rm eff}$ / log $g$ / $T_{\rm cr}$) = (1500/4.5/1800). The gray line is the case of ($T_{\rm eff}$ / log $g$ / $T_{\rm cr}$) = (1500/5.0/1800).

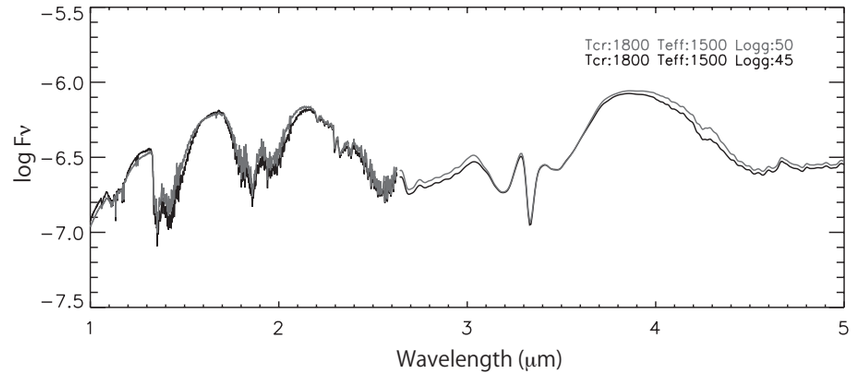


Figure 4.6: The spectral feature between 1.0 and 5.0 $\mu$m for two cases of log $g$. The black spectrum is the case of ($T_{\rm eff}$ / log $g$ / $T_{\rm cr}$) = (1500/4.5/1800) and the gray spectrum is the case of ($T_{\rm eff}$ / log $g$ / $T_{\rm cr}$) = (1500/5.0/1800).

### 4.3.2 Surface Gravity (log $g$)

Surface gravity also changes the temperature structure by effects of contraction. In case of hydrostatic equilibrium, gravity is balanced with pressure gradient. Variation in pressure changes density and temperature as shown in Figure 4.5 for two cases, ($T_{\rm eff}$ / log $g$ / $T_{\rm cr}$) = (1500/4.5/1800) and (1500/5.0/1800). Here the surface gravity log $g$ is given in the cgs unit (cm/s$^2$). When gravity gets large from 4.5 to 5.0, the surface temperature becomes a little higher by about less than 10 K. This is because that the objects contract in large surface gravity. This contraction makes the inner temperature lower than in the low gravity object. Hence the temperature gradient gets gentle. The effects of variation in log $g$ on the spectral feature are shown in Figure 4.6. The variation of spectral feature are less prominent than $T_{\rm eff}$.

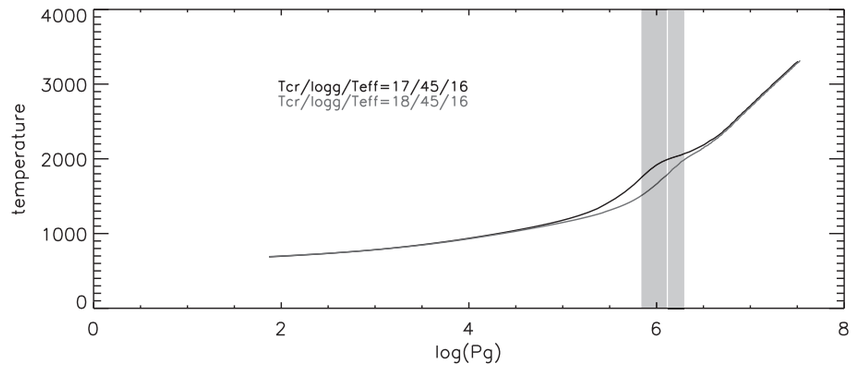


Figure 4.7: Temperature to total gas pressure for two $T_{\rm cr}$ cases. The gray line is the case of ($T_{\rm eff}$ / log $g$ / $T_{\rm cr}$) = (1600/5.0/1700). The red line is the case of ($T_{\rm eff}$ / log $g$ / $T_{\rm cr}$) = (1600/5.0/1800). The dust existing region are painted in black and gray, respectively.

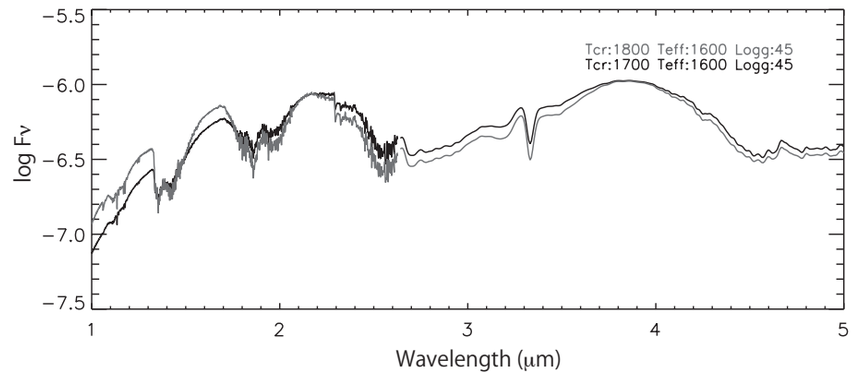


Figure 4.8: The spectral feature between 1.0 and 5.0 $\mu$m for two cases of $T_{\rm cr}$. The black spectrum is the case of ($T_{\rm eff}$ / log $g$ / $T_{\rm cr}$) = (1600/5.0/1700) and the gray spectrum is the case of ($T_{\rm eff}$ / log $g$ / $T_{\rm cr}$) = (1600/5.0/1800).

### 4.3.3 Critical Temperature ($T_{\rm cr}$)

Critical temperature $T_{\rm cr}$ is an additional parameter to determine the upper limit of the dust layer. Lower $T_{\rm cr}$ results in a thicker dust layer. The temperature around the dust layer changes significantly. The gas temperature in the dust existing region becomes higher by the warming up effect by the dust. Figure 4.7 demonstrates this effect by comparing two models for ($T_{\rm eff}$ / log $g$ / $T_{\rm cr}$) = (1600/5.0/1700) and (1600/5.0/1800). The dust layers are painted in gray and red for the model with $T_{\rm cr}$ = 1700 and 1800 K, respectively. The corresponding spectra for these temperature structure are shown in Figure 4.8. We can see that $T_{\rm cr}$ also contributes to dust extinction, which especially appears in $J$ and $H$ band regions.

## 4.4 Model Fitting of the Observed Spectra

Our purpose of this analysis is to derive the probable physical parameters for the *AKARI* samples. The wavelength region of the *AKARI* data give us information about $CH_4$, CO and $CO_2$ molecules in the brown dwarf photosphere. As explained above, carbon is transferred from CO to $CH_4$ as the temperature decreases, and the temperature of brown dwarf photosphere is just the temperature at which $CH_4$ start to appears. The wavelength range of the *AKARI* data including the strongest and non-blended $CH_4$ $\nu_3$ band at 3.3 $\mu$m is quite important for studying $CH_4$ formation. The *AKARI* wavelength range is also reflects the photosphere temperature relatively free from the dust extinction. We use the *AKARI* spectral data principally to derive the physical parameters via model fitting. However, there are some technical hurdles to overcome in our model fitting with the *AKARI* data only. In this section we explain the problem on model fitting and the fitting method to overcome the problem.

### 4.4.1 Step1 – Fitting the *AKARI* Spectra

Our model fitting consists of two processes. As a first trial of model fitting we compare the models with observed *AKARI* spectra between 2.5 and 4.15 $\mu$m. We use the data only in 2.5–4.15 $\mu$m, not to 5.0 $\mu$m for the fitting, because we know that the current model does not explain the observed spectra beyond 4.15 $\mu$m where the absorption bands of $CO_2$ at 4.2$\mu$m and CO at 4.6$\mu$m (Yamamura et al. 2010; see section 1.4) present. We follow Cushing et al. (2008) and evaluate the goodness of the model fitting by the statistic $G_k$, defined as

$$G_k = \frac{1}{n-m} \sum_{i=1}^{n} \omega_i \left( \frac{f_i - C_k F_{k,i}}{\sigma_i} \right)^2 , \tag{4.2}$$

where $n$ is the number of data grid; $m$ is degree of freedom; $\omega_i$ is the weight for the $i$-th wavelength grid (we give the weight as $\omega_i = 1$ for all data points because of no bias within each observed data); $f_i$ and $F_{k,i}$ are the flux densities of the observed data and $k$-th model, respectively; $\sigma_i$ are the errors in the observed flux densities and $C_k$ is the scaling factor given by

$$C_k = \frac{\sum \omega_i f_i F_{k,i} / \sigma_i^2}{\sum \omega_i {F_{k,i}}^2 / {\sigma_i}^2}. \tag{4.3}$$

$G_k$ is equivalent with reduced $\chi^2$, since we adopt $\omega_i = 1$ in our analysis. We examine the cases of $700 \leq T_{\rm eff} \leq 2200$ K in 100 K grid, log $g$=4.5, 5.0 and 5.5, $T_{\rm cr}$=1700, 1800, 1900 K and $T_{\rm cond}$ (no dust layer), i.e. total $16 \times 3 \times 4 = 192$ cases.

It is difficult to determine the best fit model for each *AKARI* object, because of the large error of the *AKARI* spectral data. In general when the reduced $\chi^2$ (=$G_k$) is 1$\sim$2, the model fits the observed data well. $G_k$ easily gets below unity and we have too many "good fit" models; degeneracy of model parameter takes place. This degeneracy is demonstrated in Figure 4.9 for the *AKARI* spectra of 2MASS J1507–1627(L5). We see that many models have small ($\leq 1.04$) $G_k$ between 1700 to 2000 K of $T_{\rm eff}$. In this case the minimum $G_k$ is 0.94, and the second minimum is also small, 0.97. Since the differences of

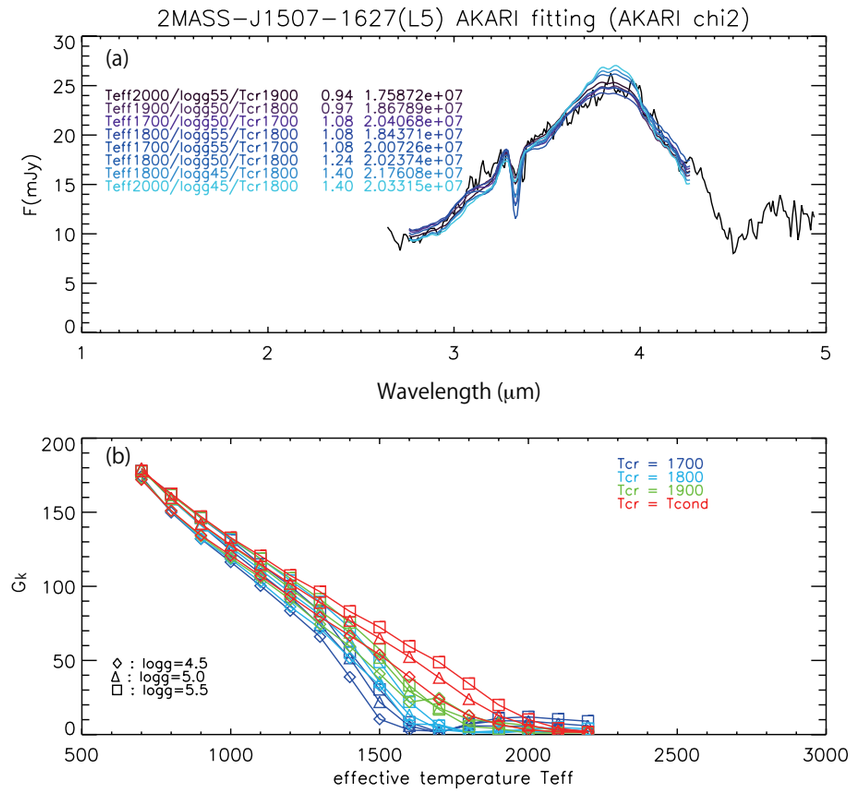


Figure 4.9: The *AKARI* spectra of 2MASS J1507–1627(L5) and good fit models are overlaid in 2.5–4.15$\mu$m. (a) The observed spectra are drawn in black. Color lines present for each model spectra. (b) $G_k$ versus effective temperature for each $T_{\rm cr}$ and log $g$. Degeneracy of parameters is seen between $T_{\rm eff}$ = 1700 – 2000 K.

$G_k$ between the models near the minimum are tiny, it is difficult to determine the best fit model.

Therefor at this step, we select candidates of the best model with the following condition.

$$G_{min} \leq G_k < G_{min} + 1, \tag{4.4}$$

where $G_{min}$ is the minimum $G_k$ value. $G_{min}$ is different from every spectral data and are not always near the unity. One of the reasons is that the error of the *AKARI* observed spectra are different for every data. The error of some data are smaller than 10% and others are larger than 10%. We regard $G_{min}$ as the best model in the current fitting of the *AKARI* data. We apply the $G_{min}$ + 1 as an upper limit, because it is reasonable to select 5 $\sim$ 20 model candidates for almost all the observed data.

### 4.4.2 Step2 – Constraining Models with the Short Wavelength Data

To constrain the models from the candidates we additionally use the spectra in the shorter wavelength range (1.0–2.5 $\mu$m), taken by IRTF/SpeX and UKIRT/CGS4. It is only possible to analyze the brown dwarf atmosphere structure in detail with the help of the short wavelength range spectra along with the

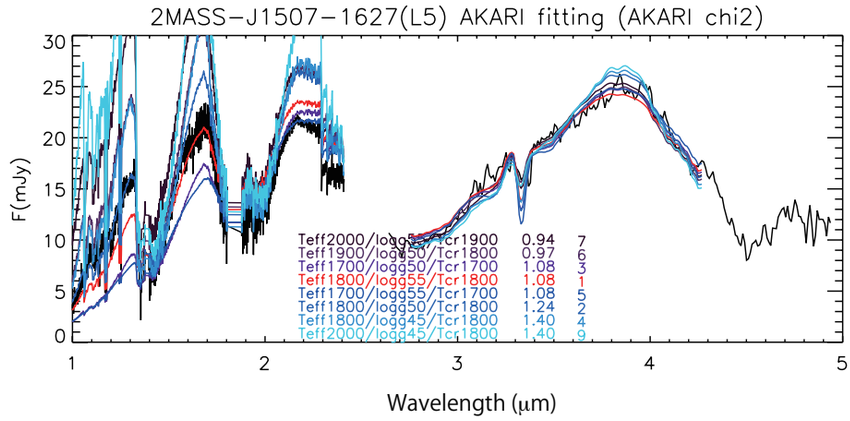


Figure 4.10: The spectra of 2MASS J1507–1627(L5) and fitting models. The degeneracy in the fitting of *AKARI* spectra is solved by adding the shorter wavelength range SpeX data. The model spectra in red color is the best fit model for the object. The order of goodness of the fit to SpeX data are shown in the right of the legend.

*AKARI* data. The wavelength region of the *AKARI* data gives us the information of $CH_4$, CO and $CO_2$ molecules in brown dwarf photosphere. On the other hand, data of the shorter wavelength range are the most sensitive to the dust presence. Thus dust extinction around this wavelength range is an indicator of dust amount. We explain the data used in the current analysis in the next section 4.4.3.

We calculate $G_k$ for the IRTF/SpeX or UKIRT/CGS4 (hereafter SpeX/CGS4) spectral data for the candidate models derived in Step 1. Since we have validated the absolute flux of the spectra to be better than 10 % (see section 2.3.4), we apply $C$ values derived in Step 1 (from AKARI) to Step 2. Figure 4.10 shows the result of the L5 dwarf 2MASS J1507–1627. We see that the degeneracy shown in Figure 4.9 is solved by Step 2.

We do not fit the *AKARI* data and SpeX/CGS4 data simultaneously. It is because that the error of two data are so different. The average relative error of the *AKARI* spectra is about 10 % (Ohyama et al. 2007), while that of the SpeX and CGS4 data is below 0.05 % (Reyner et al. 2009). This difference would give much more weight to the SpeX/CGS4 data in the fitting process. Actually, while the reduced $\chi^2$ (= $G_k$) of the *AKARI* data are between 0.1 and 100, that of the SpeX/CGS4 data are between 100 and 5000. Therefore we have to evaluate the fitting consistency in relative manner. Because of this reason, we decided to use the *AKARI* spectra first and use the SpeX and CGS4 spectra in the second step. We discuss the model fitting of each wavelength data separately in chapter5.

### 4.4.3 Additional Data Used for Fitting

#### IRTF/SpeX data

The NASA Infrared Telescope Facility (IRTF) on Mauna Kea, Hawaii, is a 3.0 meter telescope optimized for infrared observations. SpeX is a medium-resolution 0.8–5.4 $\mu$m spectrograph on board IRTF. The superiority of SpeX is to provide maximum simultaneous wavelength coverage. A high throughput prism

Table 4.1: Summary of The SpeX/CGS4 data used in the current study

| Object Name | Obs Date | Resolution | references | remark |
|---|---|---|---|---|
| 2MASS J1439+1929 | 2001 Mar 22 | 2000 | 8 | IRTF/SpeX |
| 2MASS J0036+1821 | 2004 Sep 07 | 120 | 2 | IRTF/SpeX |
| 2MASS J2224–0158 | 2001 Aug 07 | 2000 | 8 | IRTF/SpeX |
| SDSS J0539–0059 | 2000 Nov 06 | 220 | 4 | IRTF/SpeX |
| SDSS J1446+0024 | 2000 Mar 13–15 | >400 | 7 | UKIRT/CGS4 |
| 2MASS J1507–1627 | 2001 Mar 14, 22 | 1200 | 8 | IRTF/SpeX |
| | 2001 Feb 28 | 938 | 8 | IRTF/SpeX |
| GJ 1001B | 2004 Sep 07 | 120 | 5 | IRTF/SpeX |
| 2MASS J0825+2115 | 2001 Mar 12–14 | 1200 | 8 | IRTF/SpeX |
| 2MASS J1632+1904 | 2003 May 22 | 120 | 1 | IRTF/SpeX |
| 2MASS J1523+3014 | 2008 May 08 | 120 | 3 | IRTF/SpeX |
| SDSS J0830+4828 | 2006 Dec 24 | 120 | 2 | IRTF/SpeX |
| 2MASS J0310+1648 | 2005 Dec 31 | 120 | 5 | IRTF/SpeX |
| SDSS J1254–0122 | 2003 May 22 | 120 | 1 | IRTF/SpeX |
| SIMP J01365+0933 | 2006 Sep 03 | 120 | 2 | IRTF/SpeX |
| 2MASS J0559–1404 | 2001 Jan 25 | 1200 | 8 | IRTF/SpeX |
| 2MASS J1553+1532 | 2006 Apr 08 | 120 | 3 | IRTF/SpeX |
| Gl 570D | 2003 May 22 | 120 | 1 | IRTF/SpeX |
| 2MASS J0415–0935 | 2003 Sep 17 | 120 | 1 | IRTF/SpeX |

1: Burgasser et al. (2004) AJ, 127, 2856
2: Burgasser et al. (2008) ApJ, 681, 579
3: Burgasser et al. (2010) ApJ 710, 1142
4: M. Cushing (private comunication)
5: Burgasser (2007) ApJ, 659, 655
6: Burgasser et al. (2006) ApJ, 637, 1067
7: Geball et al. (2002) ApJ, 564, 466
8: Cushing et al. (2004) PhD thesis

mode that is single order long slit (60 arcsec) modes provides $\lambda/\Delta\lambda = R \sim 100$ for 0.8–2.5 $\mu$m. Using prism cross-dispersers (for 15 arcsec-long slits), the spectral resolution $R$ becomes 1000–2000 across 0.8–2.4 $\mu$m, 2.0–4.1 $\mu$m, and 2.3–5.5 $\mu$m.

Almost all brown dwarfs in our samples have been observed by Burgasser et al. (2004, 2006, 2008, 2010), Burgasser (2007) and Cushing (2004) with SpeX. Twelve data have been obtained using its low-resolution prism-dispersed mode with resolutions of 75–200 depending on the used slit-width. For these twelve objects, we retrieve the data from the SpeX Prism Spectral Libraries built by Adam Burgasser[2]. Only SDSS J0539–0059 was unpublished[3], and the data were obtained from Mike Cushing (private communication). Other six sources have been observed by SpeX using its short wavelength cross-dispersed mode (SXD) with the resolutions of 1200–2000, depending on the slit-width used. We get these data from the IRTF Spectral Library maintained by Michael Cushing[4] . The data are summarized in Table 4.1.

[2]URL; http://pono.ucsd.edu/∼adam/browndwarfs/spexprism/
[3]This data has been added in The SpeX Prism Spectral Libraries now.
[4]URL; http://irtfweb.ifa.hawaii.edu/∼spex/IRTF_Spectral_Library/

**UKIRT/CGS4 data**

SDSS J1446+0024 has not been observed with SpeX. A spectrum in 1.0–2.5 $\mu$m was observed with UKIRT/CGS4 (Geballe et al. 2002). CGS4 is the 1.0–5.0$\mu$m multi-purpose grating spectrometer on board the 3.8 m United Kingdom Infrared Telescope(UKIRT), which is sited on Hawaii Mauna Kea. CGS4 has four gratings. The data for SDSS J1446+0024 was observed using 40 line/mm grating that provided the resolution of 300–2000, which are defined by 400 $\times$ $\lambda$. The spectra were taken by two broad band filters for low and medium resolution gratings in use with CGS4, namely B1 and B2, and the wavelength range of these filters are in 1.03 to 1.34 $\mu$m and 1.43 to 2.53 $\mu$m, respectively. We get the spectral data of SDSS J1446+0024 from Dagny Looper (private communication). See Table 4.1 for the observation summary.

**Absolute Flux Calibration of Short Wavelength Spectral Data**

Since twelve SpeX data for *AKARI* samples are normalized at 1.25$\mu$m, we calibrate their absolute flux using their $J$ band photometric data given by Legget et al. (2002a) and Knapp et al. (2004) as listed in Table 3.2 (hereafter $J_{\rm p}$). These $J$ band photometry were taken with MKO filter except for SIMP J01365+0933 and 2MASS J1553+1532. We use 2MASS $J$ band photometric data (Cutri et al. 2003) for the flux calibration of the latter two objects. We estimate the integrated flux from SpeX data with MKO or 2MASS $J$ band filter transmission function $T$ by calculating equation (4.5),

$$J_{\rm spex} = \frac{\int F_\nu T(\nu) d\nu}{\int T(\nu) d\nu}. \tag{4.5}$$

After that, we scale the absolute flux of SpeX spectral data with the ratio of $J_{\rm p}/J_{\rm spex}$. We compare the $J$ band flux measured from the calibrated spectra with $J_{\rm p}$ from Legget et al. (2002a) and Knapp et al. (2004) for all objects in our samples in Figure 4.11. The integrated fluxes from six objects calibrated by Cushing et al. (2004), are also confirmed to be consistent with $J_{\rm p}$ within 10%.

The spectra of other three objects, 2MASS J1439+1929, 2MASS J0036+1821 and 2MASS J1507–1627, were observed by SpeX in 0.81–4.11 $\mu$m with a gap in 2.53–2.85 $\mu$m simultaneously, and calibrated by Cushing et al. (2004). In Figure 4.12 their *AKARI* spectra and SpeX spectra are drawn in red and black line, respectively. Both *AKARI* and SpeX/CGS4 data for each object are calibrated independently and scaled by the same factor on the plot. We can see that two spectra are consistent within 10 %, which is the error of *AKARI* spectra. The SpeX and CGS4 spectra for *AKARI* samples are shown in Figure 4.13.

The UKIRT/CGS4 data are calibrated by Geballe et al. (2002) with the 2MASS $J$ band photometry data. The six spectral data retrieved from The IRTF Spectral Library were also calibrated with the 2MASS $J$ band photometry (Cushing 2004).

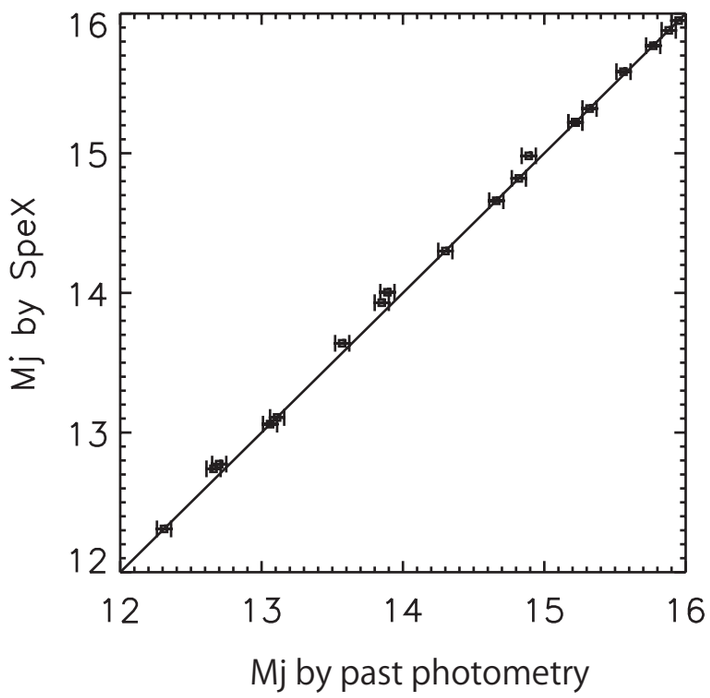


Figure 4.11: The $J$ band flux derived from SpeX/CGS4 data versus $J$ band photometry data from Legget et al. (2002a) and Knapp et al. (2004), $J_{\rm p}$. The SpeX/CGS4 absolute flux for *AKARI* objects whose flux are normalized are calibrated with $J_{\rm p}$. Thus the $J$ band flux of these objects should be equivalent with $J_{\rm p}$. The flux of other objects are also consistent within 10 %.

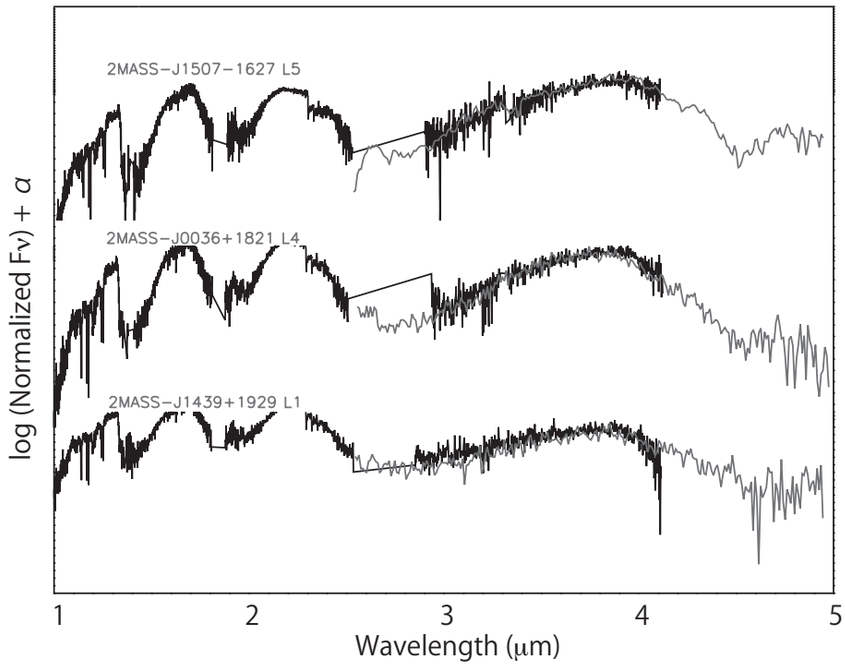


Figure 4.12: The comparison of SpeX spectral data (black) and *AKARI* spectra (gray) for three objects, 2MASS J1439+1929, 2MASS J0036+1821 and 2MASS J1507-1627. Both *AKARI* and SpeX/CGS4 data for each object are calibrated independently and scaled by the same factor on the plot.

## 4.5 Results

### 4.5.1 Behavior of the Best Fit Parameter Sets

Results of the model fitting are shown in Table 4.2. The best parameter sets are plotted with respect to the spectral types in Figure 4.14. We can see that the spectral types are in the sequence of $T_{\rm eff}$ (Figure 4.14 (a)). The result of almost constant $T_{\rm eff}$ in late-L dwarfs has already been known in the past studies. Tsuji and Nakajima (2003) argued that little change in $T_{\rm eff}$ would be caused by cloud migration from the optically thin upper region to thick inner region. We confirm this hypothesis from the derived $T_{\rm cr}$ in Figure 4.14 (c). $T_{\rm cr}$ represent the contribution of dust to the spectra. The models of lower $T_{\rm cr}$ are more affected by the dust. $T_{\rm cr} = T_{\rm cond}$ means that the dust disappears immediately after it forms; i.e., effectively no dust in the photosphere. The models with $T_{\rm cr}$ = 1700 K are the most dust affected models used in our analysis. From our fitting analysis the dust effect becomes larger with dust forming for the early- to middle-L dwarfs, and the spectra of mid-L dwarfs should have the largest amount of dust. Our result shows that the contribution of dust to the spectra becomes smaller from late-L dwarfs to late-T dwarfs. These results are important to attest the indication in Tsuji and Nakajima (2003). Our results indicate that the condition of dust layer changes dramatically in late-L type.

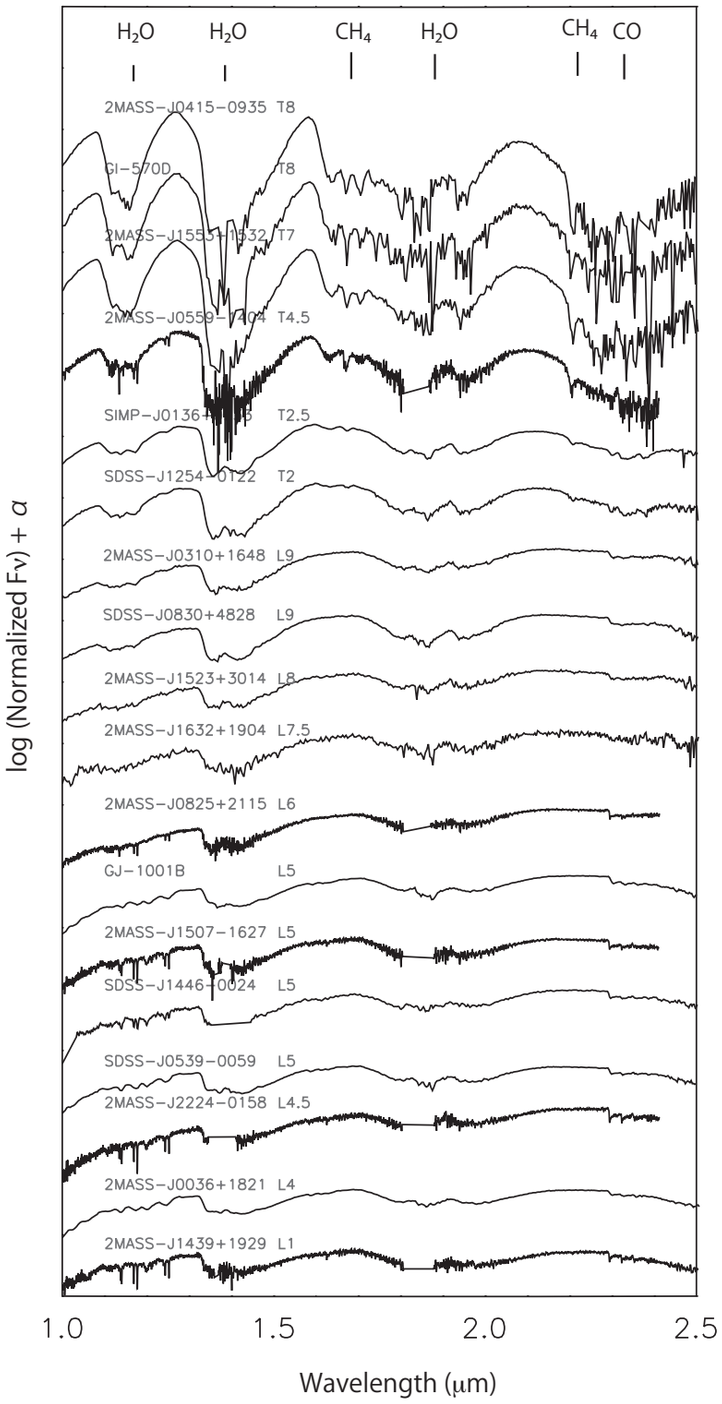


Figure 4.13: The SpeX/CGS4 spectral data in 1.0–2.5$\mu$m for *AKARI* objects.

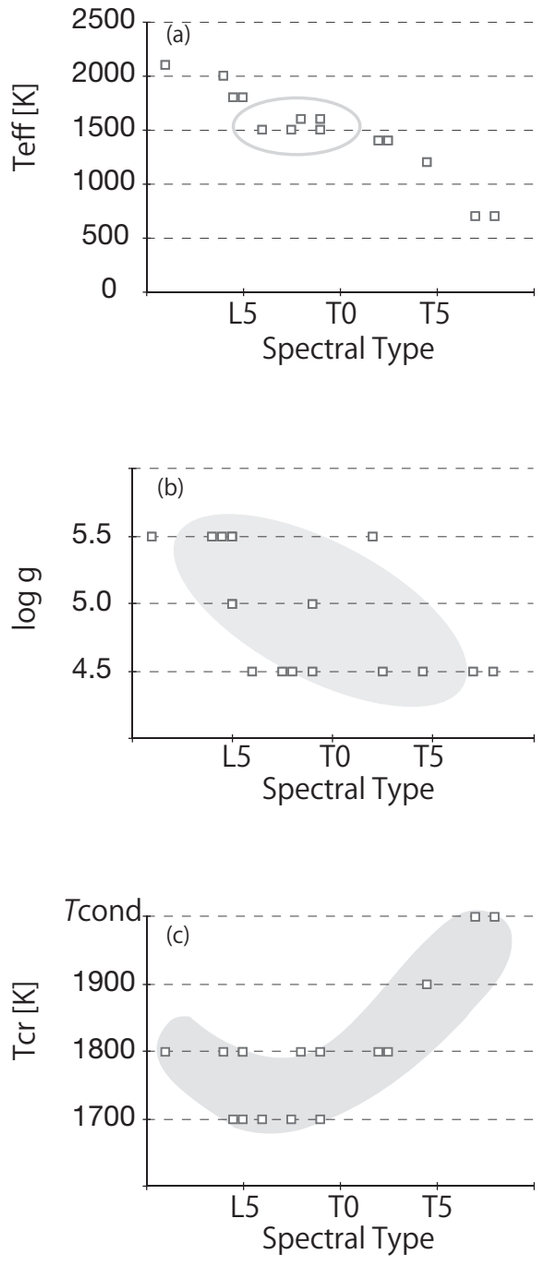


Figure 4.14: The best fit model parameters. We show (a) $T_{\rm eff}$, (b) log $g$, and (c) $T_{\rm cr}$ versus spectral type. We note that the plot of same spectral type may overlap when they have same parameters. Spectral type is a sequence of $T_{\rm eff}$ except for late-L dwarfs. log $g$ decreases toward late spectral types. $T_{\rm cr}$ is minimum at mid- to late-L types.

Table 4.2: Best fit model parameters derived by fitting the *AKARI* and the SpeX/CGS4 data

| Object number | Object Name | Sp.Type | $T_{\rm cr}$ | log $g$ | $T_{\rm eff}$ |
|---|---|---|---|---|---|
| 1 | 2MASS J1439+1929 | L1 | 1800 | 5.5 | 2100 |
| 2 | 2MASS J0036+1821 | L4 | 1800 | 5.5 | 2000 |
| 3 | 2MASS J2224–0158 | L4.5 | 1700 | 5.5 | 1800 |
| 4 | SDSS J0539–0059 | L5 | 1800 | 5.5 | 1800 |
| 5 | SDSS J1446+0024 | L5 | 1700 | 5.0 | 1800 |
| 6 | 2MASS J1507-1627 | L5 | 1800 | 5.5 | 1800 |
| 7 | GJ 1001B | L5 | 1800 | 5.0 | 1800 |
| 8 | 2MASS J0825+2115 | L6 | 1700 | 4.5 | 1500 |
| 9 | 2MASS J1632+1904 | L7.5 | 1700 | 4.5 | 1500 |
| 10 | 2MASS J1523+3014 | L8 | 1800 | 4.5 | 1600 |
| 11 | SDSS J0830+4828 | L9 | 1800 | 4.5 | 1600 |
| 12 | 2MASS J0310+1648 | L9 | 1700 | 5.0 | 1500 |
| 13 | SDSS J1254–0122 | T2 | 1800 | 5.5 | 1400 |
| 14 | SIMP J01365+0933 | T2.5 | 1800 | 4.5 | 1400 |
| 15 | 2MASS J0559–1404 | T4.5 | 1900 | 4.5 | 1200 |
| 16 | 2MASS J15532+1532 | T7 | 2000 | 4.5 | 700 |
| 17 | Gl 570D | T8 | 2000 | 4.5 | 700 |
| 18 | 2MASS J0415–0935 | T8 | 2000 | 4.5 | 700 |

### 4.5.2 Comparison of the Observed and the Best Fit Model Spectra

The spectra of observed and best fit models are compared in Figure 4.15. The derived best fit model spectra well explain the observed spectral features except for some objects noted below. We see that the fit in the entire *AKARI* region is fairly good. The noticeable deviations are seen in the $H_2O$ absorption feature around 3.0 $\mu$m and in the wavelength region longer than 4.15 $\mu$m in late-T dwarfs. The flux density around 3.0 $\mu$m in the model spectra of 2MASS J1523+3014 (L8), SDSS J0423–0414 (T0) along with three late-T dwarfs is too strong in comparison to that in the observed spectra. This result indicates that the temperatures of these objects are higher than those predicted in the models, but we can not understand the mechanism of increasing temperature in their atmospheres and forming the spectral features in detail. The wavelength longer than 4.15 $\mu$m is a known problem for brown dwarf atmosphere modeling as noted in section 1.4. It is partly because that these wavelengths are not considered in the current fitting evaluation.

We also see that $CH_4$ absorption band at 3.3 $\mu$m and $CO_2$ absorption band at 4.2 $\mu$m in model spectra are sometimes inconsistent with the observed data of other spectral types. The $CH_4$ $\nu_3$ absorption feature in the model spectra of GJ 1001B (L5), 2MASS J0825+2115(L6) and 2MASS J0310+1648(L9) are stronger than that in the observed spectra. On the other hand, the $CH_4$ P-branch in the model spectra of 2MASS J1523+3014(L8) and SDSS 0423-0414(T0) are weaker than the observed ones. We also see that the $CO_2$ fundamental band at 4.2 $\mu$m in the model spectra of SDSS J0830+4828(L9) and five T dwarfs, SDSS J1254-0122(T2), 2MASS J0559–1404(T4.5), 2MASS J1553+1532(T7), Gl 570D(T8) and 2MASS J0415–0935(T8), are shallower than that in the observed spectra. On the other hand, the $CO_2$ absorption

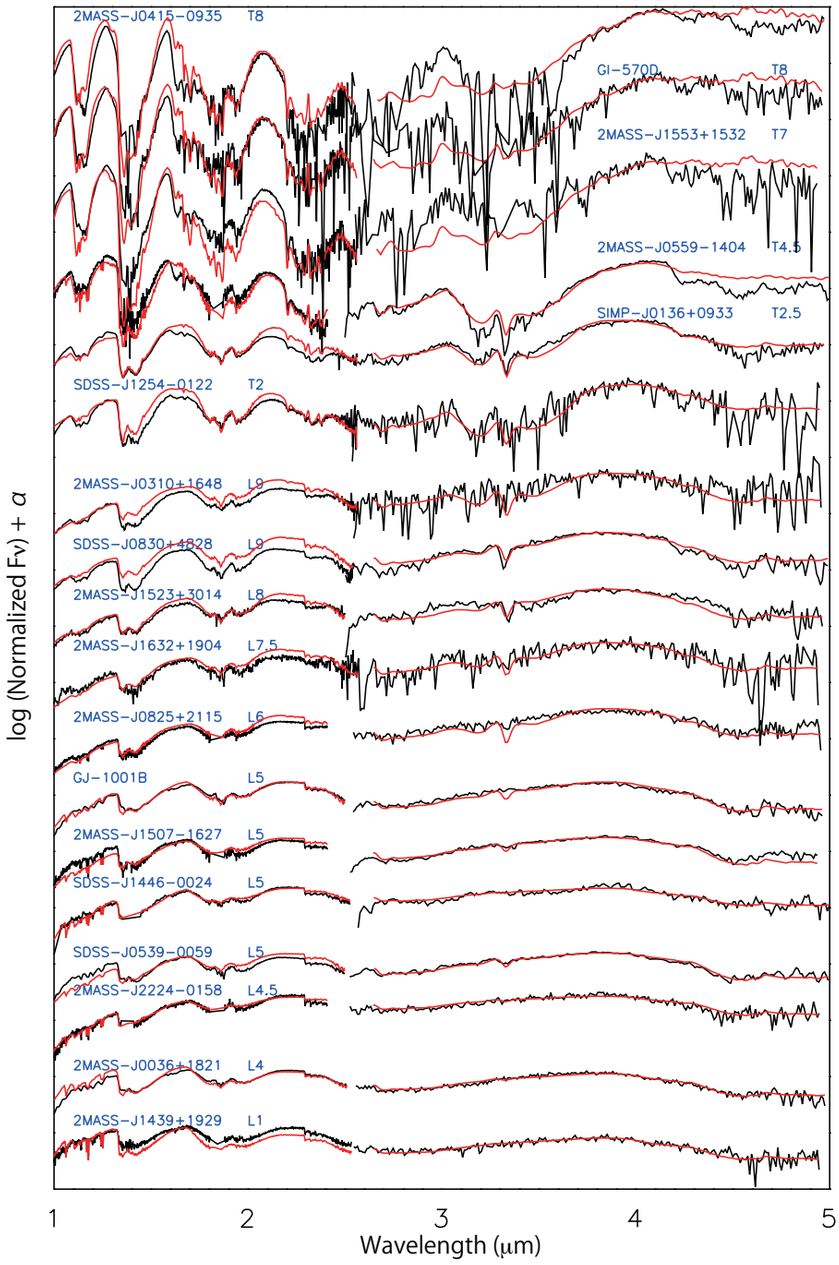


Figure 4.15: The fitting result for near-infrared spectra. The black lines are the observed data and red lines are the best fit model spectra. The spectra between 2.5 and 5.0$\mu$m are taken by *AKARI* and those between 1.0 and 2.5$\mu$m are taken by IRTF/SpeX (SDSS J1446+0024 is observed by UKIRT/CGS4).

in the model spectra of 2MASS J1523+3014(L8) and SDSS J0423-0414 (T0) are stronger than that in the observed spectra. Excess $CO_2$ absorption in SDSS J0830+4828(L9), 2MASS J0559–1404(T4.5) and 2MASS J0415–0935(T8) was reported by Tsuji et al. (2011). We find that $CO_2$ absorption band in the model is sometimes too deep and sometimes too shallow compared to the observations.

The fit in the SpeX/CGS4 region is good as a whole impression except for late-L and early-T dwarfs.

The $H$ and $K$ band flux density in the model spectra of these dwarfs are higher than that in the observed spectra. The high $K$ band flux density indicates that the temperature of photosphere is actually lower than expected by the model. This result may be caused by the limit of current brown dwarf models to apply in the broad wavelength range. In chapter 5, we investigate the separate model fitting of *AKARI* and SpeX/CGS4 spectra to discuss these problems in detail.

The $CH_4$ absorption at 1.6 $\mu$m in the late-T dwarfs are always significantly stronger than that in the model spectra. One possible reason of these deviation of molecular bands may be incompleteness of molecular opacities used in the UCM. We should confirm the effects of this speculation and consider the possible improvement. Another reason of this discrepancy could be that the $H_2O$, $CH_4$ and $CO_2$ abundances in the photospheres of these objects may be over/underestimated in the model, i.e. this argument indicates that the $H_2O$, $CH_4$ and $CO_2$ abundances in photosphere may be different from the predicted ones. We discuss the possible elemental abundance variations among brown dwarfs using the model atmosphere and the *AKARI* data in chapter 6.

### 4.5.3 Uncertainty of the Model Fitting

Here we discuss the uncertainty of the best fit model parameters. The model spectra we use for the current analysis are calculated on the 100 K grid ($T_{\rm eff}$ and $T_{\rm cr}$) and 0.5 dex grid (log $g$), and the uncertainty should be no better than the grid spacing to estimate the uncertainty. We change one of $T_{\rm eff}$, log $g$ and $T_{\rm cr}$ by one grid from the best fit value, and search for the "restricted best" model by changing the other two parameters following the same manner through Step 1 and 2. If we do not find any models satisfying $G_{min} \leq G_k < G_{min} + 1$ (here $G_{min}$ is taken from the all parameter spaces), the uncertainty of the parameter should be smaller than the grid spacing. When the best parameter is already on the edge of the parameter space; i.e., $T_{\rm eff}$ = 700 or 2200K, log $g$ = 4.5 or 5.5 and $T_{\rm cr}$ = 1700K or $T_{\rm cond}$, we only run the test on the available side of the parameter. The derived "restricted best" models (max 6 per object) are compared in Figure 4.16 with the real best fit models. In this figure the same scaling factor $C$ derived for the real best fit model and the *AKARI* spectrum is used for each object.

We see large differences in $J$ and $H$ band in some "restricted best" model spectra. We exclude the models if the scaling factor derived in $J$ and $H$ band region (1.01 – 1.81 $\mu$m, hereafter $C'$) of the SpeX/CGS4 spectra is differ more than 10 % from the observed data, regarding the uncertainty of the SpeX/CGS4 absolute flux. We show a detailed example for 2MASS J2224-0158 (L4.5) in Figure 4.17 and show the $C'$ of each model in Table 4.3, Figure 4.18 (a1), (b1) and (c1).

$C'$ of the real best fit model drawn in red square are near 1.0, except for two late-T dwarfs. As shown in the previous subsection the best model of late-T dwarfs does not explain the $CH_4$ absorption at 1.6 $\mu$m. Because of this, their $C'$ values exceed 10 %. We can see that the "restricted best" models for the case of changing $T_{\rm eff}$ and $T_{\rm cr}$ by +100K exhibit a noticeable change from the real best models. On the other hand, the case of changing $T_{\rm cr}$ by –100K and log $g$ result only minor differences. We further continue the test of changing each parameter by two grid from the real best fit model. The results are shown in Table 4.3 and Figure 4.18 (a2), (b2) and (c2). We can see that almost all the "restricted best" models do not stay within 10 % any longer, except for the case of changing two grid of log $g$. We conclude that our best fit

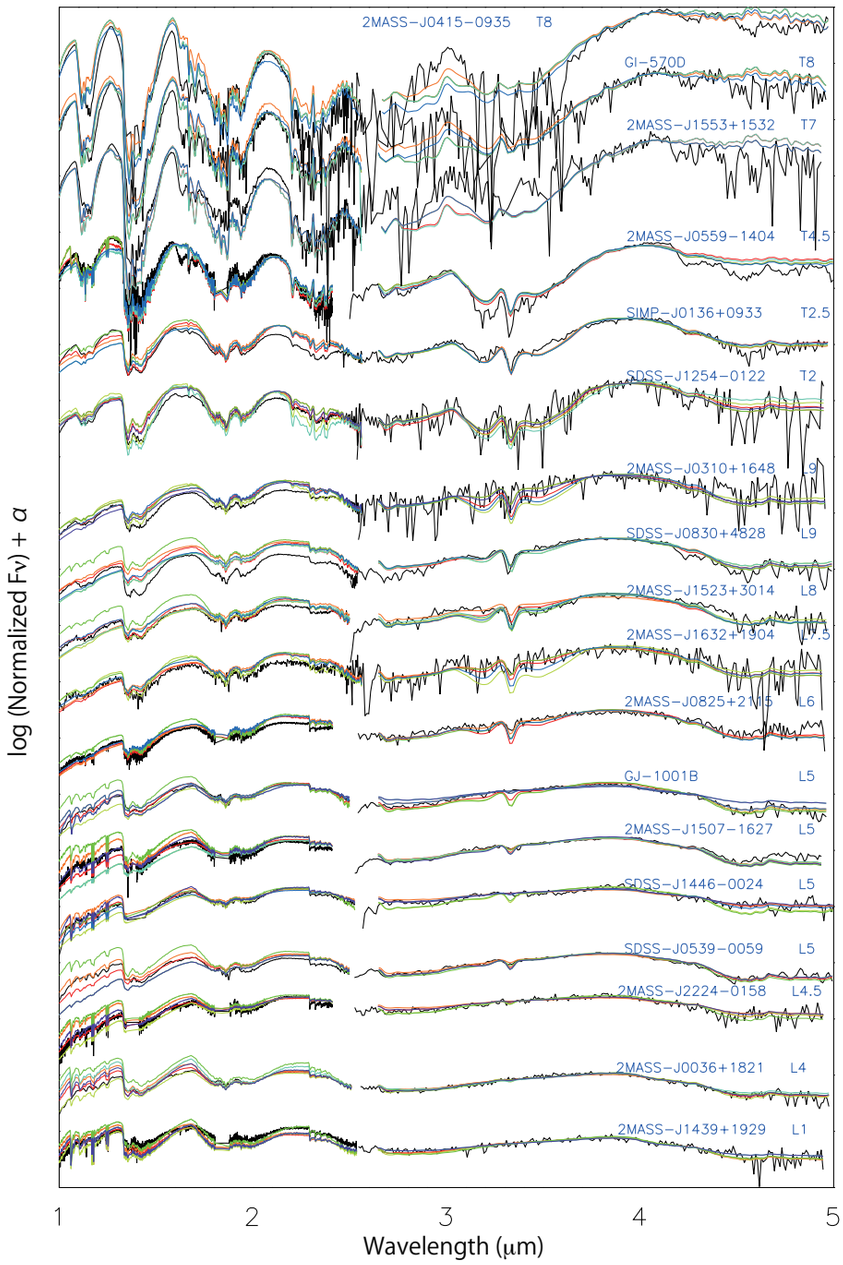


Figure 4.16: The derived "restricted best" models (max 6 per an object) are compared with the observation and the real best fit models. The real best fit model is in red and the "restricted best" models for $T_{\rm eff}$ (+100K and –100K), $T_{\rm cr}$ (+100K and –100K) and log $g$ (+0.5 and –0.5) are in orange, yellow, green, light blue, blue, and purple, respectively.

model parameters are determined at least within two grid of each parameter. $C'$ for the case of changing two grid of log $g$ still stays within 10%, but we can not change the grid of log $g$ any more. Therefor the uncertainty of log $g$ is not determined well for some objects.

Table 4.3: $C'$ values in $J$ and $H$ band region. The "restricted best" model within 10% are written in red, and within 20% in blue.

| Object Name | 1 grid | | | | | | 2 grid | | | | | |
|---|---|---|---|---|---|---|---|---|---|---|---|---|
| | $T_{\rm eff}$ | | $T_{\rm cr}$ | | log $g$ | | $T_{\rm eff}$ | | $T_{\rm cr}$ | | log $g$ | |
| | +100K | -100K | +100K | -100K | +0.5 | -0.5 | +200K | -200K | +200K | -200K | +1.0 | -1.0 |
| 2MASS J1439+1929 | 0.86 | 1.15 | 0.76 | 0.99 | 0.00 | 0.99 | 0.78 | 1.44 | 0.76 | 0.00 | 0.00 | 0.93 |
| 2MASS J0036+1821 | 0.76 | 1.09 | 0.55 | 0.67 | 0.00 | 0.81 | 0.64 | 0.00 | 0.55 | 0.00 | 0.00 | 0.67 |
| 2MASS J2224–0158 | 0.74 | 1.12 | 0.65 | 0.00 | 0.00 | 0.88 | 0.51 | 0.00 | 0.30 | 0.00 | 0.00 | 1.12 |
| SDSS J05395–0059 | 0.86 | 1.38 | 0.57 | 1.38 | 0.00 | 1.38 | 0.66 | 0.00 | 0.39 | 0.00 | 0.00 | 1.44 |
| SDSS J1446+0024 | 0.77 | 1.31 | 0.96 | 0.00 | 1.13 | 0.87 | 0.53 | 0.00 | 0.41 | 0.00 | 0.00 | 0.00 |
| 2MASS J1507–1627 | 0.74 | 1.41 | 0.57 | 1.41 | 0.00 | 0.93 | 0.57 | 0.00 | 0.41 | 0.00 | 0.00 | 0.77 |
| GJ 1001B | 0.87 | 1.24 | 0.59 | 1.06 | 0.87 | 1.06 | 0.65 | 1.78 | 0.40 | 0.00 | 0.00 | 0.00 |
| 2MASS J0825+2115 | 0.95 | 0.00 | 0.75 | 0.00 | 0.88 | 0.00 | 0.86 | 0.00 | 0.45 | 0.00 | 0.86 | 0.00 |
| 2MASS J1632+1904 | 0.93 | 0.73 | 0.77 | 0.00 | 0.85 | 0.00 | 0.90 | 0.00 | 0.53 | 0.00 | 0.83 | 0.00 |
| 2MASS J1523+3014 | 0.98 | 1.10 | 0.56 | 1.01 | 0.84 | 0.00 | 0.63 | 0.00 | 0.23 | 0.00 | 1.01 | 0.00 |
| SDSS J0830+4828 | 0.67 | 0.96 | 0.46 | 0.96 | 0.90 | 0.00 | 0.55 | 0.00 | 0.24 | 0.00 | 0.67 | 0.00 |
| 2MASS J0310+1648 | 0.77 | 0.74 | 0.77 | 0.00 | 0.82 | 0.97 | 0.89 | 0.61 | 0.53 | 0.00 | 0.00 | 0.00 |
| SDSS J1254–0122 | 0.75 | 0.72 | 0.75 | 0.81 | 0.00 | 0.83 | 0.81 | 0.81 | 0.61 | 0.00 | 0.00 | 0.87 |
| SIMP J01365+0933 | 0.94 | 0.00 | 0.79 | 1.09 | 1.09 | 0.00 | 0.88 | 0.00 | 0.48 | 0.00 | 0.94 | 0.00 |
| 2MASS J0559–14044 | 0.94 | 0.00 | 0.94 | 1.17 | 1.07 | 0.00 | 0.00 | 0.00 | 0.00 | 1.37 | 0.00 | 0.00 |
| 2MASS J1553+1532 | 1.00 | 0.00 | 0.00 | 1.06 | 1.00 | 0.00 | 0.99 | 0.00 | 0.00 | 1.05 | 0.99 | 0.00 |
| Gl 570D | 0.47 | 0.00 | 0.64 | 0.63 | 0.52 | 0.00 | 0.46 | 0.00 | 0.00 | 0.63 | 0.60 | 0.00 |
| 2MASS J0415–0935 | 0.56 | 0.00 | 0.61 | 0.61 | 0.72 | 0.00 | 0.52 | 0.00 | 0.00 | 0.61 | 0.67 | 0.00 |

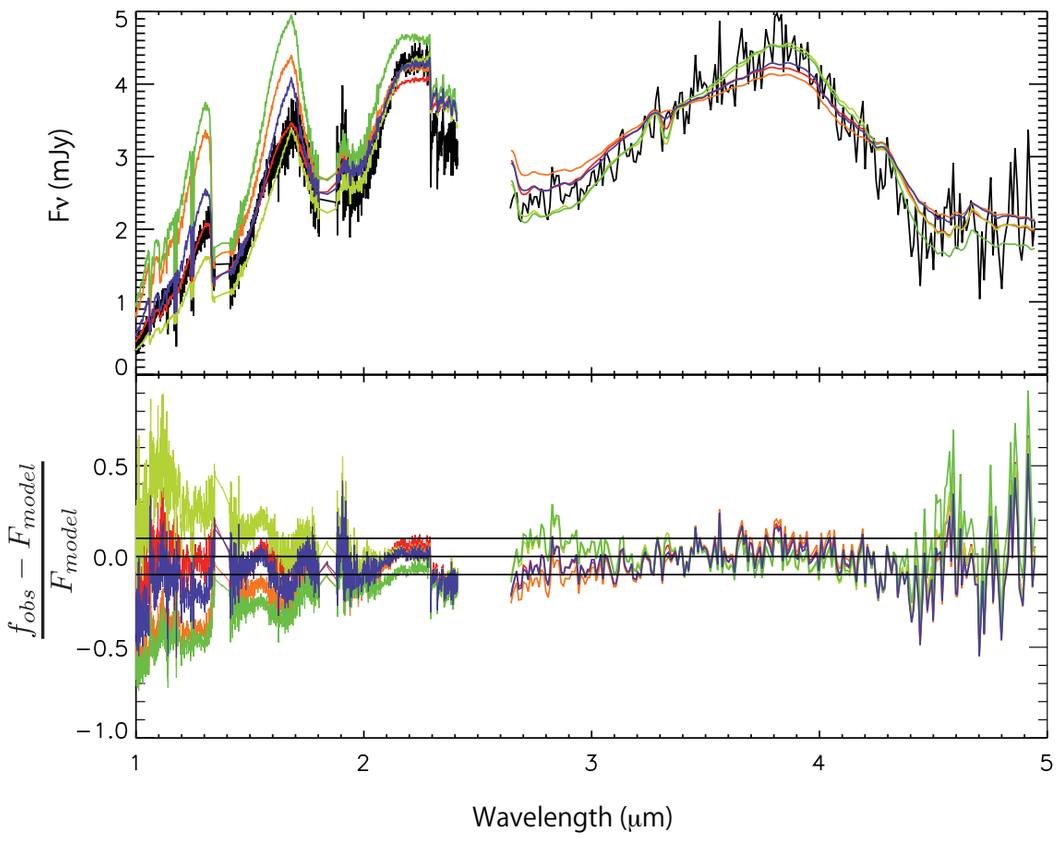


Figure 4.17: The detailed comparison of the $J$ and $H$ band for 2MASS J2224–0158 (L4.5). Colors are the same with Figure 4.16.

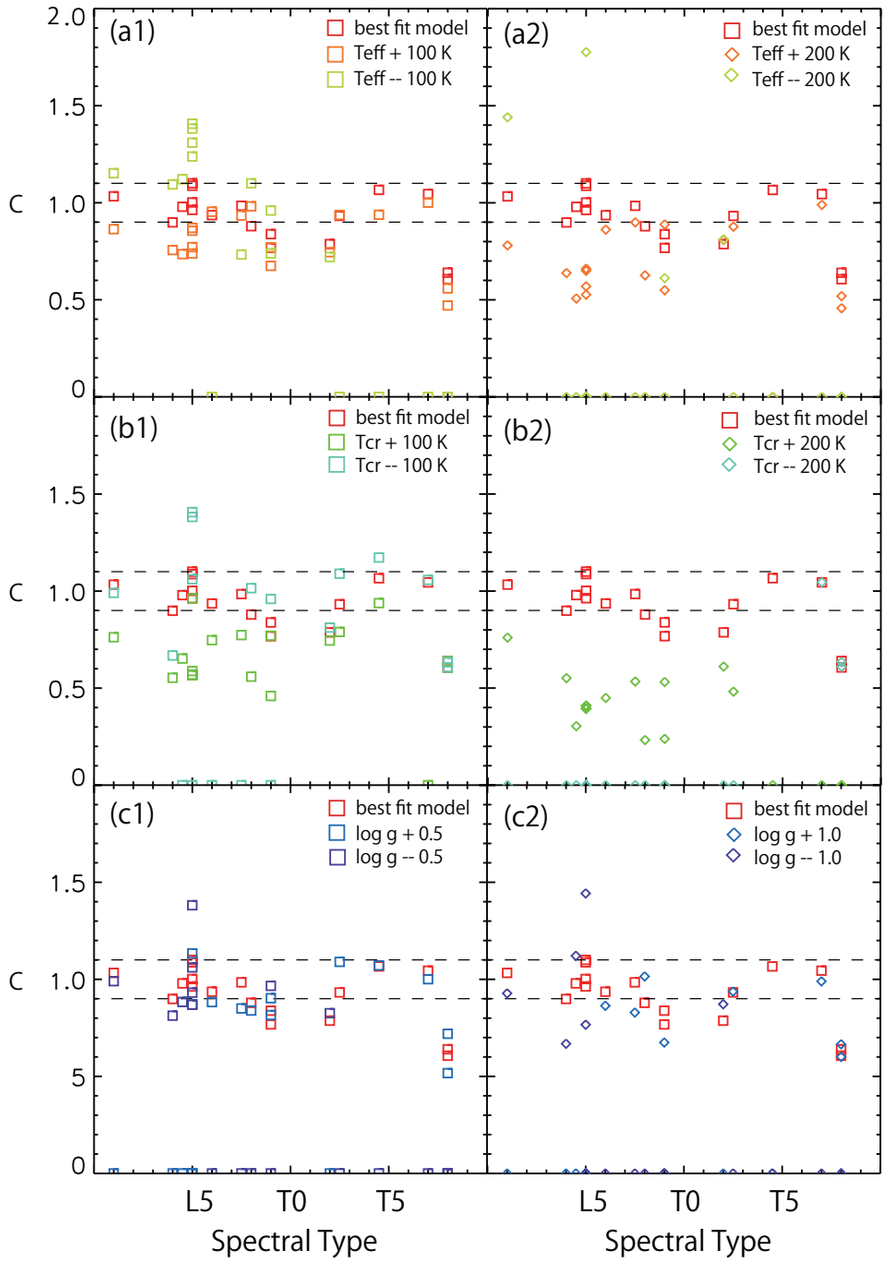


Figure 4.18: The $J-H$ band scaling factor $C'$ derived by comparison of observed and model spectra. Black dashed lines indicate $C'$ = 0.9 and 1.1. The threshold of $C'$ is based on the SpeX absolute flux error, 10 %. (a1) The case of changing one grid of $T_{\rm eff}$ . (b1) The case of changing one grid of log $g$ (c1) The case of changing one grid of $T_{\rm cr}$. (a2) The case of changing two grid of $T_{\rm eff}$ . (b2) The case of changing two grid of log $g$ (c2) The case of changing two grid of $T_{\rm cr}$.

## 4.6 Discussion

### 4.6.1 $CH_4$ Q-Branch at 3.3$\mu$m

We show that two L5 sources, 2MASS J1507–1627 and SDSS J0539–0059, show the $CH_4$ $\nu_3$ absorption band in their spectra, while the other L5 objects, SDSS J1446+0024 and GJ 1001B, do not present the band. In section 3.4.2, we suggest that the difference in L5 dwarfs with or without $CH_4$ $\nu_3$ absorption band can be in the dust effects . The derived best fit model parameters for the four L5 dwarfs are given in Table 4.4, and the model spectra are compared with the observations in Figure 4.20. In the figure, the $CH_4$ 3.3 $\mu$m absorption band in the best fit model of GJ 1001B is not seen in the observed spectra even though the overall SED agrees well. At this moment we do not have any good explanation of this result. However this result is important for future improvement of brown dwarf atmosphere models. GJ 1001B is not included in the following discussion. Generally, the $CH_4$ band is thought to be stronger in the spectra of lower effective temperature. However, in our result, $T_{\rm eff}$ is 1800 K in all objects. This indicats that the abundance of $CH_4$ molecule depends on other parameters, $T_{\rm cr}$ and/or log $g$. The object without $CH_4$ absorption, SDSS J1446+0024, has lower $T_{\rm cr}$ (1700K) than other two objects. Since $T_{\rm cr}$ determines the dust cloud thickness, SDSS J1446+0024 should be more affected by dust than other objects. The temperature of the dust existing region ($\log P_g \sim 5.5$) in the photosphere with lower $T_{\rm cr}$ is about 50 K higher than that with higher $T_{\rm cr}$ because of the warming up effects of the dust. Thus the $CH_4$ abundance in the photosphere with higher $T_{\rm cr}$ is about 3 dex larger than that with lower $T_{\rm cr}$ (Figure 4.19). The non-appearance of $CH_4$ in the spectra of SDSS J1446+0024 with lower $T_{\rm cr}$ is most likely due to the higher temperature (by 200–300 K) in the dust layer.

In addition, log $g$ of two objects showing $CH_4$ absorption band, 2MASS J1507–1627 and SDSS J0539–0059, is larger than the other two objects, SDSS J1446+0024. As shown in section 4.3.2, the inner temperature of photosphere with smaller log $g$ is 20–30 K higher than that with larger log $g$. Thus the $CH_4$ abundance is less in the photosphere of the objects with smaller log $g$.

In summary, our model fitting analysis confirms that the appearance of $CH_4$ absorption band at 3.3 $\mu$m in the L5-type spectra depends on not only effective temperature, but also dust presence and surface gravity. Surface gravity is a function of mass and radius, and the radius can be estimated as below. Since the radius of the our sources are similar to each other within 15 % (see section 4.6.2), the difference in the surface gravity by 0.5 dex comes from the difference in mass. This result indicates that the two groups of L5 dwarfs are different in their masses. For L5 dwarfs, $CH_4$ absorption appears in the spectra of massive

Table 4.4: Derived UCM parameters and scaling factor for the L5 dwarfs

| object name | $CH_4$ | $T_{\rm cr}$ | log $g$ | $T_{\rm eff}$ | $C_k$ |
|---|---|---|---|---|---|
| SDSS J1446+0024 | N | 1700 | 5.0 | 1800 | $1.76 \times 10^6$ |
| GJ 1001B | N | 1800 | 5.0 | 1800 | $1.37 \times 10^7$ |
| 2MASS J1507–1627 | Y | 1800 | 5.5 | 1800 | $1.48 \times 10^7$ |
| SDSS J0539–0059 | Y | 1800 | 5.5 | 1800 | $4.89 \times 10^6$ |

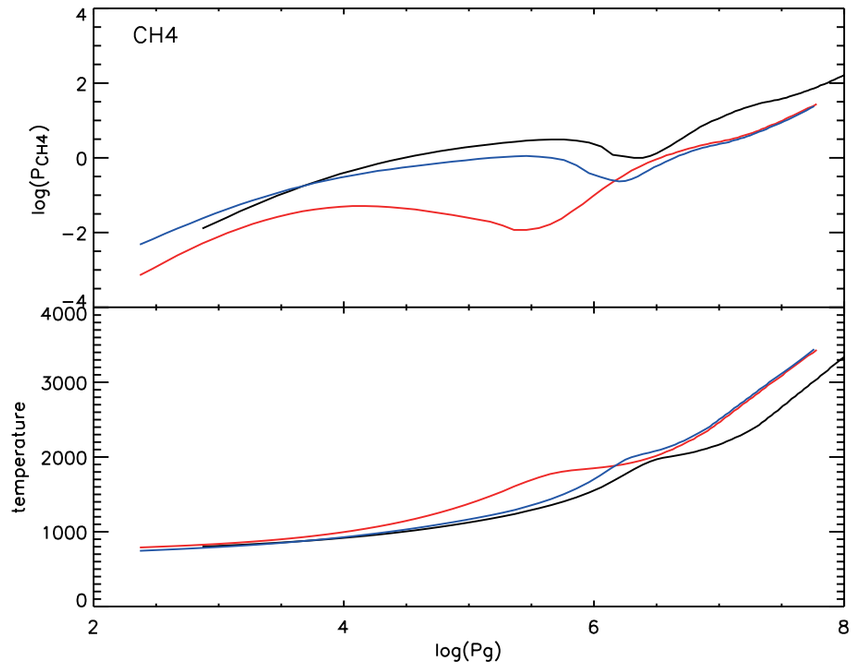


Figure 4.19: $CH_4$ partial pressure against total gas pressure. The model of ($T_{cr}$/log $g/T_{eff}$)=(1800K/5.5/1800K), (1700K/5.0/1800K) and (1800K/5.0/1800K) are drawn in black, red, and green, respectively.

objects and does not appear in the spectra of less massive objects.

### 4.6.2 Estimate of Radii of Brown Dwarfs

A constant radius near the Jupiter's value ($R_J$) has been often assumed for previous analysis of brown dwarfs. According to the theoretical study by Burrows et al. (2001), the radii of brown dwarfs older than $10^7$ yrs remain roughly constant at 0.7–1.1 $R_J$ independent of mass for a broad range from 0.3 to 70 $M_J$. The fact that the radii of old substellar objects are constant within 30 % independent of mass for a mass ranging a factor of 200 is a consequence of the competition in two equation of states between Coulomb and degeneracy effects. Since the objects held by Coulomb effect would only set a fixed density, the relation of radius and mass is $r \propto M^{1/3}$ whose polytrope index $n \sim 0.0$. On the other hand, degenerate interior results in $r \propto M^{-1/3}$ and polytrope index $n = 1.5$ (Chandrasekhar 1939). Lower mass objects like Jupiter results in a polytrope of index 1.0, and $r$ is independent of mass. Figure 4.21 taken from Burrows et al. (2001) shows that almost constant radii near the radius of Jupiter after $10^8$ yrs for the masses ranging from 0.3 $M_J$ to 0.2$M_\odot$. Burgasser (2001) derive the expected radius of an observed brown dwarf by performing a Monte Carlo simulation with evolutionary models by Burrows et al. (1997). The simulation assumes a constant birth rate and mass function. He found that the most expected radius of the object is $\sim 0.9R_J$.

$T_{eff}$ of brown dwarfs have been often estimated empirically by the assumed radius. Vrba et al. (2004) used the radius of brown dwarfs $r = 0.9\ R_J$ by Burgasser (2001) to estimate the empirical $T_{eff}$. However

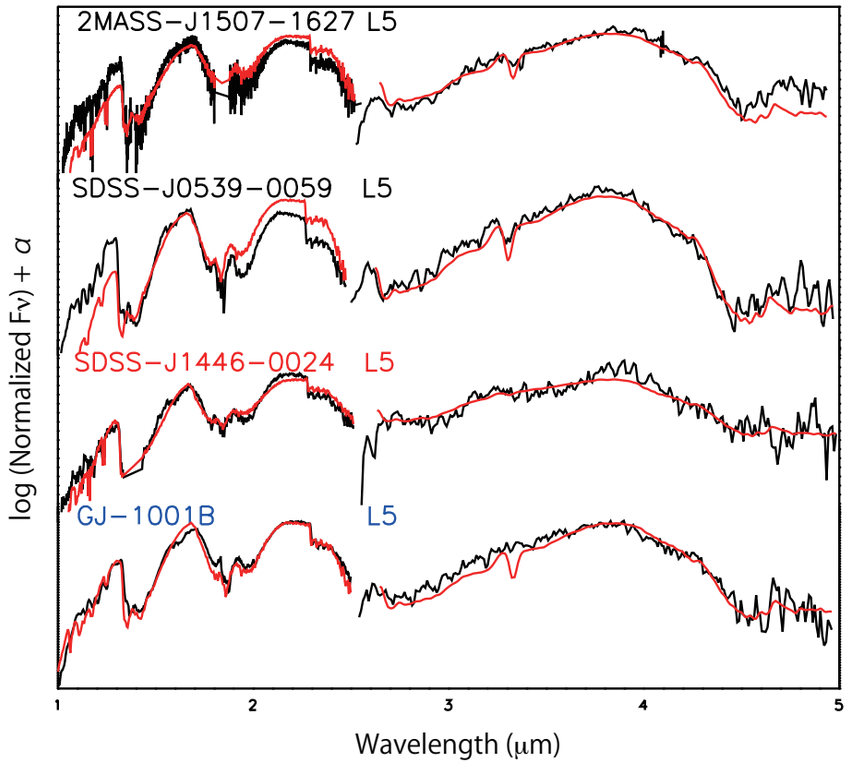


Figure 4.20: The 2.5–5.0 $\mu$m spectra of four L5 dwarfs 2MASS J1507–1627, SDSS J0539–0059, SDSS J1446+0024 and GJ 1001B. Black lines are the observed spectra taken by *AKARI* and SpeX/CGS4 and red lines are the model spectra.

$T_{\rm eff}$ derived by the UCM fitting to the observed spectra does not agree with the empirical $T_{\rm eff}$ (Yamamura et al. 2010). They reported that the radii of six dwarfs estimated by model fittings to the *AKARI* data ranges between $0.68 \sim 1.18\ R_J$. Though the average radius is $0.81\ R_J$, the radii derived from observations distribute in a wider range than that expected from Burrows (2001). They argue that the radii of brown dwarfs may not be represented by a single mean value.

We derive the radius $r$ of each dwarf using the following relation,

$$C = \left(\frac{r}{D}\right)^2. \tag{4.6}$$

where $C$ is the scaling factor defined by equation (4.3), $D$ is the distance given in Table 2.1. The result is listed in Table 4.5 and plotted against their spectral types in Figure 4.22. We estimate the uncertainty of the derived radius using the uncertainties of the distance and the scaling factor $C$ as bellow. The derived radii of 18 objects observed by *AKARI* are consistent with the theoretical radius implied by Burrows et al. (2001) within the error. The average radius is $0.89\ R_J$, and is also consistent with the predicted radius by Burgasser et al. (2001). There is a trend that the radius become smaller from early-L toward late-L dwarfs and then turns to enlarge from late-L to late-T dwarfs.

The radii of brown dwarfs decrease slowly as they evolve, because of ongoing shrinking. The radius of "planet mass" objects ($M < 0.012\ M_\odot$) reaches to the degeneracy limit at $10^{7.5}$ yrs. Eventually the radii of "planet mass" objects appear to stay slightly above $R_J$ and independent of mass. On the other hand, the objects of "brown dwarf mass" reaches the degeneracy limit at $10^{8.5}$ and ultimately the radii become constant below $R_J$. Therefore the radii of "brown dwarf mass" object is smaller than "planet mass" objects beyond $10^8$ yrs.

We find that the radii of late-L type are smaller than that of early L and T dwarfs in the *AKARI* sample. As previously noted, the radius does not monotonically decrease, in particular after the age of $10^{7.5}$ yrs as shown in Figure 4.21. The radius of relatively "planet mass" objects is small in the beginning and change of radius during their lifetime is also small. On the other hand, the radius of "brown dwarf mass" objects is large when they are young, and ultimate radius is smaller than that of "planet mass" objects. The relation of radius and mass with age change as shown in Figure 4.23. We see that there are a valley on the curves for older than $10^{7.5}$ yrs. Our result implies that inversion of radius predicted by theory is actually taking place, if differences of absolute levels of the radii are ignored. To confirm this hypothesis, we have to determine the age of *AKARI* objects. It is difficult to give the age of brown dwarfs observationally unless the case that the objects are a member of a cluster. We attempt to estimate the age from $T_{\rm eff}$ and surface gravity using Figure 4.24. This figure shows the surface gravity versus the effective temperature for dwarfs with masses from $0.30 M_J$ to $0.24 M_\odot$. We overlay dashed lines and paint the region in purple to show where the *AKARI* samples locate. The horizontal lines are drawn auxiliary for surface gravity = 4.5, 5.0 and 5.5, and the vertical lines show the effective temperature range of the *AKARI* brown dwarfs (700 to 2200K). The dotted line in red is $T_{\rm eff}$ = 1600 K that is the effective temperature of late-L dwarfs. We find that the age of the *AKARI* objects ranges between $10^8$ and $10^9$ yrs, where the theory predicts the inversion of radius. The trend found in Figure 4.21. The decreasing radius between early- to late-L dwarfs and the increasing radius to late-T dwarfs may indicate that theoretical

inversion is detected by current analysis. If this is the case it is the first observational evidence of radius inversion.

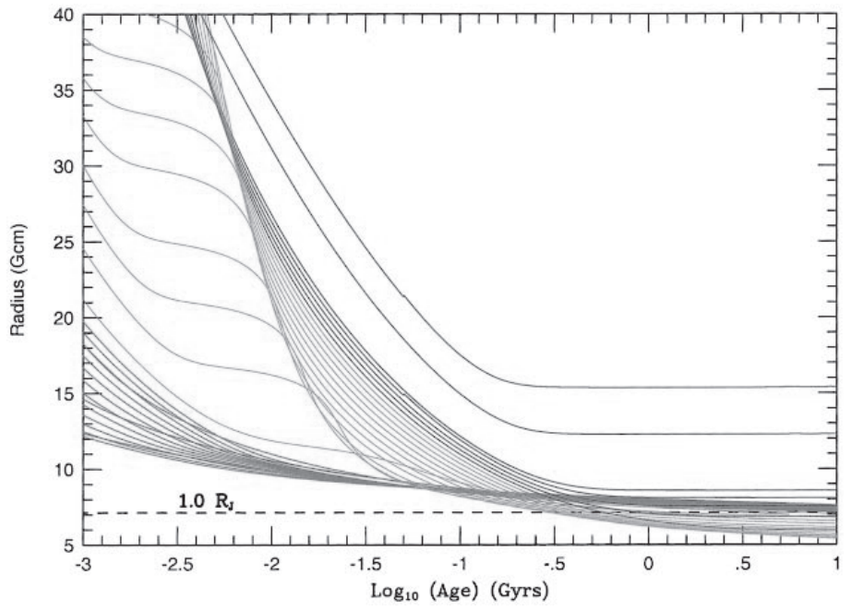


Figure 4.21: The radius (in units of $10^9$ cm) of substellar-mass objects with the masses versus the $\log_{10}$ of the age (in Gyr). The mass below 0.012 $M_\odot$, that between 0.012 $M_\odot$ and 0.08 $M_\odot$ and that above 0.08 $M_\odot$ are shown by red, green and blue (same as Figure 1.4). The radius of Jupiter is also shown by dashed line (from Burrows et al. 1997).

### Uncertainty of the Radius

The radius in this analysis is derived from the distance $D$ and the conversion factor $C$. The uncertainty of $D$ is estimated from the parallax error, about 4 mas. In order to estimate the uncertainty of $C$ we derive $C$ for "restricted best" model in section 4.5.3 (hereafter $C_2$). We show the result in Figure 4.25, where horizontal axis is spectral type and vertical axis is the ratio of the two scaling factors, $C_1/C_2$, where $C_1$ is for the best model derived by the fitting process Step 1 in section 4.4.1. Despite the absolute flux density is most affected by $T_{\rm eff}$ rather than other two parameters (Figure 4.25) all theses parameters contribute to the uncertainty of the scaling factor $C$.

Table 4.5: The derived radius for *AKARI* objects

| Object Name | Sp.Type | Radius(error) $[R_J]$ |
|---|---|---|
| 2MASS J1439+1929 | L1 | 0.98(0.09) |
| 2MASS J0036+1821 | L4 | 0.86(0.08) |
| 2MASS J2224–0158 | L4.5 | 0.82(0.1) |
| SDSS J0539–0059 | L5 | 0.80(0.09) |
| SDSS J1446+0024 | L5 | 0.72(0.11) |
| 2MASS J1507–1627 | L5 | 0.77(0.06) |
| GJ 1001B | L5 | 0.92(0.17) |
| 2MASS J0825+2115 | L6 | 0.74(0.10) |
| 2MASS J1632+1904 | L7.5 | 0.72(0.16) |
| 2MASS J1523+3014 | L8 | 0.63(0.11) |
| SDSS J0830+4828 | L9 | 0.64(0.10) |
| 2MASS J0310+1648 | L9 | 0.53(0.15) |
| SDSS J1254–0122 | T2 | 0.82(0.36) |
| SIMP J01365+0933 | T2.5 | 0.78(0.11) |
| 2MASS J0559–1404 | T4.5 | 1.10(0.19) |
| 2MASS J1553+1532 | T7 | 1.57(0.47) |
| Gl 570D | T8 | 1.01(0.23) |
| 2MASS J04151954–0935 | T8 | 0.92(0.22) |

1: This object is a known binary.

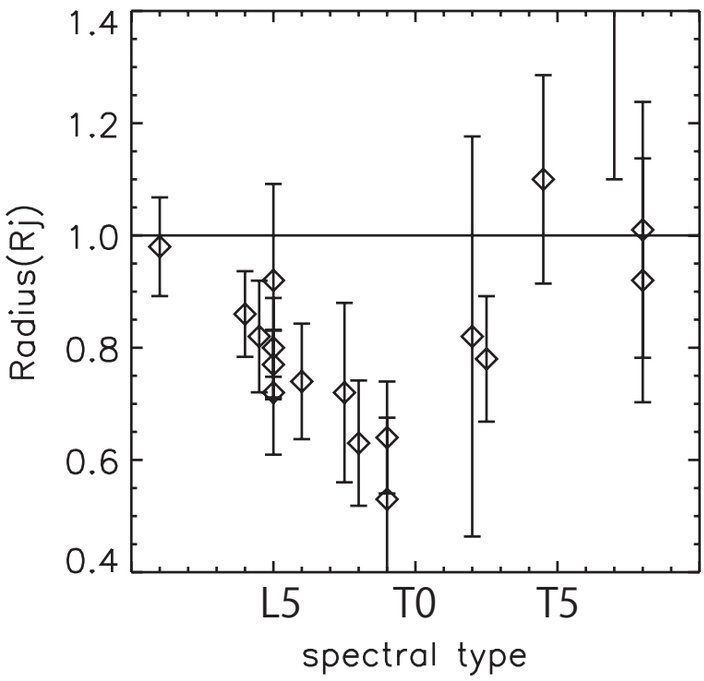


Figure 4.22: The radius derived from their distances and $C$ of the best fit model. The horizontal axis are spectral type. The uncertainty of $C$ is estimated in section 4.5.3. The Jupiter radius $R_J$ is also shown.

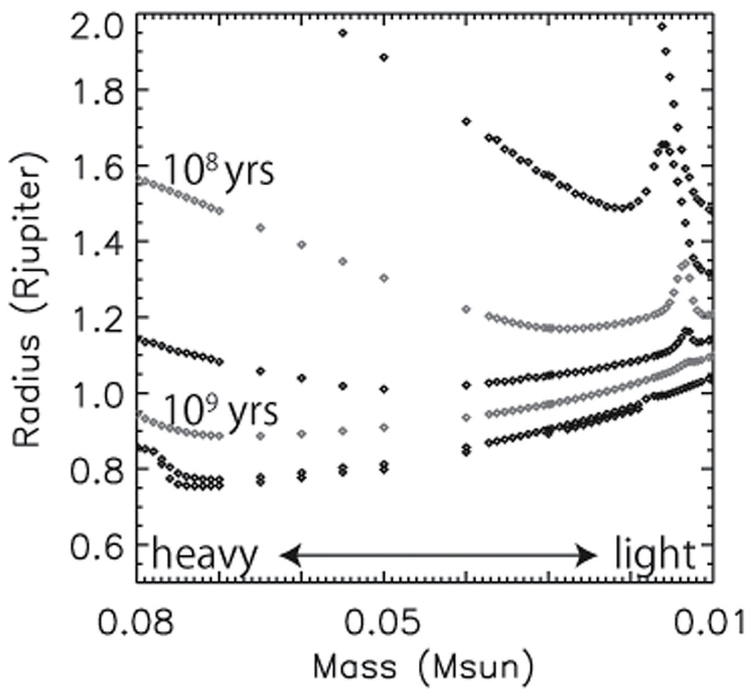


Figure 4.23: The theoretical prediction of the relation of radius and mass for different ages. The radius of relatively less massive and young objects is small and is rather stable with the ltime. On the other hand, the radius of massive objects is large when they are young, and ultimate radius is smaller than that of less massive objects. The lines are the relation of mass and radius at $10^7$, $10^{7.5}$, $10^8$, $10^{8.5}$, $10^9$, $10^{9.5}$ and $10^{10}$ yrs (top to bottom). The blue and red line shows the relation of mass and radius at $10^8$ yrs and at $10^9$ yrs, respectively. We use the data provided from Prof. Adam Burrows (in private communication).

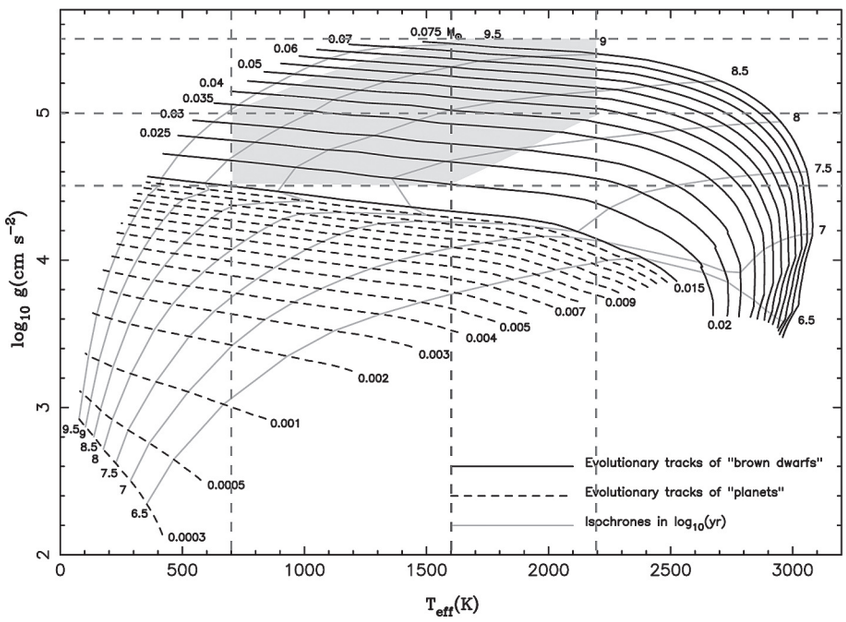


Figure 4.24: Surface gravity versus effective temperature for objects with masses range of $0.30M_J$ to $0.24M_\odot$ (Burrows et al. 2001). We added some dashed lines and painted the region where *AKARI* samples are located by gray color. The horizontal lines are drawn auxiliary for surface gravity = 4.5, 5.0 and 5.5, and the vertical lines show effective temperature range of *AKARI* brown dwarfs (2200 to 700K).

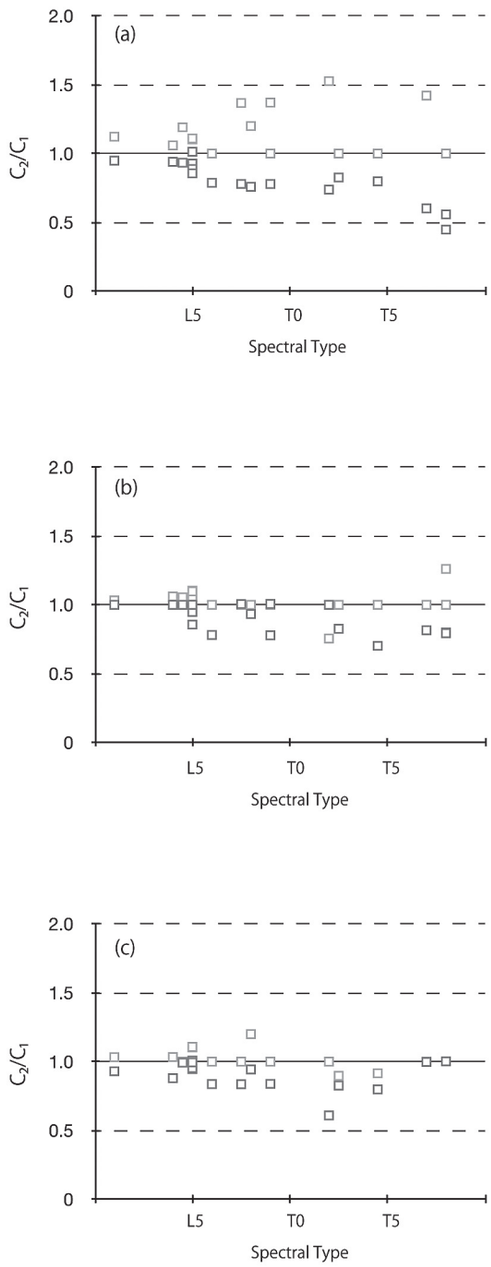


Figure 4.25: The estimated uncertainty of the scaling factor $C$ depending on the each of three model parameters. The horizontal axis is spectral type and the vertical axis is the ratio of the scaling factor of "restricted best" model to the best fit modelin section 4.4. (a)the case of changing $T_{\rm eff}$ by one grid from the best fit value, (b)the case of changing log $g$ by one grid from best fit value and (c)the case of changing $T_{\rm cr}$ by one grid from best fit value. The case of increasing one grid of each parameter is drawn in green, and the case of decreasing is drawn in blue.

# Chapter 5

# Separate Model Fitting of the *AKARI* and SpeX/CGS4 Spectra

In the analysis so far described, we search for the models that explaining both the *AKARI* and SpeX/CGS4 spectra reasonably well. However, a concern is that none of these models can fit the entire wavelength range perfectly, and there are always some deviation either in the *AKARI* or the SpeX/CGS4 wavelength. This problem of non-perfect fit in broad-wavelength range was also mentioned by Cushing et al. (2008, see section 1.4). We investigate this problem by running the model fit to each of the *AKARI* and the SpeX/CGS4 spectral data separately. We try to propose possible improvements toward the better modeling of brown dwarfs.

## 5.1 Fitting Only *AKARI* Data

We derive the best model by fitting only *AKARI* data in the same way as Step 1 shown in section 4.4.1. The spectral range used for the fitting is 2.5–4.15 $\mu$m. We show the resulted model parameters in Table 5.1 and compare the models with the observations in Figure 5.1. The models explain the overall shapes of observed spectra within the fitting wavelength range. The discrepancy in 3.0–3.5 $\mu$m $CH_4$ absorption, which arises for the best model for the *AKARI*+SpeX/CGS4 data, is solved. The fit to the $H_2O$ weak absorption around 3.0 $\mu$m, which can not be explained by the best fit model for *AKARI*+SpeX/CGS4 of late-T dwarfs, is also improved.

The almost all best models from the *AKARI* only fitting does not explain the SpeX/CGS4 spectra. The deviation from the observed spectra is larger than the models from *AKARI* +SpeX/CGS4. The entire flux level of the model spectra is significantly higher than the observed flux. We do not see the extinction by the dust in the models in *J* band wavelength range of early- and mid-L dwarfs. The $T_{\rm eff}$ derived from the *AKARI* only fitting is so high that dust does not form, and the effect of dust presence does not appear in the spectra. These models imply that the inner photosphere of early- to mid-L dwarfs is warmer. On the other hand, for late-L and early-T dwarfs the effect of dust extinction in the model spectra is smaller than that of the observations. For two late-T dwarfs, Gl 570D and 2MASS J0415–0935, and L9 dwarf, SDSS J0830+4828, the model spectra fit the observation including SpeX data quite nicely over

the entire wavelengths between 1.0 and 5.0 $\mu$m if we give appropriate scaling for each of *AKARI* and SpeX/CGS4 data. However, the scaling factors for the SpeX range ($C_{SpeX}$) and *AKARI* range ($C_{AKARI}$) are quite different. The ratio of two scaling factors, $C_{SpeX}/C_{AKARI}$ for SDSS J0830+4828, Gl 570D and 2MASS J0415–0935 are 0.55, 0.38 and 0.48 respectively. We believe that the difference is not due to the incorrect calibration of each observed data alone.

## 5.2 Fitting Only SpeX/CGS4 Data

We also show the results of model fitting with the SpeX/CGS4 data only in Figure 5.2 and Table 5.1. We see that the models agree well with the SpeX/CGS4 spectra, except for the $CH_4$ absorption at 1.6 $\mu$m in the spectra of five T dwarfs as for the case of fitting *AKARI*+SpeX/CGS4 data. The absorption band of $CH_4$ at 1.6 $\mu$m in the model are weaker than the observation. The difference of dust extinction in *J* band, which present in the comparison of the *AKARI*+SpeX/CGS4 data and the best model, does not appear in the case of fitting SpeX/CGS4 data only.

The SpeX only best fit models do not match with the observations in the *AKARI* wavelength range except for two mid-L dwarfs. The principal differences from the results of the *AKARI*+SpeX best fit models are the discrepancy in flux level in the $CH_4$ and $H_2O$ bands. The $CH_4$ around 3.3$\mu$m is not explained by the best models derived from SpeX spectra for the some objects. The model fits the almost entire spectrum of GJ 1001B from 1.0 to 5.0 $\mu$m fairly well, but not the $CH_4$ absorption at 3.3 $\mu$m. These results indicate that the SpeX/CGS4 data can not constraint the temperature of the inner photosphere well. The $H_2O$ and $CH_4$ absorption near 3.0 $\mu$m in late-T dwarfs is also inconsistent as same for the results of the both AKARI + SpeX/CGS4 data fitting. In addition, as same for the results of *AKARI* data only fitting, we see the difference of the absolute flux levels in many objects, 2MASS J1439+1929, SDSS J0539–0059, 2MASS J1507–1627, 2MASS J0825+2115, 2MASS J0310+1648, SDSS J0423–0414, SDSS J1254–0122 and 2MASS J1553+1532. The $C_{spex/CGS4}/C_{AKARI}$ are 1.29, 0.84, 0.87, 0.68, 0.57, 0.57, 0.74 and 0.84 respectively. These differences do not occur for 2MASS J1439+1929 and 2MASS J1507–1627, because we show the validity of the flux level between both data in section 4.4.3 and Figure 4.12.

## 5.3 The Model Parameters of Fitting *AKARI* or SpeX/CGS4 Data

We compare each physical parameter of *AKARI*+SpeX/CGS4 fit model, *AKARI* fit model, and SpeX/CGS4 fit model in Figure 5.3 and Table 5.1. $T_{\rm eff}$s for early-T dwarfs are almost the same in the three cases. $T_{\rm eff}$ of *AKARI* fit model for L dwarfs are higher compared to that of *AKARI*+SpeX/CGS4 and SpeX/CGS4 only fit models (Figure 5.3 (a)). $T_{\rm eff}$ of SpeX/CGS4 fit model for L dwarfs show milder variation over the spectral types and is 1800 $\pm$ 100 K for the nine of twelve sources. The resulted parameters of model fitting to *AKARI* data reflect the spectral profiles that changes due to $T_{\rm eff}$ rather than dust extinction. These results indicate that the $T_{\rm eff}$ of brown dwarfs is sensitive straightforwardly in the *AKARI* wavelength range.

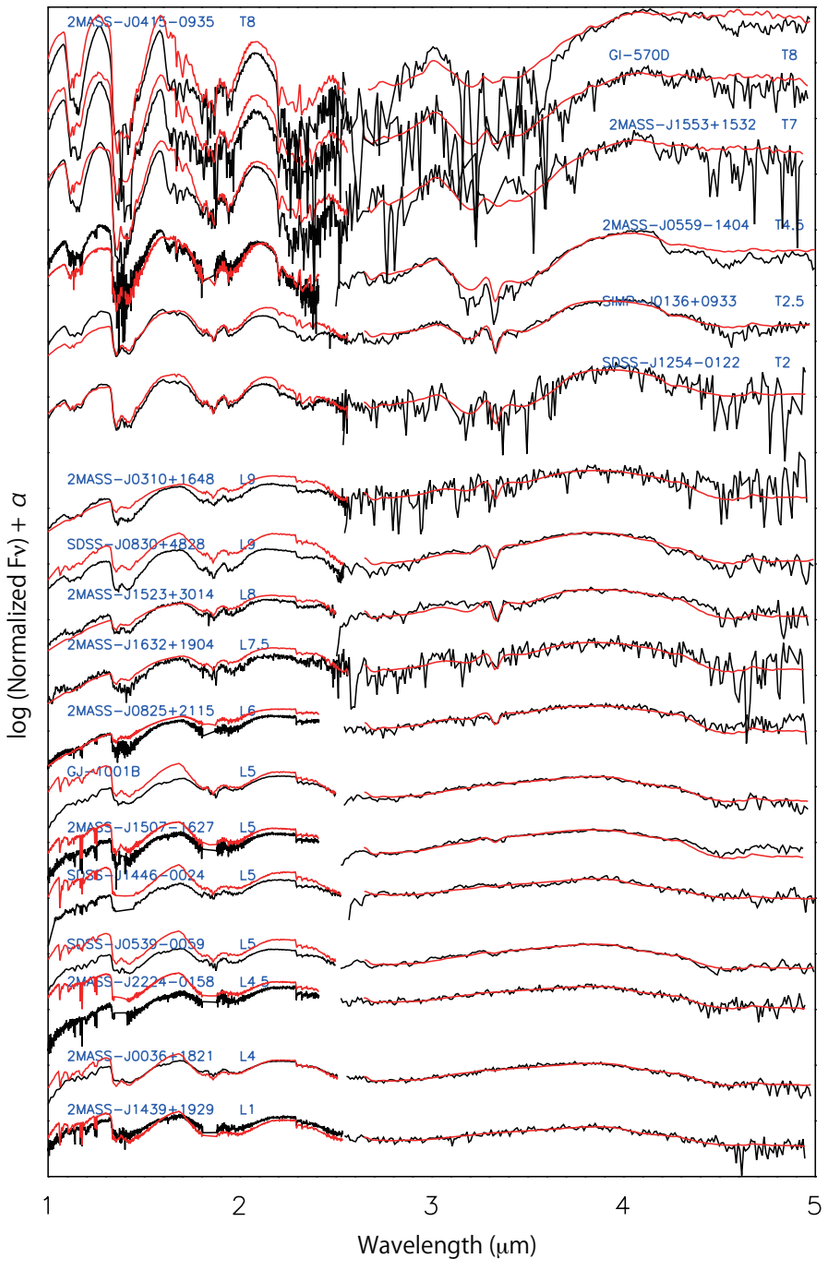


Figure 5.1: The results of the *AKARI* only fitting. The black lines are observed data and red lines are the best fit model spectra.

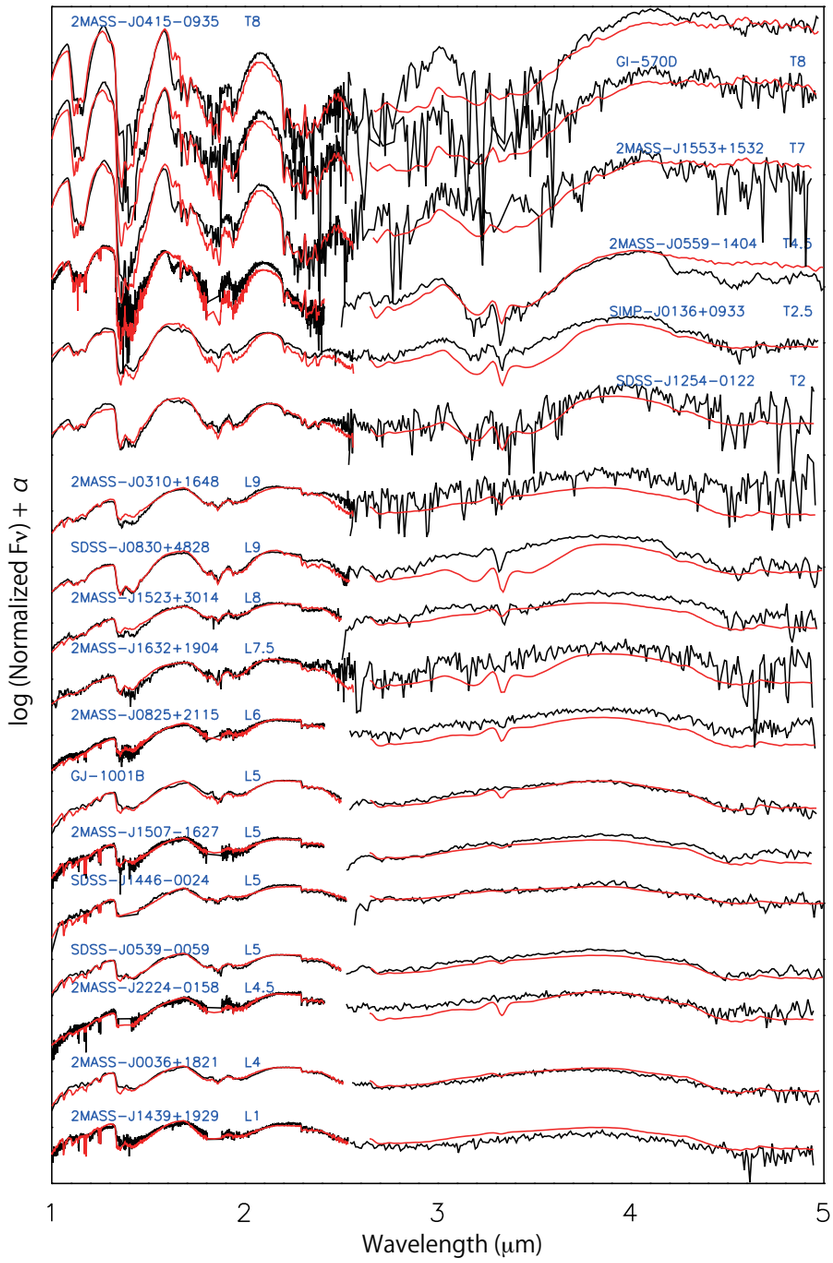


Figure 5.2: The result of the SpeX/CGS4 only fitting the *AKARI* objects. The black lines are observed data and red lines are the best fit model spectra.

The trend of $T_{\rm cr}$ is different in each best fit model. While $T_{\rm cr}$ of the *AKARI* fit models stay mostly around 1700 K and shows no particular trend, that of SpeX/CGS4 fit model exhibit recognizable changes similar to (or more prominently than) the *AKARI*+SpeX/CGS4 fit models. The resulted parameters of the model fitting to the SpeX/CGS4 data reflect the spectral profiles by the dust extinction effect, especially in $J$ and $H$ band. Thus $T_{\rm cr}$ is most sensitive to the SpeX/CGS4 data.

It is difficult to determine the best log $g$ in our model fitting, because of large grid size of the model used in the present analysis (Figure 5.3 (b)). We see a weak trend that log $g$ becomes smaller from L to T for all fit models.

Table 5.1: physical parameters derived by model fitting to the *AKARI* data

| Object Name | *AKARI*+SpeX/CGS4 | | | *AKARI* | | | SpeX/CGS4 | | |
|---|---|---|---|---|---|---|---|---|---|
| | $T_{\rm cr}$ | log $g$ | $T_{\rm eff}$ | $T_{\rm cr}$ | log $g$ | $T_{\rm eff}$ | $T_{\rm cr}$ | log $g$ | $T_{\rm eff}$ |
| 2MASS J1439+1929 | 1800 | 5.5 | 2100 | 1700 | 5.0 | 2200 | 1800 | 5.5 | 2000 |
| 2MASS J0036+1821 | 1800 | 5.5 | 2000 | 1800 | 5.0 | 2000 | 1800 | 5.5 | 1900 |
| 2MASS J2224–0158 | 1700 | 5.5 | 1800 | 1800 | 5.5 | 2200 | 1800 | 5.0 | 1700 |
| SDSS J05395–0059 | 1800 | 5.5 | 1800 | 1800 | 5.0 | 2100 | 1800 | 5.5 | 1900 |
| SDSS J1446+0024 | 1700 | 5.0 | 1800 | 1700 | 4.5 | 2100 | 1700 | 5.0 | 1800 |
| 2MASS J1507–1627 | 1800 | 5.5 | 1800 | 1900 | 5.5 | 2000 | 1800 | 5.5 | 1900 |
| GJ 1001B | 1800 | 5.5 | 1800 | 1800 | 5.0 | 2100 | 1800 | 5.0 | 1800 |
| 2MASS J0825+2115 | 1700 | 4.5 | 1500 | 1700 | 5.5 | 1700 | 1800 | 5.0 | 1700 |
| 2MASS J1632+1904 | 1700 | 4.5 | 1500 | 1700 | 5.0 | 1600 | 1800 | 5.5 | 1600 |
| 2MASS J1523+3014 | 1800 | 4.5 | 1600 | 1700 | 5.5 | 1600 | 1800 | 5.5 | 1800 |
| SDSS J0830+4828 | 1700 | 4.5 | 1500 | 1800 | 4.5 | 1700 | 1800 | 4.5 | 1500 |
| 2MASS J0310+1648 | 1700 | 4.5 | 1500 | 1700 | 5.0 | 1600 | 1800 | 5.0 | 1800 |
| SDSS J1254–0122 | 1700 | 5.5 | 1200 | 1800 | 4.5 | 1400 | 1900 | 5.0 | 1500 |
| SIMP J01365+0933 | 1900 | 4.5 | 1400 | 1700 | 4.5 | 1400 | 1900 | 5.0 | 1400 |
| 2MASS J0559–14044 | 2000 | 5.5 | 1200 | 1700 | 4.5 | 1200 | $T_{\rm cond}$ | 5.5 | 1200 |
| 2MASS J1553+1532 | 2000 | 4.5 | 800 | 1700 | 5.0 | 1000 | 1900 | 4.5 | 800 |
| Gl 570D | 2000 | 4.5 | 700 | $T_{\rm cond}$ | 4.5 | 700 | 1900 | 4.5 | 700 |
| 2MASS J0415–0935 | 2000 | 5.0 | 700 | 1800 | 4.5 | 800 | 1900 | 4.5 | 700 |

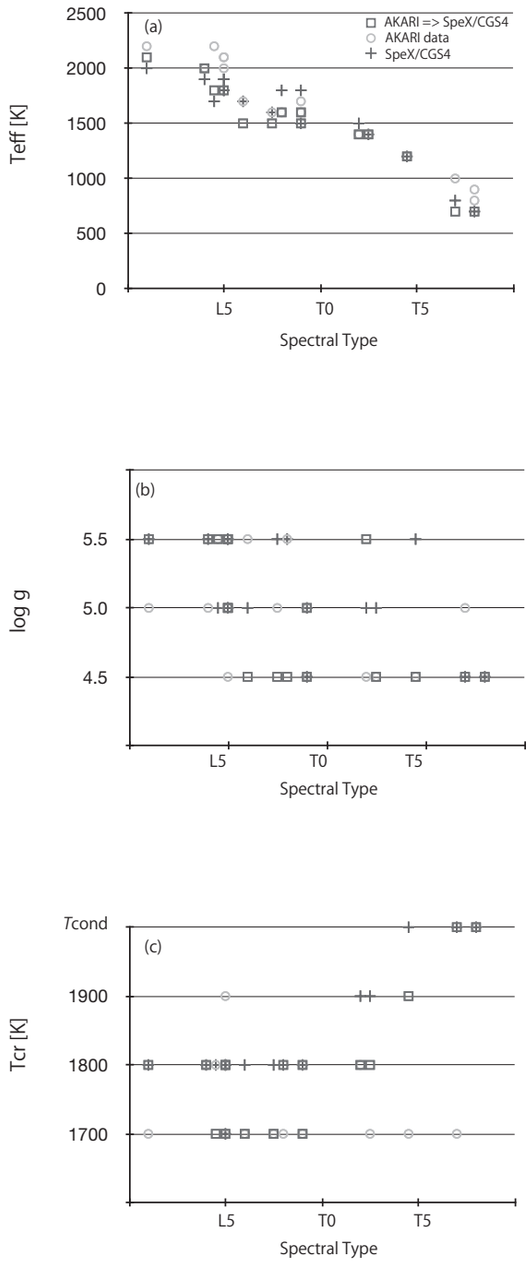


Figure 5.3: Comparison of best fit model parameters for fitting to the *AKARI*+SpeX/CGS4, *AKARI* only and SpeX/CGS4 only.

## 5.4 Discussion

We find that almost all model spectra do not explain the observation perfectly in the broad wavelength range from 1.0 to 5.0 $\mu$m at the same time. For the late-T dwarfs, the $CH_4$ 1.6 $\mu$m absorption is not consistent with any fit models. The SpeX only fit model spectra are not consistent around 3.0 $\mu$m, but the *AKARI* only fit model spectra can fit the profile around 3.0 $\mu$m. $T_{\rm eff}$ derived from *AKARI* data only fit shows high value, and the fit to the $CH_4$ 1.6 $\mu$m band is worse than that in the SpeX only model spectra. These results indicates that the *AKARI* spectra simply reflect the emission from inner high temperature region.

The model spectra of other spectral types (from L to middle-T types) including dust effect can not simply explain the deviation from the observed spectra. First we consider the cases of mid-L dwarfs. When we compare the *AKARI* fit models with the observed spectra, the fluxes of the model spectra are always higher than the observed spectra, and the *AKARI* fit models show high $T_{\rm eff}$ and low dust extinction. This is in contrast to the fact that mid-L dwarfs must be significantly affected by the dust extinction. Since the wavelength range of SpeX/CGS4 is the most sensitive to the dust extinction, we can evaluate the dust amount from the spectra in this wavelength region. From the result of the fitting of the SpeX/CGS4 data only, the effect of the dust extinction is large in the mid-L dwarfs. The inner temperature of these objects increases due to the dust. The $T_{\rm eff}$ derived in the fitting of the *AKARI* data only is larger than that derived from the *AKARI*+SpeX/CGS4. These arguments indicate that the increase of the inner temperature due to the dust is underestimated in the models than that in the actual photospheres. The dust opacity is a function of size distribution, amount and composition, and is, crudely, inversely proportional to mean particle size and gravity and is directly proportional to the pressure at the cloud base as follow,

$$\tau_\lambda \sim 75 \varepsilon Q_\lambda \phi \left(\frac{P_c}{1\mathrm{bar}}\right)\left(\frac{10^5 \mathrm{cms}^{-2}}{g}\right)\left(\frac{1\mu m}{a_p}\right)\left(\frac{1.0\mathrm{gcm}^{-3}}{\rho}\right). \quad (5.1)$$

Though the dust size assumed in the UCM is a constant value of 0.01 $\mu$m, it may be larger. The dust composition implemented in UCM are Fe, $MgSiO_3$ and $Al_2O_3$, but we should consider other dust species.

On the other hand, for late-L to mid-T dwarfs the parameters derived by the fitting of the *AKARI* data only exhibit an opposite trend from the mid-L dwarfs. From the result of the fitting of the SpeX data only, we know that the effect of the dust is relatively small. The inner photosphere temperature should stay low, and $T_{\rm eff}$ derived by fitting of *AKARI* spectra only are expected to have lower value than that derived from the *AKARI*+SpeX data. However, the $T_{\rm eff}$ of the *AKARI* only fit is higher than that from the *AKARI*+SpeX model fit, and the flux levels of the observed *AKARI* spectra at the *AKARI* wavelength region are higher than the model spectra. It is considered that the temperature of inner region directly contributing the flux in the *AKARI* wavelengths is higher than the predicted one. Little warming up effect by the dust is expected, since the dust in the atmosphere of these objects starts to disappear from the upper photosphere. Though the physical mechanism for this dust disappearance is not understood yet, it is likely that the dust migration from the upper optically thin region to the deep optically thick region. We propose that a self-consistent, more realistic theory of condensation and sedimentation in the atmospheres is the most essential in the future brown dwarf atmosphere models.

These results indicate that the model fitting to observation in a partial wavelength range may lead to wrong model and conclusion, and the model fitting using the broad wavelength range is desired to understand the actual properties of the objects. Thus it is recommended to use the *AKARI* and SpeX/CGS4 spectral data for deriving physical parameters of objects as our fitting analysis.

# Chapter 6

# Metallicity Variation in the Brown Dwarfs

As shown in section 1.4, we have a critical problem of brown dwarf atmospheres in terms of molecular abundances. The unexpectedly strong absorption band of CO in the observed spectra has not been understood yet. Yamamura et al. (2010) found that the $CO_2$ absorption band at 4.2 $\mu$m in three of six *AKARI* brown dwarfs is also stronger than predicted by the models. For this problem Tsuji et al. (2011) proposed that increasing the C and O elemental abundance could solve the problem. Actually, the excess in $CO_2$ absorption band in the spectra of the three brown dwarfs appeared to be reproduced by increasing the C and O abundances by about +0.2 dex. We have assumed the solar elemental abundance (Allende Prieto et al. 2002) in UCM and we believed that this is sufficient in analyzing the low resolution spectra of cool dwarfs. However, the assumption may not be always correct, and C and O abundances may be different in each brown dwarf.

The result by Tsuji et al. (2011) indicates that chemical composition of brown dwarfs may deviate from the solar abundance. In this chapter we calculate the atmosphere models of brown dwarfs with various elemental abundances different from the solar abundance, and investigate their effects in brown dwarf spectra. We present how the brown dwarf atmosphere structure changes and how the spectrum changes by changing elemental abundance in the UCM. Then we especially focus on the $CO_2$ band at 4.2 $\mu$m.

Tsuji et al. (2011) increased the C and O abundances by about 0.2 dex (log $A_C$ = 8.60 and log $A_O$ = 8.92) from the solar values (log $A_C$ = 8.39 and log $A_O$ = 8.69). We change the elemental abundances by approximate $\pm$0.2 dex (0.7 times less and 1.6 times larger than the solar value). The elemental abundances of solar neighborhood star [X/H] distributes between –1.0 and 1.0 dex (Bodaghee et al. 2003). Thus 0.2 dex is a reasonable variation within the common abundance range. We investigate the following cases; (1) changing all elemental abundances, (2) C abundance only, (3) O abundance only, (4) Fe abundance only, (5) C and O, and (6) C and O and Fe. Fe is one of the important elements for dust formation and we consider it in the current analysis. Table 6.1 shows the details of the elemental abundances applied in the analysis. For each case we increase and decrease the abundance. Our total investigation are 6 $\times$ 2 (increase and decrease) = 12 cases. We calculate for typical L dwarf atmosphere model ($T_{\rm cr}$ / log $g$ / $T_{\rm eff}$) = (1800K/5.5/1800K) and typical T dwarf atmosphere model ($T_{\rm cr}$ / log $g$ / $T_{\rm eff}$) = (1900K/4.5/1200K). We show the result of each calculation in section 6.1 – 6.6.

Table 6.1: Abundances of the 34 most abundant elements likely to be present in brown dwarfs. Values are listed by number relative to hydrogen in logarithmic form for +0.2dex and -0.2dex abundances

| Elements | Solar[1] abundances | ×1.6 abundances | ×0.7 abundances |
|---|---|---|---|
| H | 0.0 | 0.0 | 0.0 |
| He | –1.01000 | –0.80588 | –1.16490 |
| Li | –8.69000 | –8.48588 | –8.84490 |
| Be | –10.85000 | –10.64588 | –11.00490 |
| B | –9.40000 | –9.19588 | –9.55490 |
| C | –3.61000 | –3.40588 | –3.76490 |
| N | –4.00000 | –3.79588 | –4.15490 |
| O | –3.31000 | –3.10588 | –3.46490 |
| F | –7.44000 | –7.23588 | –7.59490 |
| Na | –5.67000 | –5.46588 | –5.82490 |
| Mg | –4.42000 | –4.21588 | –4.57490 |
| Al | –5.53000 | –5.32588 | –5.68490 |
| Si | –4.45000 | –4.24588 | –4.60490 |
| P | –6.55000 | –6.34588 | –6.70490 |
| S | –4.79000 | –4.58588 | –4.94490 |
| Cl | –6.50000 | –6.29588 | –6.65490 |
| K | –6.88000 | –6.67588 | –7.03490 |
| Ca | –5.64000 | –5.43588 | –5.79490 |
| Sc | –8.90000 | –8.69588 | –9.05490 |
| Ti | –7.01000 | –6.80588 | –7.16490 |
| V | –8.00000 | –7.79588 | –8.15490 |
| Cr | –6.33000 | –6.12588 | –6.48490 |
| Mn | –6.61000 | –6.40588 | –6.76490 |
| Fe | –4.49000 | –4.28588 | –4.64490 |
| Ni | –5.75000 | –5.54588 | –5.90490 |
| Cu | –7.79000 | –7.58588 | –7.94490 |
| Br | –9.37000 | –9.16588 | –9.52490 |
| Rb | –9.40000 | –9.19588 | –9.55490 |
| Sr | –9.10000 | –8.89588 | –9.25490 |
| Y | –9.76000 | –9.55588 | –9.91490 |
| Zr | –9.40000 | –9.19588 | –9.55490 |
| I | –10.4900 | –10.2859 | –10.6449 |
| Ba | –9.8700 | –9.6659 | –10.0249 |
| La | –10.7800 | –10.5759 | –10.9349 |

[1] Allende Prieto et al. (2002).

# 6.1 Changing All Elemental Abundances

## 6.1.1 Case of Increasing the Abundances

Firstly, we show the result for case of changing all elemental abundances. We show the comparison of the difference of chemical structure, temperature, and spectra for the case of increasing of all elemental abundances in Figure 6.1 for L dwarf model. The absorption bands in 2.4–3.8 $\mu$m and 4.2 $\mu$m become deeper by 20 and 10 %, respectively. At $J$ and $H$ band, the masking effect by dust overcomes more emission from dust-warmed-up atmosphere, and the $J$ and $H$ band fluxes drop down by 10–20 %. The surface gas temperature also decreases about 20 K because of this masking effects.

For the T dwarf model almost all molecular abundances increase almost proportionally to the increased elemental abundances, and the temperature above the dust layer ($\log P_g \leq 7$) also rises by about 50 K (Figure 6.2). The absorption band of CO and $CO_2$ becomes deeper. Especially the change of $CO_2$ band at 4.2 $\mu$m is significant, up to 20 %. The $CH_4$ abundance in deep layer decreases by $\sim 0.1$ dex, according to increased temperature. The dust effect on $J$ and $H$ band is the same for the case of L dwarf.

## 6.1.2 Case of Decrease the Abundances

The results are shown in Figures 6.3 and 6.4. The change of spectra are generally opposite to the case of increasing all elemental abundances, but the change of temperature structure more depends on $T_{\rm eff}$. For the L dwarf model, temperature of inner region ($\log P_g \geq 6$) dominated by $H_2O$ molecules decreases by 20–30 K because of decreasing $H_2O$ by $\sim 0.1$ dex. Consequently the $CH_4$ abundance in the region increases by $\sim 0.1$ dex. The surface temperature becomes higher by about 20 K because of weaker dust extinction. The $J$ band flux increases by 15 %. Since CO and $CH_4$ decreases in the surface area by about 0.1 and 0.5 dex respectively, the absorption of the both CO at 4.6 $\mu$m and $CH_4$ at 3.3 $\mu$m become weaker, despite that CO absorption band at 2.3 $\mu$m does not change. The change of the both CO and $CH_4$ bands are up to $\sim 10$ %.

The result for a T dwarf model is almost the same to the L dwarf model, for example the CO absorption band at 4.6 $\mu$m becomes weaker by 5 %. However the change of $CH_4$ band is less than that in the spectra of L dwarf model because of the saturation of the band. On the other hand, the depth of $CO_2$ absorption band at 4.2 $\mu$m decreases ($\sim 15$ %) significantly as compared to the L dwarf model. The temperature drops down due to decreasing $H_2O$ and Fe. The $J$ and $H$ band flux also increases, because of smaller dust extinction.

# 6.2 Changing Carbon Abundance

## 6.2.1 Case of Increase the Abundances

The results are shown in Figures 6.5 and 6.6. In the case of increasing C abundance only, almost O atoms are captured in CO molecule. Thus the abundance of $H_2O$ deep inside ($\log P_g \sim 7$) region of the photosphere decreases by 0.5 dex and the temperature in the region also becomes lower by about 40

K. Consequently the abundance of $CH_4$ increases by 1.0 dex. The amount of dust increases and $J$, $H$ and $K$ band fluxes are depressed by 20 %. Since temperature and molecular abundances rely on each other, it is an indisputable fact that the increasing in the surface temperature (rising up $\sim$ 50 K) correlate with the increasing of $CH_4$ and CO molecules by 0.5 and 0.2 dex, respectively. We see that the $H_2O$ and $CO_2$ absorption become shallower by 80 % and 20 %, respectively, because of the decreasing their abundances. The increase of CO abundance appears in the 2.3 $\mu$m band, but not in the 4.6 $\mu$m band.

For T dwarf model decreasing rate of $H_2O$ and increasing rate of $CH_4$ are less than the L dwarf model. As a result the entire temperature rises only a little by 10 K in the surface area. The $CH_4$ absorption band at 3.3 $\mu$m becomes deeper by 5–25 % because the band is sensitive to the change of $CH_4$ abundance in the T dwarf model. The $CH_4$ abundance increase about 0.2 dex due to rather the increasing C abundance than increasing surface temperature in the T dwarf. The CO absorption band at 4.6 $\mu$m also becomes stronger by 5 %. The $J$, $H$ and $K$ band flux does not change because of little change of the photospheric temperature and $H_2O$ abundance.

### 6.2.2 Case of Decrease the Abundances

The results are shown in Figures 6.7 and 6.8. The trend of the result for the decreasing C is generally opposite to the case of the increasing C abundance, though change of photosphere temperature does not depend on $T_{\rm eff}$ unlike the case of increasing C. When carbon abundance decreases, the both CO and $CH_4$ decrease by about 0.1 dex, but $CO_2$ stays almost the same abundance. $H_2O$ increases about 0.1 dex and temperature in deep inside also increases about 15 K. This makes the flux in $J$ and $H$ band increase by $\sim$ 10 %.

On the other hand, the abundance of $CO_2$ in the T dwarf model decreases by about 0.3 dex unlike the case of L dwarf. However the spectral feature at 4.2 $\mu$m $CO_2$ absorption band does not change noticeably. This is because that the variation of the $CO_2$ abundance is too little to change the spectral feature. $H_2O$ abundance increases only in the deep region. Additionally the effect of about 0.3 dex decreasing $CH_4$ in whole region appears in 3.0 – 4.0 $\mu$m in the model spectra as about 5–10 % weaker absorption.

## 6.3 Changing the Oxygen Abundance

### 6.3.1 Case of Increase the Abundances

The results are shown in Figures 6.9 and 6.10. The behavior of increasing O abundance is almost similar to the case of decreasing C only. Thus we understand that C and O play a dominant and compensating role. When the O abundance increases, the resultant temperature structure is different for different $T_{\rm eff}$. Thus the change of spectra also depend on $T_{\rm eff}$. For the L dwarf model, $H_2O$ and $CO_2$ abundances increase by about 0.5 dex and inner temperature rises by 40 K. Thus the abundance of CO increases about 0.2 dex and $CH_4$ decreases about 0.7 dex. Near the surface region the temperature is depressed by about 50 K with decreasing $H_2O$ abundance. Effect of the increase of $H_2O$ and $CO_2$ appears in the model spectra as deeper absorption bands. With rising inner temperature the fluxes in $J$, $H$ and $K$ band increase

by 3–25 %.

These effects by increasing O abundance are almost same for the T dwarf model. The $CH_4$ band at 3.3 $\mu$m becomes about 30 % weaker than that of the model with solar abundance. The *K* band becomes bright by $\sim$ 10 % because of rising temperature by about 50 K.

### 6.3.2 Case of Decrease the Abundances

The results are shown in Figures 6.11 and 6.12. The results of decreasing O are generally opposite to the case of increasing O abundance. The $H_2O$ and $CO_2$ are reduced. As a result the photospheric temperature at $\log P_g \geq 6$ drops down by about 50 K and $CH_4$ increases $\sim$ 0.8 dex.

The results for the case of T dwarf are shown in Figure 6.12. Similarly, temperature in the photosphere drops down by 10–70 K due to the 0.5 dex decrease of $H_2O$ abundance. The *K* band flux decreases by $\sim$ 10 % with decreasing temperature.

## 6.4 Changing Fe Abundance

### 6.4.1 Case of Increase the Abundances

The results are shown in Figures 6.13 and 6.14. For the L dwarf model, the temperature rises about 50 K above the dust layer ($\log P_g \leq 7$) by increasing Fe abundance by 0.2 dex, i.e. the amount of dust increases. Because of this the abundance of $CH_4$ decreases. The flux at *J* and *H* band decreases 3–10 % by the effect of dust extinction. The flux at *K* and *L* band increase about 2 % due to the rising the inner temperature.

On the other hand, the change of temperature for T dwarf model is the same with increasing C and O only, and the spectral feature is also identical. This result indicates that the abundance of Fe, which is one of the important elements for dust formation, does not contribute to the photospheric temperature and spectra. This is consistent with the fact that the dust in the photosphere of T dwarf exist in deep inside and not appear in the spectra.

### 6.4.2 Case of Decrease the Abundances

The results are shown in Figures 6.15 and 6.16. The case of decreasing Fe shows opposite trend with the case of increasing Fe. Temperature drop down throughout the whole photosphere in L dwarf model. As a result abundance of $CH_4$ increase by $\sim$ 0.1 dex and its absorption band become deeper by about 2 %. The flux at *J* and *H* band increases by 2–10 % due to dust extinction. For T dwarf model, we do not see any noticeable differences of chemical structure, temperature, and spectra.

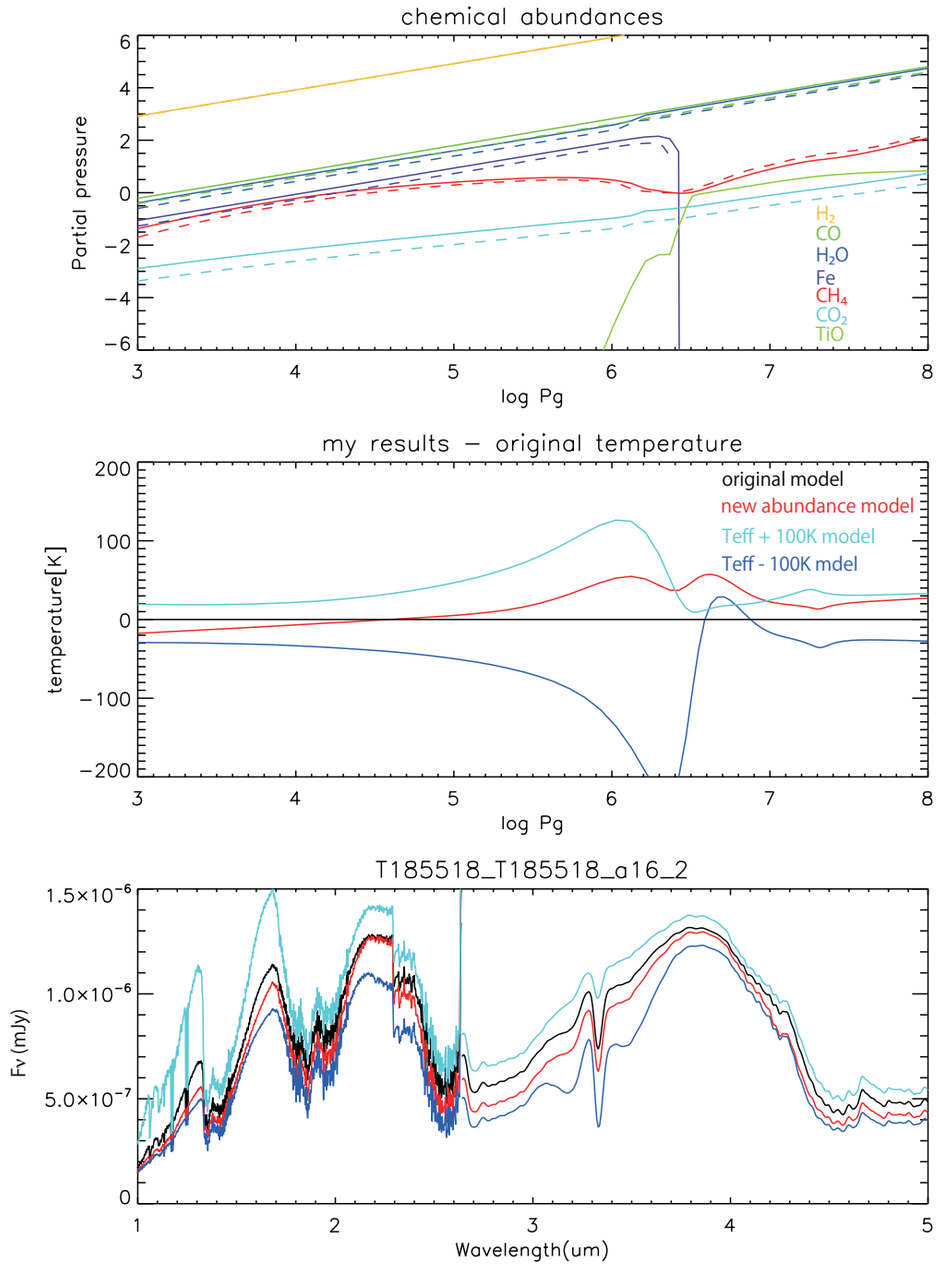


Figure 6.1: Comparison of chemical structure, difference of temperature and spectral for the case of increasing all elemental abundances at ($T_{\rm cr}$/log $g$/$T_{\rm eff}$) = (1800K/5.5/1800K) which represent the typical L dwarf. (a) total pressure log $P_g$ versus partial pressures of $H_2$, CO, $H_2O$, Fe(atom), $CH_4$, $CO_2$ and TiO molecules. The partial pressure for solar abundance model are drawn with dashed lines, and that for the increased abundance model are drawn with solid lines. (b) The difference of temperature from that of the solar abundance model drawn in black at zero. That for the increased abundance models are shown in red line. The light blue and blue lines show the models with $T_{\rm eff}$ + 100 K and $T_{\rm eff}$ - 100 K respectively with the solar abundance for comparison. (c) The spectra of the models are shown. Colors are the same as shown in (b).

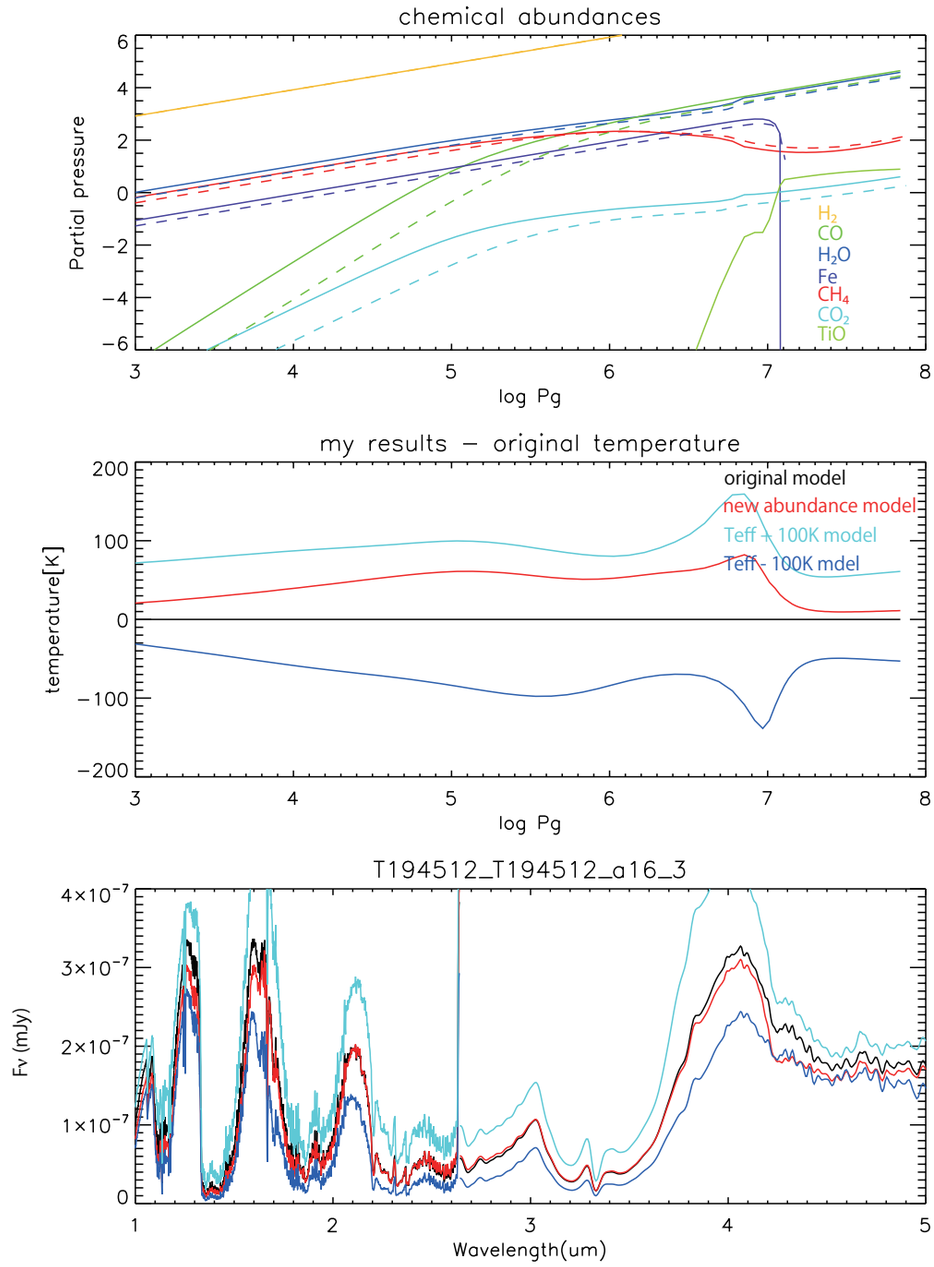


Figure 6.2: Same as Figure 6.1 but the case of increasing all elemental abundances at ($T_{\rm cr}$/log $g$/$T_{\rm eff}$) = (1900K/4.5/1200K) which represent the typical T dwarf.

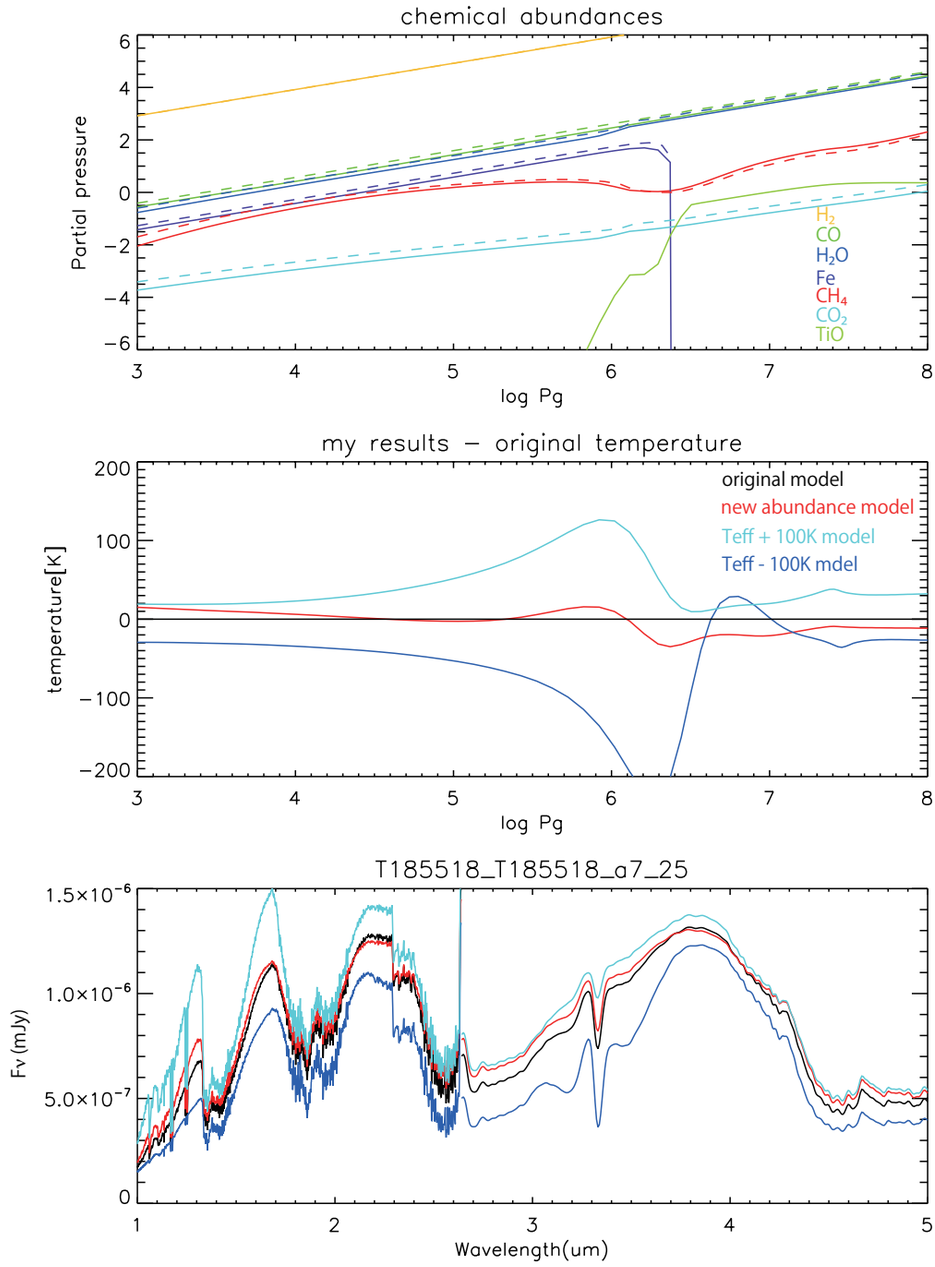


Figure 6.3: Same as Figure 6.1 but the case of decreased abundances.

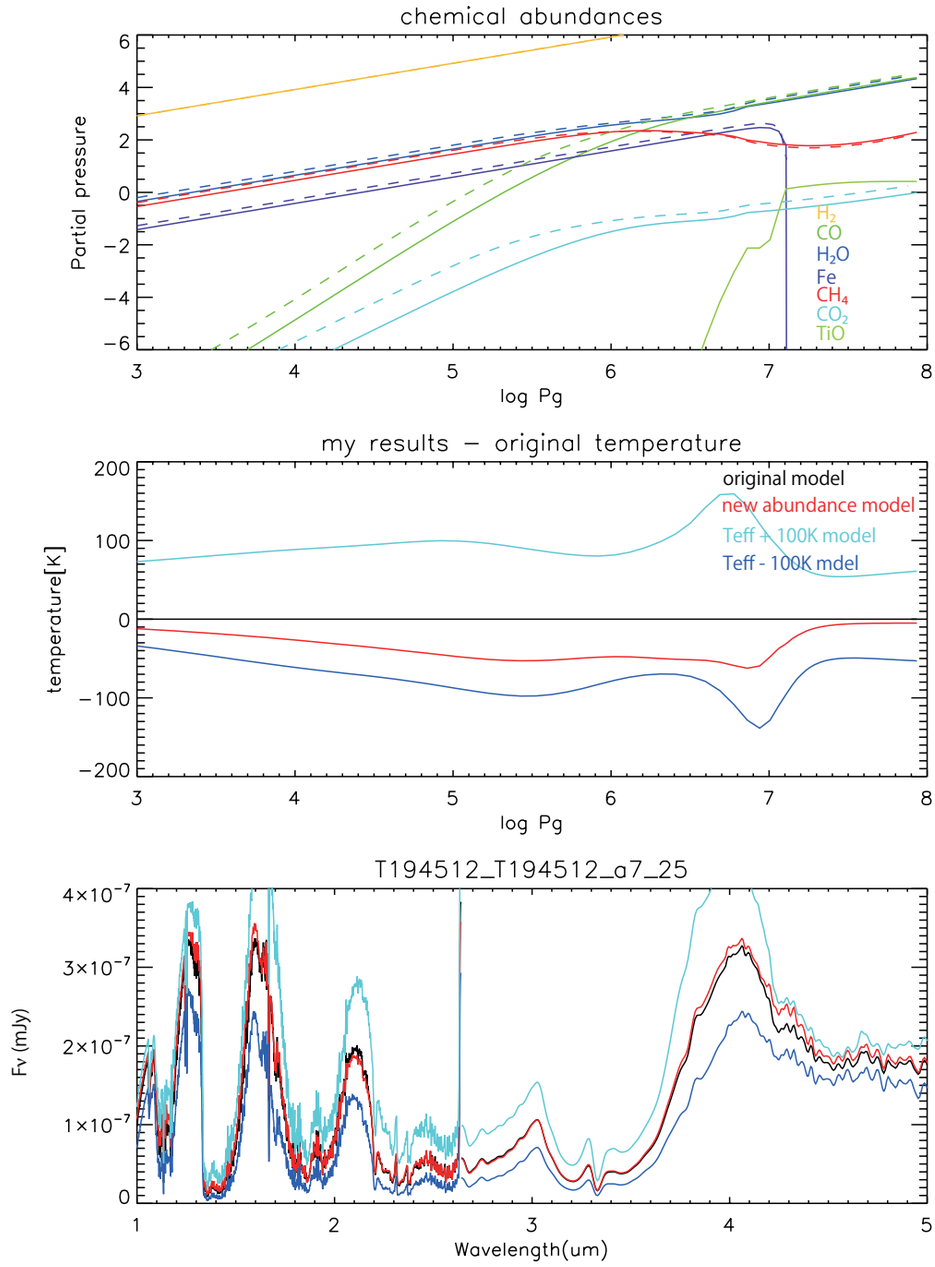


Figure 6.4: Same as Figure 6.2 but the case of decreased abundances.

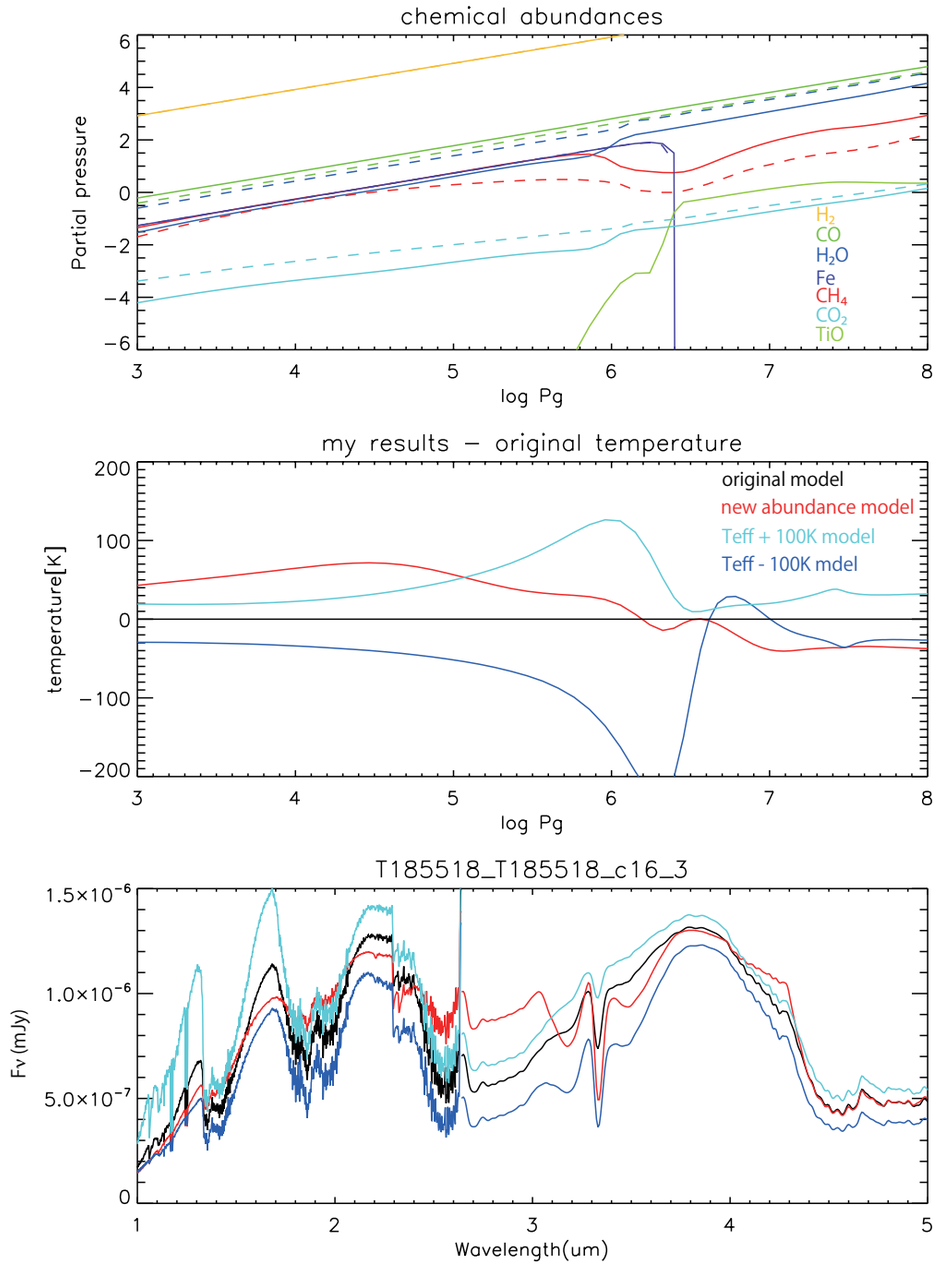


Figure 6.5: Same as Figure 6.1 but the case of increasing C abundance only.

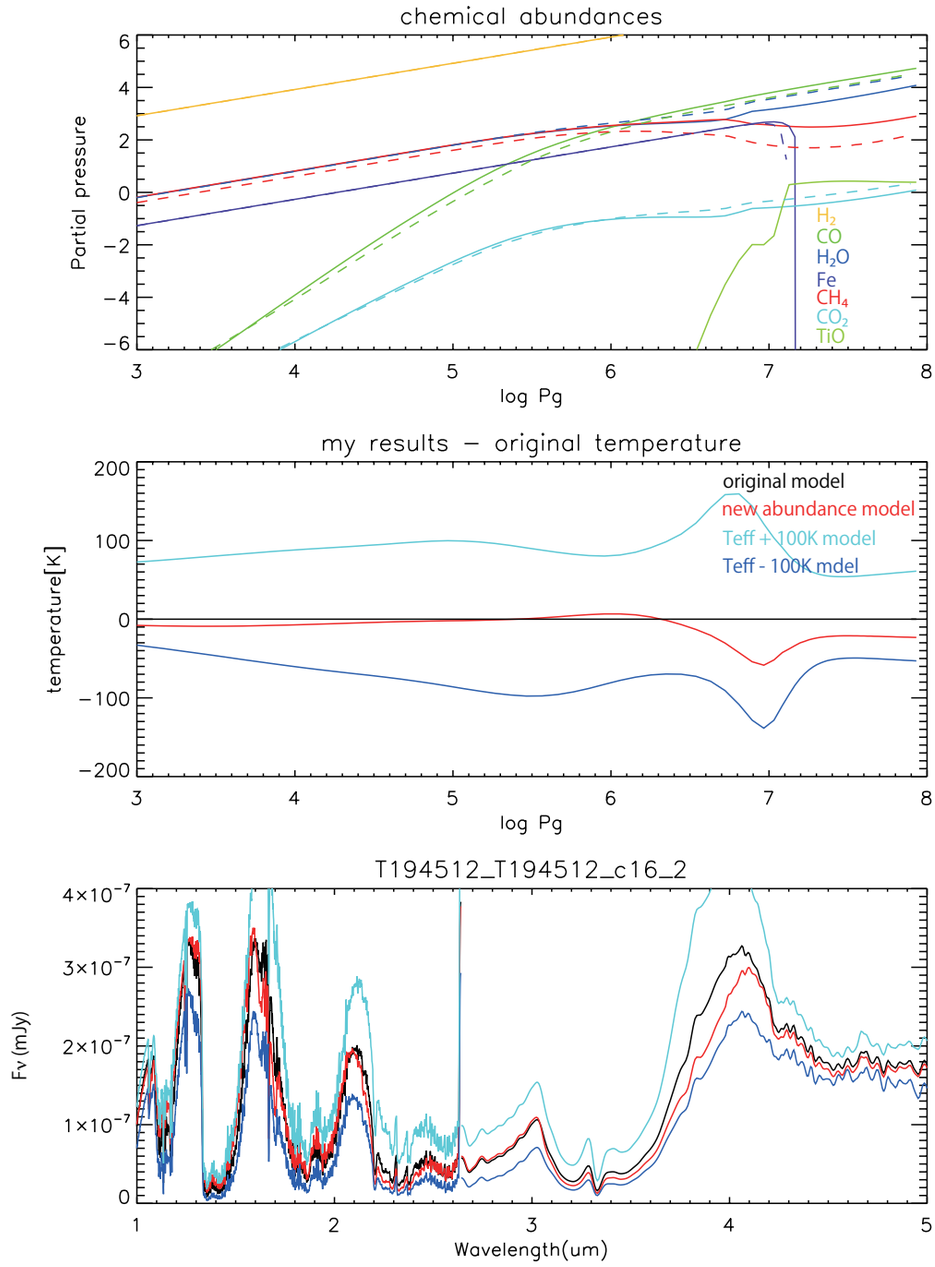


Figure 6.6: Same as Figure 6.2 but the case of increasing C abundance only.

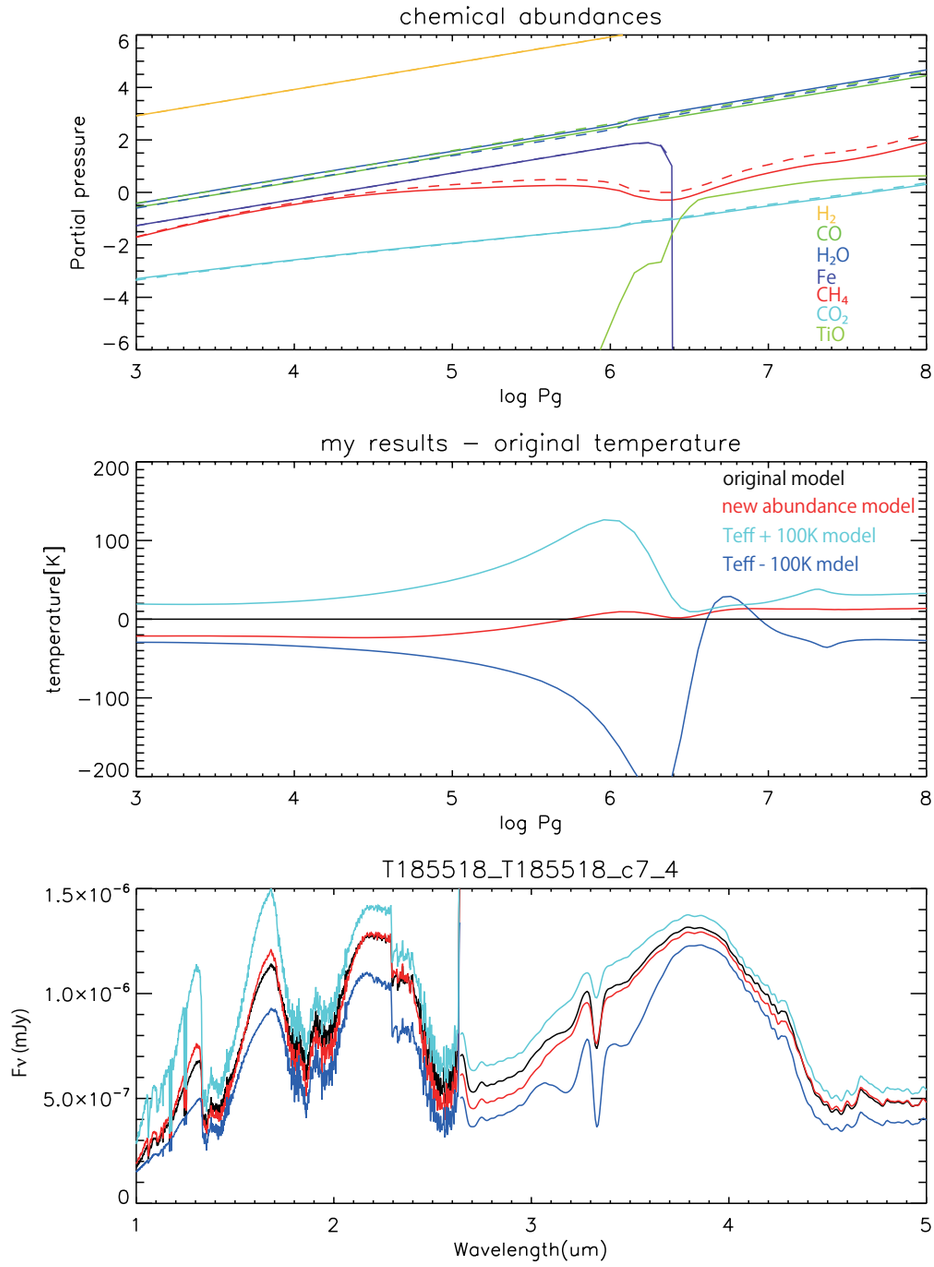


Figure 6.7: Same as Figure 6.3 but the case of decreasing C abundance only.

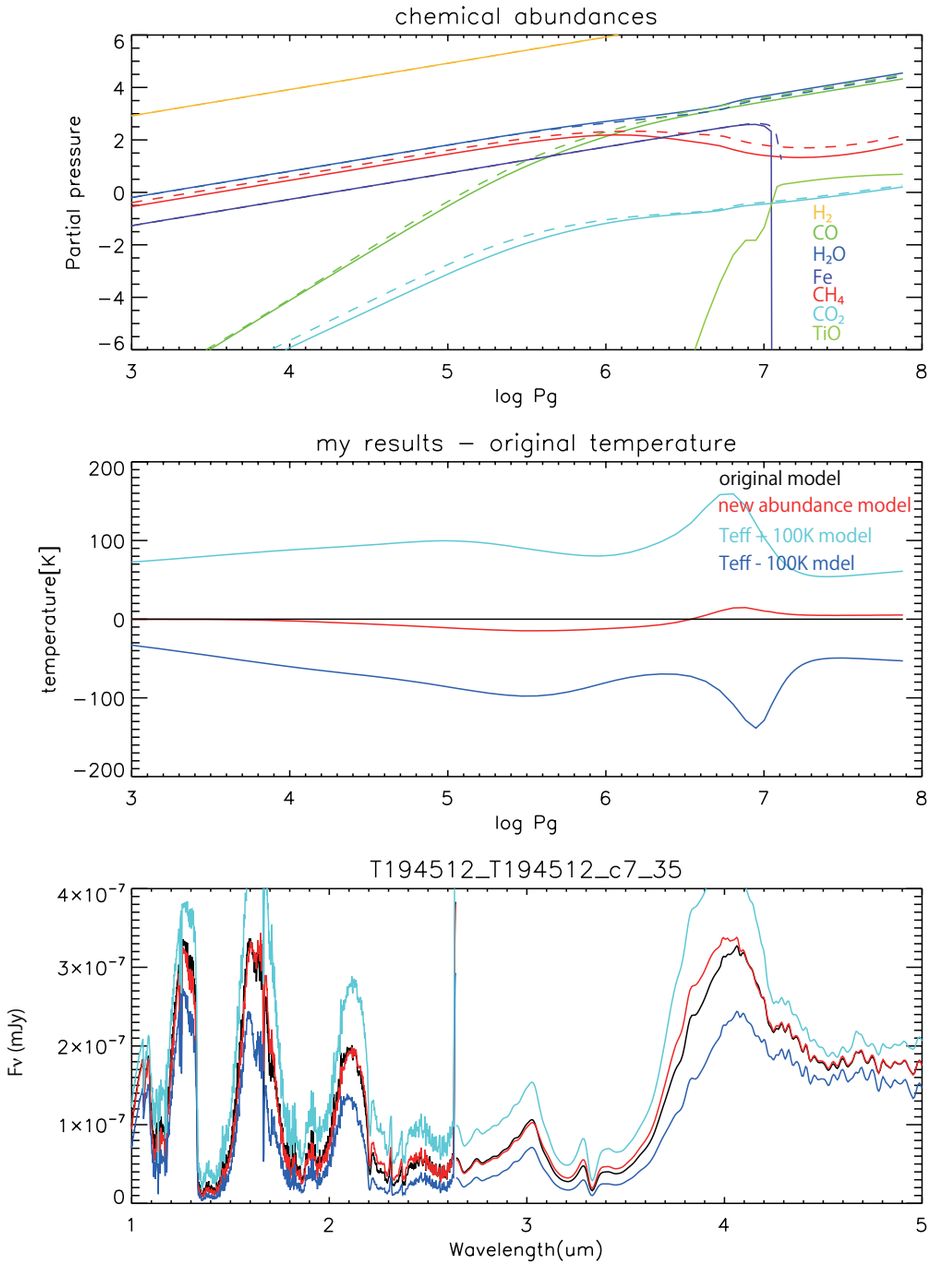


Figure 6.8: Same as Figure 6.4 but the case of decreasing C abundance only.

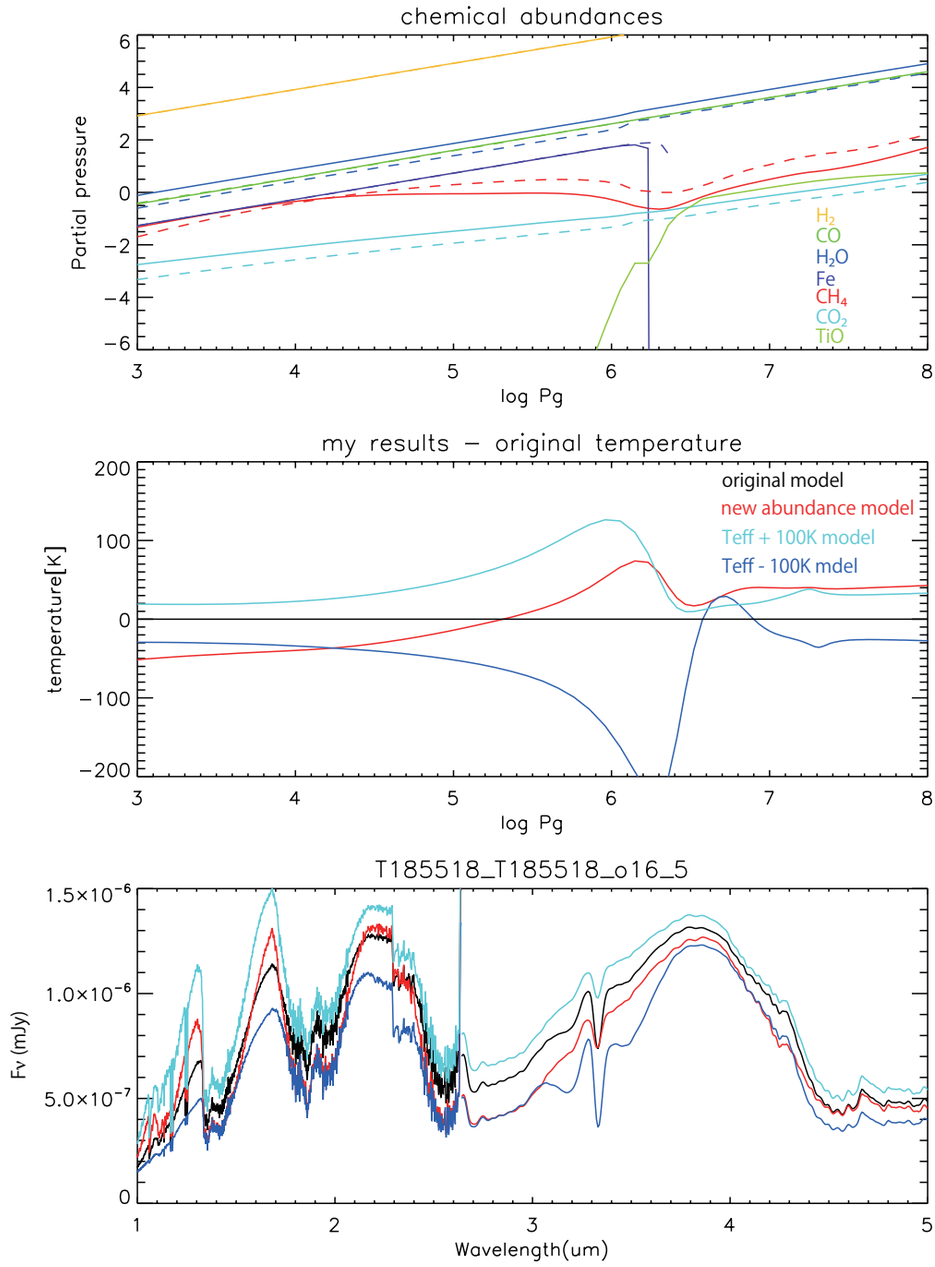


Figure 6.9: Same as Figure 6.1 but the case of increasing O abundance only.

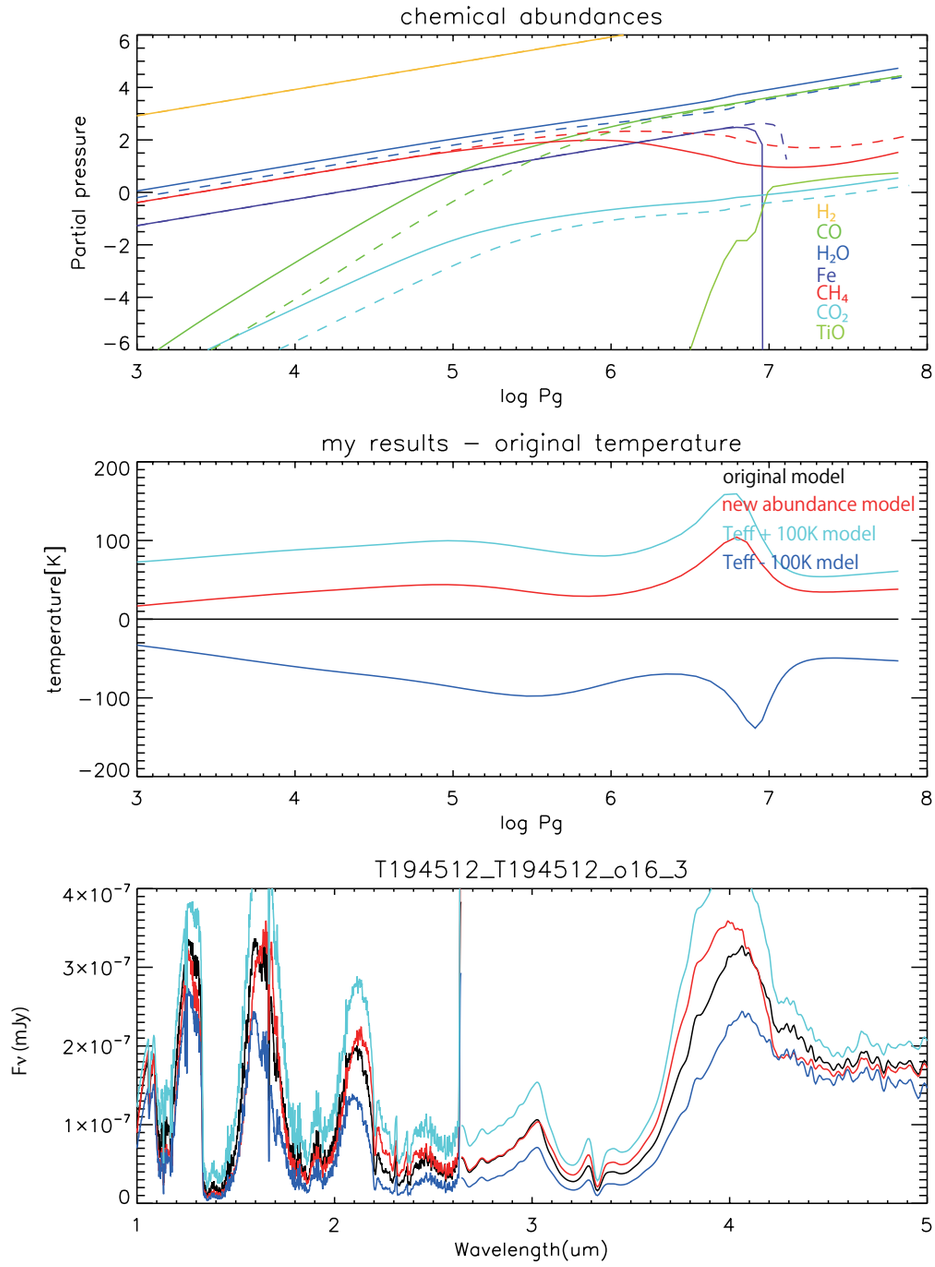


Figure 6.10: Same as Figure 6.2 but the case of increasing O abundance only.

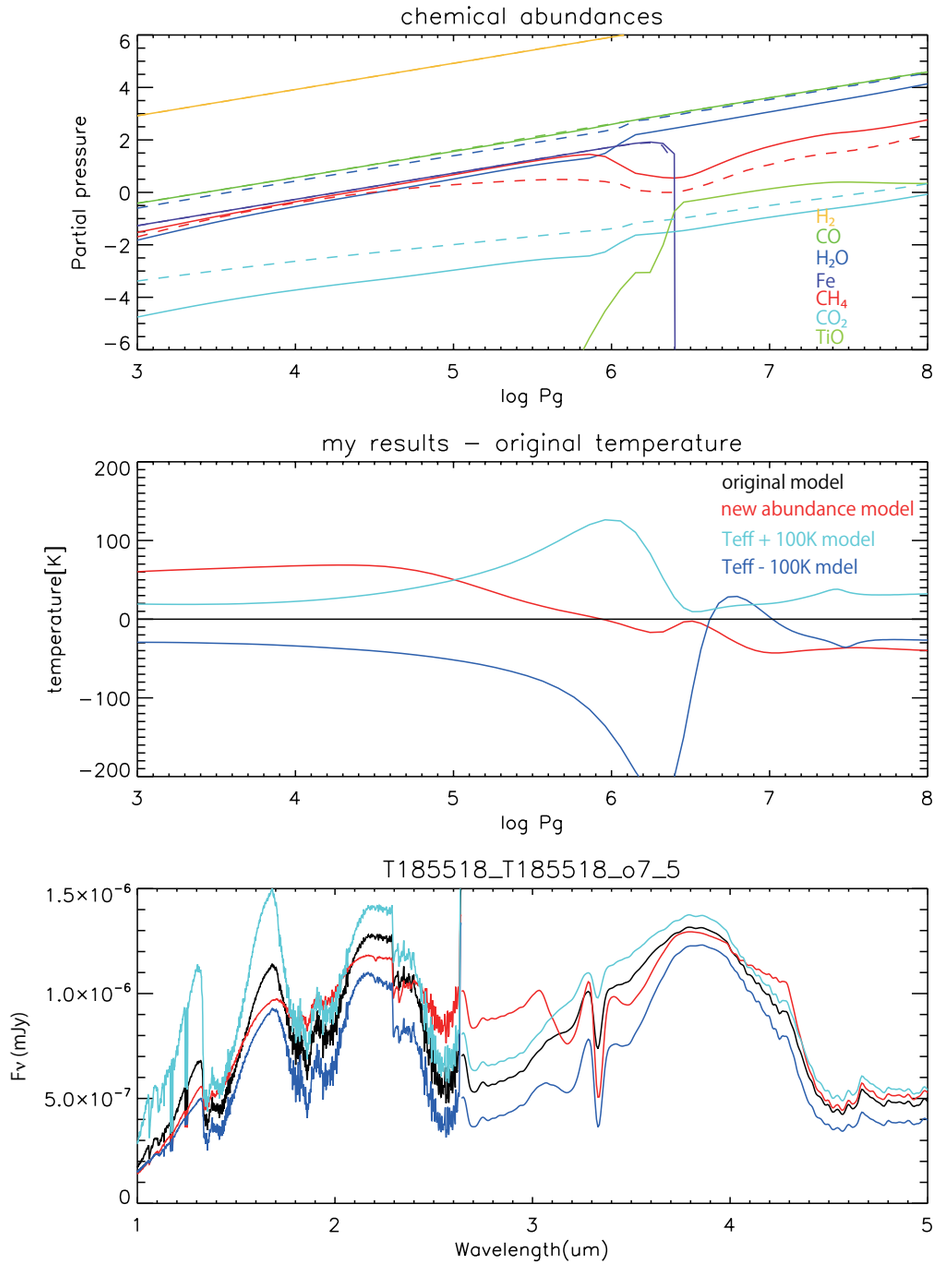


Figure 6.11: Same as Figure 6.3 but the case of decreased O abundance only.

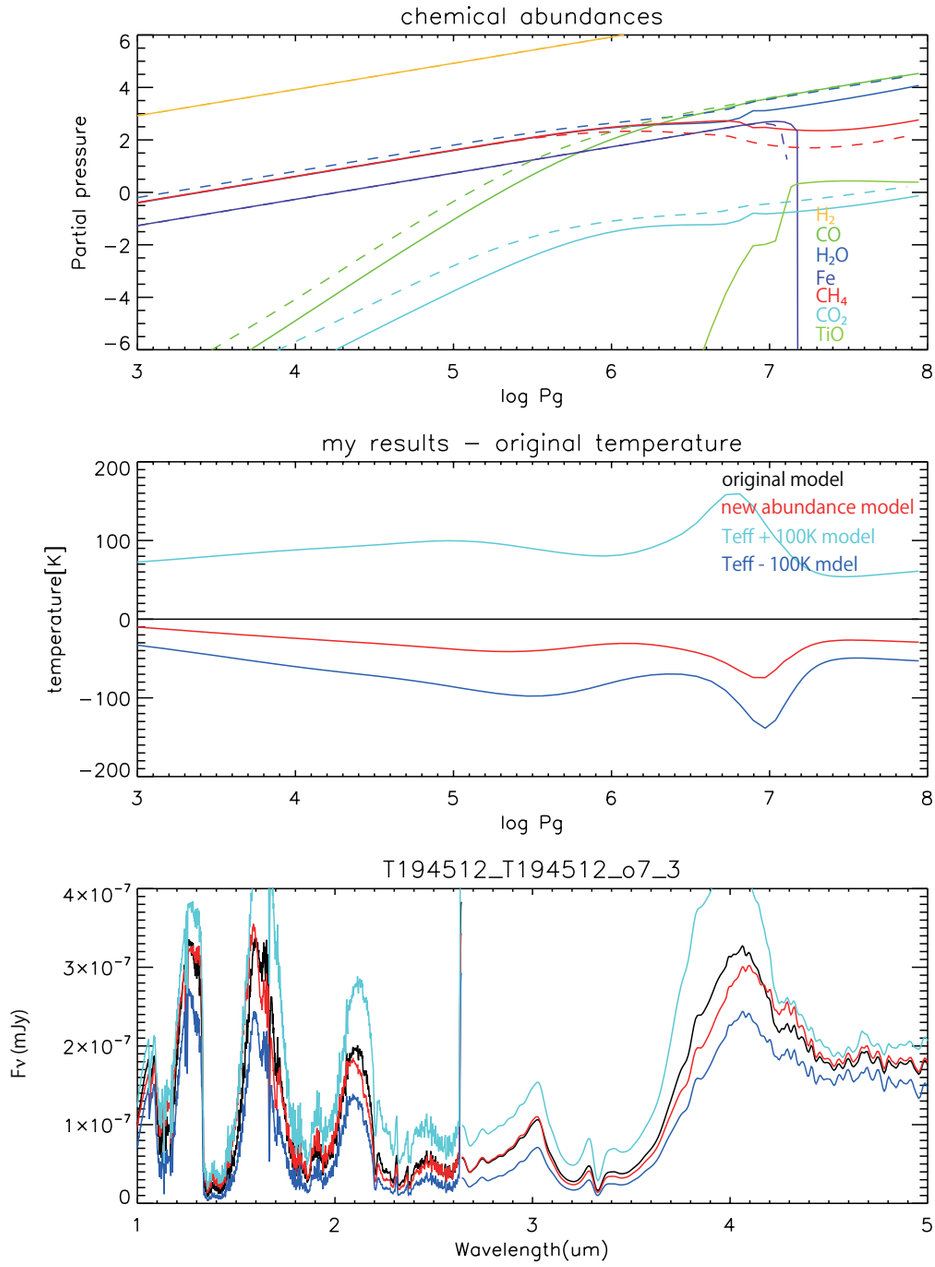


Figure 6.12: Same as Figure 6.4 but the case of decreased O abundance only.

## 6.5 Changing C and O Abundances

### 6.5.1 Case of Increase the Abundances

The results are shown in Figures 6.17 and 6.18. The variation of spectral feature is smaller than that of the model with increasing abundance of O only. We can understand this as compensating effects between the increasing C only and increasing O only. For L dwarf model, abundances of $H_2O$, CO and $CO_2$ increase by 0.5, 0.3 and 0.8 dex, respectively, in the current case. This makes temperature in the inner photosphere higher by about 20–30 K. Accordingly *K* band flux increases. The $CO_2$ abundance increase in all photosphere, then $CO_2$ absorption band becomes deeper by about 15 %. This result is consistent with Tsuji et al. (2011). The abundance of $CH_4$ decrease 0.1 dex in the inner region of photosphere, but increase 0.5 dex near the surface due to lower temperature. The $H_2O$ abundance increases in the inner region. As a result, the flux between 2.4 and 3.8 $\mu$m comes down by about 10–40 %. The flux in *J* and *H* band goes up 15–20 % because of rising temperature and decreasing dust extinction.

For T dwarf model, the chemical structure and temperature change larger than that of L dwarf model. While effect of the increasing chemical abundances does not reflect to the spectral feature, excepting for the $CO_2$ absorption band at 4.2 $\mu$m, the entire flux increases because of the rising the photosphere temperature. This result indicates that the changing of the elemental abundances in L dwarf model is contribute to the spectral feature more than that in T dwarfs, except for the $CO_2$ absorption band.

### 6.5.2 Case of Decrease the Abundances

The results are shown in Figures 6.19 and 6.20. This case is in general opposite to the increasing case. Abundances of CO, $H_2O$ and $CO_2$ decrease 0.1, 0.5 and 0.5 dex, respectively. Thus the inner temperature of photosphere drops down by 20 K and $CH_4$ abundance increases by 0.2 dex. Due to the lower inner temperature, the flux value in *J*, *H* and *K* band drop down by 5–10 %. The temperature of the photosphere of the T dwarf decreases by about 10–60 K, but the spectral feature do not change much.

## 6.6 Changing C, O and Fe Abundances

### 6.6.1 Case of Increase the Abundances

The results are shown in Figures 6.21 and 6.22. In this case abundances of $H_2O$, Fe, CO and $CO_2$ increase by about 0.2, 0.2, 0.2, and 0.5 dex, respectively. Due to the increasing abundance of Fe, dust formation is enhanced and temperature around the dust layer ($\log P_g \leq 6.5$) rises by about 100 K. The flux in *J* and *H* band change little because of the interaction between the large dust extinction and the rising temperature. The *K* band flux goes up $\sim$ 10 % by the increasing temperature. On the other hand, the change of temperature for T dwarf model is the same, up to $\sim$ 70 K, with increasing Fe only.

### 6.6.2 Case of Decrease the Abundances

The results are shown in Figures 6.23 and 6.24. The temperature structure changes inversely with the case of increasing C, O and Fe. The inner photospheric temperature drops down $\sim 30$ K by less abundant $H_2O$. For model of T dwarf the *K* band flux decreases by about 10 %. The absorption bands of CO and $CO_2$ become weaker by about 5 and 10 %, respectively.

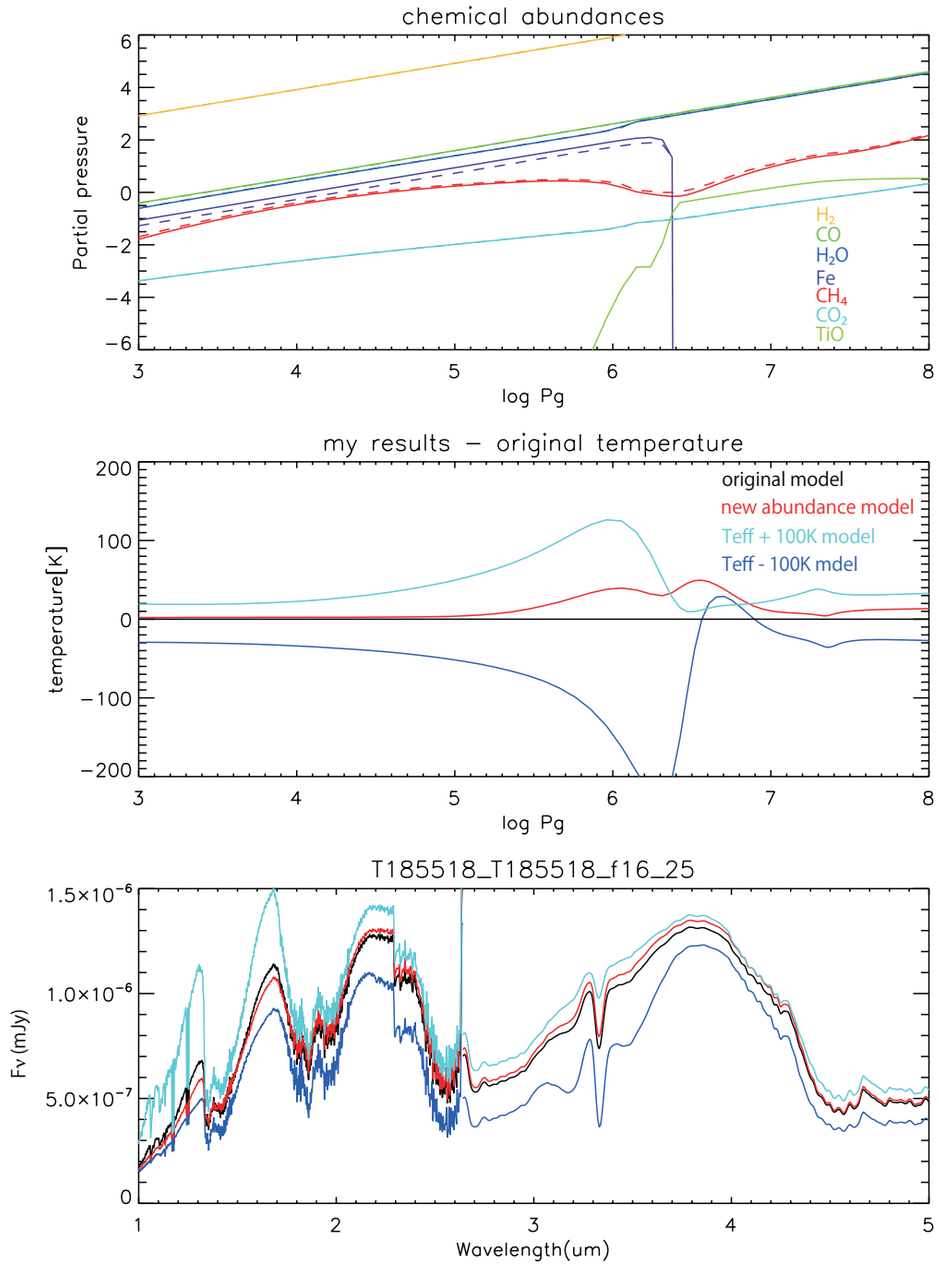


Figure 6.13: Same as Figure 6.1 but the case for increased Fe abundance only.

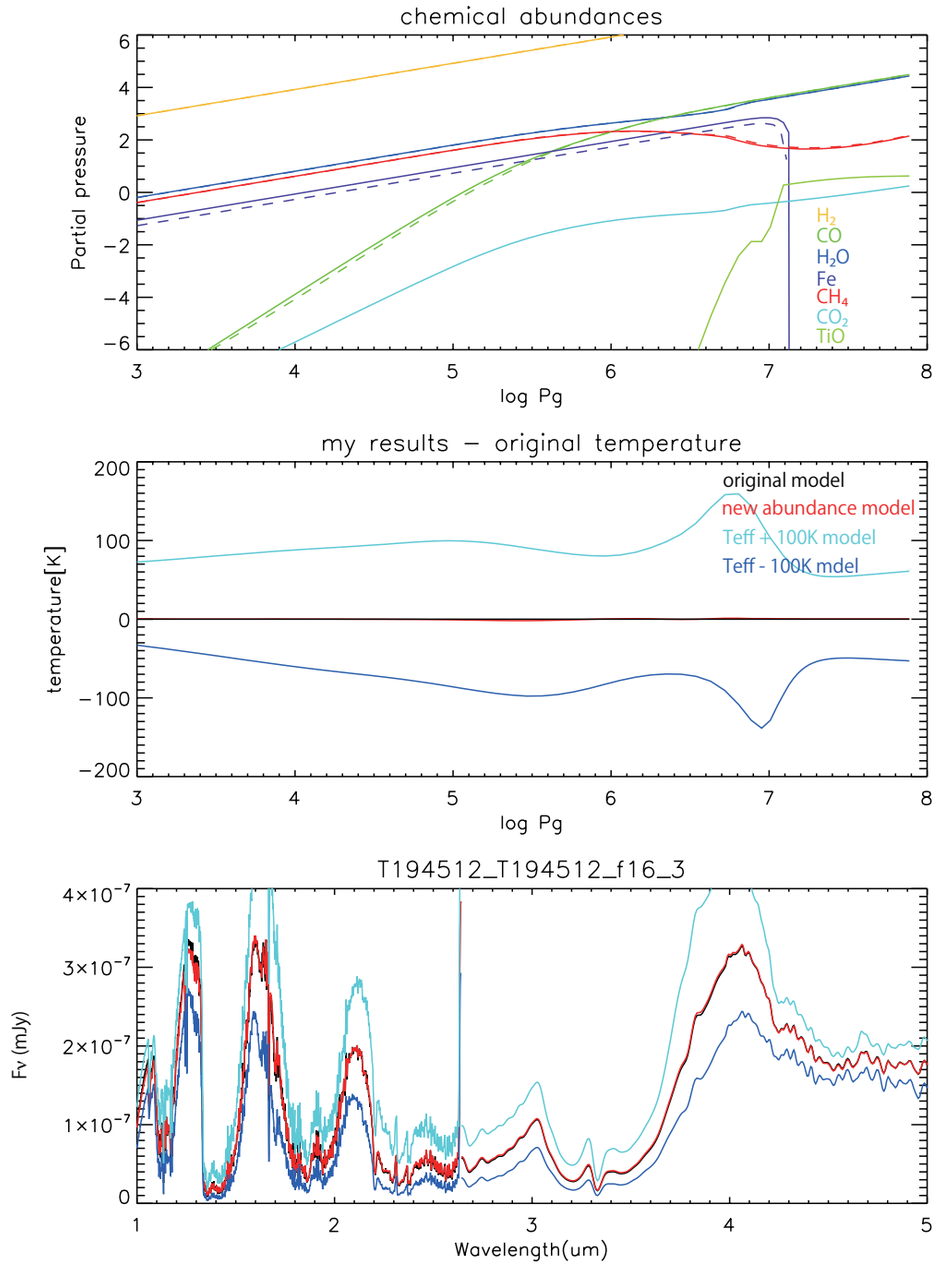


Figure 6.14: Same as Figure 6.2 but the case for increased Fe abundance only.

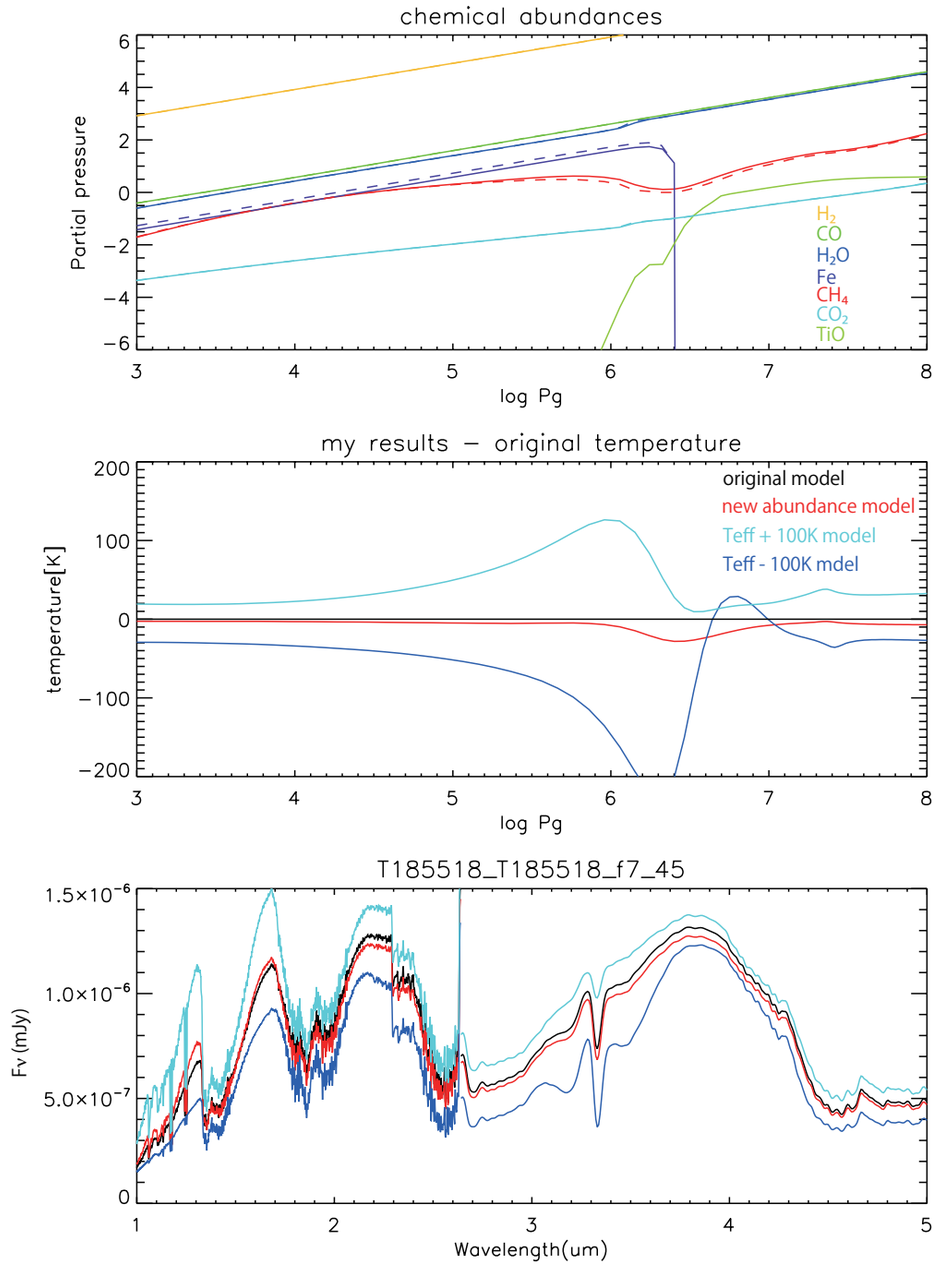


Figure 6.15: Same as Figure 6.3 but the case for decreased Fe abundance only.

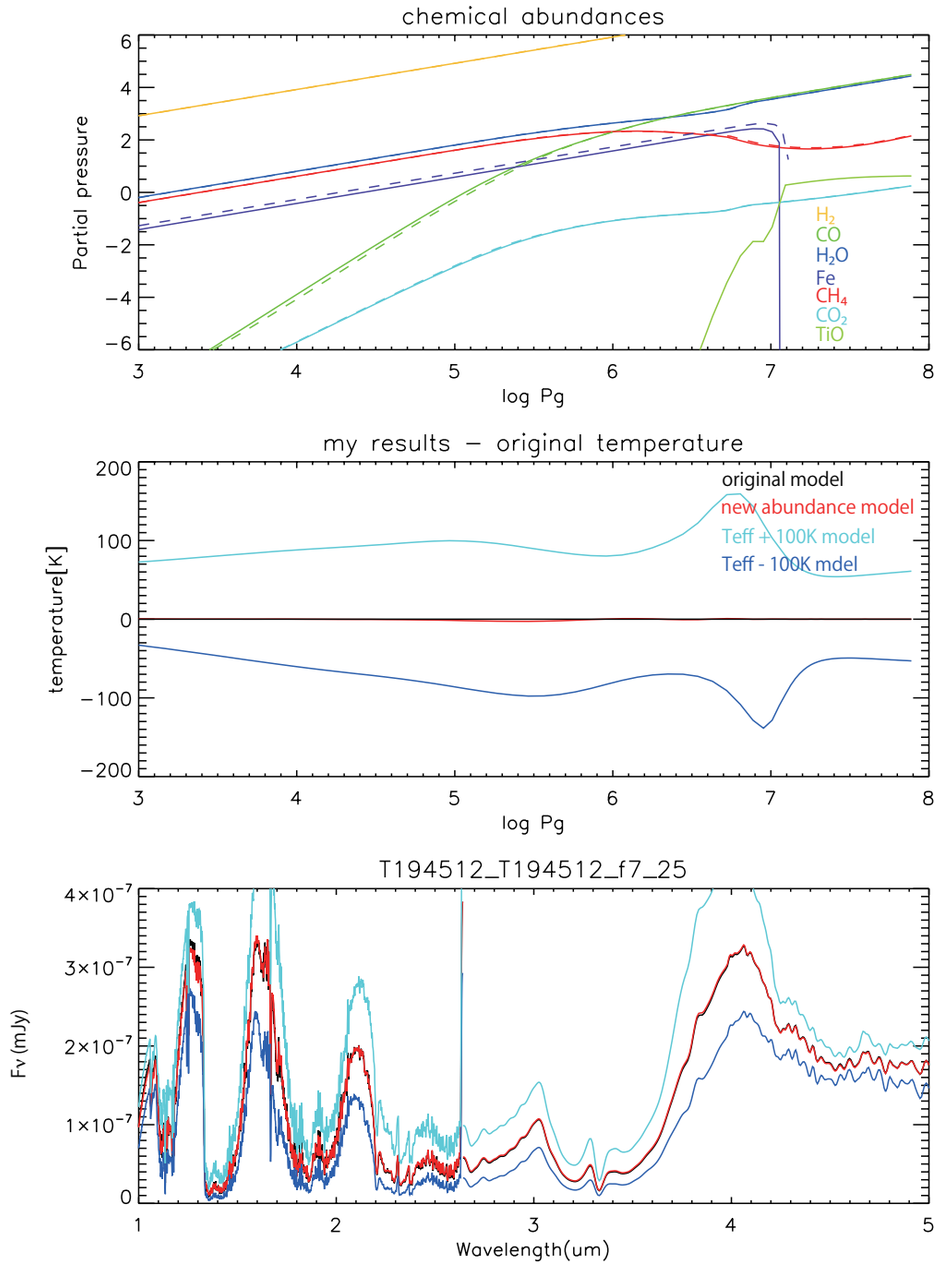


Figure 6.16: Same as Figure 6.4 but the case for decreased Fe abundance only.

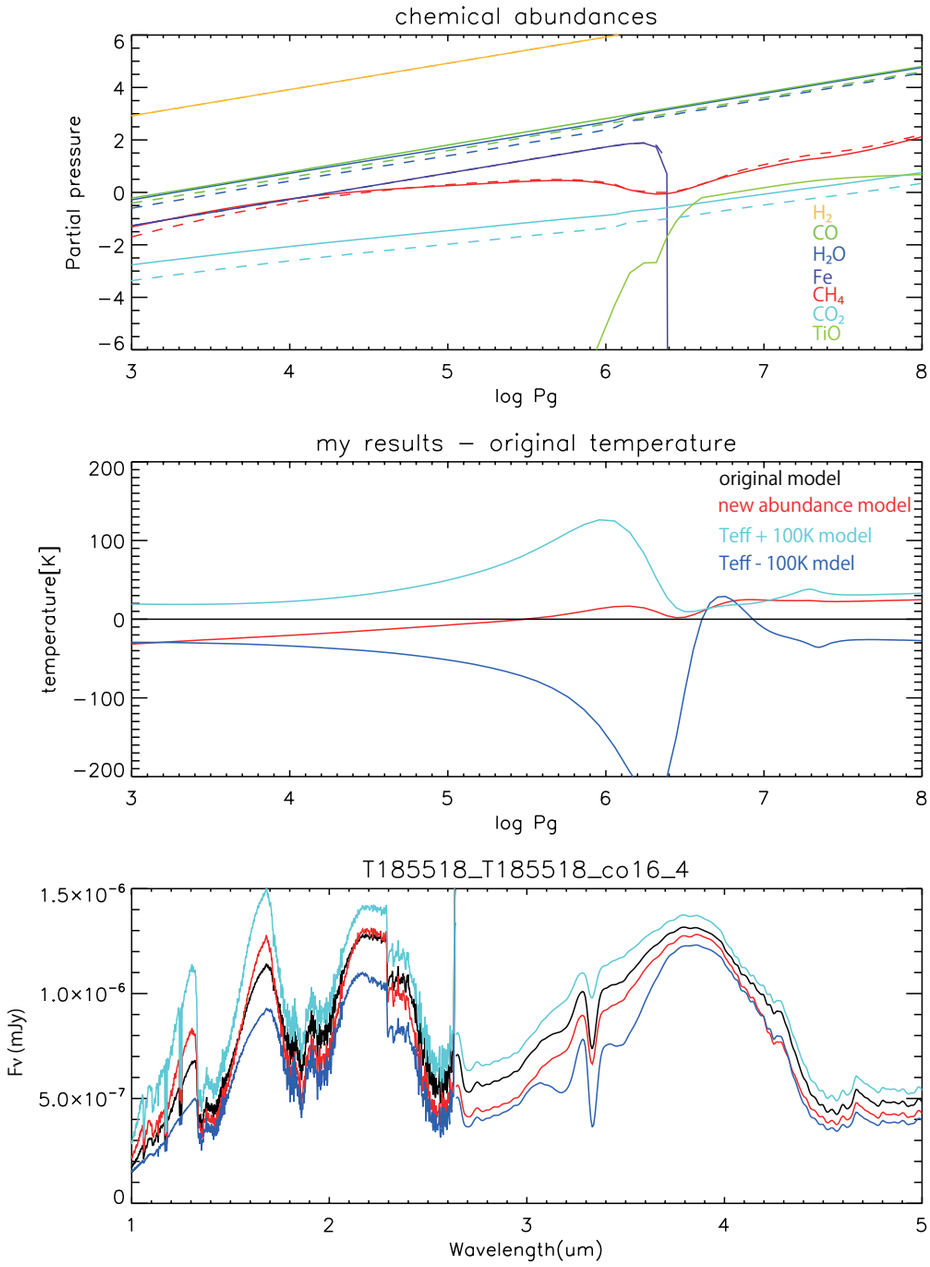


Figure 6.17: Same as Figure 6.1 but the case for increased C and O abundance.

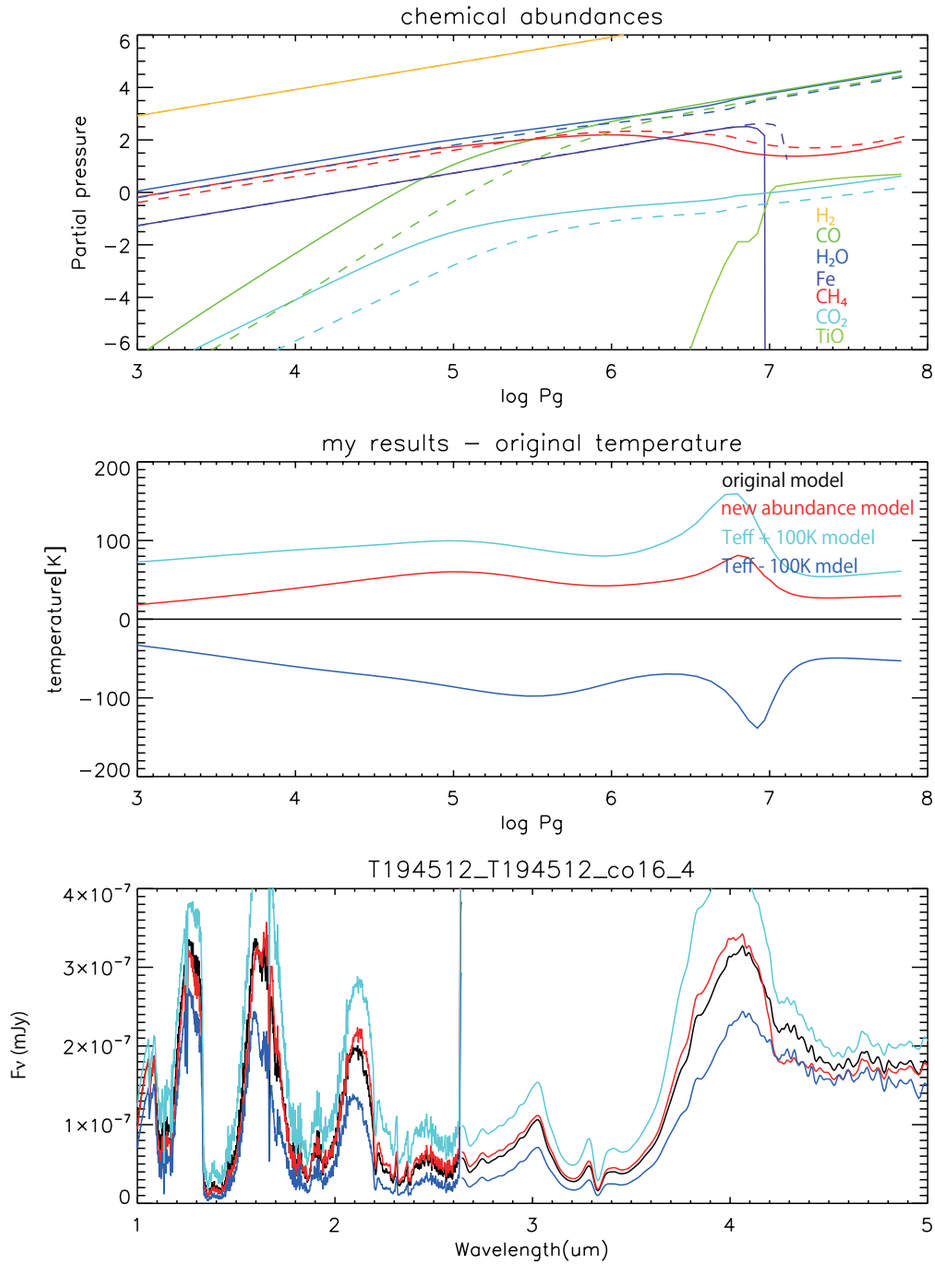


Figure 6.18: Same as Figure 6.2 but the case for increased C and O abundance.

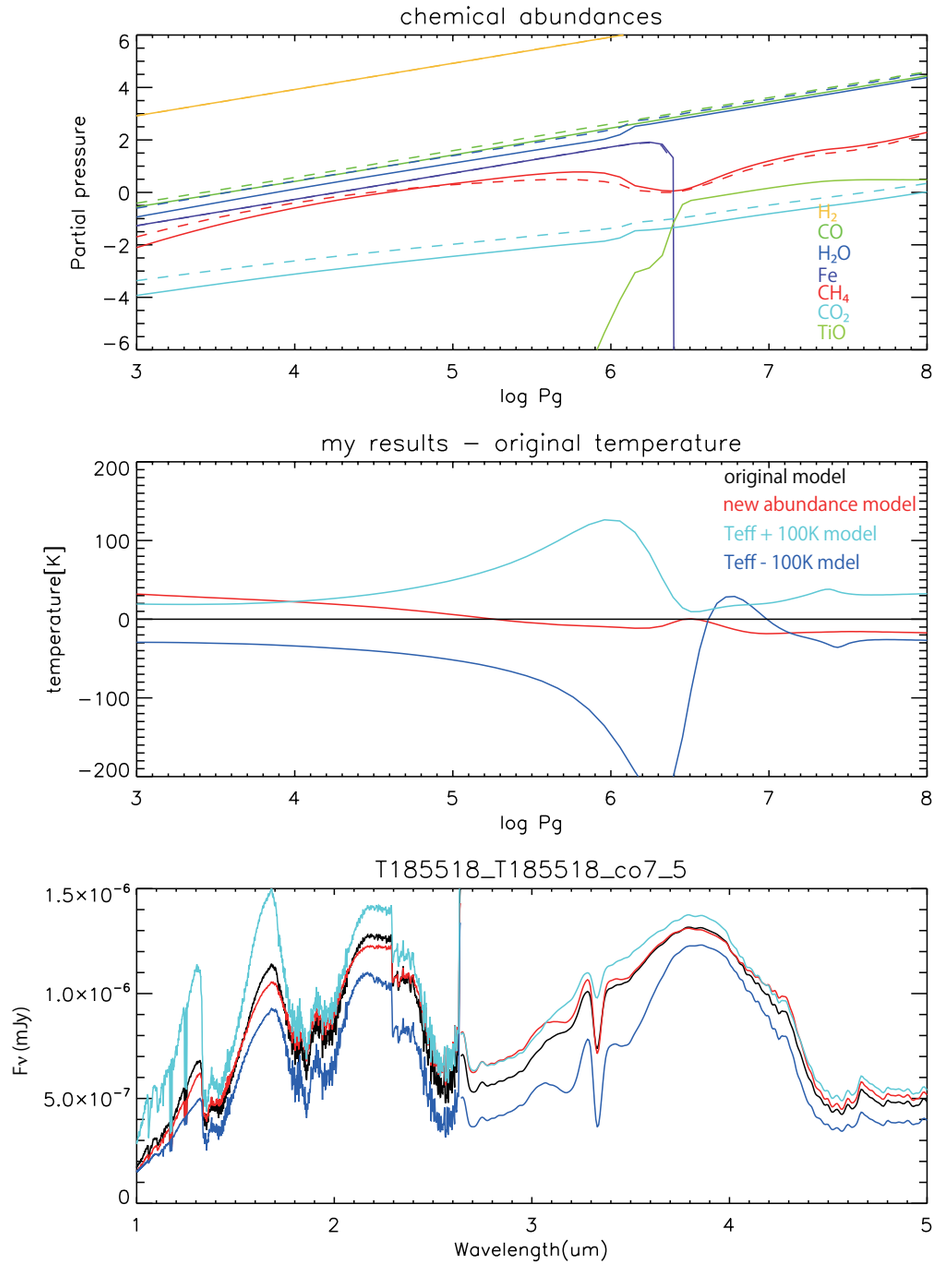


Figure 6.19: Same as Figure 6.3 but the case for decreased C and O abundance.

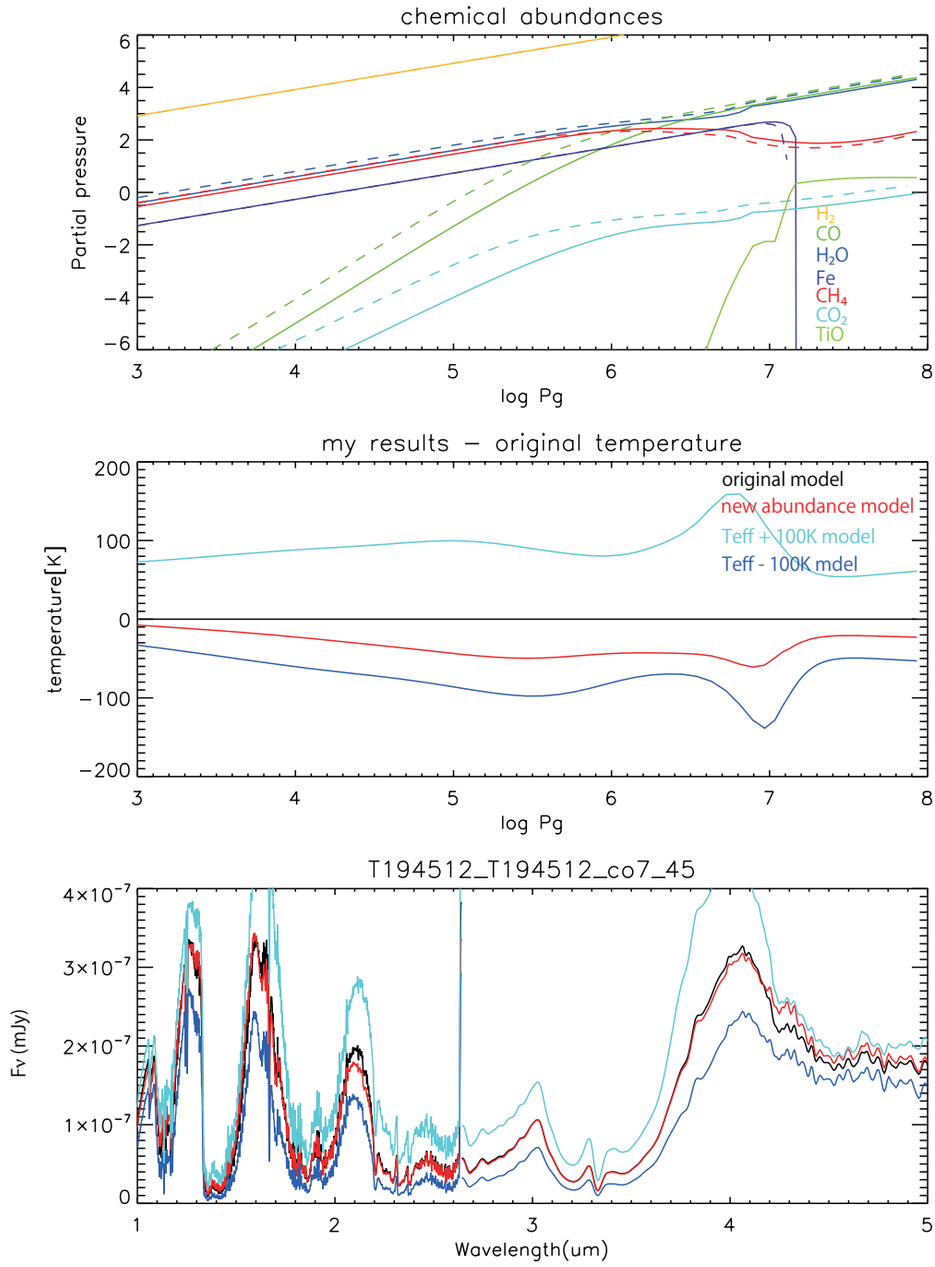


Figure 6.20: Same as Figure 6.4 but the case for decreased C and O abundance.

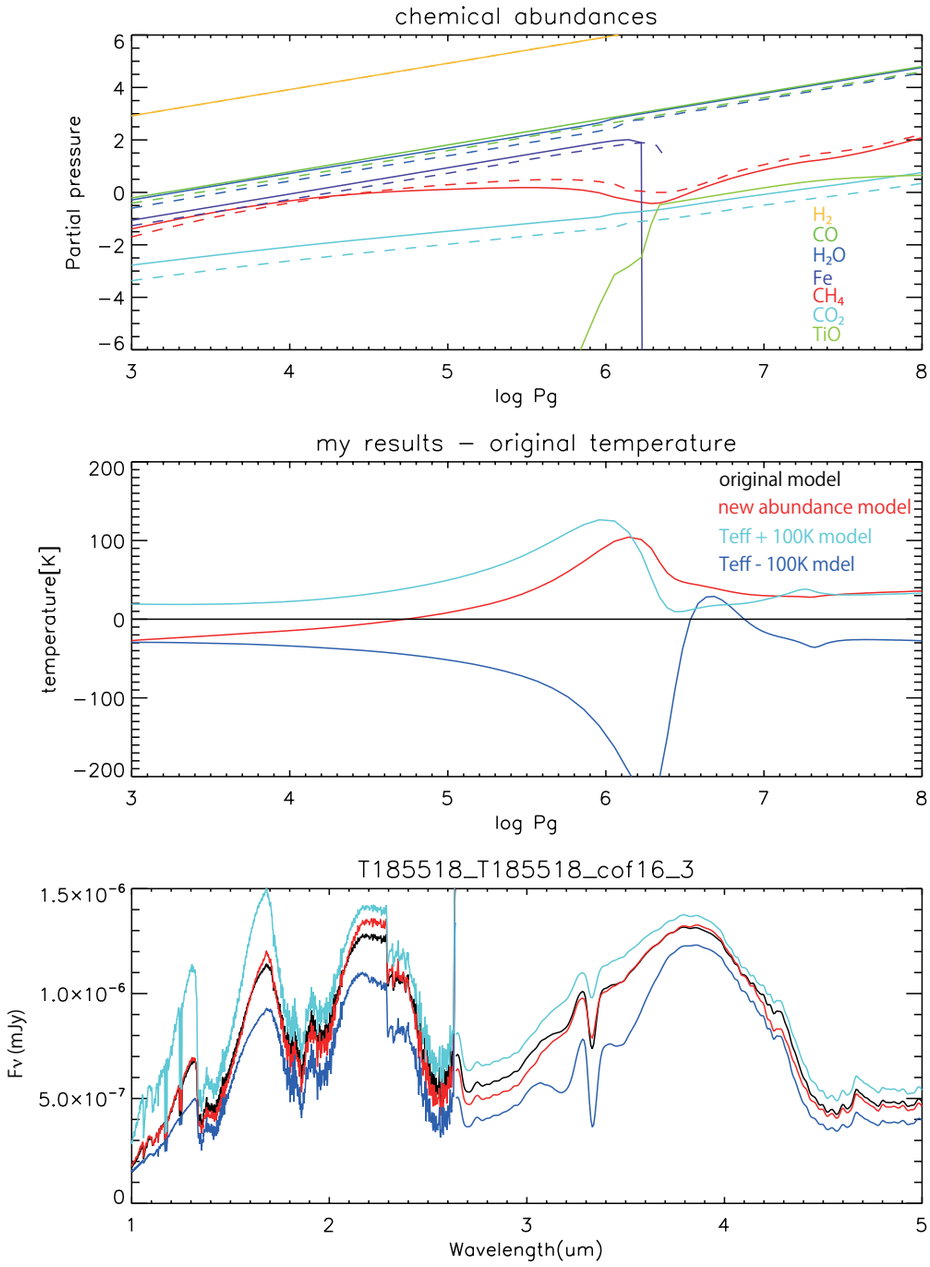


Figure 6.21: Same as Figure 6.1 but the case for increased C and O and Fe abundance.

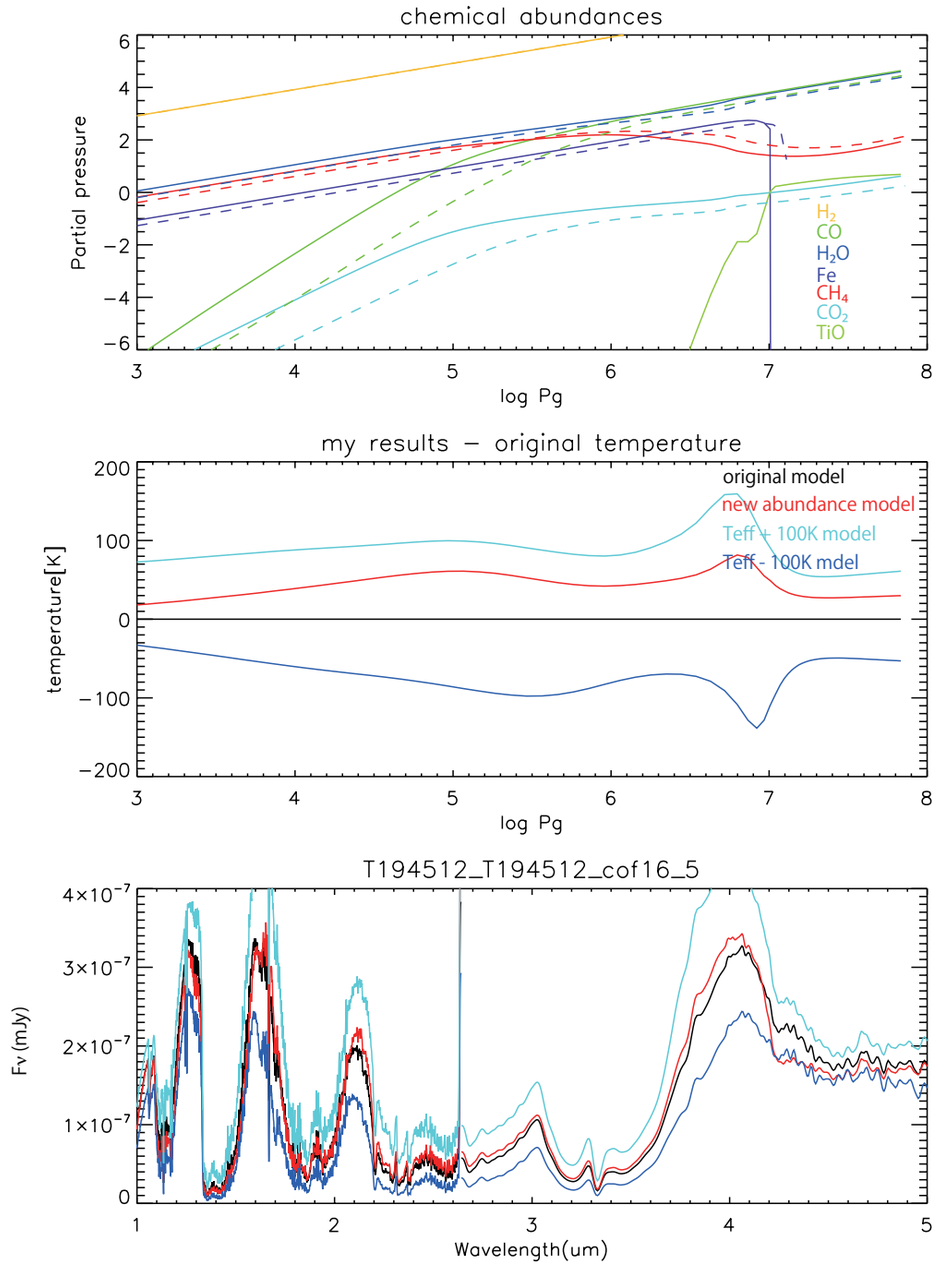


Figure 6.22: Same as Figure 6.2 but the case for increased C and O and Fe abundance.

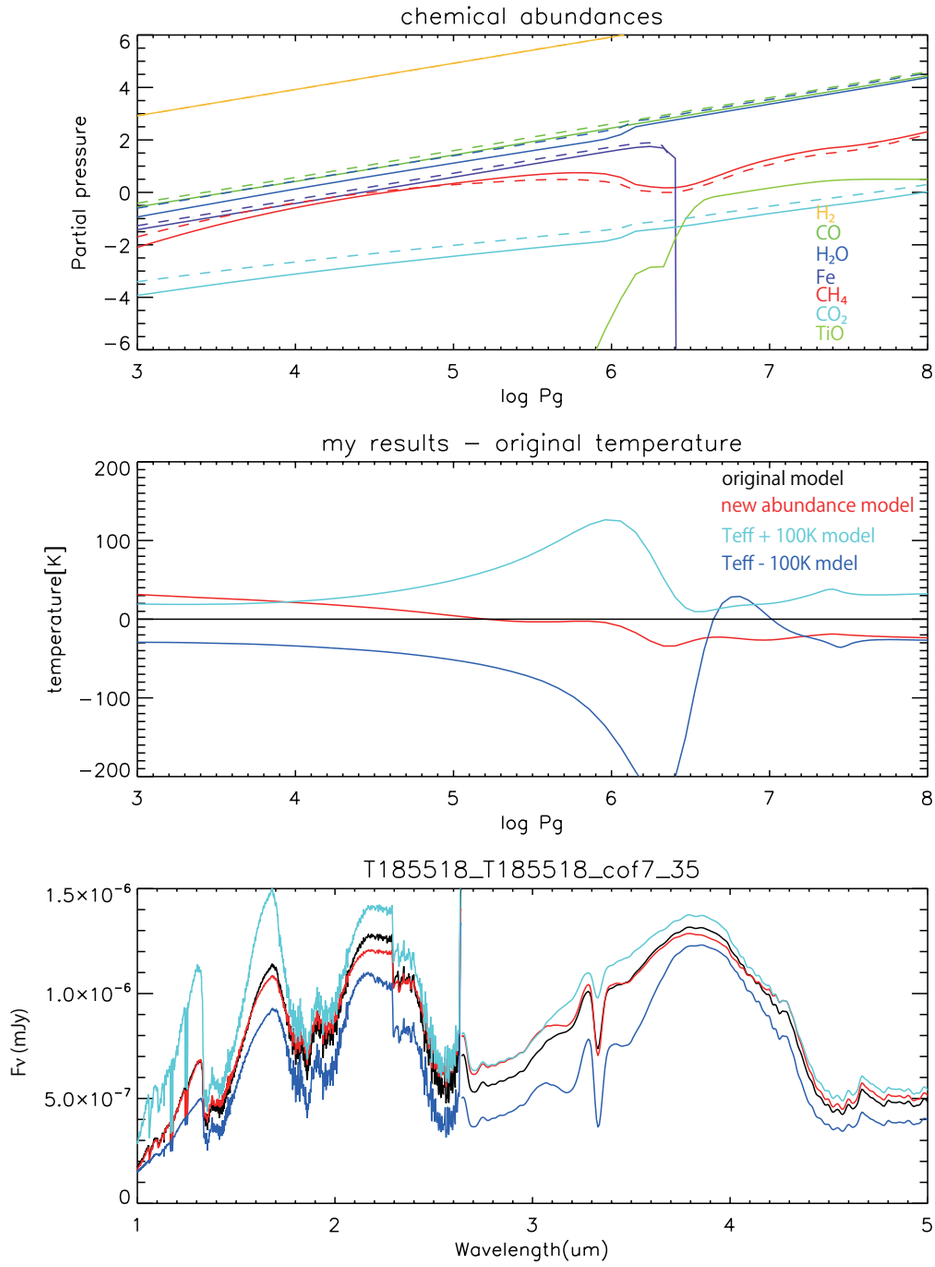


Figure 6.23: Same as Figure 6.3 but the case for decreased C and O and Fe abundance.

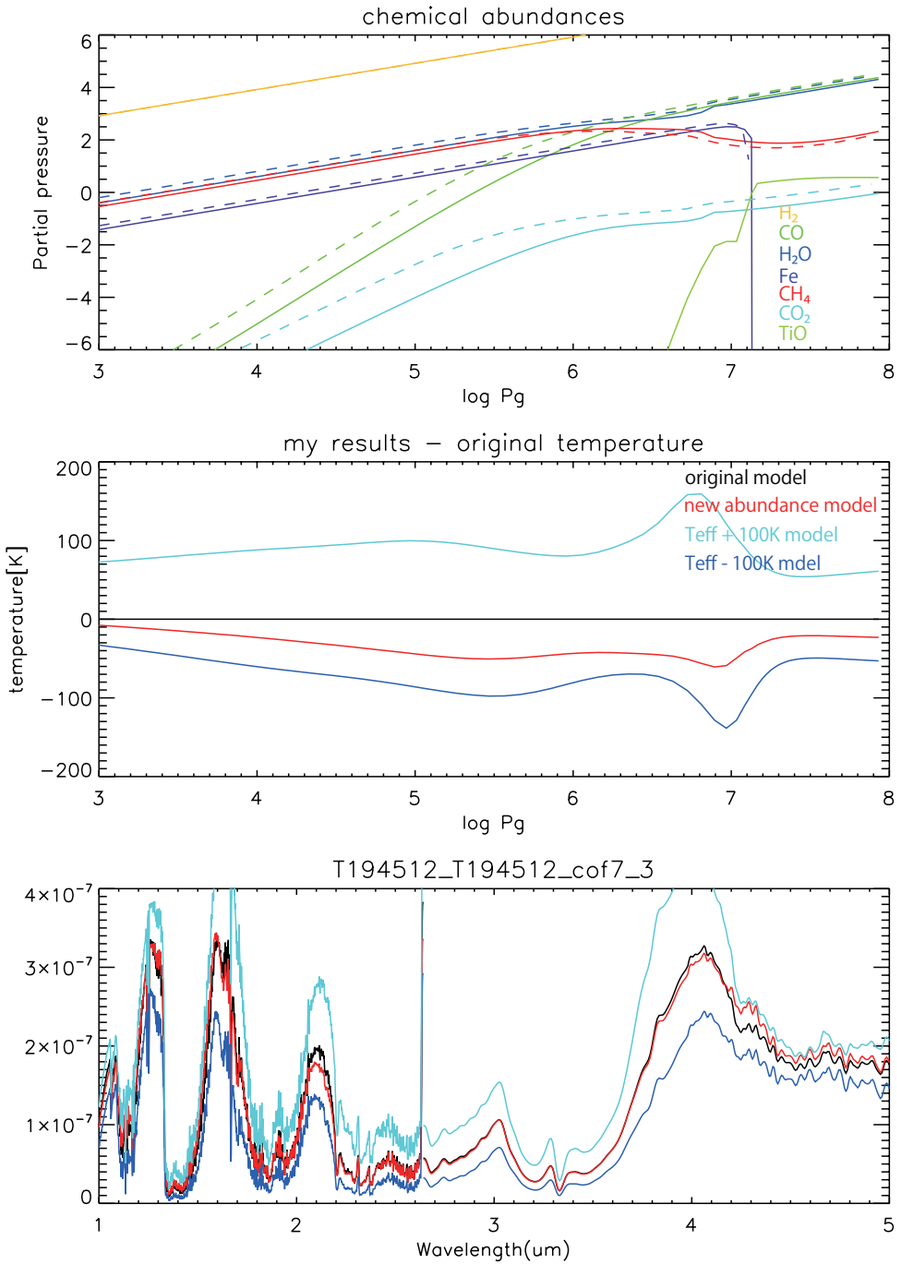


Figure 6.24: Same as Figure 6.4 but the case for decreased C and O and Fe abundance.

## 6.7 Discussion

### 6.7.1 Fitting the $CO_2$ 4.2 $\mu$m Absorption Band with the Models of Different Abundances

We calculate the models with various elemental abundances for the best fit model parameter set derived from *AKARI*+SpeX/CGS4 data in section 4.4, and investigate the behavior of $CO_2$ 4.2 $\mu$m fundamental absorption band. The six cases of changing elemental abundances are all considered. We show the comparison of the *AKARI* observed data and six model spectra for 2MASS J0559–1404(T4.5) as an example. We show the results in Figure 6.25. The $CO_2$ 4.2 $\mu$m absorption band feature in the model spectra of changing C abundance only and Fe abundance only are no better than the original model. For the models with increasing all elemental abundances, the $CO_2$ 4.2 $\mu$m feature gets deeper than the original abundance model, but not enough. For the case of increasing O abundance only, we see that the $CO_2$ 4.2 $\mu$m feature in model spectra is significantly improved, but other features in the model spectra for example $H_2O$ around 2.7 $\mu$m and $CH_4$ in 3.0–4.0 $\mu$m become worse. The $CO_2$ 4.2 $\mu$m band in model spectra of increasing "C and O", and "C and O and Fe" are quite good without changing other features. The model with changing "C and O" is similar to that with changing "C and O and Fe". Since the target is T4.5 dwarf and we see the *AKARI* spectra, the effect of Fe abundance is ignorable.

Next, we apply the model with changing "C and O" to other observations, and investigate the behavior of $CO_2$ 4.2 $\mu$m fundamental absorption band. Unfortunately, we could not calculate the models with changing abundances for the latest T dwarfs. Therefor three sources, 2MASS J1553+1532, Gl 570D and 2MASS J0415–0935, are not treated in the current study. The results are shown in Figure 6.26. We found that the $CO_2$ 4.2 $\mu$m absorption in the spectra of model with increasing "C and O" abundances fits the spectra of 2MASS J0559-1404(T4.5) and 2MASS J0830+4828(L9) better than the model with the solar abundance. This result is consistent with Tsuji et al. (2011). On the other hand, for SDSS J0423–0414(T0) and 2MASS J1523+3014(L8) the models of decreasing "C and O" give better fits than the original models. If we consider only *AKARI* wavelength region as Tsuji et al. (2011), the fits are quite good in other wavelengths. Our results imply that 2MASS J0559–1404(T4.5) and SDSS J0830+4828(L9) are metal-rich relative to the Sun, and SDSS J0423–0414(T0) and 2MASS J1523+3014(L8) are the low metallicity objects. We can say that the $CO_2$ 4.2 $\mu$m band is a unique characteristics of brown dwarfs that can be used to determine the elemental abundances. However, these models do not explain the shorter wavelength range spectra satisfactorily. To convince our results, we also have to consider the data in the shorter wavelength in the future study with improved atmosphere models.

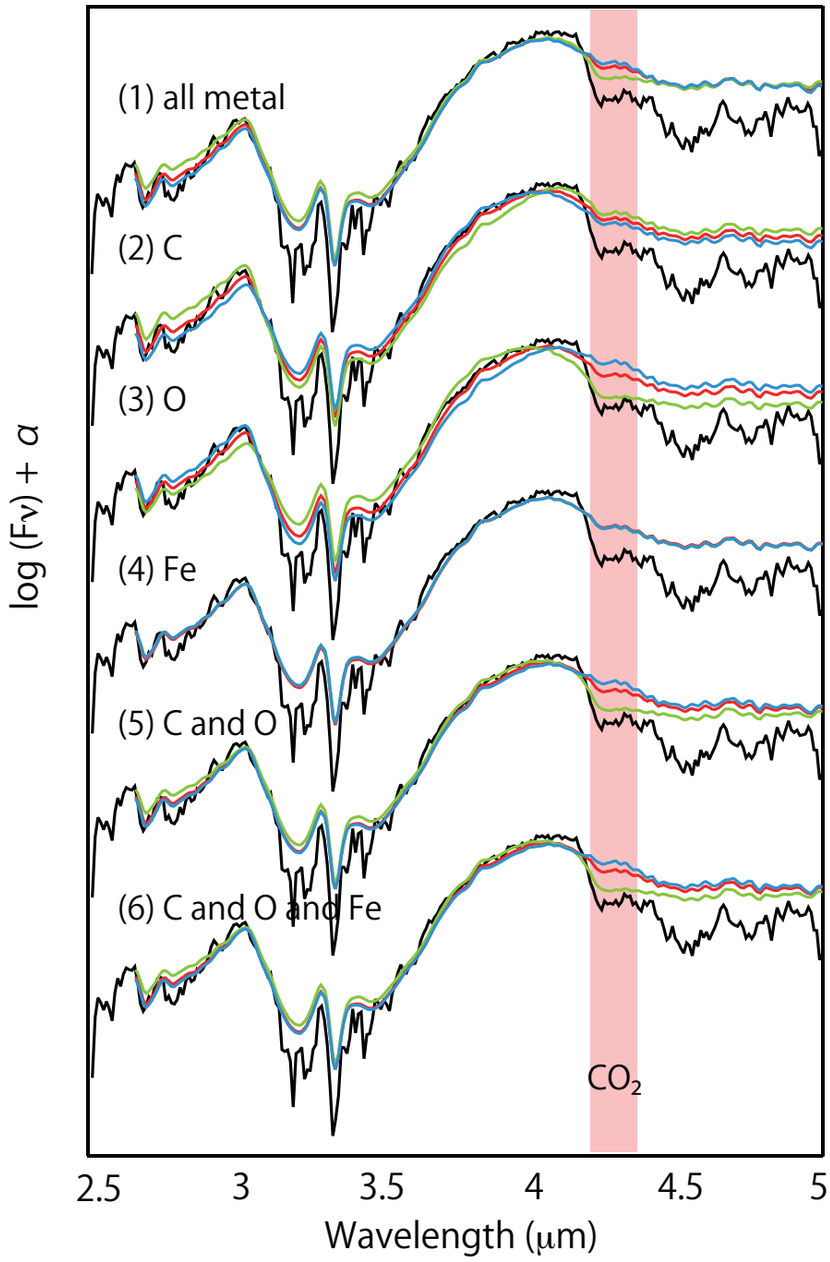


Figure 6.25: The observed and model spectra for 2MASS J0559–1404(T4.5). The model spectra of changing molecular abundance are drawn in color. Red: the model spectra of the solar abundance, green: increasing, and blue: decreasing elemental abundances. The variations of elemental abundances are 6 cases; (1) changing all elemental abundances, (2) C abundance only, (3) O abundance only, (4) Fe abundance only, (5) C and O, and (6) C and O and Fe.

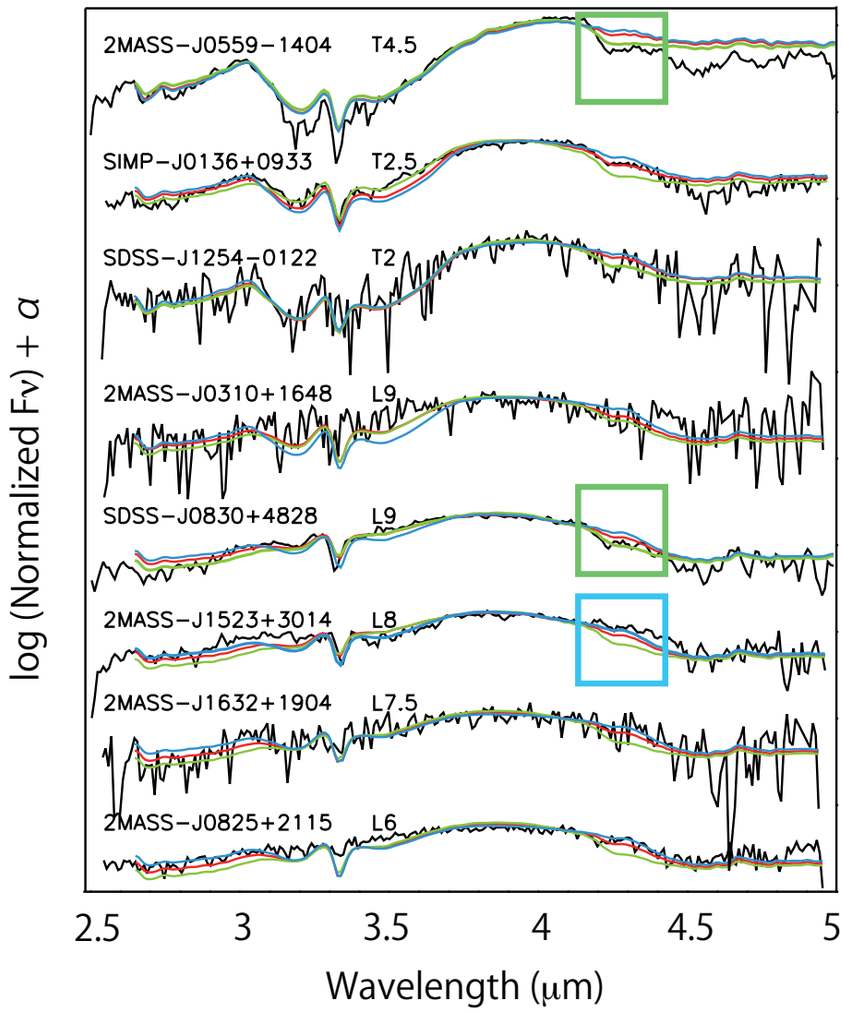


Figure 6.26: The observed and model spectra of late-L to early-T dwarf. Black lines are observed spectra, and red lines are their best fit model spectra for the solar abundance. Green and blue lines are model with increasing and decreasing C and O elemental abundances, respectively. The $CO_2$ 4.2 $\mu$m absorption feature in the spectra of two objects are explained by the model with increasing C and O elemental abundances (green square), and for the other two objects are explained by the decreasing abundances (blue square). The spectra of other five sources can be well explained by the solar abundance.

# Chapter 7

# Conclusion

Throughout this thesis we have studied brown dwarf atmospheres using *AKARI* near-infrared spectra. We conducted an observing program near-infrared spectroscopy of brown dwarfs using *AKARI*, and obtained spectra in 2.5–5.0 $\mu$m with the resolution $R \sim 120$ for 18 objects from L1 to T8. We analyzed the *AKARI* spectra with the Unified Cloudy Models (UCM). We obtained the following results.

- We identified CO, $H_2O$, $CO_2$ and $CH_4$ molecular band in the *AKARI* spectra.
  - We detected the CO 4.6 $\mu$m band clearly in the spectra of all spectral types from L1 to T8 by systematic investigation for the first time. This result indicates that CO exist in all brown dwarf atmospheres generally.
  - The detection of $CO_2$ is made for the first time with *AKARI*.
  - We investigated the behavior of the $CH_4$ 3.3 $\mu$m band systematically for the first time, and confirmed that it appears in the spectra of dwarfs as early as L5. We found that the band did not appear in some L5 dwarfs.
- We analyzed these results with the UCM. We carried out the $\chi^2$ fitting with *AKARI* and IRTF/SpeX or UKIRT/CGS4 as a subservience.
  - From our fitting analysis with the UCM, contribution of dust opacity to spectra becomes largest in the early- to middle-L dwarfs and smaller from middle-L dwarfs to late-T dwarfs. These results attest the past suggestion that almost constant $T_{\rm eff}$ along late-L dwarfs is due to the effect of dust disappearance from the optically thin upper region.
  - Our UCM analysis indicates that the condition for the presence of the $CH_4$ absorption depends on not only $T_{\rm eff}$ but also on surface gravity and dust presence. This result implies that the $CH_4$ absorption appears in the spectra of massive objects for L5 dwarfs.
  - We derived the radii of brown dwarfs and found that the radii of late-L dwarfs are smaller than that of early-L and T dwarfs. The relation between radius and mass of a brown dwarf changes with their evolution. Theory predicts that more massive object have smaller radius when the object is older than about $10^8$ yrs. We verified this theoretical prediction of radius changes along the spectral class at $10^8$ to $10^9$ yrs.

– To understand a problem that we can not determine a unique model that explains the entire wavelength range of an object perfectly, we fitted the AKARI and SpeX/CGS4 spectra separately and compared the results with these fitted to the both *AKARI* + SpeX/CGS4 data. We found that the AKARI spectra was more sensitive to the effective temperature, while dust presence was better determined by the SpeX/CGS4. We suggest that the warming-up effect due to the dust in the photosphere is underestimated in the model than that in the actual photosphere. We proposed that a self-consistent, more realistic theory of condensation and sedimentation in the atmospheres is the most essential in the future models of the brown dwarf atmosphere.

- We attempted to improve a brown dwarf atmosphere model by changing the elemental abundances.

– We found that the observed $CO_2$ absorption bands in some objects are stronger or weaker than the prediction by the model. As a first trial, we constructed a set of models with various elemental abundances. We found a possible deviation of the C and O elemental abundances from those of the solar values.

# Acknowledgement

I am very grateful to my supervisor Prof. Hiroshi Murakami (ISAS/JAXA) for giving me a great opportunity to study the infrared astronomy. My deepest appreciation goes to Dr. Issei Yamamura (ISAS/JAXA) for valuable guidance throughout my all research activity. I thank to Prof. Takashi Tsuji (NAOJ) for his kind permission to access the UCM and helpful many suggestions.

This thesis is based on observations with *AKARI*, a JAXA project with the participation of ESA. I gratefully acknowledge *AKARI* project team for providing high quality data that is critical to this study. The Multi Stack Tool Kit provided by Mr. T. Shimonishi (The University of Tokyo) was used to extract high quality spectra. Dr. Takehiko Wada (ISAS/JAXA) and Mr. Kazumi Murata (SOKENDAI) helped me photometric data calibration. Dr. Kawada (ISAS/JAXA) and Mr. Toshiaki Arai (The University of Tokyo) also discuss error estimate in detail.

Dr. Adam Burgasser (University of California, San Diego), Dr. Michael. Cushing, and Dr. Dagny. Looper (University of Hawaii) provide me observed data generously and warm encouragement.

I also thankful to Prof. Takao Nakagawa (ISAS/JAXA) for fruitful comments in Lira colloquium. The seminars organized by Prof. Hideo Matsuhara (ISAS/JAXA) increase my knowledge of expertise in astronomy and physics. Discussions with Dr. Takafumi Kamizuka (The University of Tokyo) and Dr. Kohji Tsumura (ISAS/JAXA) stimulated my work.

These works have been encouraged by many people especially in the infrared- group at the ISAS. All the staff members and secretaries, Ms. K. Hanawa, M. Ukai, H. Kimura, K. Nishimatsu. I thankful to my family for generous supports.

# Bibliography

Ackerman, A. S., & Marley, M. S. 2001, ApJ, 556, 872

Allard, F., Hauschildt, P. H., Alexander, D. R., Tamanai, A., & Schweitzer, A. 2001, ApJ, 556, 357

Allard, N. F., Allard, F., Hauschildt, P. H., Kielkopf, J. F., & Machin, L. 2003, A&A, 411, L473

Allende Prieto, C., Lambert, D. L., & Asplund, M. 2002, ApJ, 573, L137

Artigau, É., Biller, B. A., Wahhaj, Z., Hartung, M., Hayward, T. L., et al. 2008, SPIE, 7014, 66

Becklin, E. E., & Zuckerman, B. 1988, Nature, 336, 656

Bodaghee, A., Santos, N. C., Israelian, G., & Mayor, M. 2003, A&A, 404, 715

Burgasser, A. J. 2001, Ph.D. thesis, California Institute of Technology

— 2007, ApJ, 659, 655

Burgasser, A. J., Cruz, K. L., Cushing, M., Gelino, C. R., Looper, D. L., et al. 2010, ApJ, 710, 1142

Burgasser, A. J., Geballe, T. R., Leggett, S. K., Kirkpatrick, J. D., & Golimowski, D. A. 2006, ApJ, 637, 1067

Burgasser, A. J., Kirkpatrick, J. D., Brown, M. E., Reid, I. N., Burrows, A., et al. 2002, ApJ, 564, 421

Burgasser, A. J., Liu, M. C., Ireland, M. J., Cruz, K. L., & Dupuy, T. J. 2008, ApJ, 681, 579

Burgasser, A. J., McElwain, M. W., Kirkpatrick, J. D., Cruz, K. L., Tinney, C. G., & Reid, I. N. 2004, ApJ, 127, 2856

Burgasser, A. J., Wilson, J. C., Kirkpatrick, J. D., Skrutskie, M. F., Colonno, M. R., et al. 2000, AJ, 120, 1100

Burrows, A., Hubbard, W. B., Lunine, J. I., & Liebert, J. 2001, RvMP, 73, 719

Burrows, A., Marley, M., Hubbard, W. B., Lunine, J. I., Guillot, T., et al. 1997, ApJ, 491, 856

Cooper, C. S., Sudarsky, D., Milsom, J. A., Lunine, J. I., & Burrows, A. 2003, ApJ, 586, 1320

Cushing, M. C. 2004, Ph.D. thesis, Univercity of Hawaii

Cushing, M. C., Kirkpatrick, J. D., Gelino, C. R., Griffith, R. L., Skrutskie, M. F., et al. 2011, ApJ, 743, 50

Cushing, M. C., Marley, M. S., Saumon, D., Kelly, B. C., Vacca, W. D., et al. 2008, ApJ, 678, 1372

Cushing, M. C., Rayner, J. T., & Vacca, W. D. 2005, ApJ, 623, 1115

Cushing, M. C., Roellig, T. L., Marley, M. S., Saumon, D., Leggett, S. K., et al. 2006, ApJ, 648, 614

Cushing, M. C., Vacca, W. D., & Rayner, J. T. 2004, PASP, 116, 362

Cutri, R. M., Skrutskie, M. F., van Dyk, S., Beichman, C. A., Carpenter, J. M., et al. 2003, yCat., 2246, 0

Dahn, C. C., Harris, H. C., Vrba, F. J., Guetter, H. H., Canzian, B., et al. 2002, AJ., 124, 1170

Delfosse, X., Tinney, C. G., Forveille, T., Epchtein, N., Bertin, E., et al. 1997, A&A, 327, L25

Eisenhardt, P. R. M., Griffith, R. L., Stern, D., Wright, E. L., Ashby, M. L. N., et al. 2010, AJ, 139, 2455

Fan, X., Knapp, G. R., Strauss, M. A., Gunn, J. E., Lupton, R. H., et al. 2000, AJ, 119, 928

Fegley, B., Jr., & Lodders, K. 1996, ApJ, 472, L37

Geballe, T. R., Knapp, G. R., Leggett, S. K., Fan, X., Golimowski, D. A., et al. 2002, ApJ, 564, 466

Geballe, T. R., Saumon, D., Golimowski, D. A., Leggett, S. K., Marley, M. S., & Noll, K. S. 2009, ApJ, 695, 844

Golimowski, D. A., Leggett, S. K., Marley, M. S., Fan, X., Geballe, T. R., et al. 2004, AJ, 127, 3516

Griffith, C. A., & Yelle, R. V. 1999, ApJ, 519, L85

Hauschildt, P. H., Baron, E., & Allard, F. 1997, ApJ, 483, 390

Hawley, S. L., Covey, K. R., Knapp, G. R., Golimowski, D. A., Fan, X., et al. 2002, AJ, 123, 3409

Hayashi, C., & Nakano, T. 1963, PThPh, 30, 460

Helling, C., Ackerman, A., Allard, F., Dehn, M., Hauschildt, P., et al. 2008, MNRAS, 391, 1854

Helling, C., Oevermann, M., Lüttke, M. J. H., Klein, R., & Sedlmayr, E. 2001, A&A, 376, 194

Jameson, R. F., Casewell, S. L., Bannister, N. P., Lodieu, N., Keresztes, K., et al. 2008, MNRAS, 384, 1399

Kawada, M., Baba, H., Barthel, P. D., Clements, D., Cohen, M., et al. 2007, PASJ, 59, 389

King, R. R., McCaughrean, M. J., Homeier, D., Allard, F., Scholz, R.-D., & Lodieu, N. 2010, A&A, 510, 99

Kirkpatrick, J. D., Cushing, M. C., Gelino, C. R., Griffith, R. L., Skrutskie, M. F., et al. 2011, ApJS, 197, 19

Kirkpatrick, J. D., Henry, T. J., & Liebert, J. 1993, ApJ, 406, 701

Kirkpatrick, J. D., Reid, I. N., Liebert, J., Cutri, R. M., Nelson, B., et al. 1999, ApJ, 519, 802

Kirkpatrick, J. D., Reid, I. N., Liebert, J., Gizis, J. E., Burgasser, A. J., et al. 2000, AJ., 120, 447

Knapp, G. R., Leggett, S. K., Fan, X., Marley, M. S., Geballe, T. R., et al. 2004, AJ, 127, 3553

Kumar, S. S. 1963, ApJ, 137, 1126

Larimer, J. W. 1967, GeCoA, 31, 1215

Larimer, J. W., & Anders, E. 1967, GeCoA, 31, 1239

Leggett, S. K., Allard, F., Geballe, T. R., Hauschildt, P. H., & Schweitzer, A. 2001, ApJ, 548, 908

Leggett, S. K., Allard, F., & Hauschildt, P. H. 1998, ApJ, 509, 836

Leggett, S. K., Cushing, M. C., Saumon, D., Marley, M. S., Roellig, T. L., et al. 2009, ApJ, 695, 1517

Leggett, S. K., Geballe, T. R., Fan, X., Schneider, D. P., Gunn, J. E., et al. 2000, ApJ, 536, L35

Leggett, S. K., Golimowski, D. A., Fan, X., Geballe, T. R., Knapp, G. R., et al. 2002a, ApJ, 564, 452

Leggett, S. K., Hauschildt, P. H., Allard, F., Geballe, T. R., & Baron, E. 2002b, MNRAS, 332, 78

Leggett, S. K., Saumon, D., Marley, M. S., Geballe, T. R., Golimowski, D. A., et al. 2007, ApJ, 655, 1079

Lord, H. C., III 1965, lcar, 4, 279

Lorente, N. P. F., Glasse, A. C. H., Ramsay Howat, S. K., & Evans, C. J. 2008, ASPC, 394, 187

Marley, M. S., Seager, S., Saumon, D., Lodders, K., Ackerman, A. S., et al. 2002, ApJ, 568, 335

Martin, E. L. 1997, A&A, 321, 492

Martín, E. L., Delfosse, X., Basri, G., Goldman, B., Forveille, T., & Zapatero Osorio, M. R. 1999, AJ, 118, 2466

McLean, I. S., Wilcox, M. K., Becklin, E. E., Figer, D. F., Gilbert, A. M., et al. 2000, ApJ, 533, L45

Murakami, H., Baba, H., Barthel, P., Clements, D. L., Cohen, M., et al. 2007, PASJ, 59, 369

Nakajima, T., Oppenheimer, B. R., Kulkarni, S. R., Golimowski, D. A., Matthews, K., & Durrance, S. T. 1995, Nature, 378, 463

Nakajima, T., Tsuji, T., & Yanagisawa, K. 2001, ApJ, 561, L119

Noll, K. S., Geballe, T. R., Leggett, S. K., & Marley, M. S. 2000, ApJ, 541, L75

Noll, K. S., Geballe, T. R., & Marley, M. S. 1997, ApJ, 489, L87

Ohyama, Y., Onaka, T., Matsuhara, H., Wada, T., Kim, W., et al. 2007, PASJ, 59, 411

Onaka, T., Matsuhara, H., Wada, T., Fujishiro, N., Fujiwara, H., et al. 2007, PASJ, 59, 401

Oppenheimer, B. R., Kulkarni, S. R., Matthews, K., & Nakajima, T. 1995, Science, 270, 1478

Oppenheimer, B. R., Kulkarni, S. R., Matthews, K., & van Kerkwijk, M. H. 1998, APJ, 502, 932

Reid, I. N., Burgasser, A. J., Cruz, K. L., Kirkpatrick, J. D., & Gizis, J. E. 2001, AJ, 121, 1710

Saumon, D., Geballe, T. R., Leggett, S. K., Marley, M. S., Freedman, R. S., et al. 2000, ApJ, 541, 374

Saumon, D., & Marley, M. S. 2008, ApJ, 689, 1327

Saumon, D., Marley, M. S., Cushing, M. C., Leggett, S. K., Roellig, T. L., et al. 2006, ApJ, 647, 552

Schweitzer, A., Hauschildt, P. H., & Baron, E. 2000, ApJ, 541, 1004

Stephens, D. C., Marley, M. S., Noll, K. S., & Chanover, N. 2001, ApJ, 556, L97

Strauss, M. A., Fan, X., Gunn, J. E., Leggett, S. K., Geballe, T. R., et al. 1999, ApJ, 522, L61

Tanabé, T., Sakon, I., Cohen, M., Wada, T., Ita, Y., et al. 2008, PASJ, 60, 375

Testi, L., Natta, A., Shepherd, D. S., & Wilner, D. J. 2001, ApJ, 554, 1087

Tokunaga, A. T., & Kobayashi, N. 1999, AJ, 117, 1010

Tsuji, T. 2000, Dust in Very Cool Dwarfs (Cambridge: Cambridge University Press), 1st ed.

— 2002, ApJ, 575, 264

— 2005, ApJ, 621, 1033

Tsuji, T., Ohnaka, K., & Aoki, W. 1996a, A&A, 305, L1

Tsuji, T., Ohnaka, K., Aoki, W., & Nakajima, T. 1996b, A&A, 308, L29

Tsuji, T., Yamamura, I., & Sorahana, S. 2011, ApJ, 734, 73

Vrba, F. J., Henden, A. A., Luginbuhl, C. B., Guetter, H. H., Munn, J. A., et al. 2004, AJ, 127, 2948

Wilson, J. C., Kirkpatrick, J. D., Gizis, J. E., Skrutskie, M. F., Monet, D. G., & Houck, J. R. 2001, AJ, 122, 1989

Woitke, P., & Helling, C. 2003, A&A, 399, 297

— 2004, A&A, 414, 335

Yamamura, I., Tsuji, T., & Tanabé, T. 2010, ApJ, 722, 682

Zuckerman, B., & Becklin, E. E. 1992, ApJ, 386, 260